Magmatic versus amagmatic

-

a study of local seismicity and lithospheric structure at two contrasting Southwest Indian Ridge segments

Kumulative Dissertationsarbeit

zur Erlangung des Grades
- Dr. rer. nat. -
vorgelegt am Fachbereich Geowissenschaften der Universität Bremen
von

Florian Michael Schmid

Alfred-Wegener-Institut
Helmholtz-Zentrum für Polar- und Meeresforschung Bremerhaven

Bremen/Bremerhaven September 2017

Gutachter: Prof. Dr. Wolfgang Bach (Universität Bremen)
Prof. Dr. Ingo Grevemeyer (GEOMAR Kiel)

Datum des Einreichens: 1. September 2017
Datum Promotionskolloquium: 6. November 2017

Die vorliegende Promotionsarbeit wurde angefertig im Rahmen der DFG-geförderten Emmy-Noether Nachwuchsgruppe **MOVE** (Mid-ocean volcanoes and earthquakes), geleitet von PD Dr. Vera Schlindwein am Alfred-Wegener-Institut, Helmholtz-Zentrum für Polar- und Meeresforschung, Bremerhaven.

Für meinen Bruder, 'Proof' Jakob
Der viel zu früh gehen musste

Zusammenfassung

An den globalen Mittelozeanischen Rücken (MOR) wird kontinuierlich neuer Meeresboden gebildet. Über eine große Bandbreite von Spreizungsraten hinweg besitzt die dabei gebildete Kruste eine erstaunlich homogene Mächtigkeit und Zusammensetzung. Dort, wo die Spreizungsraten geringer sind als ca. 15-20 mm a^{-1}, an den sogenannten ultralangsamen Rücken, ändert sich dies jedoch drastisch. Schmelze tritt nicht mehr kontinuierlich an die Oberfläche. Stattdessen findet sich an ausgedehnten Rückensegmenten Mantelgestein am Meeresboden und eine magmatische Kruste fehlt gänzlich. Die benachbarten Segmente hingegen, oft bestückt mit großen untermeerischen Vulkanen, erhalten ungewöhnlich viel Schmelze und die Kruste ist ungewöhnlich mächtig. Die prominentesten Vertreter der ultralangsamen Rücken sind der Gakkel Rücken im eisbedeckten Arktischen Ozean und der Südwestindische Rücken (SWIR) im stürmischen Südozean. Bis heute sind die Prozesse der Entstehung neuer Lithosphäre an ultralangsamen Rücken nur bruchstückhaft verstanden.

Die Untersuchung von Mikroerdbeben an schneller spreizenden MOR mit Netzwerken von Ozeanbodenseismometern (OBS) oder Hydrophonen haben in der Vergangenheit einen entscheidenden Beitrag zum Verständnis der Entstehung neuer Ozeanlithosphäre geleistet. Die rauen Witterungsbedingungen haben bis vor kurzem jedoch jeglichen Langzeiteinsatz von OBS an ultralangsamen Rücken verhindert. Der erstmalige Langzeiteinsatz von OBS in zwei getrennten Netzwerken am ultralangsamen SWIR von 2012 bis 2013 lieferte die Datenbasis für diese Dissertationsarbeit. Die Lokationen dieser Netzwerke unterscheiden sich deutlich in der Krustenmächtigkeit, Morphologie und Lithologie. Das Oblique Supersegment Netzwerk wurde nahe 13°30'E an einem SWIR Segment installiert, an dem eine gewöhnliche magmatische Kruste fehlt und fast ausschließlich Peridotit am Meeresboden ansteht. Das Segment 8 Netzwerk befand sich nahe 65°30'E an einem SWIR Segment, an dem die magmatische Kruste sehr mächtig ist und ausschließlich Basalt am Meeresboden gefunden wurde.

Ich habe die Erdbeben-Phaseneinsätze in den Daten des Oblique Supersegment Netzwerks gepickt, die Erdbeben lokalisiert und anhand dessen einen Katalog der lokalen Seismizität mit ca. 2000 Erdbeben erstellt. Diesen Erdbebenkatalog habe ich dann genutzt, um sogenannte Yield-Strength Envelopen zu berechnen, aus denen rheologische und thermische Eigenschaften der Lithosphäre abgeleitet werden können. Den bereits vorhandenen Katalog der Mikroseismizität von dem Segment 8 Netzwerk habe ich genutzt für eine Lokale Erdbebentomographie, um ein dreidimensionales Abbild der seismischen Geschwindigkeiten unter dem Netzwerk zu bekommen.

Die Zusammenschau der Erdbebenergebnisse von beiden Netzwerken hat gezeigt, dass es systematische Änderungen in der maximalen Herdtiefe von Mikroerdbeben entlang der SWIR Spreizungsachse gibt. Generell liegen die Hypozentren tiefer unter amagmatischen Rückensegmenten und flacher unter magmatischen Segmenten.

Die maximale Tiefe von Erdbeben (der Spröd-Duktil Übergang) ist im Wesentlichen abhängig von der Temperatur. Ihre Lage zeigt deshalb auch Veränderungen in der thermischen Struktur der Lithosphäre an. Die beobachteten Undulationen des Spröd-Duktil Übergangs implizieren parallele Undulationen in der darunterliegenden Lithosphären-Asthenosphären Grenze. Vorhergehende Studien haben gefordert, dass eine solche Topographie der Lithosphären-Asthenosphären Grenze unter ultralangsamen Rücken vorhanden sein muss. Dadurch kann Mantelschmelze von amagmatischen Segmenten hin zu magmatischen Segmenten fließen und sorgt so für das ungleichmäßige Auftreten von Schmelze entlang der Rückenachse. Die beobachtete Verteilung der Mikroseismizität entlang der SWIR Achse liefert nun zum ersten mal einen geophysikalischen Beweis für diese Hypothese.
Unter dem Oblique Supersegment Netzwerk sind ausgedehnte Bereiche der oberen Lithosphäre, bis in 15 km Tiefe, komplett aseismisch und zwar genau dort wo Peridotit am Meeresboden ansteht. Dieses aseismische Verhalten kann am besten durch eine tiefreichende Serpentinisierung erklärt werden. Diese schwächt die Lithosphäre und tritt möglicherweise verstärkt an den Randstörungen des Rifttals auf. Geochemische Analysen deuten erhöhte diffusive Flussraten im Sediment nahe dieser Randstörungen an. Leicht erhöhte Methankonzentrationen in den Wasserschichten des Rifttals stammen sehr wahrscheinlich aus abiotischen Prozessen in der Lithosphäre, welche im Zusammenhang stehen mit der tiefen Serpentinisierung.
Die lokale Erdbeben Tomographie basierend auf dem Segment 8 Datensatz zeigt eine prominente Zone mit verringerten seismischen Geschwindigkeiten unter dem dortigen vulkanischen Zentrum. Dies deutet auf das Vorhandensein partieller Schmelzen unter dem Vulkan hin. Die Kombination sämtlicher seismologischer Beobachtungen hat es mir ermöglicht, das magmatische Spreizungs-Ereignis, welches noch während des OBS Experiments im Gange war, zu rekonstruieren. Mit einer Aktivitätsphase von ca. 13 Jahren ist das untersuchte Spreizungs-Ereignis erheblich länger als sämtliche zuvor beschriebene Spreizungs-Ereignisse an aktiven MOR.
Zusammenfassend lässt sich sagen, dass die Ergebnisse dieser Arbeit zum ersten Mal einen detaillierten Einblick geben in die Mikroseismizität an zwei Segmenten des SWIR. Mit der Analyse und Interpretation dieser Erdbebendaten liefert diese Arbeit einen wertvollen Beitrag zum besseren Verständnis der Entstehung neuer Lithosphäre unter ultralangsamen Spreizungsraten.

Summary

New seafloor is constantly being created at the global spanning system of mid-ocean ridges (MOR). Over a wide range of spreading rates is the produced oceanic crust of surprisingly uniform thickness and composition. An exception are ridges with spreading rates slower than 15-20 mm yr^{-1}, so-called ultraslow spreading MORs, at which the crustal thickness and composition drastically change. A totally different mode of seafloor spreading occurs, with discontinuous crustal accretion along-axis. Entire sections of the ridge axis lack an igneous crust and the neighbouring volcanoes receive more melt than the regional average. The Gakkel Ridge in the ice-covered Arctic Ocean and the Southwest Indian Ridge (SWIR) in the stormy Southern Ocean are the main representatives of the ultraslow spreading ridges. At present, the processes of lithosphere formation at ultraslow spreading rates are still poorly understood.

The investigation of microearthquakes, with networks of ocean bottom seismometers (OBS) or hydrophones, has significantly progressed our understanding of the lithosphere accretion processes at faster spreading ridges. Until recently, the rough environmental conditions prevented the long-term deployment of OBSs at the main representatives of ultraslow ridges. This thesis makes use of the first one-year long records from two OBS networks with comparable extent that had been placed at different sections of the SWIR from 2012 to 2013. The chosen sites are characterized by contrasting crustal thickness, lithology and morphology. The Oblique Supersegment network was deployed near 13°30'E where peridotites are the dominant seafloor lithology and a typical igneous crust is absent. The Segment 8 network was deployed near 65°30'E around the volcanic center of the SWIR Segment 8 where the crust is locally thickened and the seafloor consists exclusively of basalts.

I picked and located the microearthquakes for the Oblique Supersegment network and compiled an 11-month long catalogue that contains 2000 microearthquakes. This catalogue was subsequently used to calculate so-called yield-strength envelopes of the lithosphere that provide constraints on the rheological strength and the geothermal gradient below the axial valley. I further used an existing microearthquake catalogue of the Segment 8 network for a local earthquake tomography to image the 3-dimensional structure of seismic velocities below the SWIR Segment 8.

The combined seismicity catalogues from both networks showed systematic undulations in the maximum depth of faulting (brittle-ductile transition) along the SWIR axis; with deeper hypocenters below amagmatic ridge segments and shallower hypocenters below magmatic segments. The brittle-ductile transition is mainly temperature related. Thus, its position provides insight into the sub-axial thermal structure. The undulating hypocenter depths imply parallel undulations of the deeper lithosphere-asthenosphere boundary, under which molten material is constantly present. Previous studies postulated such a topography of the lithosphere-asthenosphere boundary that guides the buoyantly flowing mantle melts from amagmatic segments towards magmatic centers and thereby maintains the pattern of uneven melt supply along the SWIR. The combined microseismicity results from both OBS networks strongly support this hypothesis and provide the missing geophysical proof of this concept.

An extensive aseismic region extending to 15 km depth was found in the upper lithosphere at the Oblique Supersegment, where peridotite is the dominant lithology. The aseismic behaviour is best explained by weakening of the lithosphere by serpentinization, likely focused in aseismic shear zones that constitute the rift valley bounding faults. Geochemical sampling revealed enhanced diffusive fluxes near the scarp of a bounding fault and increased methane concentrations in the valley waters that likely stem from abiotic, serpentinization-related processes.

The local earthquake tomography of the SWIR Segment 8 network showed a prominent low-velocity anomaly below the segment's volcanic center that indicates the presence of partial melts. In addition, preceding teleseismic activity and recorded microearthquake swarms with simultaneous intrusion tremor pointed to an ongoing spreading event. It turned out that this magmatic spreading episode likely lasted already over a decade and thereby vastly exceeds the duration of all previously documented magmatic spreading episodes at active MORs.

In summary, this thesis provides for the first time a detailed insight into the microearthquake activity at two SWIR segments. The analysis and interpretation of the data presented in this thesis significantly contribute to a better understanding of the lithospheric structure and the seafloor accretion processes at ultraslow spreading MORs.

Versicherung an Eides Statt / *Affirmation in lieu of an oath*

gem. § 5 Abs. 5 der Promotionsordnung vom 15.07.2015 /

according to § 5 (5) of the Doctoral Degree Rules and Regulations of 15 July, 2015

Ich / I, Florian Michael Schmid, Buddestraße 35, 28215 Bremen, Matr. Nr. 2229329

versichere an Eides Statt durch meine Unterschrift, dass ich die vorstehende Arbeit selbständig und ohne fremde Hilfe angefertigt und alle Stellen, die ich wörtlich dem Sinne nach aus Veröffentlichungen entnommen habe, als solche kenntlich gemacht habe, mich auch keiner anderen als der angegebenen Literatur oder sonstiger Hilfsmittel bedient habe, und die zu Prüfungszwecken beigelegte elektronische Version der Dissertation (PDF) mit der abgegebenen gedruckten Version identisch ist.
With my signature I affirm in lieu of an oath that I prepared the submitted dissertation independently and without illicit assistance from third parties, that I appropriately referenced any text or content from other sources, that I used only literature and resources listed in the dissertation, and that the electronic (PDF) and printed versions of the dissertation are identical.

Ich versichere an Eides Statt, dass ich die vorgenannten Angaben nach bestem Wissen und Gewissen gemacht habe und dass die Angaben der Wahrheit entsprechen und ich nichts verschwiegen habe.
I affirm in lieu of an oath that the information provided herein to the best of my knowledge is true and complete.

Die Strafbarkeit einer falschen eidesstattlichen Versicherung ist mir bekannt, namentlich die Strafandrohung gemäß§ 156 StGB bis zu drei Jahren Freiheitsstrafe oder Geldstrafe bei vorsätzlicher Begehung der Tat bzw. gemäß§ 161 Abs. 1 StGB bis zu einem Jahr Freiheitsstrafe oder Geldstrafe bei fahrlässiger Begehung.
I am aware that a false affidavit is a criminal offence which is punishable by law in accordance with § 156 of the German Criminal Code (StGB) with up to three years imprisonment or a fine in case of intention, or in accordance with § 161 (1) of the German Criminal Code with up to one year imprisonment or a fine in case of negligence.

Bremen, den 1.9.2017 — Florian Michael Schmid

Table of Contents

1 Introduction and Motivation

1.1 The role of ultraslow spreading mid-ocean ridges

Where oceanic plates drift apart they create an impressive continuous submarine mountain range - the global spanning mid-ocean ridge (MOR) system. Mid-ocean ridges are the earth's main locus of molten rock and heat from the asthenosphere (*Rubin*, 2014; *Stein and Stein*, 1994). Moreover, they host oases of deep-sea life, often around hydrothermal vent sites (*Konn et al.*, 2015), in the otherwise mostly desert-like abyss. When detailed seafloor maps became available in the 1970s and 1980s it was found that the general shape, the axial seafloor depth and further characteristics of MORs are predominantly a function of the average velocity at which opposing plates drift apart (*DeMets et al.*, 1994). The following classification scheme of MORs evolved, as the state of knowledge progressed, and is nowadays widely used:

Ridge class	**Full spreading rate [mm a^{-1}]**
Fast spreading	> 80
Intermediate spreading	50-80
Slow-spreading	20-50
Ultraslow spreading	< 20

About 15% of the global spanning MOR system (Figure 1.1), that has a total length of approximately 60,000 km, open slower than 20 mm a^{-1} and thus belong to the ultraslow spreading class. Ultraslow ridges include the Arctic Ridge System - comprising Gakkel Ridge, Lena Trough, Knipovich Ridge - and the Southwest Indian Ridge (SWIR) as their largest members. Shorter MOR sections spreading at ultraslow rates are the Mid-Cayman Rise and the Mohns Ridge (Figure 1.1).
The crustal thickness of the oceanic lithosphere is commonly used as a direct observable and robust measure for the amount of melt produced at MORs. Compilations of geophysical and geochemical data showed that away from fracture zones, hot spots and marginal basins the crustal thickness, the rare earth element concentrations and the bulk crustal composition are remarkably uniform in most of the ocean basins except from the slowest spreading ridges (Figure 1.2; *Bown and White*, 1994; *Reid and Jackson*, 1981; *White et al.*, 1992).

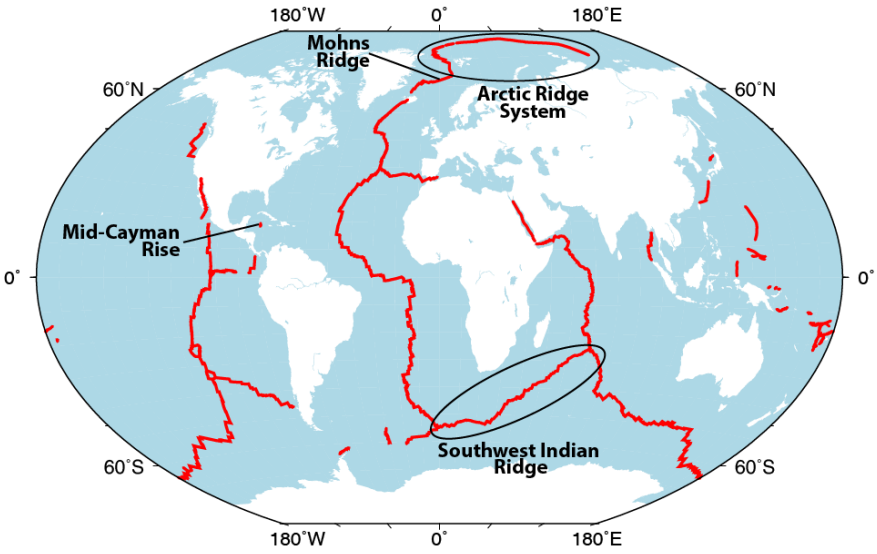

Figure 1.1 Global overview map that shows the location of all active oceanic spreading centers in red, compiled from plate boundary location dataset of *Bird* (2003). All spreading centers opening at 20 mm a^{-1} or slower are labelled. Note, the Arctic Ridge System includes, from west to east, the Knipovich Ridge, the Lena Trough and the Gakkel Ridge. In most of the literature the Mohns Ridge is not considered as part of the Arctic Ridge System.

Where the spreading rates are lower than 15-20 mm a^{-1} these properties of the ocean lithosphere experience drastic changes (*White et al.*, 2001). Due to reduced mantle upwelling velocities the conductive heat loss is of importance for the thermal regime at the slowest spreading ridges and hampers the production of melt (*Bown and White*, 1994; *White et al.*, 1992, 2001). Accordingly, theoretical models predict a vastly reduced melt production at ultraslow spreading ridges (*White et al.*, 2001).

Within the last two decades a number of geoscientific expeditions targeted ultraslow spreading ridges to widen our understanding of their structure, composition and the processes of lithospheric accretion. Geophysical studies revealed the existence of extensive amagmatic segments at ultraslow ridges that are characterized by an exceptionally thin or absent crust (*Cannat et al.*, 2003; *Jokat and Schmidt-Aursch*, 2007; *Jokat et al.*, 2003) where mantle rocks are regularly exposed (*Dick et al.*, 2003; *Sauter and Cannat*, 2010; *Sauter et al.*, 2008). Amagamtic segments are a feature that is unique to ultraslow spreading ridges (*Dick et al.*, 2003; *Standish et al.*, 2008). *Dick et al.* (2003) argued that these ridge sections represent a new form of plate boundary that may assume any orientation relative to the spreading direction and can therefore replace transform faults.

The discovery of prominent magmatic centers inbetween the amagmatic segments was very unexpected from the results of the melting models. At those magmatic centers the crust can reach thicknesses up to 9.5 km (*Dick et al.*, 2003; *Jokat et al.*, 2003; *Li et al.*, 2015; *Muller et al.*, 1999). Magmatic centers often host impressive axial volcanoes that are capable of explosive eruptions (*Schlindwein and Riedel*, 2010; *Sohn et al.*, 2008) and unusually strong earthquake swarms (*Müller and Jokat*, 2000; *Schlindwein*, 2012). The overthickened crust beneath these magmatic centers implies a melt flow that is way above the regional average (*Cannat et al.*, 2003; *Muller et al.*, 1999; *Sauter and Cannat*, 2010). Several authors attribute this enhanced melt flow to the focussing of melts

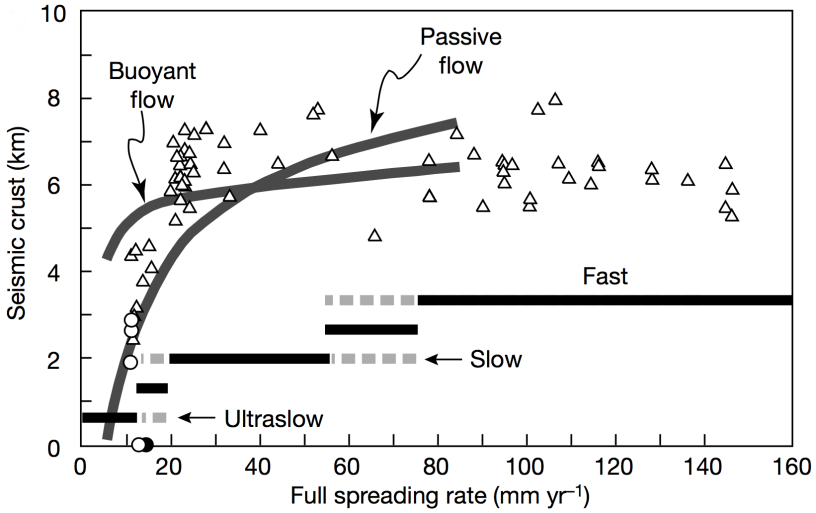

Figure 1.2 Plot of mid-ocean ridge crustal thickness in relation to spreading rate from *Dick et al.* (2003). White triangles show results of seismic surveys from *White et al.* (2001) and white circles represent results from the Gakkel Ridge (*Jokat et al.*, 2003). Solid black curves show crustal thicknesses derived from different melting models incorporating passive flow (*Phipps Morgan et al.*, 1987) or buoyant flow (*Sotin and Parmentier*, 1989). Horizontal bars indicate the ranges of spreading rates for different ridges classes. The broken lines indicate a typical overlap in the tectonic styles for the three principal ridge classes.

below magmatic centers supported by a topography of the permeability boundary layer (PBL) at the lithosphere-asthenosphere boundary (LAB; Figure 1.3) that guides melt from magma starved segments towards melt-rich magmatic centers (*Cannat et al.*, 2003; *Montési et al.*, 2011; *Sauter and Cannat*, 2010; *Standish et al.*, 2008).

The pronounced variability in crustal thickness between amagmatic segments (often devoid of any igneous crust) and magmatic centers is the highest of all MOR classes (*Cannat et al.*, 2003, 2008; *Minshull et al.*, 2006; *Muller et al.*, 1999; *Standish et al.*, 2008). Changes in the ridge geometry, mantle composition and thermal structure that would have only a minor effect on faster ridges strongly affect the crustal production and tectonics at ultraslow ridges (*Cannat et al.*, 2006, 2008; *Dick et al.*, 2003; *Sauter and Cannat*, 2010; *Standish et al.*, 2008). To investigate the causes and consequences of this pronounced variability in melt supply along the ultraslow MORs is subject to current research and one of the overarching goals of this PhD-project.

Due to the remote locations of the main representatives of ultraslow ridges in the central Arctic and Southern Ocean the global seismological network merely detects earthquakes that are stronger than magnitude m_b 3.8 - 4.0 at these plate boundaries (*Läderach*, 2012; *Läderach et al.*, 2012; *Schlindwein*, 2012). A comprehensive analysis of 35 years of teleseismic activity along the axes of the Arctic and Southwest Indian Ridges, away from fracture zones (*Schlindwein*, 2012) revealed distinct patterns differing from the observations at faster spreading ridges. Tectonic and magmatic processes, in particular during discrete spreading events, at ultraslow ridges are often associated with earthquakes of $M_u \geq 5.0$ (*Korger and Schlindwein*, 2012; *Läderach et al.*, 2012) which is less common at faster ridges (*Schlindwein*, 2012; *Solomon et al.*, 1988).

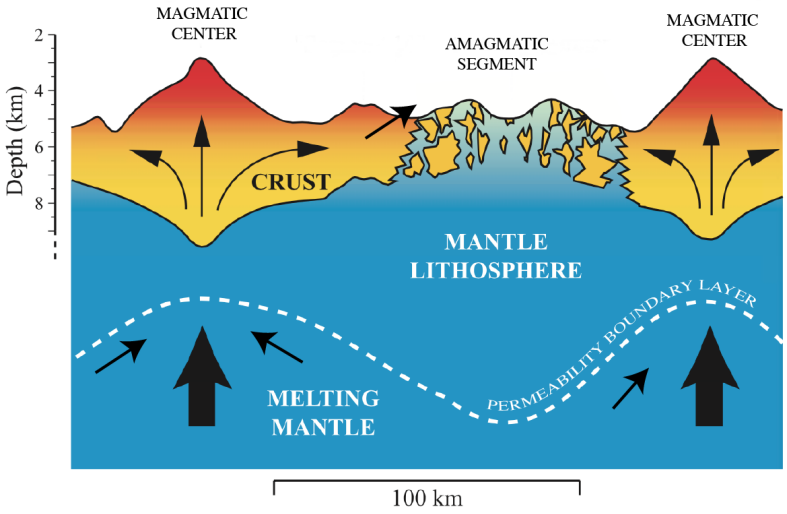

Figure 1.3 Cartoon illustrating the possible magma supply and focussing mechanism at the eastern SWIR, modified from *Sauter et al.* (2004a). It is proposed that melts migrate along an undulating permeability boundary layer towards magmatic centers along the ridge axis. Subsequently melts are distributed in the crust. Note that the permeability boundary layer and the melt distribution processes in the crust are purely hypothetical and not based on observations.

Earthquake swarms of eight or more events typically occur at centers or segments of clear magmatic nature where the crustal thickness is increased. This is in contrast to observations from the slow spreading Mid-Atlantic Ridge where earthquake sequences occur more frequently in regions of thinner crust and increased tectonism, often coinciding with segment ends (*Simão et al.*, 2010; *Smith et al.*, 2003). Exceptional was an earthquake swarm of strong magnitudes and long duration that occurred at the 85°E volcanic center on the Gakkel Ridge (*Korger and Schlindwein*, 2012; *Müller and Jokat*, 2000). This swarm was accompanied by explosive strombolian volcanic activity (*Schlindwein and Riedel*, 2010; *Sohn et al.*, 2008). Mainshock-aftershock sequences are frequently observed at the Mid-Atlantic Ridge (*Simão et al.*, 2010) but hardly at the ultraslow ridges (*Schlindwein*, 2012).
Another aspect that is only marginally touched in this thesis project but raises the scientific interest in ultraslow MORs, is the unexpectly numerous occurrence of hydrothermal plumes and vent sites (*Baker et al.*, 2004; *Edmonds et al.*, 2003; *German et al.*, 2010). Early studies at faster spreading MORs found a linear relation between the incidence rate of hydrothermal plumes along the ridge axes and the spreading rate at MORs (*Baker et al.*, 1996) predicting a very low incidence at ultraslow ridges. Instead, plume surveys at the Gakkel- and Southwest Indian Ridges found much higher abundances of plumes and vent sites than expected (*Baker et al.*, 2004; *Edmonds et al.*, 2003; *German et al.*, 1998). To date several active vents at ultraslow ridges are explored in detail (e.g. *German et al.*, 2010; *Pedersen et al.*, 2010; *Tao et al.*, 2011) most of which are located on volcanic centers. Since some axial regions of ultraslow riges are not jet systematically surveyed further vent discoveries may be expected (*Beaulieu et al.*, 2015).

In recent years the Southwest Indian Ridge became a target for the exploration of seafloor massive sulfides and other polymetallic deposits. Exploration licenses are granted by the International Seabed Authority for the area between 46°E and 56°E (*Tao et al.*, 2014). Ongoing research focuses on the feasibility of the discovered deposits that are mostly associated with magmatic segments (e.g. *Tao et al.*, 2014; *Yang et al.*, 2016).

1.2 The ultraslow Southwest Indian Ridge - SWIR

The Southwest Indian Ridge (SWIR) represents the divergent boundary between the African and Antarctic plates that opens with an average rate of ~14 mm a^{-1} (Figure 1.4; *DeMets et al.*, 1994). The SWIR extends from the Bouvet Triple Junction in the South Atlantic Ocean to the Rodriguez Triple Junction in the Indian Ocean (Figure 1.4) and has a total length of ~7700 km (*Sauter and Cannat*, 2010).

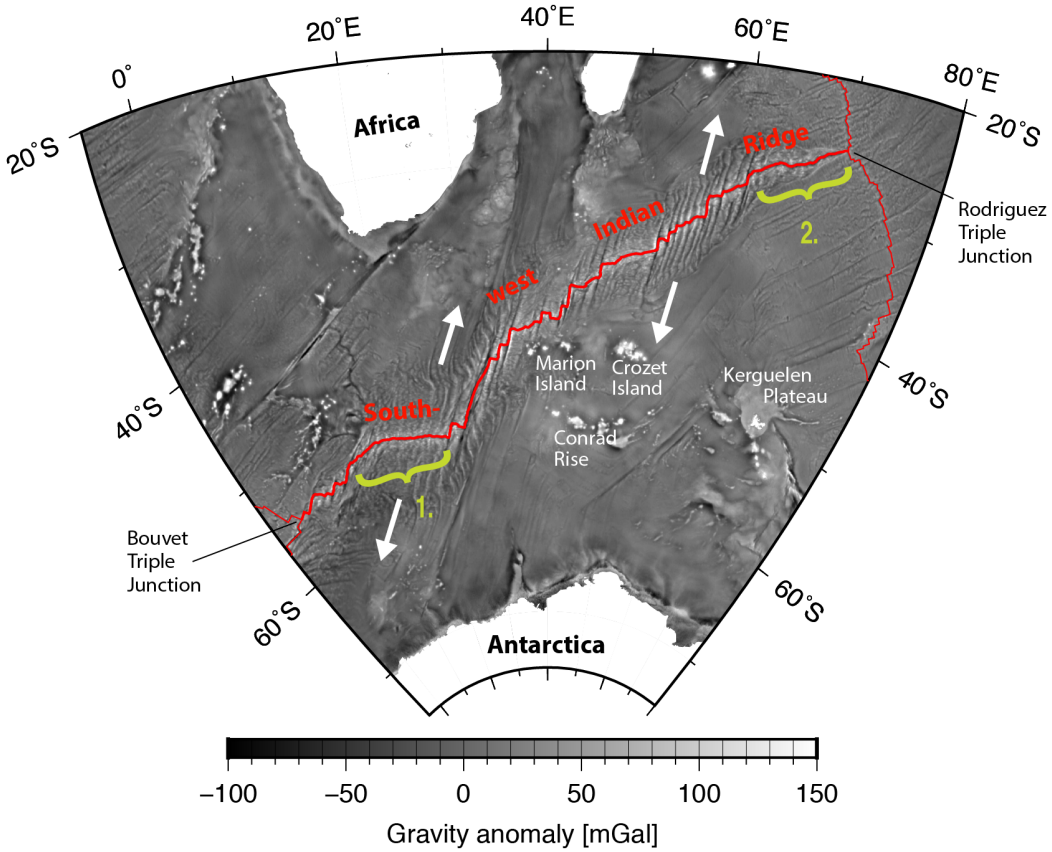

Figure 1.4 Free-air gravity anomalies of the Southwest Indian Ridge (SWIR) region derived from satellite sea-surface altimeter measurements (*Sandwell et al.*, 2014). The red line indicates the SWIR spreading axis. White arrows indicate the trend of the ridge-normal opening direction which has an average rate of 14 mm a^{-1} along the SWIR (*DeMets et al.*, 1994, 2010). Green parentheses show extended sections without fracture zones. 1. 9°30'-25°E region including the Orthogonal and Oblique Supersegments. 2. Easternmost region of the SWIR.

Generally, the ridge follows an oblique trend relative to the spreading direction and in particular between 25°E and 60°E the axis is offset by numerous extensive fracture zones (Figure 1.4). Long stretches of the ridge axis devoid of fracture zones occur between 9°30'-25°E and east of 60°E (Figure 1.4). These sections are considered to be similar to the Gakkel Ridge, that is completely free of fracture zones (*Michael et al.*, 2003). Fracture zones alter the subaxial thermal structure and lead to deviations in the melt-flow which complicates the mechanisms of melt migration and extraction below the ridge (*Montési et al.*, 2011). Thus, fracture zone free sections of the SWIR are seen as a natural laboratory to investigate the melt production, migration, extraction and the crustal accretion at ultraslow rates (*Cannat et al.*, 2008; *Standish et al.*, 2008). In both areas, the 9°30'-25°E region and the easternmost portion of the SWIR, there are several unique characteristics that raised the scientific interest and motivated a number of research cruises in the last two decades. These two regions also hosted the submarine seismological experiments that provided the data bases for this PhD-project. Below the special characteristics and major previous findings from both regions are outlined.

The 9°30'-25°E SWIR region

Based on the apparent transition in ridge axis obliquity this region was further subdivided into the Orthogonal Supersegment (16-25°E) and the Oblique Supersegment (9°30'-16°E) (Figure 1.5; *Dick et al.*, 2003). Seafloor rocks from the Orthogonal Supersegment are of almost entirely basaltic composition and this region shows a continuous central magnetic anomaly. Thus, the seafloor generation is of predominantly magmatic nature (*Dick et al.*, 2003; *Grindlay et al.*, 1998). This segment is morphologically and geophysically similar to the slow spreading Mid-Atlantic Ridge (*Grindlay et al.*, 1998).

West of 16°E, the ridge axis obliquity gradually increases, the rift valley becomes slightly deeper (*Standish et al.*, 2008) and there is no continuous central magnetic anomaly. Nevertheless, two pronounced magnetic anomalies on the ridge axis coincide with the morphological highs of the Joseph Mayes Seamount and the Narrowgate cross-axis high (Figure 1.5; *Dick et al.*, 2003; *Standish et al.*, 2008). Prominent negative mantle bouguer anomalies and the mere recovery of basaltic rocks at the two sites indicate the presence of a thick crust below these punctuated volcanic centers (*Dick et al.*, 2003). The highly oblique, ~180 km long amagmatic section between the Joseph Mayes Seamount and the Narrowgate magmatic centers shows the possibly lowest effective spreading rate of all active MORs of ~7.8 mm $^{-1}$ (Figure 1.5; *Bach et al.*, 2002; *Dick et al.*, 2003; *Standish et al.*, 2008). Although dredging returned about 34% of basaltic rocks from this amagmatic segment they may not represent the bulk lithospheric composition but originate from thin basalt flows overlying the mainly peridotitic seafloor (*Dick et al.*, 2003). Several studies investigated the effects of ridge geometry, mantle heterogeneities as well as efficiencies in melt production and melt extraction on the distribution of melt along the Oblique Supersegment (*Montési and Behn*, 2007; *Montési et al.*, 2011; *Standish et al.*, 2008).

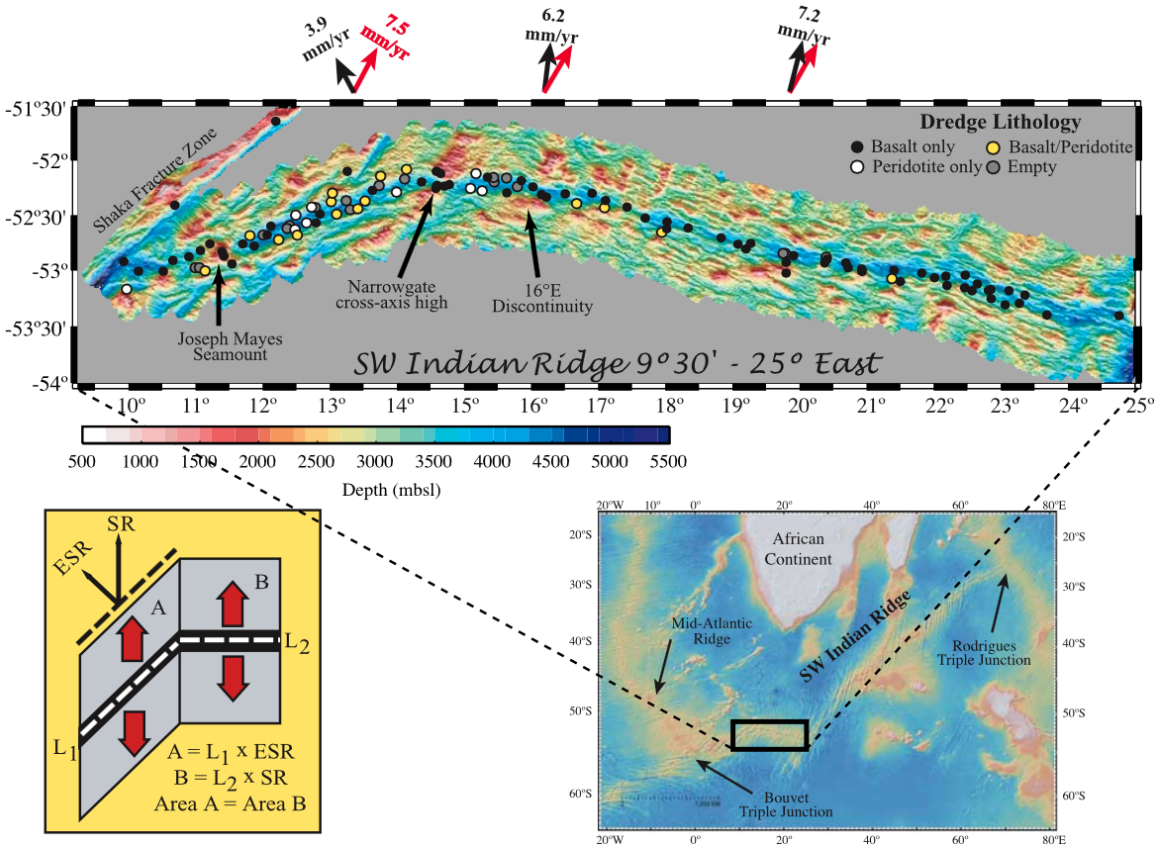

Figure 1.5 Bathymetry and dredged rock lithologies at the SWIR 9°30' - 25°E from *Standish et al.* (2008). Red arrows indicate the directions of plate divergence and black arrows indicate the effective spreading rate (ESR) with respective numbers giving half-rates. Points on the uppermost panel indicate dredge locations with color code referring to found lithologies. The lower left panel illustrates the relations of spreading rate and effective spreading rate for the segments of different obliquity. Note that the 16°E discontinuity marks the boundary between the Oblique Supersegment (to the West) and the Orthogonal Supersegment (to the East).

All studies have in common a hypothetical topography of the PBL at the LAB that guides melt from amagmatic segments and supports melt focussing below magmatic centers where the lithosphere is supposedly thinnest, (Figure 1.6, *Standish et al.*, 2008). However, a direct proof of this concept was still missing and could now be established through the results of microearthquake activity that is presented in chapters 4 and 5. Generally, heterogeneities in the source occur to be of higher importance for mid-ocean ridge basalt (MORB) compositions at the Orthogonal Supersegment and the melt extraction processes seem to be of higher importance for MORB compositions along the Orthogonal Supersegment (Figure 1.6, *Standish et al.*, 2008). The proposed melt focussing is further a consequence of the ridge segmentation-pattern and the efficiency of melt extraction according to the results of numerical models (*Montési and Behn*, 2007; *Montési et al.*, 2011).

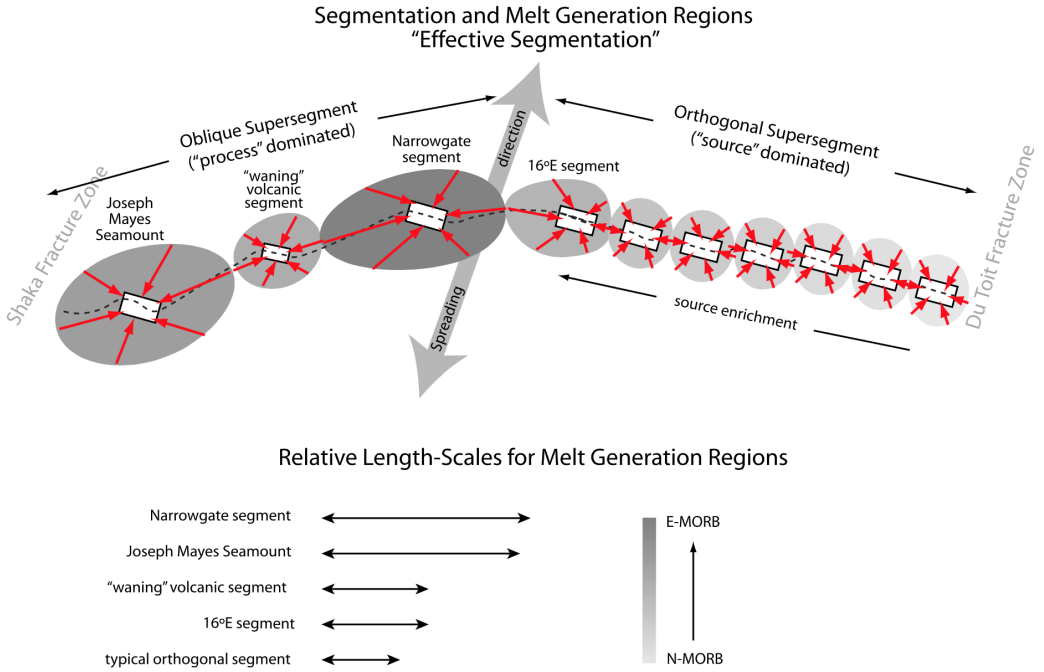

Figure 1.6 Cartoon from *Standish et al.* (2008) illustrating the magmatic segmentation at the fracture zone free 9°30' - 25°E section of the SWIR. Red arrows show simplified directions of melt flow towards magmatic segments, inspired by the model of *Montési and Behn* (2007). Gray shaded ovals represent the "effective segmentation" for each magmatic segment.

The easternmost SWIR (Melville Fracture Zone to Rodriguez Triple Junction)

Between the Melville Fracture zone and the Rodriguez Tripple Junction the SWIR axial valley has an average 4700 m which is exceptionally deep for MORs (*Cannat et al.*, 1999; *Sauter and Cannat*, 2010). This is mirrored by the thin crust that has an average thickness of about 3 km (*Cannat et al.*, 1999; *Muller et al.*, 1999). Based on gravity anomalies and magnetization, *Cannat et al.* (2003) found that this SWIR section is characterized by an anomalously low melt supply but a few magmatic centers (Segment 8, 11, 14 on map 1.7) appear to receive more melt than the average. The unusually low overall melt supply may be the result of an compositionally anomalous mantle (*Meyzen et al.*, 2003). The occurrence of prominent axial magmatic centers was ascribed to an along-axis melt migration and focussing beneath magmatic centers (*Cannat et al.*, 2003; *Sauter et al.*, 2004b), as *Standish et al.* (2008) hypothesized for the melt supply at the Oblique Supersegment. The crustal thickness in the off-axis domains of this SWIR section appears highly variable, which lead to the conclusion that magmatic centers are short-lived and present pattern of segmentation is variable in time (*Cannat et al.*, 2003; *Sauter et al.*, 2004b). This is in contrast to magmatic centers at the Gakkel Ridge and the Narrow Gate magmatic center which show off-axis volcanic ridges, documenting sustained magmatic activity over longer times spans (*Dick et al.*, 2003; *Michael et al.*, 2003).

Bathymetric and side-scan sonar surveying the off-axis regions of the easternmost SWIR sections revealed a previously unknown type of seafloor that is characterized by a thin (or absent) crust, smooth fabric, very little magmatism and extensive detachment surfaces exposed to the sea bed (Figure 1.7 *Cannat et al.*, 2008; *Sauter et al.*, 2013).

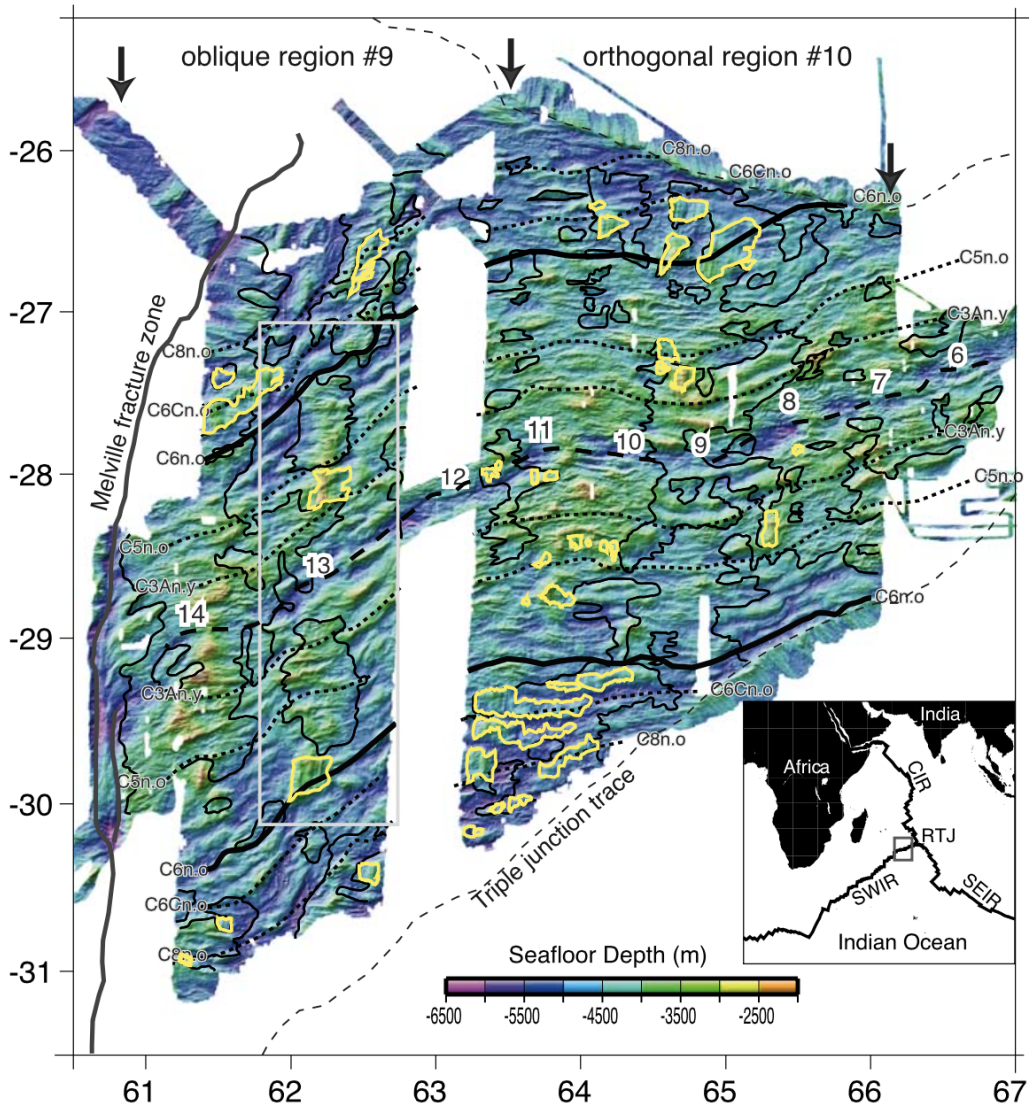

Figure 1.7 Bathymetry of the eastern most SWIR from *Cannat et al.* (2008). Numbers indication SWIR axial sections according to the naming scheme of *Cannat et al.* (2003); heavy black dashed line indicates the ridge axis and thin black dashed lines (parallel to ridge axis) are isochrones derived from magnetics. Areas framed in yellow show seafloor domains that are inferred to consist of exhumed detachment surfaces. Areas framed with thin black lines are terranes with numerous scarps and volcanic cones.

1.3 The use of studying microearthquakes at mid-ocean ridges

Mid-ocean ridges are among the magmatically and tectonically most active zones on our planet. This is mirrored in maps of seismic activity that show very frequent earthquakes of predominantly weak magnitudes along the oceanic spreading centers. The possibly most important aspects of recording microearthquakes at MORs are to gain knowledge about their occurrence and characteristics as well as the faulting activity at specific ridge sections (e.g. *Kong et al.*, 1992; *Solomon et al.*, 1988). Often, the magmatic, tectonic and seismic activity are strongly linked at active MORs. This is nicely demonstrated in the case of dyke emplacements at MORs or terrestrial rifts (e.g. on Iceland). Stress accumulates in the lithosphere due to the divergence of opposing plates and is eventually released during discrete rifting periods (e.g. *Buck et al.*, 2006; *Wright et al.*, 2012). Rifting episodes are commonly preceeded by sequences or swarms of earthquakes (e.g. *Buck et al.*, 2006; *Korger and Schlindwein*, 2012; *Sohn et al.*, 1998). The subsequent intrusion of melt into the crust is usually accompanied by earthquake activity following the tip of the dyke as it forces its way through the crust (e.g. *Sigmundsson et al.*, 2015).
Apart from witnessing tectonic, magmatic and in some places hydrothermal activity microearthquakes can be used to investigate the compositional, thermal and rheological structure of the lithosphere. Active seismic experiments are often not capable of resolving the sub-crustal structure in MOR settings. Using local earthquake tomography in regions of abundant sub-crustal seismicity can also provide structural information about these domains. One aim of this thesis project is to perform a local earthquake tomography for the SWIR Segment 8 volcanic center.
Compilations of depth-frequency-distributions of earthquakes may be used to establish yield-strength envelopes (YSE) of the lithosphere (see chapter 7 for details). The YSEs may then be used to gain knowledge about the lithsopheric strength and draw conclusions about the thermal structure.

During the past decades microearthquake studies based on installations of networks of ocean bottom seismometers (OBS), at the axes of slow- to fast spreading ridges advances to our understanding of the spreading processes at these MORs. The harsh environmental conditions above their major representatives of ultraslow spreading MORs (perennial sea-ice cover above the Arctic Gakkel Ridge, and stormy oceans above the SWIR) had until recently prevented the deployment of ocean bottom seismometers. This thesis project makes use of the first long-term deployments of ocean bottom seismometers at the ultraslow SWIR to investigate in detail the microearthquake activity at two localities that represent antipodal endmembers in terms of melt supply.

1.4 Motivation for this thesis and scientific questions addressed

Short-term, reconnaissance-style deployments of seismometers on ice-floes above the Gakkel Ridge (*Korger and Schlindwein*, 2013; *Schlindwein et al.*, 2007, 2015) and the Lena Trough (*Läderach and Schlindwein*, 2011; *Läderach et al.*, 2011) provided first impressions of the microearthquake activity at ultraslow spreading MORs. However, these experiments were too short to allow detailed insights into the lithospheric structure and modes of deformation, but they motivated subsequent long-term deployments of OBS at the SWIR. The technical characteristics and deployment sites of the OBS networks at the SWIR, that provided the seismological database for this thesis, are outlined in the following chapter 2.
The main motivation for the deployment of two networks of OBS at the SWIR spreading axis and moreover for this PhD-project were to capture the long-term microearthtquake activity at two different segments of ultraslow MOR axis that are antagonistic in terms of melt-supply. The seismicity distribution would then be used to identify systematic variations in the thickness of the brittle lithosphere along the spreading axis. The seismicity catalogues also allow to investigate the modes of deformation and lithospheric accretion at the different SWIR sites. During the course of the PhD-project new hypotheses and questions evolved. The ultimate scientific questions that constitute the keystones for this thesis are summarized in the following and will be adressed in the concluding chapter 8.1 of this thesis.

- How thick is the brittle lithosphere at magmatic and amagmatic ridge sections? How is the thickness of the brittle lithosphere related to general changes in lithology?
- Is the previous hypothesis of an undulating LAB that guides melt towards magmatic centers supported by the along-axis distribution of maximum hypocenter depths?
- Where do melts reside in the lithosphere underneath magmatic centers? How long may they persist during spreading episodes?
- What is the role of serpentinization in the deformation of mainly peridotitic lithosphere? What are the implications of extensive serpentiniation for the axial valley environment?

2 Materials and Methods

2.1 Two networks of ocean bottom seismometers at the SWIR

Two networks of ocean bottom seismometers (OBS) deployed from late 2012 to late 2013 at the ultraslow spreading SWIR (Figure 2.2) provided the seismological datasets for this PhD-project. Both networks were equipped with identical instruments of the LOBSTER-type (long term ocean bottom seismometer for tsunami and earthquake research; Figure 2.1). The OBS systems were manufactured by the company K.U.M, Umwelt- und Meerestechnik Kiel Gmbh and were managed in the "Deutscher Geräte-Pool für Amphibische Seismologie (DEPAS)", at the AWI Bremerhaven. The used OBS comprised a Guralp CMG-40T broadband seismometer that, according to the manufacturer, recorded ground motions between frequencies of 60 s and 50 Hz with a flat instrument response. The attached HighTech Inc HTI-04-PCA/ULF hydrophones had a dynamic frequency range of 100 s - 8 kHz. The instrument's recording units consisted of 24 bit digitizers and were set to record the input signals at a sampling rate of 100 Hz.

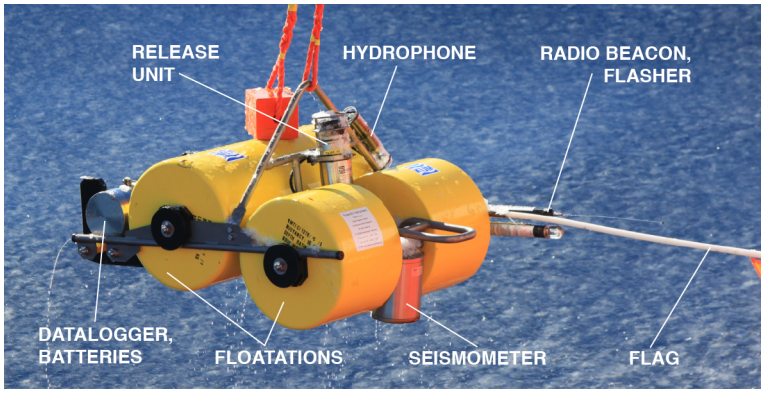

Figure 2.1 LOBSTER-type OBS instrument (Long Term Ocean Bottom Seismometer for Tsunami and Earthquake Research) upon recovery without anchor weight. Similar ocean bottom seismometers were deployed in both networks at the SWIR, Figure 2.2.

One network of initially ten OBS was installed in December 2012 at an amagmatic section of the Oblique Supersegment (Figure 2.2) during RV Polarstern cruise ANT-XXIX/2 (*Boebel*, 2013). This network was recovered during RV Polarsten cruise ANT-XXIX/8 after five short wide-angle seismic profiles had been shot across the stations (*Schlindwein*, 2014). Unfortunately, only nine of the stations could be recovered of which one suffered from a failure of the recording unit (*Schlindwein*, 2014). Ultimately, eight stations returned data.

The other network of eight OBS was installed around the axial volcano on SWIR Segment 8 (Figure 2.2). The deployment of stations was accomplished in the framework of a larger scale seismological experiment that had the overarching goal to investigate the La Reunion mantle plume (www.rhum-rum.net) (*Barruol and Sigloch*, 2013; *Stähler et al.*, 2016). Both networks had a similar extent along the ridge axis and a inter-station distance of ~20 km to allow for a comparable sensitivity to earthquakes occurring inside the networks.

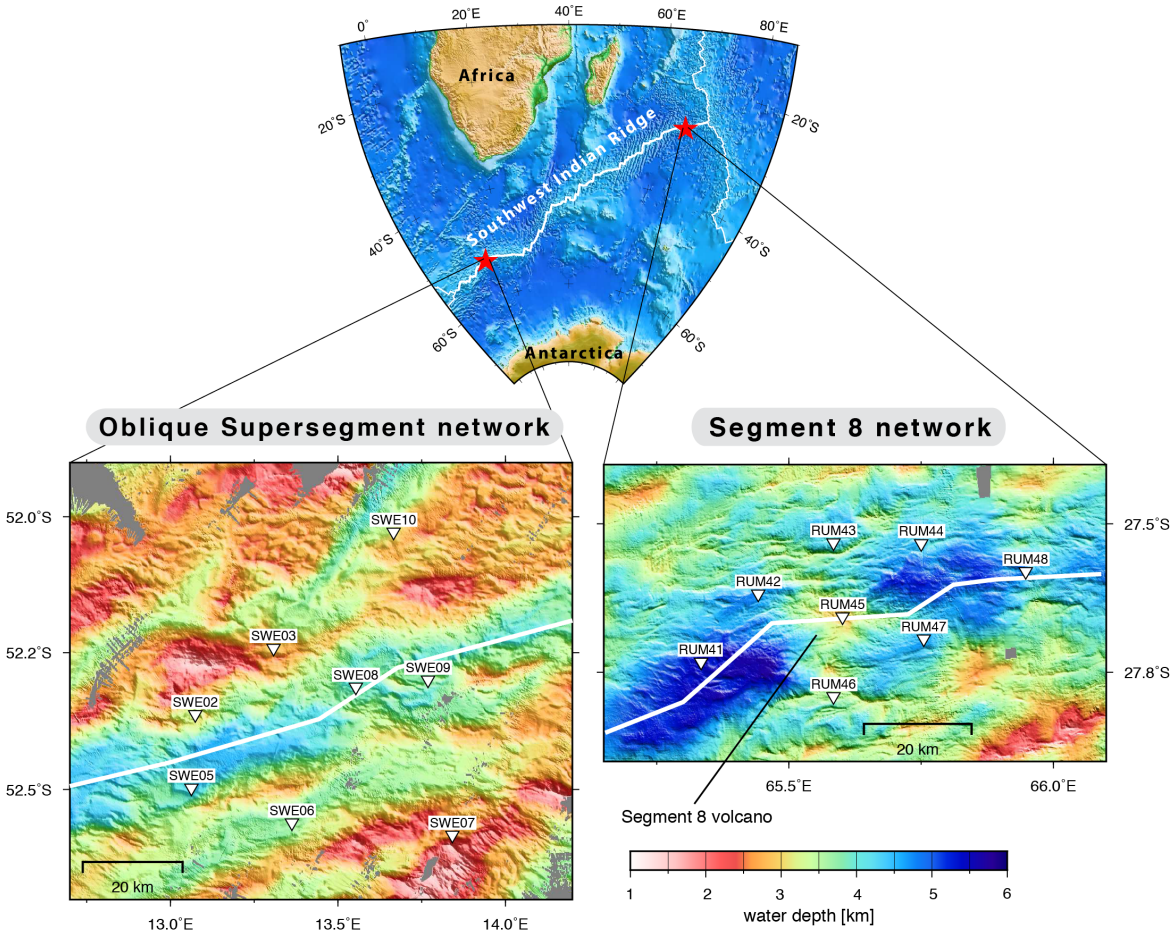

Figure 2.2 Bathymetric maps with station locations for the two OBS networks deployed at the SWIR from late 2012 to late 2013. The solid white line in the two lower panels gives the approximate location of the ridge axis.

2.2 Overview of methods

The following three sections provide an overview of the main methods used during this thesis project. However, I do not intend to give exhaustive insights as all of the methods are established seismological approaches that have been applied in several studies before. Instead, I will provide the general concepts and the considerations that motivated the choice of the specific earthquake location algorithms and the local earthquake tomography algorithm used. The method of constructing yield-strength envelopes on the basis of depth-frequency distributions of earthquakes that was used in the fourth publication is explained in detail in chapter 7.3.2.

2.2.1 Data handling and processing

The internal clocks of all OBS dataloggers were synchronised with the GPS time signal prior to the deployment. Upon recovery the clocks of all dataloggers, that were still running, were synchronised again with the GPS time and the time offset (predicted skew) was recorded. The seismological data were downloaded and stored in day-long files. An LTA/STA (long-term-average/short-term-average) trigger was used to detect local earthquakes in the continuous waveforms. The trigger parameters were first tested on a month-long subset of data and manually checked to not omit useful events. Short seismogram sections were extracted for each identified event and stored in an event database. For the SWIR Oblique Supersegment I performed all the steps of data processing using the SEISAN software (*Havskov and Ottemoeller*, 1999). For this network, the LTA/STA trigger returned a total of 2639 detections that fall into a time span of 348 days. Waveforms with phase onsets of a sample event are plotted in Figure 2.3.

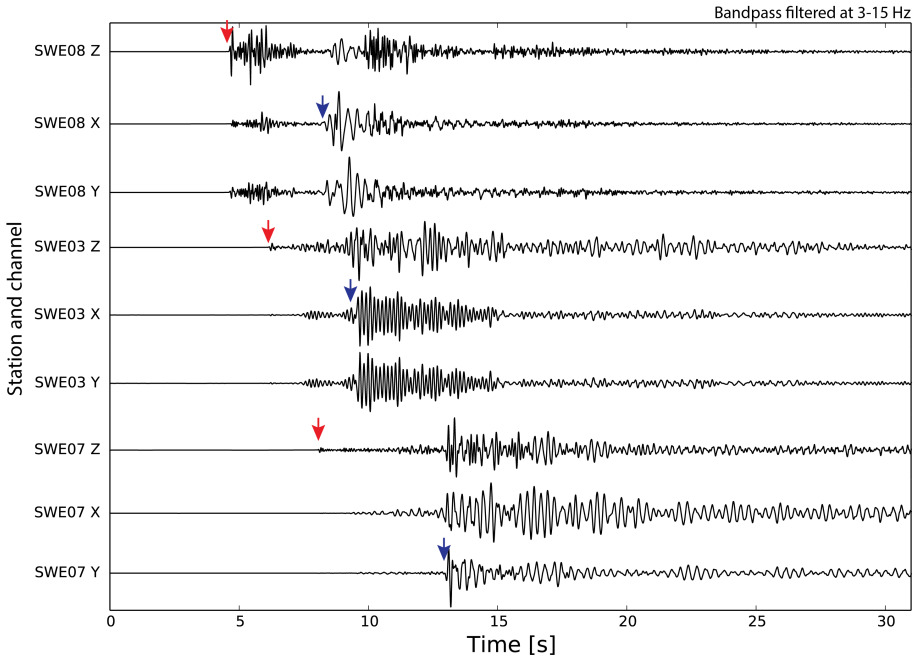

Figure 2.3 Seismogram records of a local earthquake with magnitude $M_l = 2.72$ that occurred at 14 km depth beneath the SWIR Oblique Supersegment network (Figure 2.2). Red arrows indicate *P*-phase onsets, blue arrows indicate *S*-phase onsets.

The picking of *P* and *S*-phase onsets was performed manually and produced 1964 events that have arrival time picks on at least three or more stations. The discrepancy in the event number before and after the picking tells that the LTA/STA trigger parameters were defined conservatively, to rather include a few more events, that are not pickable, than overlooking useful events.
A common issue in submarine seismology is the drift of the datalogger's internal clocks during OBS deployments (*Hannemann et al.*, 2013). In all instruments deployed in the Oblique Supersegment network (Figure 2.2) the internal clocks were still running when the instruments were recovered allowing a synchronisation with GPS time. Due to limited battery capacities in all the stations deployed in the Segment 8 network the internal clocks had discontinued operation at the time of recovery, preventing a synchronization to the GPS time.
Records of the ambient seismic noise provide a possibility to determine the relative clock-drift between different stations of a common network (*Hannemann et al.*, 2013; *McNamara and Buland*, 2004). The ambient noise cross-correlation for the station-pair SWE03 and SWE08 (Figure 2.4) reveals a time offset around two seconds at the end of the deployment. This is confirmed by the time offset between both station estimated via synchronization to GPS time (a list of estimated skew values is provided in appendix, tables A.2 and A.2). For the Segment 8 network all stations where cross-correlated with station RUM042 which was the last one of the network that stopped recording. The task of ambient-noise cross-correlation, using the method of *Hannemann et al.* (2013), was performed by J. R. Scholz in the scope of a Diploma thesis project (*Scholz*, 2014). A summary of all skew values is provided in Appendix A.1.

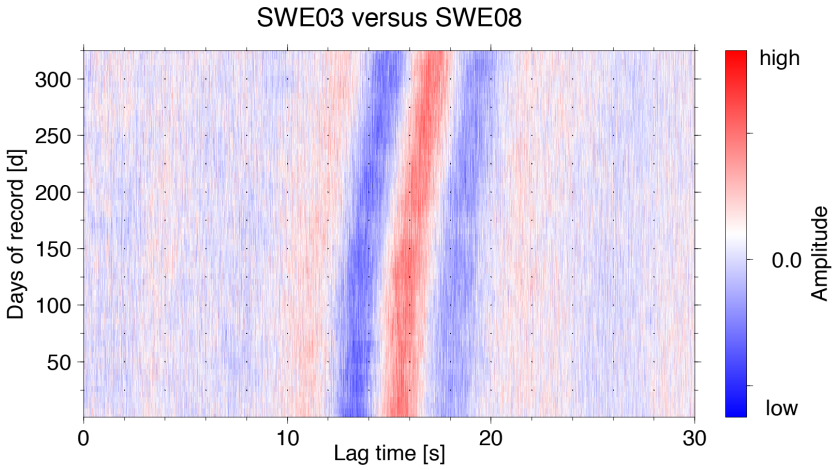

Figure 2.4 Amplitude of 20 d stacks of cross-correlated traces from station SWE03 and SWE08 of the Oblique Supersegment network, Figure 2.2. Note the change in the amplitude maximum over the days of record, suggesting a clock-offset between both instruments of roughly 1.8 s at the end of the deployment. A summary of determined clock drift values is provided in Appendix A.1.

For the later earthquake location it is of importance to know the seafloor location of the deployed OBS as precisely as possible. The most desirable way of determing the seafloor position is probably lowering the instrument on a wire, which is time-consuming but ship-time was sparse during the deployment cruises. Thus, the instruments were released at the surface, sank down at ~0.5 m s^{-1} and after release they ascended at ~1.1 m s^{-1} back to the sea surface.

All instruments of the Oblique Supersegment network that had recorded the airgun pulses generated prior to the recovery (SWE02, SWE03, SWE05, SWE07, SWE08; *Schlindwein*, 2014) could be relocated at the seafloor by fitting the hyperbola of direct wave arrivals. A sample plot with the relocated position of station SWE08 is provided in Appendix A.1. For all other stations of the two networks a seafloor position at 2/3 distance between the deployment and recovery sites was inferred, based on the assumption that currents are constant and the sinking time is approximately twice as long as the rising time. For all stations, that could be relocated, the horizontal distance of the 2/3 location (between deployment and recovery) to the relocated seafloor position ranged between 30 and 300 m (see Table 5.3). Seafloor locations and water depths of all stations are provided in Appendix A.1.

2.2.2 Location of earthquakes

The location of earthquakes in space (x_0, y_0, z_0) and time (t_0), based on the records of *P*- and *S*-phase arrival time onsets at multiple seismic stations on the earth's surface, is a fundamental problem in seismology. *Geiger* (1910) was the first to approach the earthquake location problem by using an iterative least-squares technique. A number of different algorithms for earthquake location on teleseismic, regional and local scales have been developed since, many of which utilized a modified versions of the *Geiger* (1910) technique (*Havskov et al.*, 2012; *Lienert et al.*, 1986). The HYPOSAT algorithm of *Schweitzer* (2001) is also based on the iterative least-squares technique and was developed with the intention to use the largest possible amount of information available for the event location. In practice this means that besides *P* and *S*-phase onsets also travel time differences and ray parameters can be used for the hypocenter inversion (*Schweitzer*, 2001). This is of particular value for events recorded by a limited number of stations only, as is the case for the experimental setup of the two networks deployed at the SWIR (Figure 2.2).

A very crucial aspect in earthquake location is the knowledge of seismic velocities in the subsurface. The velocity model incorporated into the location procedure has a crucial impact on the results (*Kennett and Engdahl*, 1991). Active seismic experiments are often used to investigate the velocity structure of the lithosphere and the resulting 2-D velocity models are commonly used to construct 1-D velocity models for the location of regional and local earthquakes. For the SWIR Oblique Supersegment network I used a short wide-angle seismic profile, that was achieved from airgun pulses generated above the network before the station recovery (*Schlindwein*, 2014), to construct a 1-D velocity model for the region below the network. The wide angle seismic profile and the constructed 1-D velocity model are presented in chapter 5. For the SWIR Segment 8 a 1-D velocity model was constructed on the basis of a nearby wide-angle seismic profile (*Minshull et al.*, 2006).

All earthquakes were located independently of each other with the HYPOSAT routine. Relative location algorithms are developed with the aim to improve the location result for earthquakes relative to each other that are physically related, e.g. occurred in spatial proximity or are related to the same fault. The results of such algorithms may resolve seismically active structures in better clarity (*Waldhauser and Ellsworth*, 2000). I used the HYPODD double-difference algorithm of *Waldhauser and Ellsworth* (2000) which is the possibly most popular software for relative earthquake source location. The HYPODD algorithm was used in combination with the dataset of *P* and *S*-phase arrivals from the SWIR Oblique Supersegment network and the results are presented in chapter 5.
The compilation of the microearthquake catalogue for the SWIR Oblique Supersegment network and the completion of the microearthquake catalogue for the SWIR Segment 8 network, compiled by V. Schlindwein, A. Plötz and J.-R. Scholz, marked the first cornerstones of this PhD-project. All later steps of local earthquake tomography and constructing yield-strength profiles for the axial lithosphere were based on these two catalogues.

2.2.3 Local earthquake Tomography

Seismic tomography has the overarching aim to image the 3-D structure of properties in the subsurface such as *P* and *S*-wave seismic velocities, attenuation, scattering and others. Local earthquake tomography (LET) is applied to image the seismic velocity structure in confined regions of the lithosphere that contain spatially distributed earthquakes and is based on the installations of seismometer networks above the region of interest. Volcanoes, active rifts or plate boundaries are regions that are typically investigated by LET. A number of LET algorithms have been developed during the last decades for different purposes and with different intentions. Before I started to work on an LET, incorporating the acquired microearthquake catalogues from the SWIR, I performed a thorough literature study with the aim of identifying available LET algorithms, suitable to the task. In this case, the main requirements on the LET algorithm searched for were: Travel time residuals should be calculated and provided by the algorithm to assess the quality of the resulting tomography model. There should be the possibility to also invert the 3-D structure of Vp/Vs ratios in the subsurface. Further, it should be easy enough to use, that I am be able to operate the algorithm and produce results within a couple of months. The outcomes of this literature search showed, that there are three algorithms available, that satisfy the requirements mentioned and are summarized in following table.

Algorithm (developer)	FMTOMO (N. Rawlinson)	LOTOS (I. Koulakov)	SIMULPS12 (D. Eberhart-Phillips)
Reference	*Rawlinson and Sambridge* (2004); *Rawlinson and Urvoy* (2006)	*Koulakov* (2009)	*Eberhart-Phillips* (1990, 2002)
General features & main purpose	Based on fast marching method (FMM). Model structure is represented by subhorizontal layers in spherical coordinates.	Tomographic algorithm for simultaneous inversion of P- and S-velocity structure and source coordinates. Claims to be easy to operate and is well documented and widely used.	Damped-least-squares, full matrix inversion intended for use with natural local earthquakes, with or without shots. Events must occur within a target volume and be measured by a grossly homogeneous network of station above the target volume.
Limitations?	All interfaces must completely span the horizontal dimenstions (salt dome, plume e.g. are difficult to incorporate). Software is not so easy to handle e.g. to construct model grid	Not for active seismics	Computationally costly, owing to the full matrix inversion and lots of ray tracing.
Which phases are inverted?	P, S, and converted phases.	P and S Simultaneous inversion of Vp/Vs-ratio possible.	P, S and $S-P$ travel time differences
Is there an output of residuals?	no information	yes	no information

Table 2.1 Overview of algorithms suitable for the task of local earthquake tomography studies at the SWIR.

I decided to use the LOTOS algorithm of *Koulakov* (2009). The choice was motivated by the capability of the algorithm to invert the structure of Vp/Vs ratios in the subsurface, the availability of travel-time residuals and moreover by the easy availability and applicability of the software. Further reasons were the possibility to join Ivan Koulakov and his team, who are the developers of the LOTOS algorithm and have plenty of experience with LET studies in volcanic settings. Methodical and practical details on the LOTOS algorithm are provided in the methods section of chapter 6.

A LET was conducted on the basis of the microearthquake dataset of the SWIR Segment 8 network (Figure 2.2), which is presented in chapter 6. Moreover, a LET was performed incorporating the SWIR Oblique Supersegment microearthquake dataset. However, the soft sediments covering much of the seafloor in the area (*Schlindwein*, 2014) posed a challenge to the LET results that could not be solved without further knowledge about the sediment layer properties (thickness, seismic velocities). Thus, the LET results from the Oblique Supersegment did not allow for an interpretation of the underlying lithosphere.

During the work with the LOTOS software (*Koulakov*, 2009) I developed a series of shell-scripts for the plotting of results that make use of the generic mapping tools (*Wessel et al.*, 2013) and the Perl scripting language. The scripts may be found on the CD accompanying the thesis.

3 Contributions to Scientific Journals

3.1 Technical summary of the manuscripts

This chapter presents brief, technical summaries of the scientific publications which I produced in the scope of this PhD project or in which I contributed significant parts. The four publications are in fulltext reprinted in chapters 4-7 and focus on different aspects of the structure and the lithospheric accretion processes at two different sites along the ultraslow spreading SWIR. Contentual connections between the individual publications are also mentioned, wherever present. Each summary includes a paragraph that describes my contribution and the individual contributions of all co-authors.

Publication I:
Mid-ocean-ridge seismicity reveals extreme types of ocean lithosphere

Authors: Vera Schlindwein[1] **and Florian Schmid**[1]

[1]Alfred-Wegener-Institute, Helmholtz-Centre for Polar- and Marine Research, Bremerhaven, Germany

Published in June 2016 in *Nature*, **535**, 7611, doi:10.1038/nature18277.

This publication (chapter 4) presents two one-year spaning datasets of microearthquake activity at two different segments of the SWIR and a shorter dataset from the Knipovich Ridge. The study represents an unprecedented overview of local seismicity at ultraslow spreading MORs. Based on the distribution of seismicity and the maximum depth of hypocenters conclusions are drawn about the along-axis thermal structure and seismic behaviour of the investigated areas. The most important findings are the seimological approval of systematic undulations in the lithosphere-asthenosphere boundary depth along the spreading axis that is important for a previously hypothesised concept to explain the uneven melt supply at ultraslow ridges. The discovery of a vast aseismic portion of the lithosphere, that is most likely a consequence of deep-reaching serpentinization is of great interest, not only for geophysicists but also for geochemists, biologists and geodynamic modellers.
V. Schlindwein led the seismicity surveys, compiled the hypocentre data for sites 2 and 3 and wrote the manuscript.

My personal contribution in this work includes the processing and compilation of the earthquake catalogue for site 1 at the SWIR Oblique Supersegment. Moreover I contributed significant parts to the discussion and interpretation of the results.

Publication II:
Microearthquake activity, lithospheric structure, and deformation modes at an amagmatic ultraslow spreading Southwest Indian Ridge segment

Authors: Florian Schmid[1] and Vera Schlindwein[1]

[1]Alfred-Wegener-Institute, Helmholtz-Centre for Polar- and Marine Research, Bremerhaven, Germany

Published in July 2016 in *Geochemistry, Geophysics, Geosystems*, **17**, doi:10.1002/2016GC006271.

This publication (chapter 5) presents a one-year spanning catalogue of 1740 microearthquakes at the SWIR Oblique Supersegment. It presents the earthquake locations, magnitudes and for some of the events focal mechanism. Besides, a short wide-angle seismic profile is presented that was used to derive a velocity model for the event location. As the presented microearthquake catalogue is also part of publication I there is some content-related overlap in both works. In contrast to publication I this paper describes in much more detail the earthquake catalogue. It additionally draws some inferences about the apparent mode of deformation incorporating the focal mechanism results. The most important findings are the occurrence of hypocenters down to 31 km beneath the axial seafloor, which is exceptional for a MOR setting. The undulating brittle-ductile transition depth and the aseismic deformation down to 20 km in certain areas, as an effect of fluid circulation and serpentinization are further important findings.
I processed the seismic data, located and evaluated the microearthquakes and wrote the manuscript. V. Schlindwein supervised the project and commented on the text.

Publication III:
Magma plumbing system and seismicity of an active mid-ocean ridge volcano

Authors: Florian Schmid[1], Vera Schlindwein[1], Ivan Koulakov[2], Aline Plötz[1,3] and John-Robert Scholz[1,4]

[1]Alfred-Wegener-Institute, Helmholtz-Centre for Polar- and Marine Research, Bremerhaven, Germany

[2]Trofimuk Institute of Petroleum Geology and Geophysics SB RAS, Novosibirsk, Russia Novosibirsk State University, Pirogova 2, 630090, Novosibirsk, Russia

[3]Institue of Geophysics and Geology, University of Leipzig, Germany.

[4]Present address: Laboratoire GeoSciences Reunion, Universite de La Reunion, Institut de Physique du Globe de Paris, Sorbonne Paris Cite, UMR CNRS 7154, Universite Paris Diderot, F-97744 Saint Denis, France.

Published in February 2017 in *Scientific Reports*, 7:42949, doi:10.1038/srep42949.

This publication (chapter 6) presents the local seismicity and the results of a local earthquake tomography at the SWIR Segment 8 volcano. The underlying earthquake catalogue was included in publication I but not exhaustively discussed there. This publication investigates the lithospheric structure below the volcano by the local earthquake tomography, discusses in detail the earthquake activity, including two swarms and describes the observation of an intrusion swarm. The results indicate a volume of partial melt beneath the volcano and elevated temperatures in the lithosphere over an extended along-axis region. Incorporating also enhanced teleseismic activity that occurred ~13 years prior to our experiment we are able to reconstruct an ongoing spreading episode at this SWIR section.
I performed the tomographic inversions, processed the seismic data for tremor analysis and wrote the manuscript with comments from all co-authors. V. Schlindwein supervised the project and contributed to the picking of earthquakes. I. Koulakov developed the local earthquake tomography code and supervised the related work on the dataset. A. Plötz and J.-R. Scholz contributed to the picking of seismic phases and performed a first location of hypocenters.

Publication IV:
Lithospheric strength, thermal structure, diffusive geochemical fluxes and microbial activity in the ultraslow spreading Southwest Indian Ridge axial valley

Authors: Florian Schmid[1], Massimiliano Molari[2], Vera Schlindwein[1], Norbert Kaul[3], Wolfgang Bach[3,4], Martin Vogt[4,5], Niels Jöns[3,4,*], Christian Hansen[3,4], Maren Walter[4,5], Ellen Damm[1] and Antje Boetius[1,2,3,4].

[1]Alfred-Wegener-Institute, Helmholtz-Centre for Polar- and Marine Research, Bremerhaven, Germany

[2]Max Planck Institute for Marine Microbiology, Bremen, Germany

[3]Department of Geosciences, University of Bremen, Germany

[4]MARUM, Center for Marine Environmental Sciences, University of Bremen, Germany

[5]Institute of Environmental Physics, University of Bremen, Germany

*Present adress: Department of Geology, Mineralogy and Geopyhsics, Ruhr-Universität Bochum, Germany

Submitted to *Geochemistry, Geophysics, Geosystems* in August 2017.

This publication (chapter 7) presents results from a multidisciplinary cruise to the SWIR Oblique Supersegment. Yield-strength envelopes of the lithosphere are presented that were constructed on the basis of depth-frequency distributions of local earthquakes from the seismicity catalogue presented in publications I and II. The yield-strength envelopes show a very weak upper lithosphere down 18 km depth which is best explained by deep serpentinization to these depths, likely focussed in shear zones of deep boundary faults. Seafloor heat flow determinations from this region show a strong variability of the heat flow in the axial valley and do in most of the investigates sites not correlate with the magnitude of estimated geochemical fluxes.

Plumes of elevated methane were found in the axial valley, whose source is most likely abiotic methane production associated with serpentinization. The water column 3-helium and manganese concentrations are low which indicates that there is no currently active high-temperature hydrothermal vent system at this SWIR section. Seafloor images revealed particle clouds that likely produced the turbidity anomalies observed during numerous oceanographic casts.

I conceived the idea of producing a multidisciplinary manuscript and got all parties involved. I further calculated the yield-strength envelopes, processed the oceanographic data, created all figures and wrote most of the manuscript. M. Molari processed the sediment geochemical- and microbiological samples and contributed the respective methodical manuscript sections. V. Schlindwein lead the cruise and supervised the project. N. Kaul collected and processed the heat flow data. W. Bach contributed the water column methane and manganese results and wrote the respective methods sections. M. Vogt and M. Walter contributed oceanography data and the water column noble gas results. N. Jöns and C. Hansen contributed to the water column methane measurements. E. Damm contributed carbon isotopic measurements of the sediment porewaters and the water column. A. Boetius was co-PI of the cruise and supervised the microbiological sampling on board. All co-authors commented on the manuscript.

4 Mid-ocean-ridge seismicity reveals extreme types of ocean lithosphere

Authors: Vera Schlindwein[1] **and Florian Schmid**[1]

[1]Alfred-Wegener-Institute, Helmholtz-Centre for Polar- and Marine Research, Bremerhaven, Germany.

Published in June 2016 in *Nature*, **535**, 7611, doi:10.1038/nature18277.

4.1 Abstract

Along ultraslow-spreading ridges, where oceanic tectonic plates drift very slowly apart, conductive cooling is thought to limit mantle melting1 and melt production has been inferred to be highly discontinuous (*Bown and White*, 1994; *Dick et al.*, 2003; *Michael et al.*, 2003; *Sauter and Cannat*, 2010). Along such spreading centers, long ridge sections without any igneous crust alternate with magmatic sections that host massive volcanoes capable of strong earthquakes (*Schlindwein*, 2012). Hence melt supply, lithospheric composition and tectonic structure seem to vary considerably along the axis of the slowest-spreading ridges (*Cannat et al.*, 2006). However, owing to the lack of seismic data, the lithospheric structure of ultraslow ridges is poorly constrained. Here we describe the structure and accretion modes of two end-member types of oceanic lithosphere using a detailed seismicity survey along 390 kilometres of ultraslow-spreading ridge axis. We observe that amagmatic sections lack shallow seismicity in the upper 15 kilometres of the lithosphere, but unusually contain earthquakes down to depths of 35 kilometres. This observation implies a cold, thick lithosphere, with an upper aseismic zone that probably reflects substantial serpentinization. We find that regions of magmatic lithosphere thin dramatically under volcanic centers, and infer that the resulting topography of the lithosphere–asthenosphere boundary could allow along-axis melt flow, explaining the uneven crustal production at ultraslow-spreading ridges. The seismicity data indicate that alteration in ocean lithosphere may reach far deeper than previously thought, with important implications towards seafloor deformation and fluid circulation.

4.2 Main text

Mid-ocean ridges continuously produce new ocean lithosphere that consists of a layer of ocean crust (on average 6–8 km thick) underlain by mantle lithosphere (*White et al.*, 2001). The upper part of the mantle lithosphere is mechanically strong and brittle to temperatures of 650 ± 100 °C (*Anderson*, 1995) and is referred to here as elastic lithosphere. The base of the oceanic lithosphere is defined by an isotherm of 1,000–1,300 °C (*Cannat*, 1996). Once the spreading rate drops below about 20 mm a^{-1} conductive cooling reduces melt production and a different class of mid-ocean ridge forms that produces anomalous ocean lithosphere in 10%–20% of the world's oceans (*Dick et al.*, 2003). Geological exploration of the poorly accessible ultraslow spreading ridges in the Arctic Ocean and the Southwest Indian Ocean revealed up to 100-km-long rift sections with mantle rocks exposed at the seafloor (*Dick et al.*, 2003; *Michael et al.*, 2003; *Sauter and Cannat*, 2010), indicating little mantle melt production. Between these sections pronounced volcanic centers receive more melt than the regional average and show an over-thickened crust (*Sauter and Cannat*, 2010). Further observations that clearly distinguish ultraslow-spreading ridges from other mid-ocean ridges are the unexpectedly high incidence rate of hydrothermal plumes relative to the low magma budget (*Edmonds et al.*, 2003), a particular, smooth seafloor morphology (*Cannat et al.*, 2006) and the potential to produce moment magnitude M > 6 earthquakes (*Schlindwein*, 2012). However, the lithospheric structure of ultraslow-spreading ridges is little known. Classic terms that describe the ocean lithosphere, such as 'crust' and 'Moho', lose their meaning in the absence of magmatism (*Cannat*, 1993). Active-source seismic imaging of this anomalous lithosphere has been conducted only recently at the most accessible parts of ultraslow-spreading ridges and is unable to characterize lithospheric structure beyond its shallowest domains (*Niu et al.*, 2015).

Records of local seismicity have greatly advanced our understanding of active spreading processes, the lithospheric structure and the thermal regime of most spreading ridges (*Escartin et al.*, 2008) but no such data exist for ultraslow-spreading ridges. Following a 10-day feasibility study near Logachev Seamount on Knipovich Ridge (*Schlindwein et al.*, 2013) (Figure 4.1, site 2), we undertook the first concerted effort to compare the seismicity of contrasting magmatic and amagmatic sections of ultraslow spreading ridges. We recorded local earthquakes on one of the most extensive amagmatic sections of ultraslow spreading ridges, the oblique supersegment on the Southwest Indian Ridge (SWIR) (Figure 4.1, site 1), with eight ocean bottom seismometers (OBSs) for a period of 11 months in 2012–2013 (*Schlindwein*, 2014). The data set is unique because the long-term deployment of OBSs in the stormy Furious Fifties (the area between 50°S and 60°S, which is prone to strong winds), where only few research vessels can operate, has not been attempted before. A similar OBS network was installed simultaneously at a magmatic section, the Segment-8 volcanic center on the eastern SWIR (Figure 4.1, site 3) where an episode of teleseismic earthquake swarms occurred between 1996 and 2003 (*Schlindwein*, 2012).

We determined the hypocenter locations of all of the recorded microearthquakes (see Methods). Figure 4.1 and Extended Data Figures 4.4, 4.5, 4.6 show a distinct image of hypocenter depths along 390 km of ultraslow-spreading ridges representing the prevalent background seismicity at local magnitudes of M_l = 0.5–3. The unprecedented clarity and consistency of the seismicity throughout the three representative sections allows us to state three key observations that expand previous knowledge of mid-ocean-ridge seismicity with important inferences for lithospheric structure.

1. Earthquakes reach maximum depths of 35 km below the seafloor in areas with peridotite exposure, surpassing by far the deepest known mid-ocean-ridge earthquakes at about 15 km depth (*Dusunur et al.*, 2009).

2. The clear lower boundary of seismicity, which provides constraints on the thickness of the axial elastic lithosphere (see Methods), varies dramatically along-axis, thinning by up to 15 km under volcanoes or sites of basalt exposure.

3. Regions in the upper lithosphere are entirely aseismic. They occur mainly in peridotite-dominated ridge sections and extend to 15 km depth (Figure 4.1; site 1, 40–75 km along the profile).

Melt flow along an undulating permeability boundary near the lithosphere–asthenosphere boundary towards magmatic centers is a key hypothesis in ultraslow ridge research that has been put forward by several authors (*Cannat et al.*, 2003; *Montési et al.*, 2011; *Standish et al.*, 2008) to account for the pronounced variations in the crustal thickness, seafloor rock composition and tectonic structure observed along ultraslow spreading ridges. Our data show that the base of the elastic lithosphere as imaged by maximum hypocenter depths varies dramatically along-axis, being shallowest under volcanic centers (Figure 4.1). If we assume that the permeability boundary near the lithosphere–asthenosphere boundary displays the same topography (see Methods) we can estimate the along-axis extent of the catchment areas where melts can flow upslope towards magmatic centers. These areas are at least 60–120 km in length and are hence consistent with the typical segment lengths of ultraslow-spreading ridges of about 100 km (*Cannat et al.*, 1999, 2003). Our data thus provide geophysical support for the hypothesis of melt focusing over segment-scale distances.

Peridotite may alter to mechanically weak phyllosilicates such as serpentinite (lizardite) in fractures that are penetrated by seawater up to temperatures of about 400 °C (*Amiguet et al.*, 2012; *Schwartz et al.*, 2013). Volume fractions of only 10% serpentinite can drastically reduce the strength of the lithosphere and may lead to strain localization in distinct aseismic shear zones (*Escartin et al.*, 2001). We propose that the extensive aseismic regions, observed in peridotite-dominated, amagmatic ridge sections (Figure 4.1; site 1, 40–75 km along the profile), result from serpentinization of the upper lithosphere either along distinct, deep-reaching shear zones that concentrate strain or through pervasive alteration of at least 10% of the mantle rocks. In this interpretation, the observed low seismic velocities at these depth levels (Extended Data Figure 4.1b) reflect partial serpentinization (*Escartin et al.*, 2001).

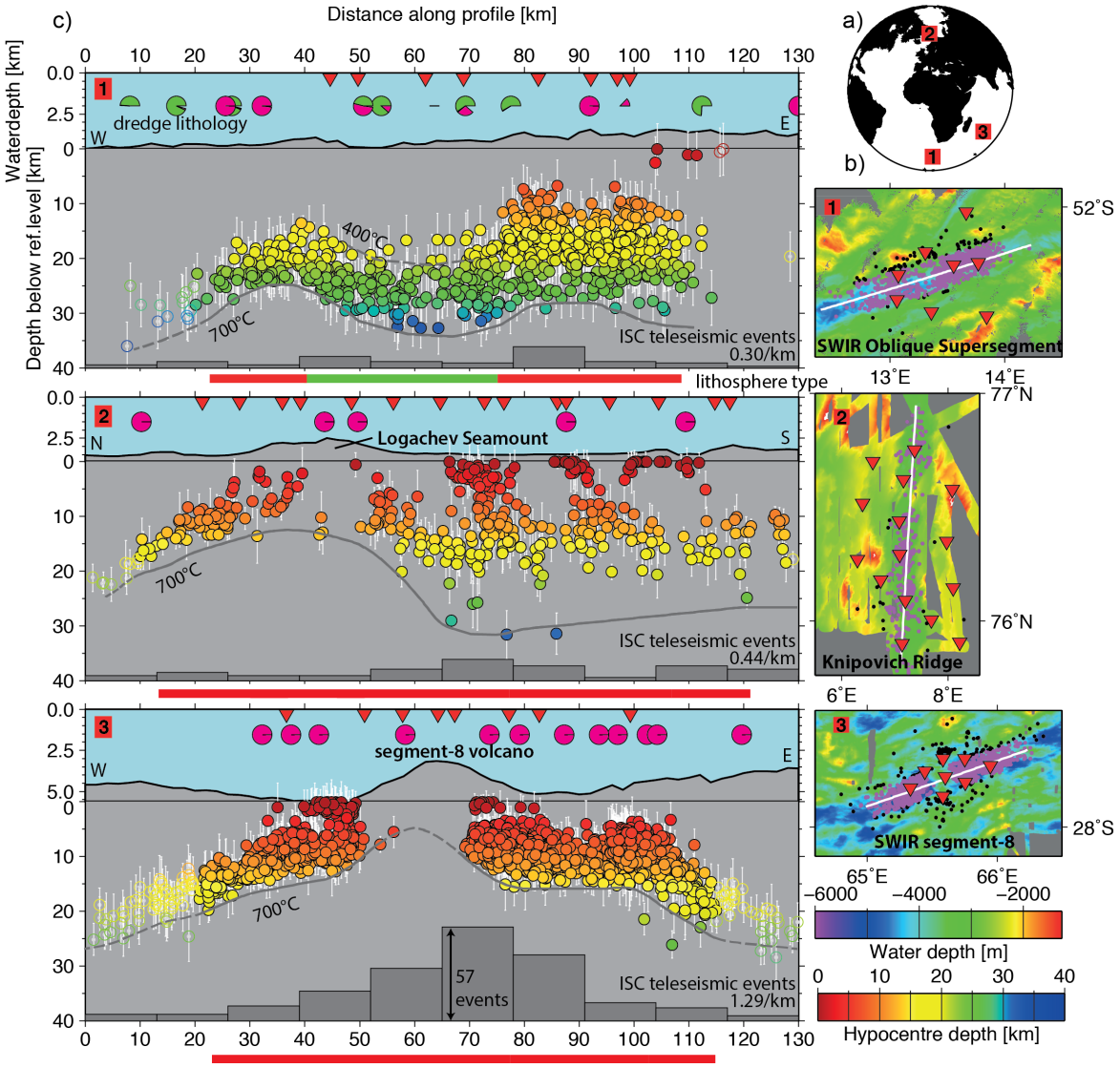

Figure 4.1 Along-axis seismicity of ultraslow-spreading ridges. a, Study sites 1–3 on Knipovich Ridge and the SWIR. b, Maps of the study areas. White lines indicate the positions of transects in c. Red triangles are the OBS positions. Black dots mark earthquake locations, magenta dots are earthquakes that are projected onto the transects in c. All high-resolution bathymetry data are from RV Polarstern except SWIR segment-8 *Cannat et al.* (2006). c, Along-axis hypocenter depths (indicated by the colour coding, open circles are for those beyond the network) with error bars showing the 95% confidence level. The temperature regime is indicated by the estimated isotherms (grey lines, dashed where uncertain). The grey histograms indicate the numbers of teleseismic earthquakes from the Reviewed Bulletin of the International Seismological Centre (*Storchak et al.*, 2015) along the ridge axis (*Schlindwein*, 2012) with the average event rates per kilometre of the rift axis labelled. The bathymetry is exaggerated vertically by a factor of 2.5 above the reference level (defined by the deepest OBS) marked by a thin horizontal line. The dredge lithology is shown in the pie charts (site 1 data from *Dick et al.* (2003), data for sites 2 and 3 are from http://www.earthchem.org/petdb): green, peridotite; magenta, basalt. The lithosphere type (green for amagmatic, red for magmatic) is indicated underneath the profiles where the OBS network provides sufficient constraint.

The onset of seismicity, and hence of brittle faulting below, occurs at a depth where temperatures of roughly 400 °C (for the estimate see Methods) are reached and serpentinite becomes unstable. The upper limit of seismicity in amagmatic regions may therefore image the serpentinization front at previously unknown depths of up to 15 km. This implies in turn that fluid circulation extends to these depths to alter the mantle rocks, exploiting major shear zones or a network of microfractures (*Rouméjon and Cannat*, 2014).

The adjacent magmatic regions, however, exhibit brittle deformation at depths of 8–15 km in the upper mantle or even throughout the lithosphere (Figure 4.1; site 1, 75–115 km along the profile, site 2). Serpentinization in these mantle domains is apparently less pronounced and cannot effectively reduce the shear strength, so these regions of the mantle behave more like normal ocean lithosphere, where serpentinization is commonly confined to the uppermost mantle (*Escartin et al.*, 2001; *Rouméjon and Cannat*, 2014). We therefore speculate that differences in lithospheric composition favour serpentinization of the upper mantle in amagmatic lithosphere but limit serpentinization of magmatic lithosphere at the same depth levels. Alternatively, there may be differences in the connectivity of the fluid pathways that enable or prevent deeply penetrating water circulation in amagmatic and magmatic lithosphere, respectively.

To assess the relevance of our local seismicity surveys we examined the teleseismic earthquake record of ultraslow-spreading ridges (*Schlindwein*, 2012). The average numbers of earthquakes per kilometre of rift axis (for calculation see Methods) confirm the different deformation styles of predominantly magmatic and amagmatic rift segments (Figures 4.1 and 4.2 and Extended Data Figure 4). Figure 4.2 and Extended Data Figure 4 illustrate these differences for Gakkel Ridge and the SWIR, respectively: more abundant, stronger and often clustered earthquakes coincide with basalt exposure and a strong central magnetic anomaly in the magmatic Western Volcanic Zone, whereas reduced seismicity correlates with the occurrence of peridotite and an absence of magnetic anomalies in the Sparsely Magmatic Zone. Earthquakes there tend to be connected to minor basalt exposures. Volcanic centers may host extensive teleseismic earthquake swarms despite their locally thin elastic lithosphere (Figure 4.1, site 3). The repeated teleseismic earthquake swarms between 1996 and 2003 at the Segment-8 volcano potentially mark a phase of magmatic activity (*Schlindwein*, 2012). The complete absence of seismicity underneath the volcano during our survey in 2012–2013 may therefore be a result of increased temperatures caused by recent magmatism.

From the teleseismic and local seismicity records, we can thus define two end-member types of ocean lithosphere representative for ultraslow-spreading ridges (Figures 4.1, 4.2, 4.3). The first type, ‘amagmatic lithosphere’, has an elastic thickness of up to 35 km and lacks an igneous crust. Its serpentinized mantle rocks carry only weak magnetization (*Sauter et al.*, 2008) and are prone to deep-reaching serpentinization that results in aseismic deformation in the upper part of the lithosphere. Amagmatic lithosphere therefore shows a prominent reduction in seismicity. The second type, ‘magmatic lithosphere’, is thinner and shallows towards volcanoes. A thin, igneous crust carrying a remanent magnetization is present (*Sauter et al.*, 2008). Magmatic lithosphere is stronger, with considerable seismicity throughout its elastic portion.

As it has experienced some melting and melt migration, we speculate that a different lithospheric composition may prevent extensive serpentinization. Dredge statistics from Gakkel Ridge and the SWIR show a higher percentage of gabbroic veins in magmatic lithosphere than in amagmatic lithosphere (*Sleep and Warren*, 2014), potentially suggesting that more melts are being trapped at shallower levels in magmatic lithosphere (Figure 4.3). However, as both extensive alteration to large depths and trapped melts could account for the observed low seismic velocities in our one-dimensional velocity models of the lithospheric mantle (Extended Data Figures 4.4b, 4.5b and 4.6b), our data can highlight only the different deformation styles of magmatic and amagmatic lithosphere, not determine their petrologic cause. Future high-resolution seismic studies combined with geological sampling are needed to determine the detailed velocity structure and composition of the end-member types of lithosphere described here.

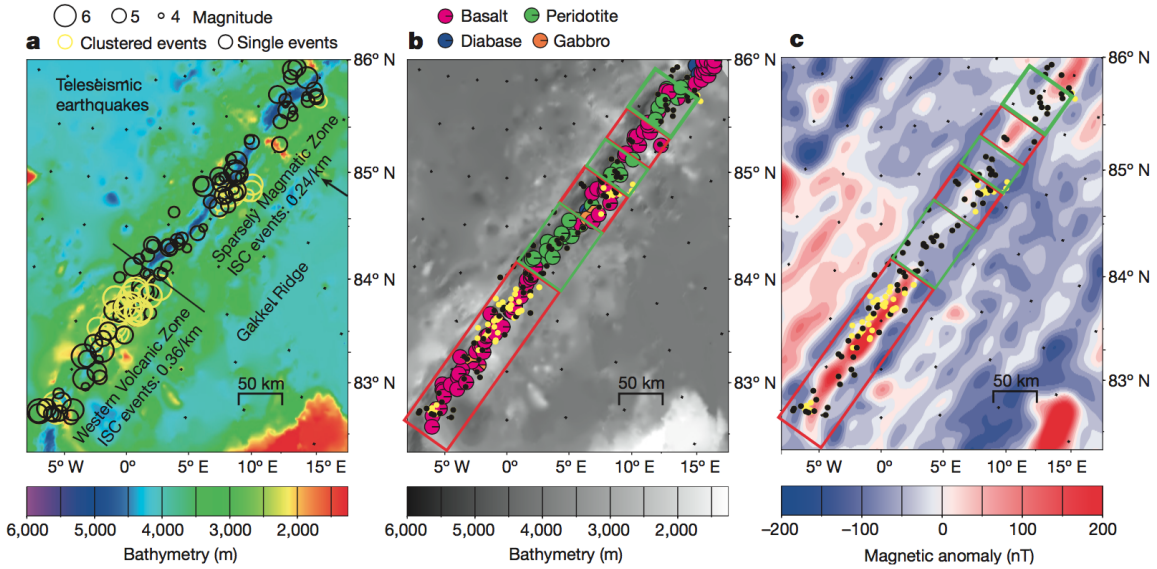

Figure 4.2 Contrasting magmatic and amagmatic sections of Gakkel Ridge. a, Teleseismic earthquake activity (open circles, scaled with magnitude) over the bathymetry. Yellow circles mark earthquake clusters of two or more events related in time and space. Off-axis highs (arrow) extending away from the ridge axis indicate the long-term stability of this segmentation pattern. Teleseismic event rates are also indicated for comparison between sections. b, Dredge lithology. Data from *Michael et al.* (2003). c, Magnetic anomalies. Data from *Maus et al.* (2009). Earthquakes from a are shown by the dots. Magmatic lithosphere (red boxes) shows more and stronger earthquakes, basalt exposure and magnetic anomalies. Amagmatic lithosphere (green boxes) shows less seismicity, peridotite exposure and lacks a central magnetic anomaly.

However, the recognition of these lithosphere types and their geophysical characteristics leads to a conceptual advance in the understanding of ultraslow lithosphere accretion, which we sketch in Figure 4.3 for Gakkel Ridge. The extensive circulation of water through amagmatic lithosphere may further cool and thicken the lithosphere locally, leading to a pronounced topography of its base that enables along-axis flow of melt on the segment scale towards the topographic shoals under magmatic zones.

These magmatic zones vary in size from tiny patches in amagmatic zones (Figure 4.1; site 1, 35 km and 90 km along the profile, see also the Sparsely Magmatic Zone in Figures 4.2 and 4.3), to volcanic centers with different thermal and magmatic states (Figure 4.1, sites 2 and 3, and the Eastern Volcanic Zone in Figure 4.3) and to robustly magmatic zones with extended along-axis magmatism (the Western Volcanic Zone in Figures 4.2 and 4.3). Lithospheric thinning is observed in all cases but the vertical amount and the lateral extent vary. The complete lack of seismicity at volcanic centers observed in our short survey period may indicate high temperatures connected to recent magmatic activity; it is likely to be transient given the observed teleseismic earthquake activity in these areas over longer periods. The variable appearance of magmatic lithosphere may therefore be caused by differences in lithospheric thickness, together with differences in the geometry and effectiveness of melt extraction26, and by differences in melt availability, which is dependent on the mantle composition and fertility (*Sauter and Cannat*, 2010). In addition to spatial variability, melt delivery is also expected to vary in time at a given location. As seismicity provides only snapshots in time of the lithospheric structure, the variable appearance of magmatic lithosphere also reflects different stages in its temporal evolution.

We show that lithospheric thinning in magmatic sections is not the only factor that produces a topography of the lithosphere-asthenosphere boundary. The proposed deep-reaching serpentinization of amagmatic lithosphere implies extensive water circulation that in turn results in the cooling of the lithosphere from above. Spatially variable cooling of the lithosphere may therefore also contribute to enhancing the topography of the lithosphere–asthenosphere boundary. Once this topography is established, the process is self-sustaining. Gakkel Ridge, Knipovich Ridge and the western SWIR show off-axis highs that extend away from volcanic centers in the spreading direction and a spatially stable seafloor magnetic anomaly pattern (Figure 4.2), both of which document long-term stability of the lithospheric accretion modes. Any reorganization of this pattern as observed on the eastern SWIR requires large instabilities such as a rapid cooling and thickening of the lithosphere at magmatic centers to prevent further melt pooling (*Cannat et al.*, 2003).

Our study provides geophysical constraints on the along-axis thermal structure of ultraslow spreading ridges, against which a multitude of petrologic models of ultraslow spreading (*Cannat et al.*, 2008; *Montési et al.*, 2011; *Sleep and Warren*, 2014) can be validated. A further insight is that ultraslow spreading ocean lithosphere exhibits a completely different deformation mode that we attribute to alteration of mantle rocks reaching 15 km depth.

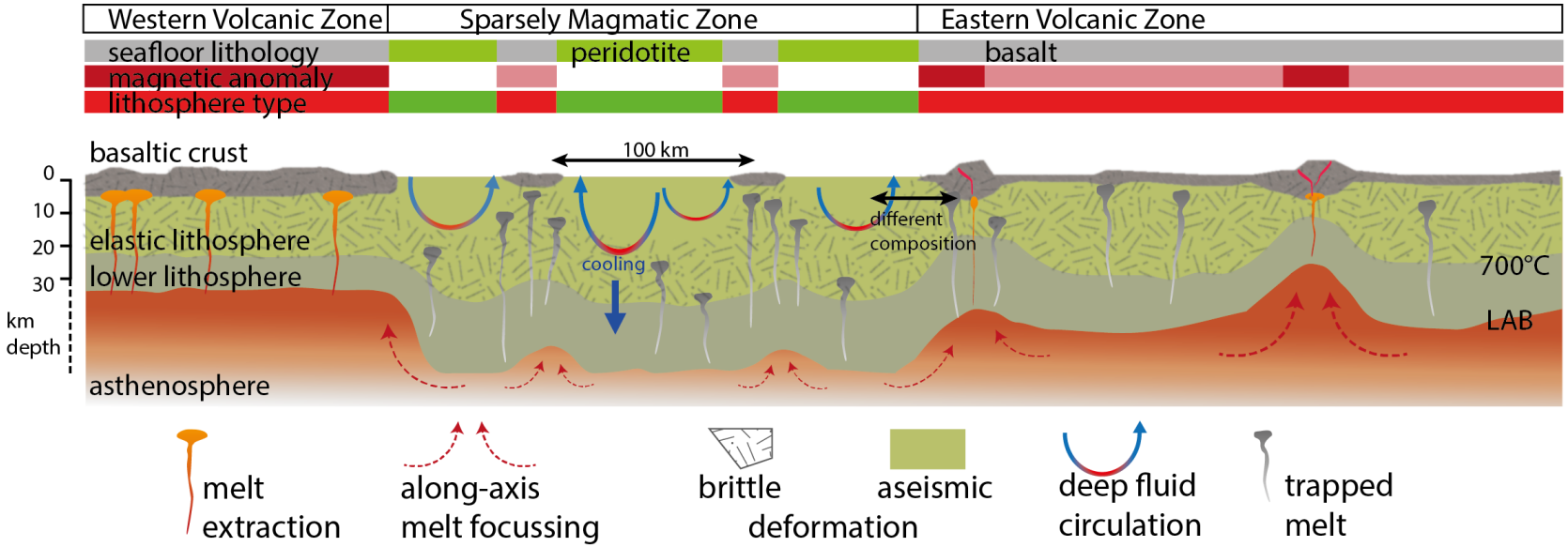

Figure 4.3 Conceptual sketch of the two lithosphere types at the Gakkel Ridge. Scales are approximate. Deep-reaching alteration in amagmatic ridge sections cools and further thickens the lithosphere. The pronounced topography of the lithosphere–asthenosphere boundary focuses melts towards magmatic sections. Melt ascent there may result in a different lithospheric composition that is less prone to alteration and demonstrates brittle behaviour, whereas amagmatic lithosphere can deform aseismically.

This deformation style distinguishes ultraslow-spreading ridges from faster-spreading ridges: slow-spreading ridges show a dominant pattern of higher levels of seismicity at the colder, magma-poor segment ends (*Escartin et al.*, 2008), in contrast to what we observe at the ultraslow-spreading ridges where less seismicity is associated with amagmatic regions. Exhumation of mantle lithosphere along major detachment faults produces substantial earthquake activity at the Mid-Atlantic Ridge (*Escartin et al.*, 2008; *Simão et al.*, 2010). The seismicity delineates the detachment faults to depths of 7 km into the shallow upper mantle (*deMartin et al.*, 2007). At ultraslow-spreading ridges, detachment faulting is also thought to be a fundamental process in mantle rock exhumation (*Sauter et al.*, 2013) and the generation of smooth seafloor (*Cannat et al.*, 2006), but our study suggests that deformation along such shear zones occurs entirely aseismically owing to deep-reaching serpentinization, explaining the contrasting seismicity pattern of slow- and ultraslow-spreading ridges.

Serpentinization in young oceanic lithosphere is generally believed to be limited to shallow depths of 4–6 km below detachment faults, but its extent is generally difficult to estimate from seismic velocities or rock samples gained from dredging or drilling (*Rouméjon and Cannat*, 2014). Our data suggest that in the extensive amagmatic regions of ultraslow-spreading ridges serpentinization and fluid circulation may reach far deeper into the mantle than previously assumed.

4.3 Acknowledgements

This study was enabled by grants SCHL853/1-1 and SCHL853/3-1 of the German Science Foundation to V.S. Instruments were borrowed from the DEPAS pool. We acknowledge the efforts of the crews of RV *Polarstern* cruises ANT-XXIX/2+8 and ARK-XXIV/3, RV *Meteor* cruise M101 and RV *Marion Dufresne*. *Nature* thanks S. M. Carbotte and the other anonymous reviewer(s) for their contribution to the peer review of this work.

4.3.1 Author contributions

V.S. planned and conducted the surveys, processed data for site 3 and wrote the paper. F.S. processed data from site 1. Both authors discussed the results and commented on the manuscript.

4.4 Methods

Data processing

Seismic signals were identified with a short time average/long time average trigger in the continuous data stream of the OBSs, optimized for detecting all local earthquakes. All of the triggered events were reviewed by an analyst and spurious events were removed. P- and S-wave arrivals of all of the local earthquakes that were recorded by three or more stations were subsequently hand-picked and located with the linear least-squares algorithm Hyposat (*Schweitzer*, 2001), which also constrains the inversion with S–P travel-time differences.

One-dimensional velocity model

To derive a minimum one-dimensional velocity– depth profile, as commonly used in earthquake location (*Kissling et al.*, 1994), we used the results of refraction seismic surveys (*Jokat et al.*, 2012; *Minshull et al.*, 2006; *Schlindwein*, 2014) conducted within each of the study sites (Extended Data Figures 4.4a, 4.5a and 4.6a). We extracted smoothed average velocity–depth profiles for the upper 5 km, where the refraction seismic data provided sufficient ray cover. We thus constructed an initial velocity model and located all of the earthquakes. We used this preliminary location run to select a subset of well recorded events of at least 5 km depth that are situated within the network of stations. These events are considered the most sensitive to changes in the velocity model. We then tested a wide range of conceivable sub-Mohorovicic discontinuity (sub-Moho) velocities but kept the velocity model in the crust fixed as constrained by refraction seismic data. We located the subset of well constrained events for each velocity model and assessed the performance of each velocity model. We selected the velocity model that provided the lowest average root mean squared travel-time residual while still locating a large number of events. This final velocity model (Extended Data Figures 4.4b, 4.5b and 4.6b, red) was then used to locate all earthquakes.

Robustness tests

To assess the effects of the choice of velocity model on the location results and in particular to evaluate the reliability of the large hypocenter depths obtained, we performed several robustness tests. We located all of the events with a slow end-member velocity model with velocities reduced by 0.3 km s^{-1} compared with the final model and a fast end-member velocity model that consisted of a 4-km-thick crust underlain by velocities of 8 km s^{-1}, as is common for oceanic crust (*White et al.*, 1992) (Extended Data Figures 4.4b, 4.5b and 4.6b). Both low and high end-member velocity models produced a considerably poorer fit to the phase arrivals of all earthquakes as seen from the average root mean squared travel time residual in Extended Data Table 1. Fast sub-Moho velocities resulted in a failure to determine the hypocenter depth of many events at all three locations. The location algorithm had to fix the hypocenter depth to converge on the results.

The number of well-determined hypocenter depths with depth errors of less than 5 km is therefore much smaller for the high-velocity model and illustrates its inappropriateness.

We further examined the effect ofvariations in the velocity model by ± 0.3 km s^{-1} on hypocenter depth. The reduced velocity model is identical to the low-velocity end-member model tested above (Extended Data Figures 4.4b, 4.5b and 4.6b, orange). For the faster-velocity model we increased the velocities of the final velocity model by +0.3 km s^{-1} throughout but kept 8.0 km s^{-1} at 40 km depth fixed (Extended Data Figures 4.4b, 4.5b and 4.6b, purple) to avoid the convergence problems described above. Faster velocities again produced a poorer fit to the data and yielded fewer reliable hypocenter depths (Extended Data Table 2). These, however, are on average slightly shallower than hypocenters located with lower-velocity models. Changes in the average hypocenter depth are in all cases smaller than the average depth error and they are much smaller than the along-axis depth variations of the band of seismicity shown in Figure 4.1 and interpreted here. Prominent deviations from the one-dimensional minimum velocity model due to local heterogeneities in the subsurface result in non-zero average station residuals rather than substantially shifting hypocenters. On site 3, the station located on the crest of the volcano showed a positive S-phase residual of on average 0.232 s. Omitting this station from the location procedure did not distort the pattern of hypocenters interpreted.

Selection and display of hypocenters

Extended Data Figures 4.4, 4.5, 4.6 show all 5,379 located earthquakes with a hypocenter solution, irrespective of location accuracy. These figures hence include also all smaller events. For Figure 4.1 we imposed a maximum hypocenter depth error of 5 km as the sole quality criterion, fulfilled by 903, 441 and 2,625 events in data sets 1–3, respectively. The cross-sections displayed in Figure 4.1 are based on a total of 3,664 events within 9.4 km of the cross-section profile. These events have a mean horizontal error of ± 3.5 km, a mean depth error of ± 2.7 km and an average root mean squared travel-time residual of 0.24 s. Their locations were calculated from on average 15.5 phases at 6.3 stations, the closest station being on average 7.2 km away. For the majority of the events, the distance to the closest recording station is hence smaller than the hypocenter depth, which is generally considered necessary to obtain good hypocenter solutions. In Figure 4.1, we highlight events outside the network where the distance to the next station becomes larger than the hypocenter depth. For these events, hypocenter depths have to be interpreted with care.

The band of seismicity was in all cases more or less flat-lying in the across-axis direction. Therefore, the projection of the hypocenters onto the cross-sections did not distort the seismicity pattern. Extended Data Figures 4.4c, 4.5c and 4.6c reveal no systematic dependence of hypocenter depth on projection distance. Aseismic regions interpreted here are furthermore not a consequence of earthquake selection as they appear in the full data set (Extended Data Figures 4.4, 4.5, 4.6) in the same way as in Figure 4.1, indicating that these areas are also devoid of the weaker events that were omitted from Figure 4.1.

Teleseismic events

Teleseismic earthquakes are used from a compilation (*Schlindwein*, 2012) of reviewed locations of the Bulletin of the International Seismological Centre occurring from 1976 to 2010 within 30 km of the rift axis for the Gakkel and Knipovich ridges and within 35 km of the rift axis for the SWIR owing to the larger location uncertainties there. A single-link cluster analysis identified earthquake clusters in time and space. Owing to their long observation period, teleseismic earthquake catalogues of mid-ocean ridges can reproduce the main features of along-axis seismicity variations on a regional scale that are visible in more complete catalogues of hydroacoustically recorded events (*Simão et al.*, 2010). We project the event locations onto our profiles in Figure 4.1 and count the number of teleseismic events in our 35-year-long catalogue in bins of 13 km, displayed as histograms in Figure 4.1. We further calculate the average number of events per kilometre of the rift axis for comparison of the considered rift sections in Figures 4.1 and 4.2 and Extended Data Figure 4. As the mean location uncertainty of the teleseismic events is about ±31 km for the SWIR compared with ±12 km at Gakkel Ridge (*Schlindwein*, 2012), we cannot unambiguously assign individual earthquakes to either amagmatic or magmatic subsections of the oblique supersegment, in particular. We therefore calculate seismicity rates for entire segments (Figure 4.2 and Extended Data Figure 4) or major portions thereof (Figure 4.1) for comparison with adjacent segments. The average seismicity rates of the predominantly amagmatic supersegments contain some earthquakes that are connected with minor occurrences of magmatic lithosphere there. Purely amagmatic lithosphere may have even lower seismicity rates and the difference in the seismicity rate between amagmatic and magmatic lithosphere may be more pronounced. Figure 4.2 and Extended Data Figure 4 show the individual teleseismic earthquake locations compared with a global map of magnetic anomalies (*Maus et al.*, 2009). Events that are part of clusters of two or more events occurring in close relation in time or space are highlighted. Note that such clusters occur only in regions of magmatic lithosphere.

Estimates of lithosphere temperature

Absolute temperatures at the transition depth from brittle to ductile behaviour are discussed by several authors (*Anderson*, 1995; *Chen and Molnar*, 1983; *McKenzie et al.*, 2005) and their estimates range between 550 °C and 750 °C. For mid-ocean-ridge lithosphere compositions, preference is given to higher temperatures within this range (*Cannat*, 1996). As mantle hotter than about 650 °C cannot build up long-term stresses, the base of seismicity and the transition between ductile and brittle rheologies have been associated with isotherms (*Anderson*, 1995). We therefore assume here that the maximum depth of seismicity delineates an isotherm of about 700 °C. This value was chosen arbitrarily, the exact temperature is irrelevant for our conclusions. To obtain a crude estimate of the depth of the 400 °C isotherm in limited along-axis areas we assume a constant temperature gradient between the seafloor and the depth of the 700 °C isotherm. We furthermore assume that the 1,200 °C isotherm, used as a proxy for the lithosphere–asthenosphere boundary, has roughly the same along-axis topography as the 700 °C isotherm. Temperature fields calculated for mid-ocean-ridge axes

(*Chen and Molnar*, 1983; *Montési and Behn*, 2007; *Sleep and Warren*, 2014) show approximately constant spacing of isotherms in the brittle lithosphere and similar shapes of the 700 °C and 1,200 °C isotherms, justifying our assumptions.

4.5 Extended data figures

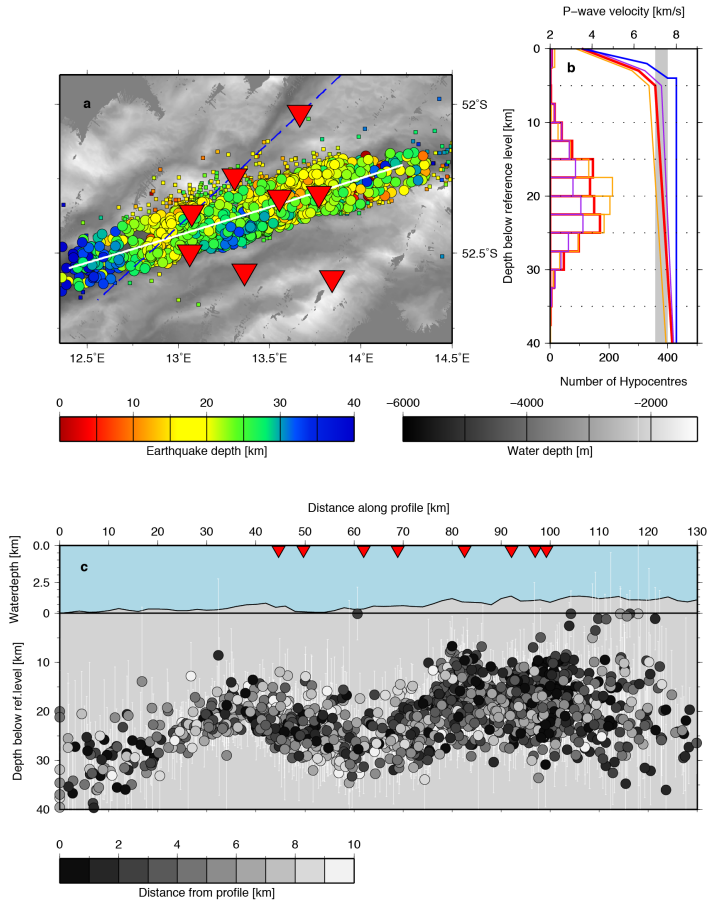

Figure 4.4 Earthquake location at survey site 1 including poorly located events. a, Epicenters (circles) colour-coded by hypocenter depth. Earthquakes not projected onto the cross-section (white line) in c are shown by squares. The red inverted triangles show OBS locations and the dashed blue line shows the position of the refraction seismic line (*Schlindwein*, 2014) used to constrain velocities in the uppermost lithosphere. b, The final velocity model used for earthquake location is shown in red, and the velocity models used for the robustness tests are shown in blue (the fast end-member representing a thin crust with ultramafic rocks underneath) orange (a velocity reduction of 0.3 km s^{-1} relative to the final model) and purple (a velocity increase of 0.3 km s^{-1} relative to the final model). Velocities of 7.0–7.6 km s^{-1} (grey bar) are considered anomalously low for lithospheric mantle. The histograms show the distribution of hypocenter depths obtained for the different velocity models. Faster models result in fewer well-located events, but the depth distribution is similar (see Extended Data Table 4.1). c, Cross-section of the hypocenters projected onto the axis and colour-coded according to the distance from the profile. The topography of the seismicity band is not an artefact of projection because at all depth intervals the earthquakes from various off-axis distances are present. The aseismic regions remain devoid of seismicity even when all poorly located earthquakes are shown.

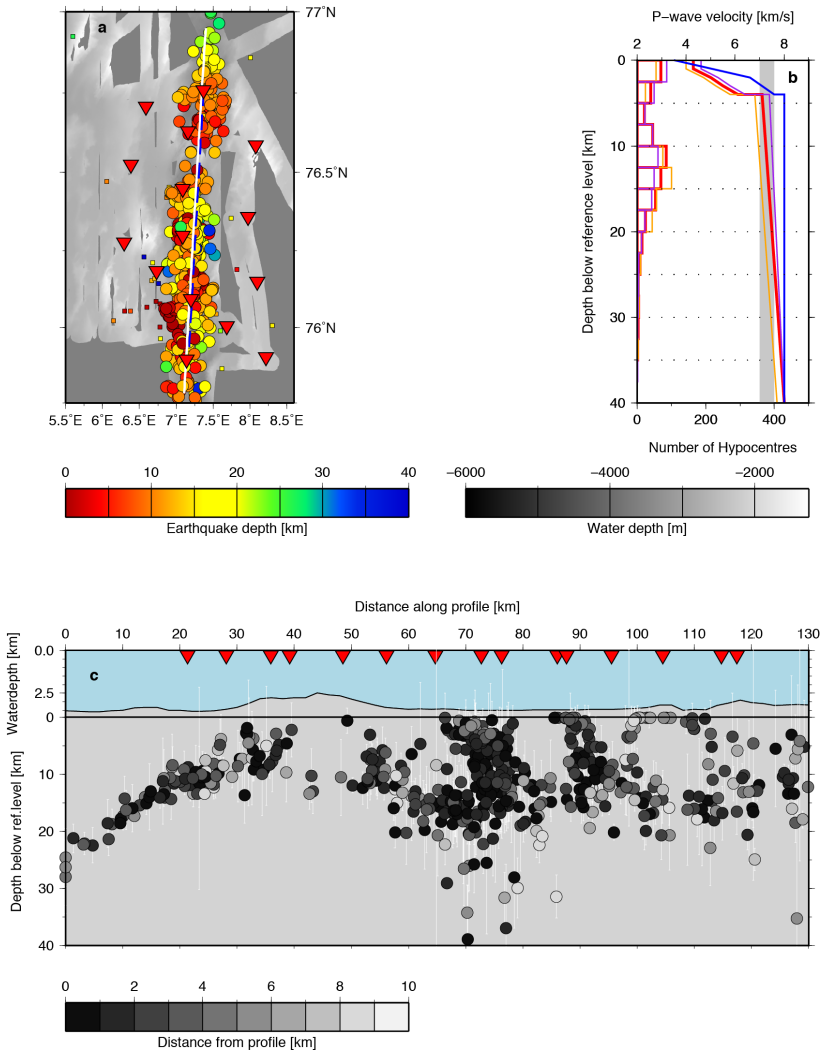

Figure 4.5 Earthquake location at survey site 2 including poorly located events. a, Epicenters (circles) colour-coded by hypocenter depth. Earthquakes not projected onto the cross-section (white line) in c are shown by squares. The red inverted triangles show OBS locations and the dashed blue line shows the position of the refraction seismic line (*Jokat et al.*, 2012) used to constrain velocities in the uppermost lithosphere. b, The final velocity model used for earthquake location is shown in red, and the velocity models used for the robustness tests are shown in blue (the fast end-member representing a thin crust with ultramafic rocks underneath) orange (a velocity reduction of 0.3 km s^{-1} relative to the final model) and purple (a velocity increase of 0.3 km s^{-1} relative to the final model). Velocities of 7.0–7.6 km s^{-1} (grey bar) are considered anomalously low for lithospheric mantle. The histograms show the distribution of hypocenter depths obtained for the different velocity models. Faster models result in fewer well-located events, but the depth distribution is similar (see Extended Data Table 4.1). c, Cross-section of the hypocenters projected onto the axis and colour-coded according to the distance from the profile. The topography of the seismicity band is not an artefact of projection because at all depth intervals the earthquakes from various off-axis distances are present. The aseismic regions remain devoid of seismicity even when all poorly located earthquakes are shown.

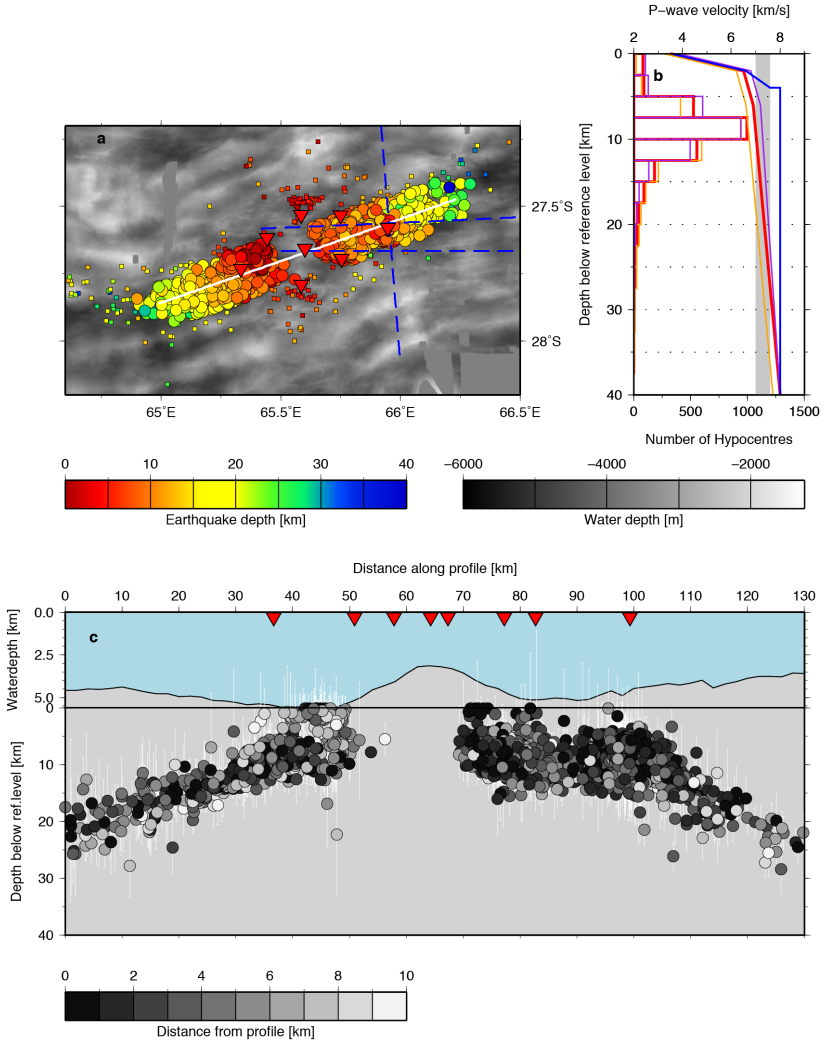

Figure 4.6 Earthquake location at survey site 3 including poorly located events. a, Epicenters (circles) colour-coded by hypocenter depth. Earthquakes not projected onto the cross-section (white line) in c are shown by squares. The red inverted triangles show OBS locations and the dashed blue line shows the position of the refraction seismic lines (*Minshull et al.*, 2006) used to constrain velocities in the uppermost lithosphere. b, The final velocity model used for earthquake location is shown in red, and the velocity models used for the robustness tests are shown in blue (the fast end-member representing a thin crust with ultramafic rocks underneath) orange (a velocity reduction of 0.3 km s^{-1} relative to the final model) and purple (a velocity increase of 0.3 km s^{-1} relative to the final model). Velocities of 7.0–7.6 km s^{-1} (grey bar) are considered anomalously low for lithospheric mantle. The histograms show the distribution of hypocenter depths obtained for the different velocity models. Faster models result in fewer well-located events, but the depth distribution is similar (see Extended Data Table 4.1). c, Cross-section of the hypocenters projected onto the axis and colour-coded according to the distance from the profile. The topography of the seismicity band is not an artefact of projection because at all depth intervals the earthquakes from various off-axis distances are present. The aseismic regions remain devoid of seismicity even when all poorly located earthquakes are shown.

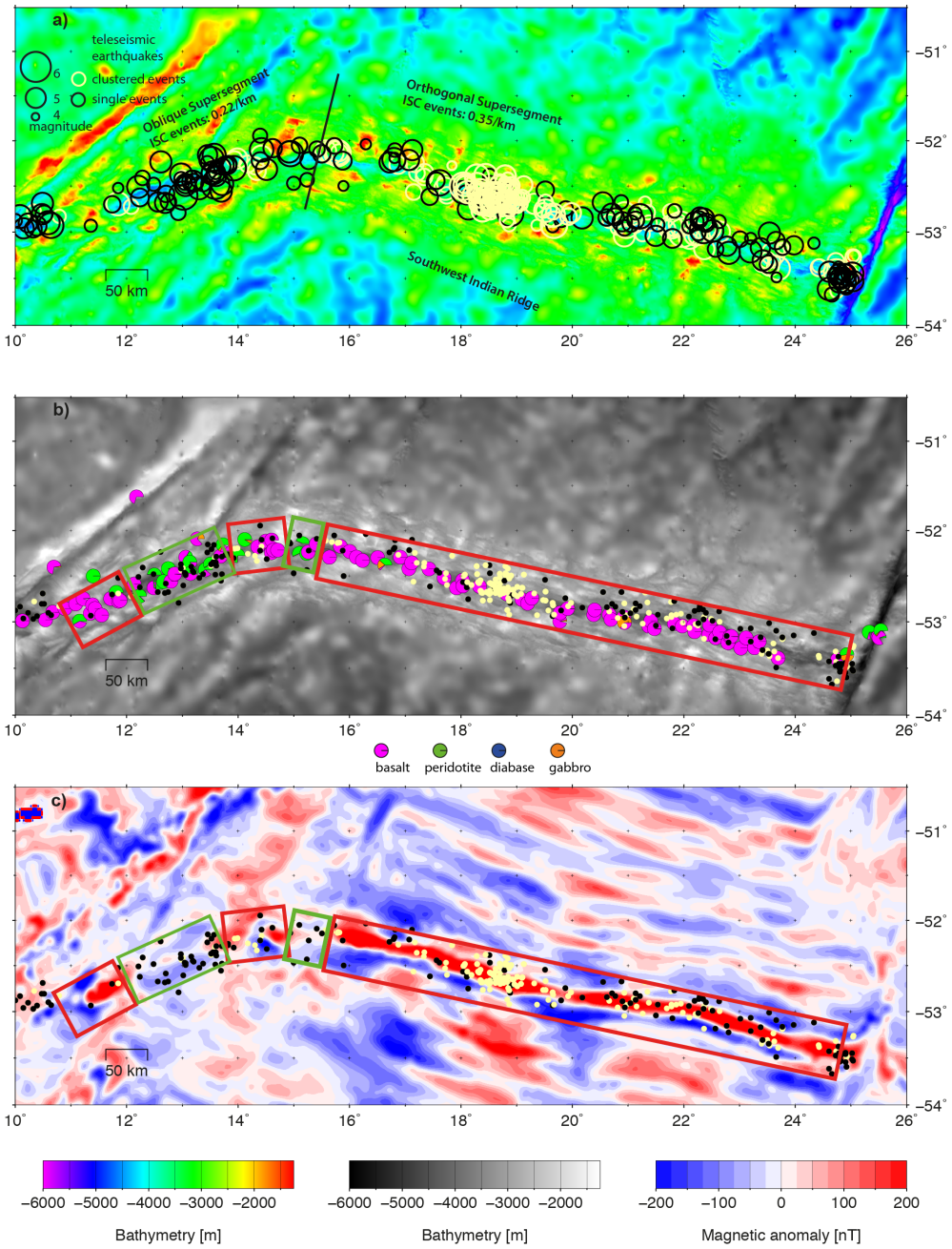

Figure 4.7 a, Teleseismic earthquake activity (open circles, scaled with magnitude) over bathymetry. The light yellow circles mark earthquake clusters of two or more events that are related in time and space. Data from *Schlindwein* (2012). b, Dredge lithology. Data from *Dick et al.* (2003). c, Magnetic anomalies. Data from *Maus et al.* (2009). Earthquakes from a are shown by the dots. The predominantly magmatic orthogonal supersegment shows more abundant and often clustered teleseismic earthquakes and a marked magnetic anomaly. The predominantly amagmatic oblique supersegment shows less seismicity and peridotite exposure. Areas of magmatic and amagmatic lithosphere within this segment are defined from the seafloor lithology and magnetic patterns. The differences in the event rates within segments (see Figure 4.2) are not visible here owing to a large uncertainty in earthquake locations.

4.6 Extended data tables

Site, Velocity model	No. of earthquakes located	Average rms residual [s]	No. of earthquakes with depth solution	No. of earthquakes with depth error < 5 km
Site 1				
Slow-end	1960	0.502	1896	990
Final	1959	0.485	1871	903
Fast-end	1959	0.546	1556	242
Site 2				
Slow-end	737	0.286	631	461
Final	736	0.264	614	441
Fast-end	744	0.364	441	181
Site 3				
Slow-end	2874	0.226	2880	2557
Final	2974	0.196	2894	2625
Fast-end	2970	0.235	1998	1555

Table 4.1 Location performance of the final one-dimensional velocity models and end-member models. Note, The final velocity model of each site achieved the best fit to all of the observed phases. The high end-member velocity models produce fewer and unstable hypocenter depths.

Site, Velocity model	No. of earthquakes located	No. of earthquakes located with depth error < 5 km	Average depth [km]	Average depth error [km]
Site 1				
-0.3 km s^{-1}	1960	990	20.3	3.8
Final	1959	903	20.2	4.0
+0.3 km s^{-1}	1960	929	20.0	4.1
Site 2				
-0.3 km s^{-1}	737	461	12.2	2.8
Final	736	441	10.9	2.6
+0.3 km s^{-1}	738	403	9.6	2.7
Site 3				
-0.3 km s^{-1}	2974	2557	10.6	2.5
Final	2974	2625	9.5	2.3
+0.3 km s^{-1}	2970	2497	8.8	2.3

Table 4.2 Dependence of the hypocenter depths on the velocity model. Note, only inverted hypocenter depths with a depth error of less than 5 km are included in the average values. The individual distributions are shown in Extended Data Figures 4.4b, 4.5b and 4.6b for each site. Note that the changes in average depth due to variations of the velocity model are in all cases smaller than the average depth error.

5 Microearthquake activity, lithospheric structure, and deformation modes at an amagmatic ultraslow spreading Southwest Indian Ridge segment

Authors: Florian Schmid[1] **and Vera Schlindwein**[1]

[1]Alfred-Wegener-Institute, Helmholtz-Centre for Polar- and Marine Research, Bremerhaven, Germany.

Published in July 2016 in *Geochemistry, Geophysics, Geosystems*, **17**, doi:10.1002/2016GC006271.

Key Points:

- Deepest so far recorded hypocenters beneath a mid-ocean ridge at 31 km depth.
- Brittle-ductile transition undulates considerably along the ridge axis.
- Aseismic deformation down to 20 km, due to serpentinization.

5.1 Abstract

While nascent oceanic lithosphere at slow- to fast spreading mid-ocean ridges (MOR) is relatively well studied, much less is known about the lithospheric structure and properties at ultraslow MORs. Here we present microearthquake data from a one-year ocean bottom seismometer deployment at the amagmatic, Oblique Supersegment of the ultraslow spreading Southwest Indian Ridge. A refraction seismic experiment was performed to constrain upper lithosphere P-velocities and results were used to construct a 1D-velocity model for earthquake location. Earthquake foci were located individually and subsequently relocated relative to each other to sharpen the image of seismically active structures. Frequent earthquake activity extends to 31 km beneath the seafloor, indicating an exceptionally thick brittle lithosphere and an undulating brittle-ductile transition that implies significant variations in the along-axis thermal structure of the lithosphere. We observe a strong relation between petrology, microseismicity distribution and topography along the ridge axis: Peridotite dominated areas associate with deepest hypocenters, vast volumes of lithosphere that deforms aseismically as a consequence of alteration and the deepest axial rift valley. Areas of basalt exposure correspond to shallower hypocenters, shallower and more rugged axial seafloor. Focal mechanisms deviate from pure extension and are spatially variable. Earthquakes form an undulating band of background seismicity and do not delineate discrete detachment faults as common on slow spreading ridges. Instead, the seismicity

band sharply terminates to the south, immediately beneath the rift boundary. Considering the deep alteration, large steep boundary faults might be present but are entirely aseismic.

5.2 Introduction

The creation process of new oceanic lithosphere is essentially governed by the speed opposing plates drift apart (e.g. *Bown and White*, 1994; *Reid and Jackson*, 1981). At mid-ocean ridges (MOR) spreading faster than 20 mm a^{-1} melt supply, crustal thickness and petrologic composition are surprisingly constant (e.g. *Bown and White*, 1994). As spreading rates drop below 20 mm a^{-1}, conductive cooling influences the ridge thermal structure and causes a drastic reduction in magmatism (*Bown and White*, 1994). However, petrological and geophysical studies from the ultraslow (< 20 mm a^{-1} spreading rate) Arctic Ridge System and the Southwest Indian Ridge (SWIR) revealed centers of robust magmatism, separated by long amagmatic segments that expose mantle rocks (*Dick et al.*, 2003; *Jokat and Schmidt-Aursch*, 2007).

Previous experiments at ultraslow MORs showed that the crust is very heterogeneous and often absent (e.g. *Cannat*, 1996; *Jokat et al.*, 2003; *Minshull et al.*, 2006), thus strongly differs from the average 7-8 km thick, layered oceanic crust (*White et al.*, 2001). Lithosphere produced at ultraslow spreading MORs constitutes 10-20% of all ocean basins (*Bown and White*, 1994). A detailed understanding of the processes that create and maintain the segmentation into magmatic centers and amagmatic segments of ultraslow ridges still poses a major challenge for ongoing MOR research.

The investigation of microearthquake activity with ocean bottom seismometer (OBS) and hydrophone deployments represents a well-established approach to image active processes of tectonic, magmatic and hydrothermal activity beneath MORs (e.g. *Crawford et al.*, 2013; *Kong et al.*, 1992; *Tilmann et al.*, 2004; *Wolfe et al.*, 1995). However, all to date performed long-term (> few days) studies on microearthquake activity at MORs focus on slow to fast spreading ridges. Previous earthquake studies on ultraslow ridges were based on teleseismic catalogs (*Korger and Schlindwein*, 2012; *Müller and Jokat*, 2000; *Schlindwein*, 2012) or reconnaissance style deployments of seismometers on drifting ice floes (*Korger and Schlindwein*, 2013; *Läderach et al.*, 2012; *Schlindwein et al.*, 2015). The perennial Arctic sea ice cover and stormy oceans above the SWIR have until now prevented long-term OBS deployments at ultraslow ridges.

In this study we present the results of a 10 OBS network deployed for 12 months on an amagmatic, oblique spreading segment of the SWIR. At this segment the exposure of lithospheric mantle (*Dick et al.*, 2003; *Standish et al.*, 2008) and remnants of ancient hydrothermal activity (*Bach et al.*, 2002) was known. During the OBS recovery cruise, combined with a search for hydrothermal activity, we performed a wide angle-seismic survey across the OBS network, to estimate upper lithosphere *P*-wave velocities (*Schlindwein*, 2014). The featured experiment was designed in conjunction with a similar sized, synchronously operated OBS network (*Schlindwein and Schmid*, 2016), installed on a magmatically active SWIR segment with the intention to compare the seismicity at both experiment sites and study the spreading processes at two very contrasting ultraslow MOR segments.

The main objective of this paper is to describe for the first time the long-term microearthquake activity and to analyze its geological and tectonic implications for an amagmatic ultraslow spreading SWIR segment.

5.3 Geological setting

The SWIR forms the boundary between the African- and Antarctic plates (Figure 5.1), which are diverging at an average velocity of 14-16 mm a^{-1} (*DeMets et al.*, 1994). The SWIR starts at 55°S latitude near the Bouvet Triple junction. It trends obliquely to the spreading direction towards northeast and is offset towards the north along several major north-south trending transform faults till it reaches Rodriguez Triple junction at 27°S latitude. However, a long SWIR section free of transforms is found between 9°E and 25°E which by means of morphology and dredged rock petrology is subdivided into the Oblique (9°-16°E) and Orthogonal (16°-25°E) Supersegments.

The Orthogonal Supersegment is characterized by a series of en echelon magmatic segments, with >90% basalts and a continuous magnetic anomaly (*Dick et al.*, 2003; *Grindlay et al.*, 1998). Towards the west, the ridge axis gradually increases its obliquity until 14°30'E (Figure 1b). From here until 11°30'E the axis remains 56° oblique (*Montési et al.*, 2011) with respect to the spreading direction. Due to obliquity, the effective spreading rate (normal to the ridge axis) is only ~7.8 mm yr−1 full rate (*Dick et al.*, 2003), resulting in slow presumed rates of mantle upwelling, possibly the slowest beneath all MORs (*Bach et al.*, 2002). Despite very low mantle upwelling and excess cooling we find two axial highs of basaltic composition (*Dick et al.*, 2003) with prominent magnetic anomalies, the Joseph Mayes Seamount (JMS) and Narrowgate magmatic segment (NG; see Figure 5.1) indicating the presence of robust, though very focused magmatism along the Oblique Supersegment. Between JMS and NG as well as west of JMS and east of NG are three oblique amagmatic spreading segments characterized by a deep axial rift valley, the abundant occurrence of peridotites, only scattered basalts and the absence of gabbroic rocks (*Dick et al.*, 2003).

5.3.1 The 11°35'-14°15'E amagmatic accretionary segment

Amagmatic accretionary segments are an integral part of ultraslow spreading ridge tectonics (*Standish et al.*, 2008) that can achieve any orientation relative to the spreading direction and thus are able to substitute transforms (*Dick et al.*, 2003). Hereafter the term amagmatic accretionary segment is exclusively used to refer to the 11°35'-14°15'E section of the SWIR, where our experiment was located. The amagmatic accretionary segment links the JMS and NG and shows no central magnetic anomaly (Figure 5.1b,c.). Single large low-angle fault surfaces with on average 1.2 km throw and 6 km heave construct the rift valley walls (*Bach et al.*, 2002) that are presumably composed of massive, altered peridotite blocks (*Standish et al.*, 2008), as bathymetry and petrology imply (Figure 5.1).

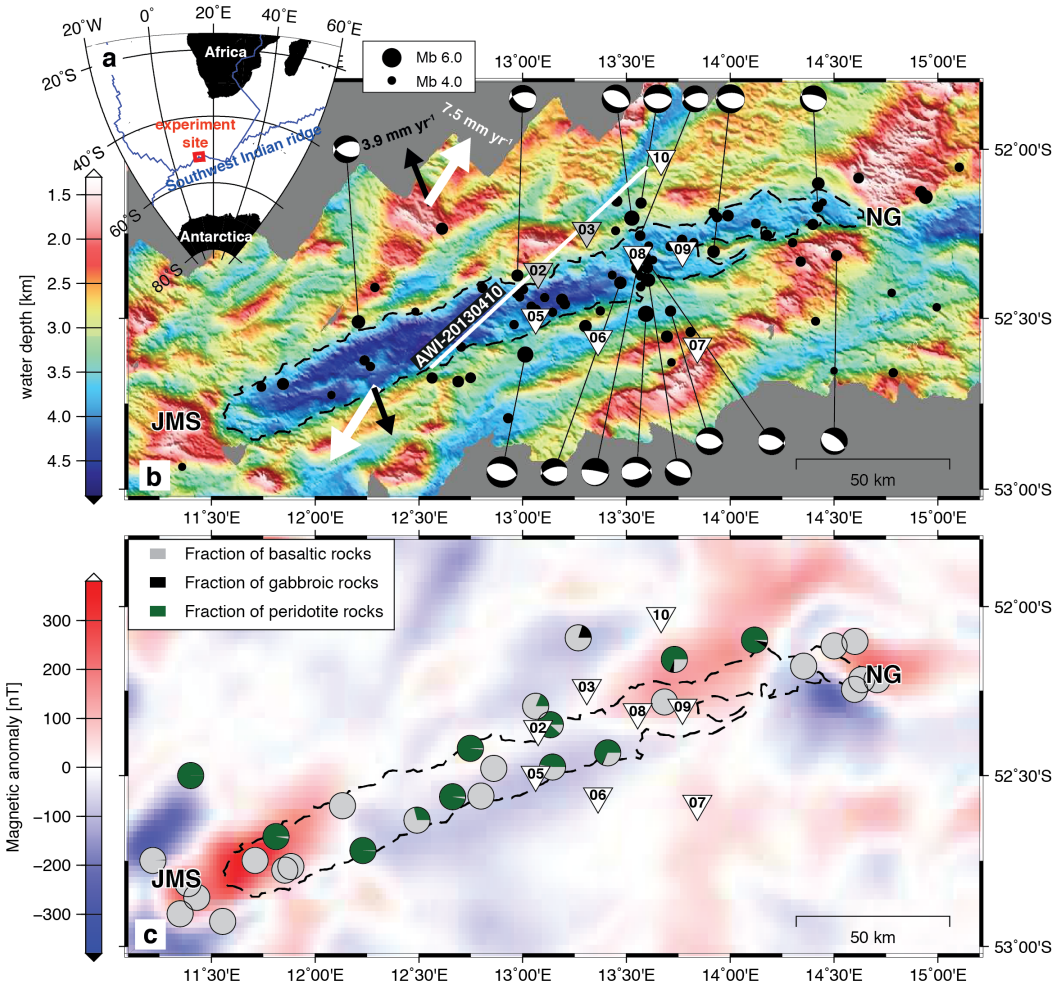

Figure 5.1 Survey area overview (a), teleseismic activity, petrology and magnetic anomalies. b) Shipboard bathymetry map of the survey area (compiled from RV Knorr cruise KN 162 (*Bach et al.*, 2002; *Dick et al.*, 2003) and RV Polarstern cruise ANT XXIX/8 (*Schlindwein*, 2014)). Inverted triangles: ocean bottom seismometer (OBS) stations. Gray stations were used for the wide-angle seismic profile AWI20130410 (solid white line). Dashed black line gives 3.5 km depth contour roughly outlining the extent of the 11°35'-14°13'E oblique amagmatic accretionary segment between Joseph Mayes Seamount (JMS) and Narrowgate (NG) magmatic centers. White and black arrows indicate absolute and effective spreading directions, respectively (*Dick et al.*, 2003). Black dots give ISC epicenters (*International-Seismological-Centre*, 2012) for the 01.01.1976 – 01.10.2012 period. Beach balls represent centroid moment tensor solutions (*Ekström et al.*, 2012). c) EMAG2 magnetic anomaly map (*Maus et al.*, 2009) and petrology of dredged rock samples compiled from several cruises (*Dick et al.*, 2003, Dick pers. comm., 2015).

Eruption ages of scattered basalts from the rift valley floor are younger towards the rift valley walls, suggesting accretion of new lithosphere might be accommodated by active boundary faults on either side of the axial valley, that might additionally serve as pathways for upward migration of magma and/or fluids (*Standish and Sims*, 2010).

5.3.2 Teleseismic earthquake activity

The manually reviewed International Seismological Centre (ISC) catalog (*International-Seismological-Centre*, 2012), contains 98 teleseismic registered events of magnitudes 3.7-6.0 mb for the period January 1976 to October 2015 within the 53°-52°S and 11°-15°E perimeter of the Oblique Supersegment (Figure 5.1a). Due to the remote location, teleseismic events are associated with large horizontal location uncertainties (approx. ± 10 km) and imprecise hypocenter depths. *Läderach et al.* (2012) estimated an ISC catalog magnitude of completeness for the area of 4.2 mb. Centroid Moment Tensor solutions (*Ekström et al.*, 2012) are available for 15 events, indicating normal fault source mechanisms throughout with fault planes striking rather perpendicular to the spreading direction than parallel to the rift valley walls. Teleseismic events along the amagmatic segment occur within and out to 50 km beyond the axial rift valley. While little teleseismic activity is connected to the JMS and NG magmatic centers, numerous events cluster around 52°20'S; 13°35'E in the axial valley of the amagmatic accretionary segment, where our network was deployed (Figure 5.1).

5.4 Methods

5.4.1 Acquisition of active and passive seismic data

During R/V Polarstern cruise ANT XXIX/2 in December 2012 we deployed a network of 10 free-fall OBS equipped with Güralp CMG-40T broadband seismometers and HiTech Inc hydrophones. One year later, nine instruments could be recovered of which eight returned data (Figure 5.1b). OBS recorded continuously at a sample rate of 100 Hz, internal clocks were synchronized prior deployment and after recovery and a linear clock drift was assumed in between. OBS positions on the seafloor were estimated from direct water wave airgun arrivals for stations S02, S03, S05, S07 that had not turned off recording before airgun operations started. A seafloor position at 2/3-distance between the deployment and recovery positions at the sea surface was assumed for stations S06, S08, S09 and S10.

5.4.2 Wide-angle seismic profiling

Prior to the recovery of instruments, five wide-angle seismic profiles were shot across the OBS network. We used 4 G-gun type airguns of 520 cubical inch total volume, fired every 60 s at a pressure of 200 bar, achieving ~150 m shot point spacing (*Schlindwein*, 2014). Some instruments had stopped recording before the airgun operations commenced and seismic signals were recorded only at five instruments S02, S03, S05, S07, S08. Thus, we obtain one wide-angle seismic profile AWI20130410

with sufficient ray coverage to establish a reversed 2D P-wave model. Profile AWI20130410 crosses the amagmatic segment in an almost flow-line parallel direction, prolonging approx. 50 km onto the African plate (Figure 5.1b). We used the RAYINVR software (*Zelt and Smith*, 1992) for forward modeling and subsequent model inversion. The model seafloor topography was retrieved from multibeam bathymetry.

Seismic data quality is strongly influenced by the rough, hard seabed and arrivals are complex due to scattering from topography (Figure 5.1a). Correct phase identification was only possible after some initial travel time modeling. We used the OBS hydrophone channel for phase arrival picking as it exhibits the best signal-to-noise-ratio (SNR). Picking uncertainties were calculated from the SNR around the picks and range from 40-125 ms.

Our initial P-wave model comprised 4 layers (Figure 5.2b) – the water body and three sub-seabed layers of decreasing velocity gradients, top down. Seismic velocity and velocity gradients immediately below the seafloor are well constrained by high amplitude turning rays from this layer, labeled Pc1, observed at distances up to 16 km. Turning rays from deeper layers (Pc2, Pc3, Figures 5.2a,b) exhibit inhomogeneous amplitudes and are absent in places. Where the ray coverage is highest, between profile kilometers 40-80 (Figure 5.2c) we extracted five 1D velocity profiles and plot their outline as gray shaded polygon in Figure 3, serving as basis for the hypocenter location.

5.4.3 Event detection and location with HYPOSAT

Passive seismological data were handled and processed with the SEISAN software (*Havskov and Ottemoeller*, 1999). A short-term-average/long-term-average (STA/LTA) trigger was used to identify seismic events in the continuous data, using a STA window of 5 s, a 100 s LTA window, a trigger ratio of 8, a detrigger ratio of 1.5 and minimum trigger duration of 6.5 s. The trigger was applied either to the vertical component or hydrophone channel - whichever showed a better SNR. Traces were 3-15 Hz band pass filtered prior to event detection. We consider all detections to be a seismic event if detected at 5 or more stations within a time window of 45 s.

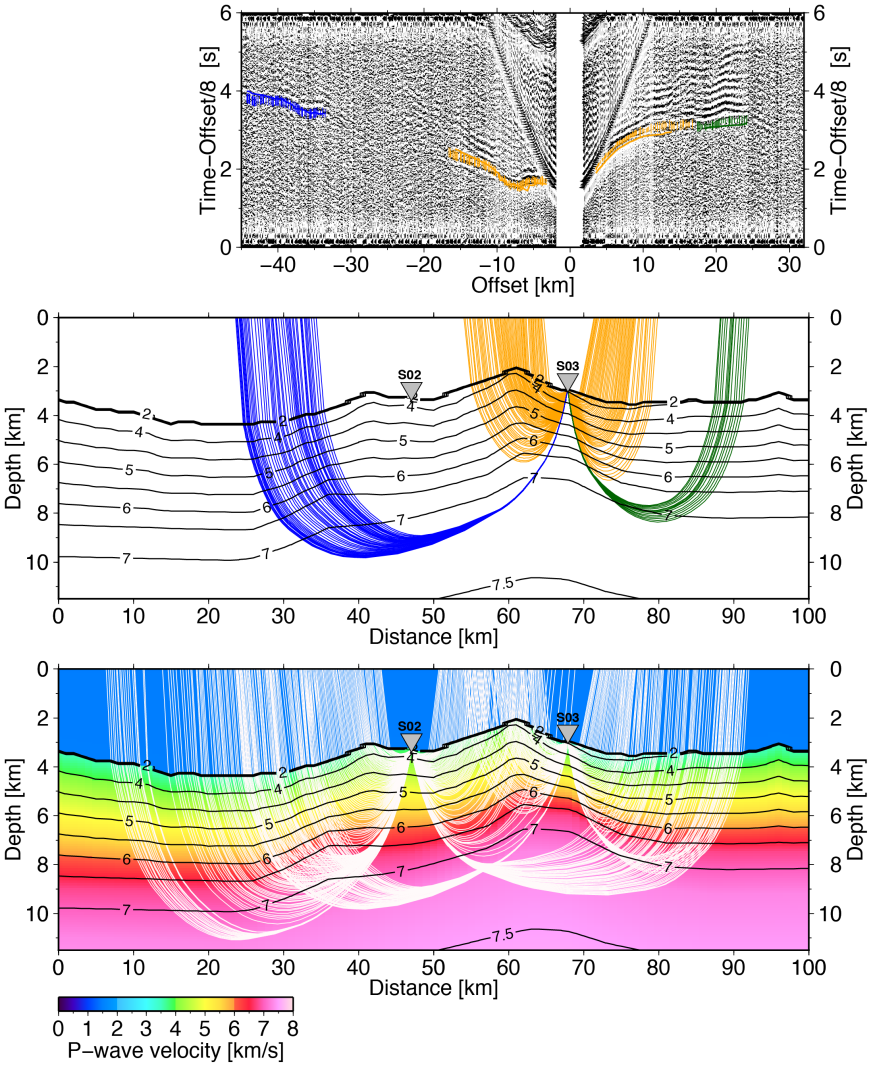

Figure 5.2 Wide-angle seismic results. a) Seismic record section for station S03, displayed at a reduction velocity of 8 km s^{-1} and gain proportional to range. Colored bars give phase onset picks and associated picking uncertainties for refracted phases of different model layers. b) Modeled P-wave ray paths for station S03. Color code represents different phases and is identical to associated phase arrival picks in above panel. Contour lines show model P-wave velocities, contour labels are spaced at 0.5 km s^{-1}. Inverted triangles mark OBS positions. c) Modeled P-wave ray paths for stations S02, S03 (white lines) and contours of model P-wave velocities.

Trigger results were manually checked afterwards, whereupon 74 % of the triggers appeared to be events for which more than 5 phase onsets (including P- and S-phases) at different stations could be picked by an analyst. We located the hypocenters with the least squares HYPOSAT routine (*Schweitzer*, 2001) on the basis of a 1D P-wave velocity model, partially derived from the wide-angle seismic profile AWI20130410 (Figure 5.2, Figure 5.3): In the top 3.5 km we adopted the results of the wide-angle seismic profile. To constrain deeper velocities we took a subset of 67 earthquakes that occurred within the network and for which are P- and S-phase onsets are available at all stations. The subset was repeatedly located while the velocity was systematically altered. The top 3.5 km and the lower end (50 km, Vp = 8.04 km s^{-1} (*Kennett and Engdahl*, 1991)) were kept fixed. We varied the depth, velocity gradients and incorporated Moho-interface-like steps in tested velocity profiles. A number of different tested velocity profiles and associated statistics for located events can be found in supplements Figure 5.11 and Table 5.2.

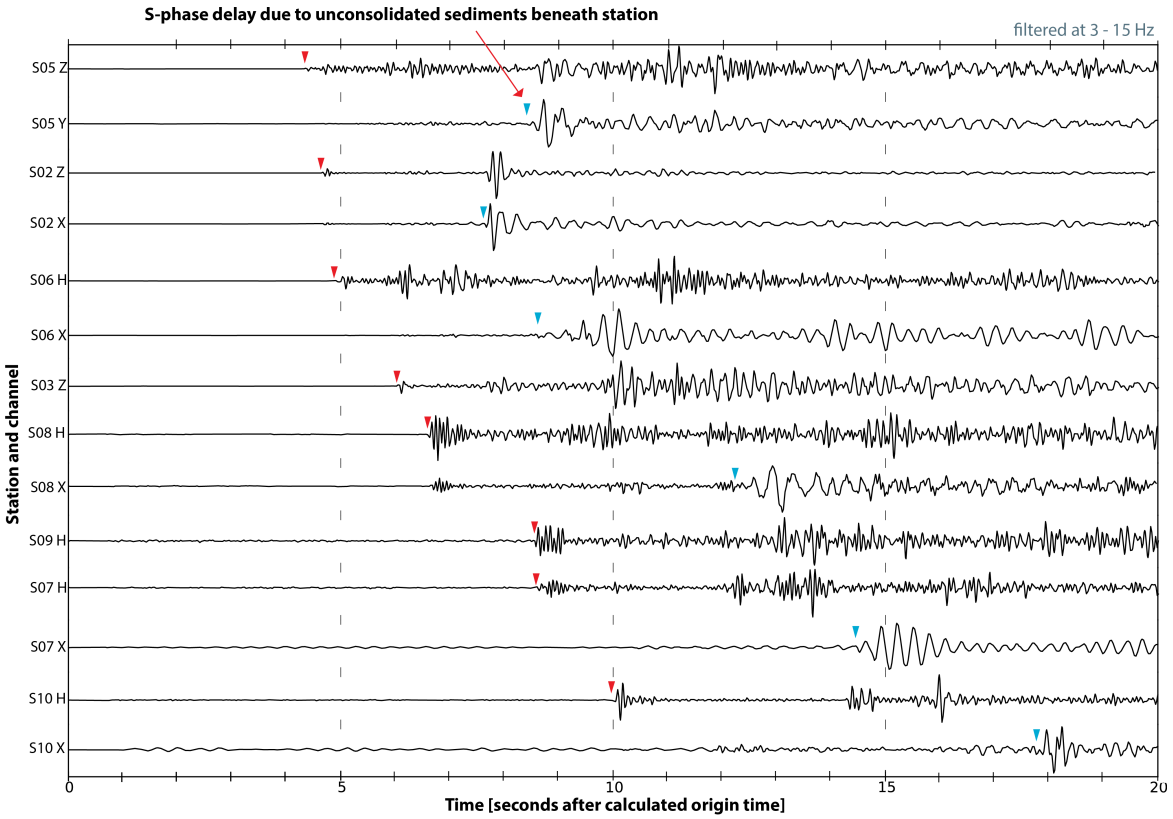

Figure 5.3 Waveforms of an exemplary event (origin time at 26 December 2012 15:18:57.56) located nearby stations S05 and S02 at 28 km beneath seafloor. Red and blue markers indicate P and S-phase arrival picks, respectively. Note that a large S-P travel time differences at stations S05 and S02 point to a deep hypocenter.

Moreover, the velocity model was designed as simple as possible introducing not more than three layers. In terms of average RMS travel time residuals, size of the 95 % confidence error ellipse and the hypocenter depth error the best results were achieved for a Vp of 7.0 km s^{-1} at 5 km, constantly increasing to 8.04 km s^{-1} at 50 km (Figure 5.3). S-phase velocities were calculated from the P-phase velocity model, assuming a Vp/Vs-ratio of $\sqrt{3}$. We used this model for hypocenter location with the HYPOSAT and HYPODD routines.

The hypocenter inversion was initiated with a priori fixed source depth at 5 km and hypocenter depth was inverted subsequently. Fixed-depth and depth-inverted solution – if successful – were saved as output. An initial location run with the HYPOSAT routine indicated systematic P- and S-phase delays at stations S05, S06 and S08. Layered strata above the acoustic basement were observed in the sub-bottom profiling echo sounder data in the vicinity of the affected stations. Recovered gravity cores from RV Polarstern cruise ANT XXIX/8 (*Schlindwein*, 2014) indicate soft and oversaturated sediments. We attribute the systematic phase delay to a layer of unconsolidated deep-sea sediments in the axial rift valley. The thickness of the sedimentary layer could only be poorly constrained by echo sounder data as rough topography in most places scatters the signal pulse, preventing acoustic imaging. Sediments are thicker than 150 m, wherever imaged.

We therefore incorporate a 200 m thick sediment layer with Vp = 1.8 km s^{-1} and Vs = 0.3 km s^{-1} for station correction at S05, S06 and S08. From the HYPOSAT generated catalog we selected for each event the depth-inverted solution with the lowest average RMS misfit of travel time residuals as input for the relocation procedure. Where no depth-inverted solution was available we used the fixed-depth solution of lowest RMS misfit instead.

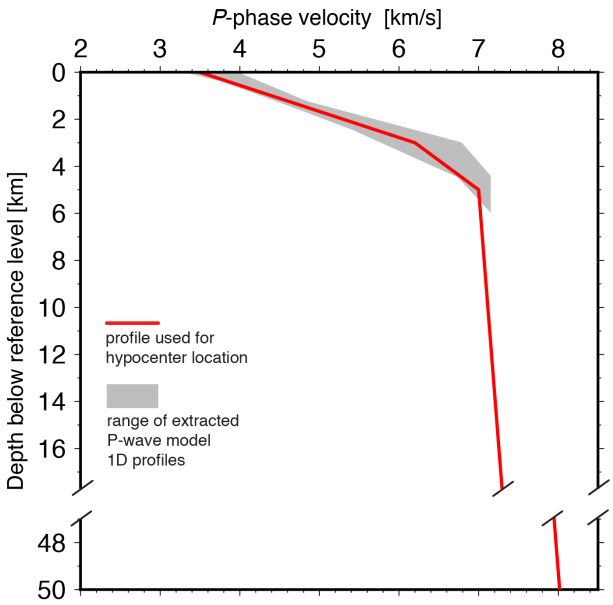

Figure 5.4 One-dimensional P wave velocity model (solid red line) used for the location of local earthquake hypocenters. Gray polygon outlines the range of 1D velocity profiles extracted between profile kilometers 40–80 from profile AWI20130410 results (Figure 5.2).

5.4.4 Estimation of M_l magnitudes

Earthquake magnitudes were calculated using the local magnitude scale Ml (*Bullen and Bolt*, 1985): $M_l = log_{10} \cdot A + 2.56 \cdot log_{10} \cdot D - 1.67$, where A is the maximum displacement in nm on a Wood Anderson instrument and D is the epicentral distance in km, valid for 10 < D < 600 km *Shearer* (2009). We modified the above magnitude scale by using the hypocentral distance instead of the epicentral distance, for the following reason: Numerous hypocenters are located immediately beneath the OBS network (Figure 5.5b), the epicentral distance is often considerably smaller than the true ray path and therefore the epicentral distance would grossly underestimate the attenuation of seismic phases. Amplitudes were picked at vertical components of stations S02, S03 and S07 only. Amplitudes at stations S05, S06 and S08 were affected by unconsolidated sediments and for stations S06, S09, S10 the vertical channel baseline was close to saturation due to malfunctioning sensors.

5.4.5 Relocation of earthquakes with HYPODD

After locating hypocenters individually with the HYPOSAT routine, we used the HYPODD double-difference earthquake location algorithm of *Waldhauser and Ellsworth* (2000) to improve relative location accuracies. HYPODD makes use of differential travel times between event pairs at common

stations and thus reduces model biases. The double-difference method can collapse diffusely distributed, individually located foci into sharper images of seismically active structures (*Waldhauser and Ellsworth*, 2000). However, only events that are in proximity to each other or somehow physically connected can be jointly relocated whereas isolated events have to be omitted *Waldhauser and Ellsworth* (2000). We calculated differential travel times from phase pick data and cross-correlated P-phase onsets. For events that have similar waveforms, more precise differential travel times can be estimated by cross-correlating the waveforms. We cross-correlated all hydrophone records, for a window of 3 s around the P-phase onsets and calculate the differential travel times if the correlation is >0.9 at three or more stations for one event pair. Pick and cross-correlation differential travel times were combined for relocation with the HYPODD routine. In total, 799 events could be relocated that are mostly within the perimeter of the OBS network, most of which are associated with one large cluster. During the relocation procedure some events became air quakes or got rejected because of large residuals. We used the least squares conjugate gradients method (*Paige and Saunders*, 1982) to solve the system of double-difference equations. However, location errors determined by this method are supposed to be generally underestimated (*Waldhauser and Ellsworth*, 2000). The relocation was repeated with different input data (pick data only, cross-correlation data only, and all data) and different starting locations (HYPOSAT locations or cluster centroid) to test and verify the stability of the relocation results. The results of these so-called robustness tests may be found in the Supporting Information Figure S4.

5.5 Results and discussion

5.5.1 Upper lithosphere properties from wide-angle seismics

Essential findings from our active seismic experiment are the lack of prominent PmP Moho reflections or upper mantle head waves Pn (Figure 5.2a) and low seismic velocities in the deeper part of the profile which are well below the usual 8.0 km s^{-1} of oceanic upper mantle (e.g. *White et al.*, 2001). Although observed refracted phases and missing reflected phases imply the absence of pronounced impedance contrasts in the subsurface, we introduced layers to our model to allow for a change of velocity gradients with depth. In general, velocity contours along the profile are paralleling the surface and we observe a velocity gradient constantly decreasing with depth, without a Moho interface (Figure 5.4). Observed turning rays could be modeled down to 11 km beneath sea level, where they indicate layer velocities of 7.2 km s^{-1}.

Our results imply the upper lithosphere to be vastly departing from usual oceanic crust and upper mantle (*White et al.*, 2001). Dredged rock samples along the seismic profile yield peridotites and basalts but hardly gabbros (*Dick et al.*, 2003), (Figure 5.1c). The fact that gabbros and partially serpentinized peridotites have similar seismic velocities (e.g. *Carlson*, 2004; *Horen et al.*, 1996) precludes any compositional inferences solely from our seismic data. The absence of obvious impedance contrasts makes a clear distinction between crust and upper mantle intricate.

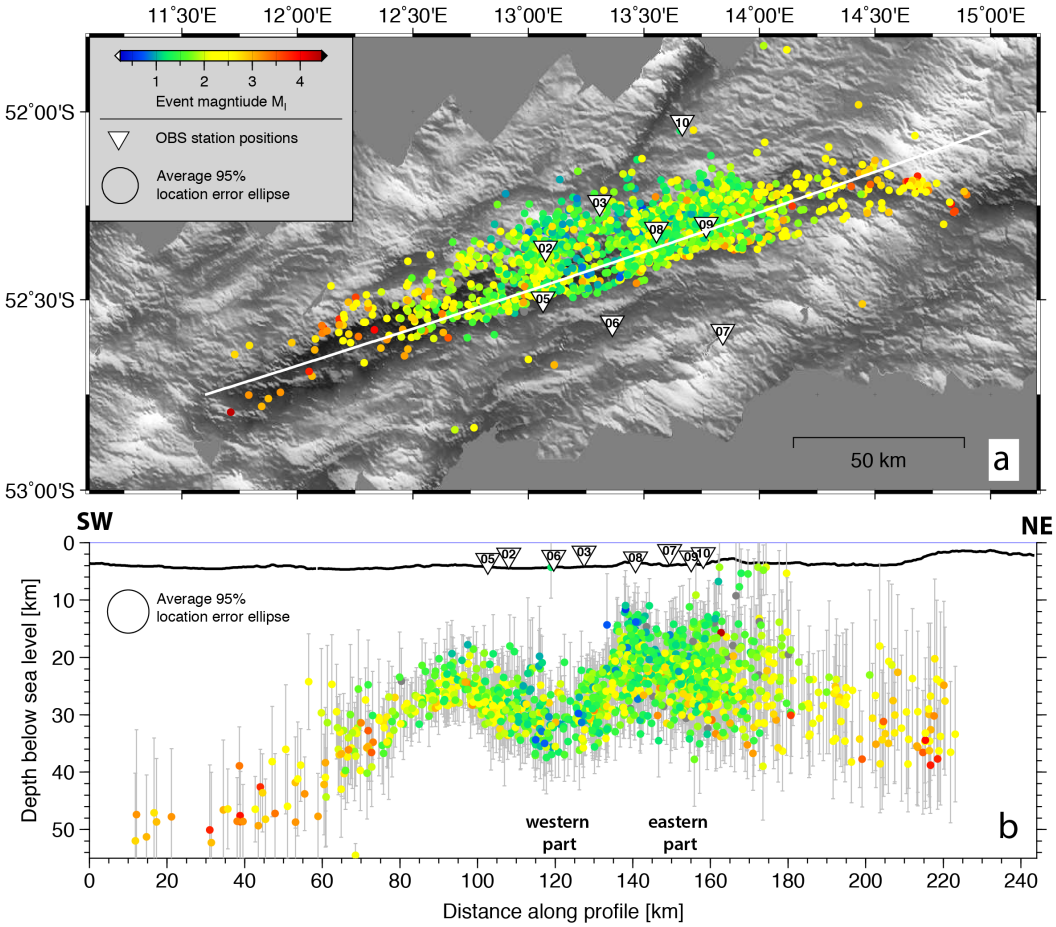

Figure 5.5 Epicenter and hypocenter solutions of HYPOSAT located events. (a) Bathymetry (data origin as in Figure 1) with epicenters and color code representing magnitudes. Solid white line indicates location of cross section below. Inverted triangles show OBS positions. (b) Cross section along the rift axis with projected hypocenters within 10 km to profile. Gray bars give depth errors. Vertical exaggeration: 1.5. Note that location errors and magnitudes increase further away from the seismic network.

The upper lithosphere might rather be referred to as a mix of scattered erupted basalts at the seafloor *Dick et al.* (2003); *Standish and Sims* (2010), gabbroic intrusions, and a peridotitic country rock that is altered at decreasing grade to greater depth.

5.5.2 Seismicity in space and time

Results of HYPOSAT locations

The possibly most exciting results of this study are the observation of unexpectedly deep hypocenters down to 31 km beneath the seafloor and an extensive portion of the upper axial lithosphere that is completely aseismic. The exceptional depths of hypocenters particularly in the western part of the survey area can already be inferred from the large travel time differences between *S* and *P*-phases for the event in Figure 3 that is located close to stations S05 and S02.

Events in catalog	1740
Time span of catalog	7. Dec. 2012 till 20 Nov. 2013 (348 days)
Range of magnitudes in catalog	M_l 0.58 - 4.36
Mean RMS residual	0.47 s
Mean S-major [a]	5.366 km
Mean S-minor	3.965
Mean depth error	5.558 km
Average no. of phases used for location [b]	15.971

Table 5.1 Statistics of the achieved microearthquake catalog, located With HYPOSAT.

[a] S-major and S-minor refer to the semimajor and semiminor half axis of the 95% confidence error ellipsoid, respectively.
[b] The average number of phases used for location also includes S-P travel time differences.

Through the HYPOSAT location procedure 1959 events could be located. Solutions with a semimajor axis of the 95% error ellipsoid >15 km, a depth error >15 km, and an average RMS residual of travel times >1.0 s were rejected from further analysis and have not been plotted in the related figures. By this selection process we achieve a catalog of 1740 events (Table 5.1). Histograms of travel time residuals for all events and for individual stations and phases may be found in Supporting Information Figure 5.13. To quantify the effect of the station correction on the location results, a set of 18 randomly chosen events (that have phase picks at all stations) were located with and without applying the sediment correction. The sediment correction enables a more stable location result, with in general smaller depth uncertainties and a smaller RMS value compared to a location without the sediment correction (Supporting Information Figure 5.12). When stations sitting on soft sediments (S05, S06, and S08) are omitted, the RMS further decreases, which indicates that the sediment correction does not entirely compensate effects of strongly varying seismic velocities in the shallow subsurface (cf. residual histograms in Supporting Information Figure 5.13). However, excluding these stations from location results in the sparse network with limited hypocenter location capability that results partly in larger depth errors.

Overall, changes in hypocenter solutions introduced by the sediment correction are small, causing hypocenters to be on average about 2 km shallower inside the network (see Supporting Information Figure 5.12). Beyond 30 km outside the network little to no more magnitude Ml < 2.0 events can be detected, location uncertainties and depth errors increase (Figure 5.5b). Hypocenters at the western end of the survey area bear large azimuthal gaps in station coverage (exceeding 315°) due to the network geometry. As a consequence, the depth sensitivity deteriorates considerably for these events. We omit distant events (further 30 km outside the network) from subsequent description and geological interpretation (Figure 5.5).

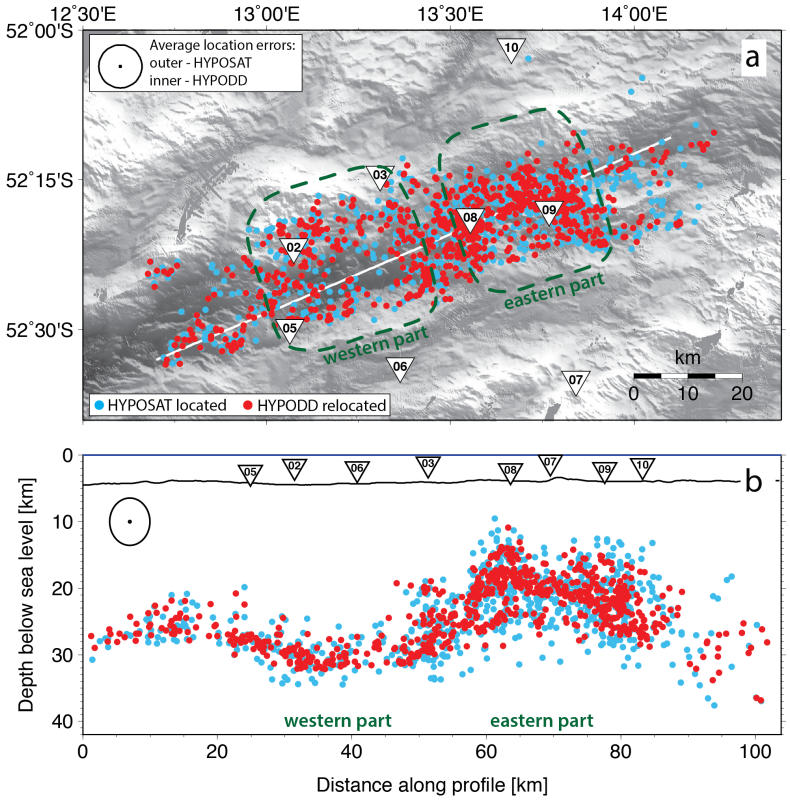

Figure 5.6 Comparison of HYPODD relocated hypocenters to HYPOSAT solutions. (a) Bathymetry with relocated events (red) and HYPOSAT locations of all relocated events (blue). White line shows position of cross section below. Ellipses in upper left corner represent HYPOSAT (outer ellipse) and HYPODD (inner ellipse) average location errors. See text for details. (b) Depth cross section along the ridge axis displaying projected hypocenters within 5 km distance of profile.

The recorded seismicity is concentrated in the axial valley, abruptly terminating at the southern flank and gradually diminishing across the northern flank (Figure 5a). Hypocenters form a distinct band of seismicity undulating in depth and vertical extent along the rift axis (Figure 5b) with maximum hypocenter depths from 28 to 35 km. For further description of the results and later geological interpretation, we will hereafter subdivide the survey area beneath the OBS network in two parts (western and eastern) based on the spatial seismicity distribution: The western part — SW of profile km 140 in Figure 5b (W of 13°30'E) — is mainly characterized by a vast volume of the upper lithosphere devoid of seismic activity. This part also comprises deepest hypocenters within the survey area, reaching 35 km below sea level and dredge samples yield mostly peridotites (Figure 5.1). The eastern part — NE of profile km 140 in Figure 5b (E of 13°30'E) — is characterized by shallower events and hypocenters generally occupying a larger depth range where numerous basalts have been dredged.

Results of HYPODD relocated hypocenters

The relative relocation of hypocenters with HYPODD intended to better resolve and image seismically active structures beneath the ridge axis. In total, 799 of the 1959 individually located hypocenters could be relocated, indicating these events to be not isolated but somehow physically related among each other. Most of the relocated foci (777 of 799) are organized in one large cluster, where single events are successively interlinked.
In comparison to HYPOSAT solutions, relocated hypocenters collapse within the seismicity band, narrowing down the vertical extent of the seismicity band and sharpening the image (Figure 5.6b). In the horizontal domain relocated hypocenter solutions show a similar distribution as HYPOSAT locations (Figure 5.6a). Results of robustness tests with different input data and different starting locations (Supporting Information Figure 5.14) generally replicate the undulating band of seismicity and the lack of shallow earthquakes in the western part, indicating the quality of relocation results.
Figure 5.7 illustrates the difference in seismicity distribution between the eastern and western parts (cross sections to left and right-hand side, respectively) of the survey area. In the western part the seismicity mimics a slightly southward tilted surface at 25–30 km beneath sea level. For the eastern part, seismicity occupies a larger depth range, occupying a conic-shaped lithosphere volume.

Results focal mechanisms

We used P-phase polarities and FOCMEC (*Snoke et al.*, 1984) to determine best fitting double-couple source mechanisms for events with azimuthal gaps smaller 120°. We obtained sufficiently well-constrained focal mechanisms for 22 events that have magnitudes of $2.17 < M_l < 3.15$ and hypocenters at 19–30 km depth (Figure 5.8). Fault mechanisms are diverse and have variable strike orientations. Beside five normal faults and eight reverse faults there are nine solutions that produce double couples of high-angle or subhorizontal fault planes. Apparently, microearthquake focal mechanisms mostly differ from the purely normal faulting mechanisms of the teleseismic events in Figure 5.1b.

Earthquake magnitudes

The spatial seismicity distribution described above is stable in time throughout the entire survey period (Figure 5.9): We observe a nearly constant event rate of 4.7 events per day, homogeneously distributed magnitudes over time (Figure 5.9e) and no signs of swarm activity or main shock-aftershock sequences (Figures 5.9d,e). For this analysis, we included only events within 30 km of the network (Figure 5.9a) to avoid a sampling bias toward stronger magnitudes from outside the network (Figure 5.5). We therefore propose the recorded earthquakes to document the prevailing background seismicity of the monitored lithosphere. The most frequent magnitude Ml 1.6 was estimated as the magnitude of completeness (Mc) for the achieved catalog (Figure 5.9c). For the magnitude range of $1.6 < M_l < 3.0$ the recorded seismicity obeys the Gutenberg-Richter relation (*Gutenberg and Richter*, 1956), but beyond M_l 3.0 earthquakes are less frequent than predicted, possibly due to the limited observation period.

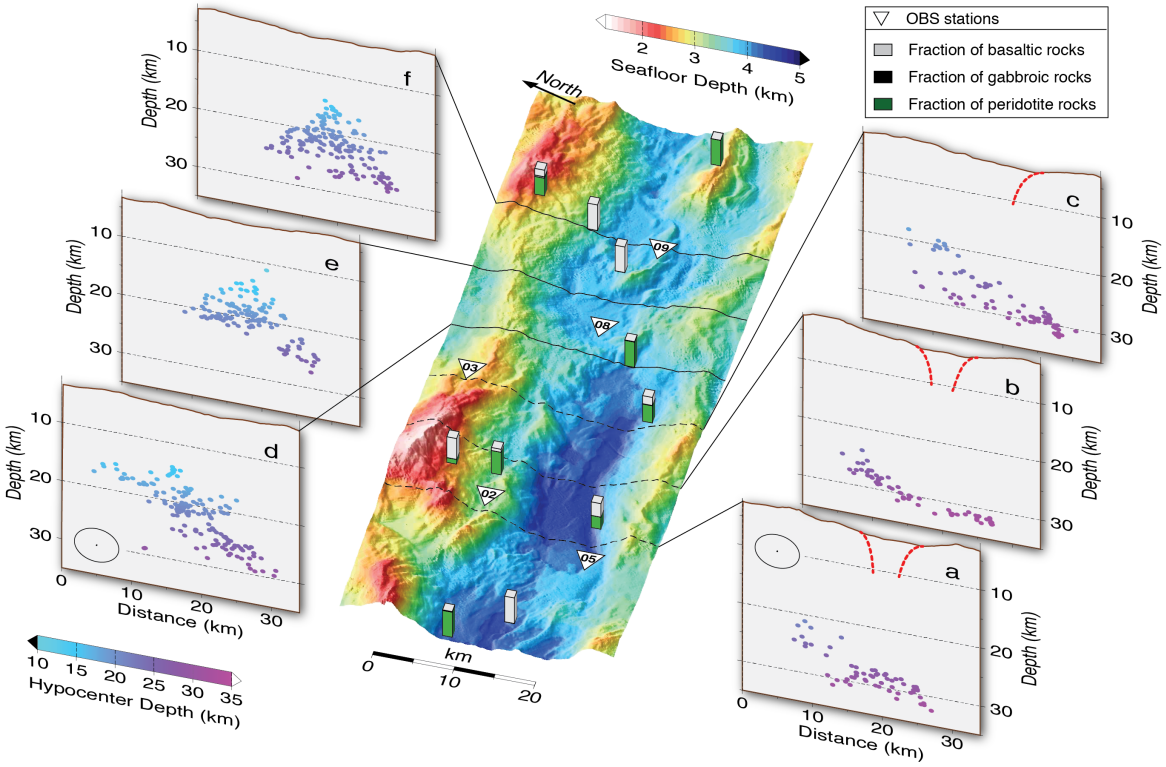

Figure 5.7 Distribution of HYPODD relocated hypocenters, bathymetry, and petrology across the axial rift valley in the survey area seen from southwest. Vertical sections (a–f) are perpendicular to the rift axis, spaced at 10 km apart with projected hypocenters with color code representing depth. We only plot events that are within 5 km distance to each section. Ellipses in Figures 5.7a,d represent location uncertainties (cf. Figure 5.6). Note that possible subsurface continuation of fault scarps (dashed red lines) finds no expression in seismicity.

5.5.3 Deep hypocenters indicate exceptionally thick brittle lithosphere

Our experiment reveals the so far deepest hypocenters recorded beneath any MOR axis. Previous studies of microearthquake activity beneath MOR spreading axes found the deepest hypocenters (with reference to the seafloor) at 1.8 km beneath the fast spreading East Pacific Rise (*Bohnenstiehl et al.*, 2008), at 9 km beneath the slow spreading Mid Atlantic Ridge (*deMartin et al.*, 2007; *Kong et al.*, 1992; *Tilmann et al.*, 2004; *Toomey et al.*, 1985), and at 20 km beneath the ultraslow spreading Knipovich Ridge (*Schlindwein et al.*, 2013). Observing frequent earthquake foci down to 31 km beneath the seafloor (35 km below sea level) in our study area (Figures 5–7) clearly pushes the limits of how thick brittle lithosphere at active MORs can be. The exceptional thickness of the brittle lithosphere is potentially a consequence of the spreading obliquity. The results of an analytical corner flow model of *Montési and Behn* (2007) for the SWIR oblique supersegment suggest the lithospheric thermal structure to be mainly controlled by the effective spreading rate.

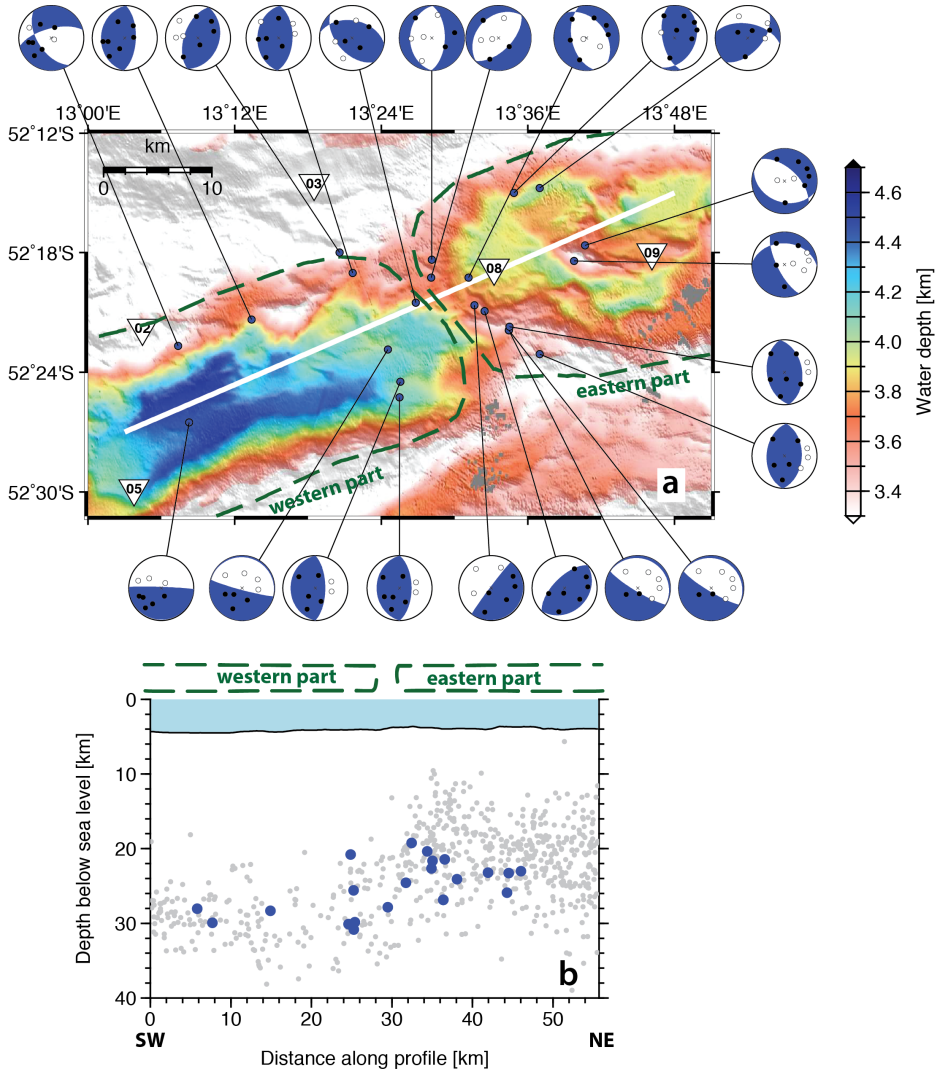

Figure 5.8 (a) Best fitting double-couple moment tensor solutions for HYPOSAT located events with clear P-phase onset polarities at all stations. White line shows location of the below section. Note the enhanced bathymetry color scale to highlight structures in the axial valley. (b) Vertical section with projected hypocenters for focal mechanisms (blue) and remaining HYPOSAT located hypocenters (gray).

5.5.4 Brittle-ductile transition as proxy for the axial thermal structure

The brittle-ductile transition demarking the lithospheric region beneath which brittle failure becomes unlikely is mainly temperature controlled (*McKenzie et al.*, 2005). Absolute brittle-ductile transition temperatures were discussed by several authors (e.g. *Anderson*, 1995; *Chen and Molnar*, 1983; *McKenzie et al.*, 2005; *Wiens and Stein*, 1983). Considering the different studies, an average temperature of 650 6 1008C satisfies the range of estimates. However, for our findings the absolute temperature is of less importance than relative changes in the depth of the brittle-ductile transition (Figure 5.10).

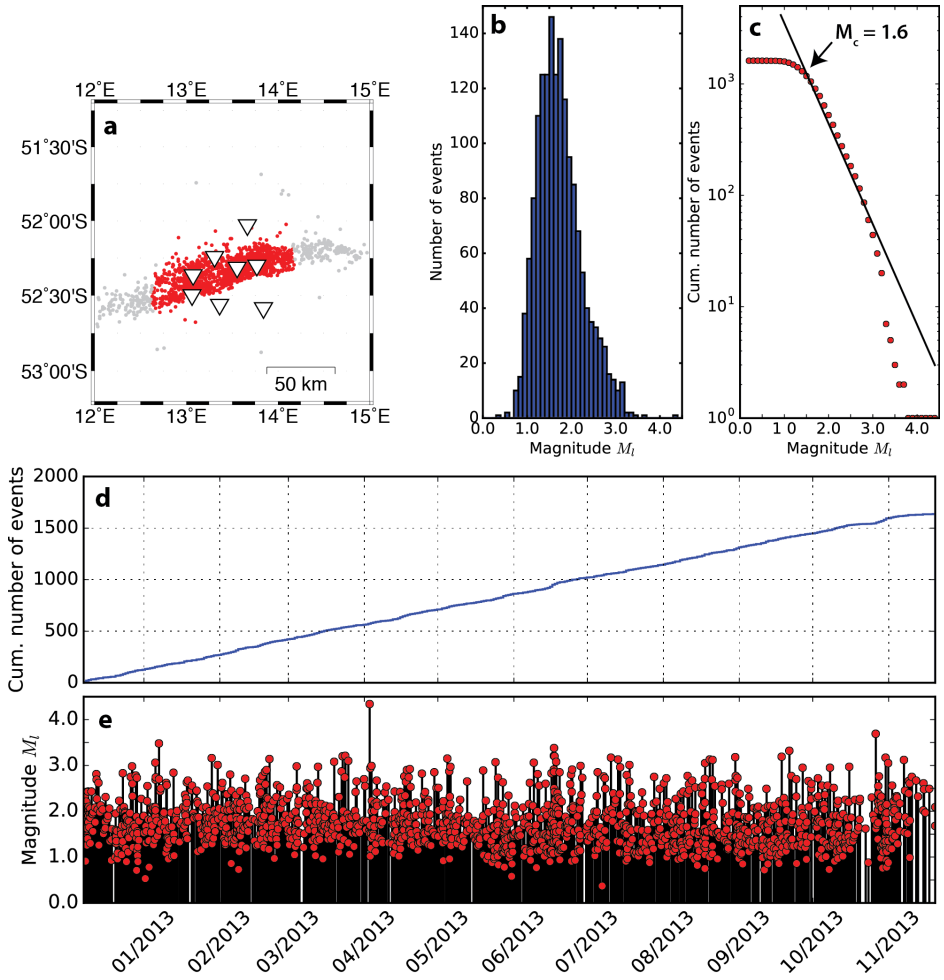

Figure 5.9 Magnitude analysis of HYPOSAT located events. (a) Distribution of events considered for magnitude analysis (red) and those omitted (gray). (b) Histogram of magnitude occurrence. (c) Frequency magnitude distribution. (d) Temporal evolution of the cumulative event number and (e) temporal occurrence of magnitudes.

Presuming a constant temperature at the brittle-ductile transition across the survey area, the maximum hypocenter depths of recorded earthquakes provide a robust indicator for the thermal structure along the ridge axis (*Schlindwein and Schmid*, 2016). Extrapolated to greater depth and hotter domains, the observed temperature structure suggests an undulating Lithosphere-Asthenosphere-Boundary (LAB) along the ridge axis. That is a key element for the conceptual model of *Standish et al.* (2008), to explain the along axis variation in melt formation and crustal thickness at the SWIR. *Standish et al.* (2008) propose the LAB topography to guide melts from amagmatic segments toward volcanic centers (e.g., NG and JMS) thereby propelling the distinct segmentation of ultraslow ridges *Dick et al.* (2003); *Sauter and Cannat* (2010). Our results, showing significant variations in the lithospheres thermal structure along the ridge axis, provide solid evidence for this concept.

Although our study area does not cover prominent volcanic centers like NG and JMS, even subordinate magmatic centers indicated by basalt exposure and rougher axial valley morphology (Figure 5.10; 30 and 80 km) are underlain by somewhat hotter lithosphere with a shallower brittle-ductile boundary than in between where mantle rocks are exposed.
Thus, we observe a general relation between lithospheric composition and thermal structure. Basaltic areas are associated with thinner, warmer lithosphere and peridotitic areas are related to thicker, cooler lithosphere. This concept is confirmed by further microseismicity observations from a magmatically robust SWIR segment around 65°E and the Knipovich Ridge in the Arctic *Schlindwein and Schmid* (2016); *Schlindwein et al.* (2013).

5.5.5 Aseismic deformation as indicator for hydrothermalism

One of the most unexpected results in the microearthquake distribution is a vast upper lithosphere volume devoid of seismic activity (Figures 5b, 6b, and 10, western part) in areas that are dominated by mantle rock exposure. We infer the aseismic lithosphere to be a consequence of deep-reaching fluid circulation and subsequent formation of phyllosilicates in cracks and fissures (e.g. *Amiguet et al.*, 2012; *Andreani et al.*, 2007) that have a drastically reduced shear strength in comparison to unaltered mantle rocks *Amiguet et al.* (2012); *Escartin et al.* (2001). The process of lithospheric weakening through initial cracking—associated with microearthquake activity, subsequent intrusion of seawater, and formation of phyllosilicates—is continuously progressing as new lithosphere of mainly peridotitic composition is formed *Amiguet et al.* (2012). *Rouméjon and Cannat* (2014) suggest this process as quasi-instantaneous on geological time scales. The magnetic anomalies reveal a slightly weaker magnetization in the western part (Figure 5.1c), indicating the serpentinized lithosphere to be less magnetic than the basalt bearing eastern part. This is in agreement with findings further east at the SWIR, where the magnetic signature of the SWIR axis correlates with the abundance of basalts *Sauter and Cannat* (2010).

An estimated geothermal gradient for the western part of the survey area, presuming a brittle-ductile transition at 650°C, suggests the lower limit of the aseismic lithosphere at temperatures of 400–500°C. This agrees with the upper limit of the serpentine stability field, considered at 390–460°C *Evans* (2004); *Schwartz et al.* (2013). However, there is little constraint on maximum temperatures limiting the onset of serpentinization *Evans* (e.g. 2004); *Schwartz et al.* (e.g. 2013). Relocated hypocenters indicate a sharp upper limit of the seismicity band in the western part (Figures 5.7a–c). Here we suggest the upper limit of the seismicity band to coincide with the temperature stability field of serpentine phases that are stable above (at temperatures lower approximately 400°C) and cause weakening of the lithosphere. Bearing in mind the deepened brittle-ductile transition in the western part of the survey area (Figure 5.10) and the present deep-reaching fluid circulation, we propose that intruding seawater might have a significant cooling impact on the axial lithospheric thermal structure, if persistent on geological time scales.

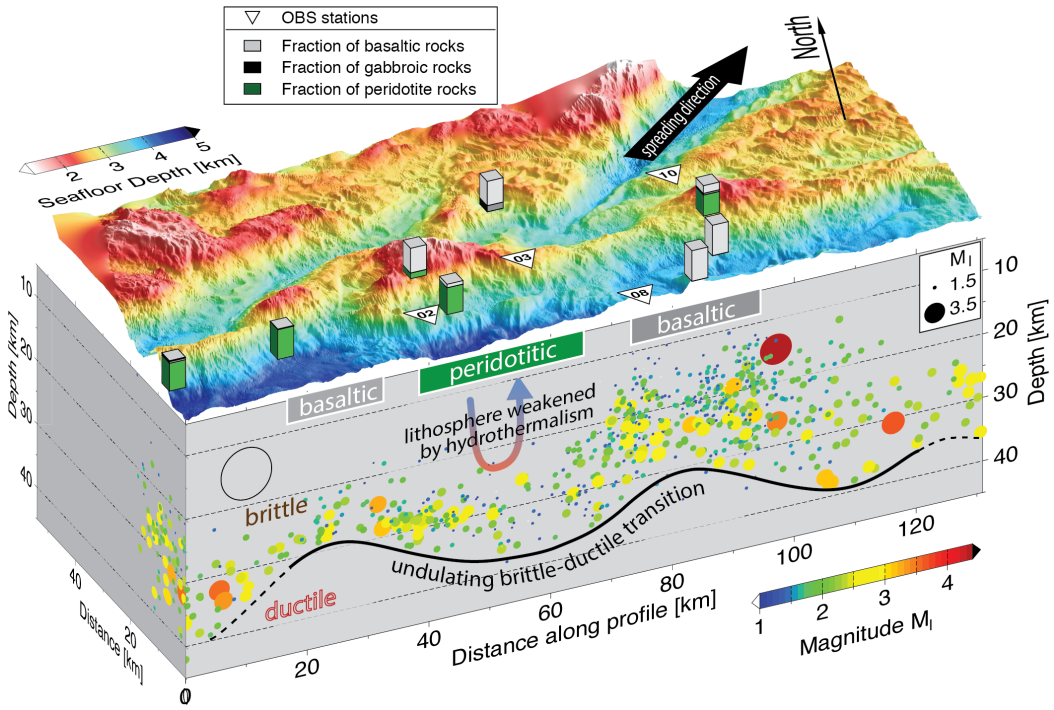

Figure 5.10 Pseudo-3-D view at upper lithosphere and seafloor in the survey area figuring the major findings deduced from the distribution of local seismicity. Front edge is parallel to ridge axis. Note that bathymetry is plotted at larger vertical exaggeration than vertical sections. Vertical bars give position and quantitative composition of dredged rock petrology. Dots on vertical section represent projected HYPODD relocated hypocenters, with color code and size according to magnitude. Black ellipse represents average location error. Terms "basaltic" and "peridotitic" qualitatively describe the characteristics of the upper lithosphere, deduced from dredged rock petrology.

5.5.6 Deformation modes

The diversity of focal mechanisms and strike orientations imply a complex deformation across the network — departing from pure extension — that is at least partially a consequence of the spreading obliquity at this SWIR segment. Although HYPODD relocated hypocenters provide a sharpened image of seismically active structures in the brittle lithosphere, there are no indications for the typical geometry of detachments that show narrowly confined seismicity in a major fault zone steepening with depth (e.g. *deMartin et al.*, 2007; *Escartin et al.*, 2008). We rather observe a flat lying band of deep seismicity that terminates abruptly in the south but shallows toward the north (Figures 7a–7c).

For the western part of the survey area (Figures 5.7a–c, 5.8, and 5.10) we propose a near-lateral deformation along this seismically active surface. Apart from two source mechanisms, all fault plane solutions in this area suggest a subhorizontal potential fault plane with gentle dip angles. However, dip and slip directions vary such that no distinct sense of motion along this narrowly confined band of seismicity can be determined. For this area a structural relation between surface fault scarps and the seismicity beneath appears unlikely.

Figures 5.7a–c show potential subsurface prolongations of boundary faults (dashed red lines). Neither of these has a depth continuation in the form of a seismically active fault. The upper lithosphere is aseismic and the deep seismicity band shows no near-vertical pattern or any other trends that may link them to surface structures. In the eastern part of the survey area (Figures 5.7d-f, 5.8, and 5.10) the seismicity occupies are larger depth interval. Here eight focal mechanisms occur associated to a NW-SE striking topographic ridge, crossing the axial valley at 13°30'E. While five events beneath the SE portion of this ridge yield reverse faults or high angle/subhorizontal fault planes, three events beneath the NW portion of the ridge yield normal faults and thereby document the small-scale heterogeneity in faulting kinematics. We propose seismically active faulting at this part of the survey area to be associated with the tectonic formation of the axial valley relief. Considering the occurrence of basalts, implying magmatic intrusions beneath, high-angle reverse faults might also be associated with dyking (e.g. *Khodayar and Einarsson*, 2004; *Kong et al.*, 1992).

We assume teleseismic earthquakes to be associated with different tectonic processes than microearthquake activity. Significantly stronger teleseismic events document discrete rifting episodes of purely extensional kinematics. Microearthquakes document very localized deformation and may originate from hydrothermally induced fracturing (*Crawford et al.*, 2013), volumetric expansion through serpentinization (*Andreani et al.*, 2007), or thermal contraction (*Khodayar and Einarsson*, 2004) besides a purely tectonic origin.

A striking result is the sharp termination of seismicity at the southern rift valley boundary that is present in both parts of the survey area, east and west (Figures 5a and 6a). The seismicity truncates at 25–30 km depth below sea level beneath the southern rift valley wall without any sign of a seismically active vertical fault linking the seismicity at depth to the expression of the boundary fault at the seafloor (Figure 5.7). We therefore speculate that the sharp southern boundary of seismicity marks a prominent zone of weakness, extending throughout the lithosphere that effectively decouples the Antarctic plate on segment scale and prevents stress accumulation there. On the African plate, in contrast, seismicity extends further beyond the axial valley (Figures 5.5a and 5.6a) and only gradually dies out. The bathymetry partly reflects this asymmetric deformation pattern. The southern rift valley wall is formed by a continuous ridge followed to the south by a rift parallel trough and a second rift parallel ridge (Figure 1b). In the north, the bounding rift valley wall has far more topography, and no continuous second ridge paralleling the ridge axis. Seismicity extends across the much broader northern rift mountains into the basin behind (Figure 5.5a). This supports our suggestion of asymmetric spreading with signs of deformation apparent in seafloor morphology. This marked asymmetry is not obvious from the teleseismic earthquake records (Figure 5.1b). Either the location uncertainty of the teleseismically determined epicenters is too large to make out the asymmetry or again, large- magnitude seismic events are associated with a different deformation process.

In particular for the western part of the survey area we observe similarities to the SWIR axis around 62°20'E (western corridor of *Sauter et al.* (2013)): The oblique spreading axis, the dominant exposure of mantle rocks, low-angle fault surfaces with considerable heave that show no corrugations, spreading axis parallel ridges and troughs beyond the axial valley. For the western part of the survey area we suggest a similar mode of deformation and mantle exhumation as *Sauter et al.* (2013) propose for the 62°20'E SWIR region. However, microearthquake activity does not confirm the existence of high-angle detachment faults—that are essential to the proposed concept—possibly due to extensive serpentinization and aseismic slip in potential fault zones.

5.6 Conclusions

The discussed, 1 year spanning catalog of background seismicity at the SWIR plate boundary allows detailed insights to the rheological state, thermal structure, and mode of deformation in nascent lithosphere.

1. We report the deepest so far registered hypocenters beneath any active MOR, reaching 31 km below the axial seafloor implying an unusually thick brittle lithosphere for the amagmatic oblique supersegment.

2. Along the ridge axis we observe a general relation between petrology, topography, and microearthquake activity: Peridotite-dominated areas associate with deeper hypocenters, deep-reaching hydrothermalism, and a deeper and smoother axial valley. Where basalts are exposed hypocenters are shallower, occupying a larger depth range and the axial seafloor is generally shallower and more rugged.

3. We observe an undulating brittle-ductile transition along the ridge axis, indicating significant variations in the lithospheric thermal structure along the ridge axis. Extrapolating these undulations to greater depth, we conclude a topography of the LAB that is a key element of a conceptual model by *Standish et al.* (2008) that suggests the along axis migration and focusing of melts at magmatic centers. Thus, our results provide seismologic evidence for a previous hypothetical model to explain the processes of melt migration and segmentation at ultraslow MORs.

4. We discovered vast volumes of aseismic axial lithosphere that we believe to result from widespread deep-reaching hydrothermal circulation that alters mantle rocks to phyllosilicates with little shear strength. This process occurs mainly in amagmatic sections and contributes to further cool the lithosphere.

5. Focal mechanism and relative-relocated hypocenters of microearthquakes indicate a spatially variable mode of deformation that departs from pure extension and is at least partially a consequence of the spreading obliquity. No typical detachment fault geometry was found but instead we observe a flat-lying band of seismicity with subhorizontal motion on small scales. We conclude teleseismic events, producing merely normal fault mechanisms, document a different process than microearthquakes with diverse focal mechanisms.

6. The microseismicity distribution sharply terminates at the southern rift valley limit and gradually diminishes across the northern valley boundary, indicating an asymmetry in the deformation modes on both sides of the spreading axis, that is also reflected in the off axis topography.

5.7 Acknowledgements

We acknowledge the support of the R/V Polarstern crews during expeditions ANT-XXI/2 and ANT-XXIX/8. Instruments were provided by the AWI DEPAS OBS pool. Passive and active seismic data as well as earthquake locations are available upon request from V. Schlindwein (Vera.Schlindwein@awi.de). We thank C. Gromoll for his contribution to magnitude picking. This study was funded through the DFG Emmy-Noether Program, grant Schl.853/1-1. Figures were produced with the public domain GMT software (*Wessel et al.*, 2013).

5.8 Supporting information

Appended Figure 5.11 shows velocity models tested in order to identify the optimum velocity model for the location and relocation of hypocenters. A subset of 67 well-located earthquakes situated beneath the network and detected at all stations was used to assess the performance of the different velocity models. Figure 5.12 presents the location differences for 18 randomly chosen events that have been repeatedly located with and without a sediment layer correction. Figure 5.13 shows histograms of the travel time residuals of P- and S-phases at the individual stations calculated for all earthquakes in the catalogue. Here the sediment correction had been applied.

Figure 5.14 shows the effect of different configurations on the results of the hypocenter relocation procedure with HYPODD. Table 5.2 documents average location parameters (residuals and spatial uncertainties) for velocity models plotted in Figure 5.11. Table 5.3 gives estimated differences between OBS seafloor positions from air gun water wave arrival and positions interpolated between deployment and recovery.

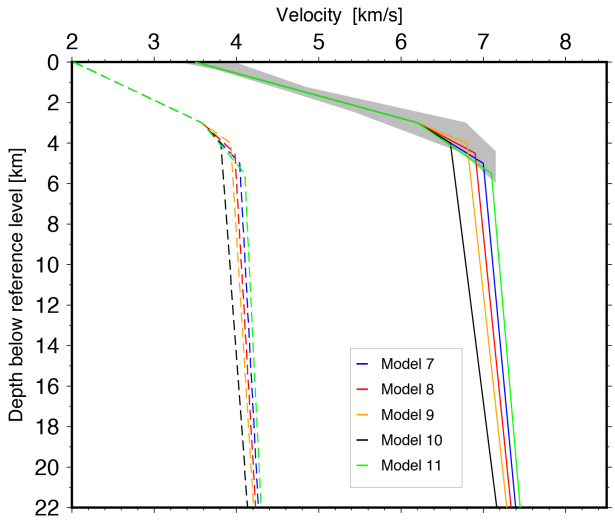

Figure 5.11 Plot of different velocity models (Vp: solid, Vs: dashed) tested to determine the optimum velocity model for hypocenter location. Model 7 was considered best in terms of location performance (Table 5.2) and used for the location and relocation of hypocenters. Gray shaded area represents Vp velocities from refraction seismic profile AWI20130410 (Figure 5.2).

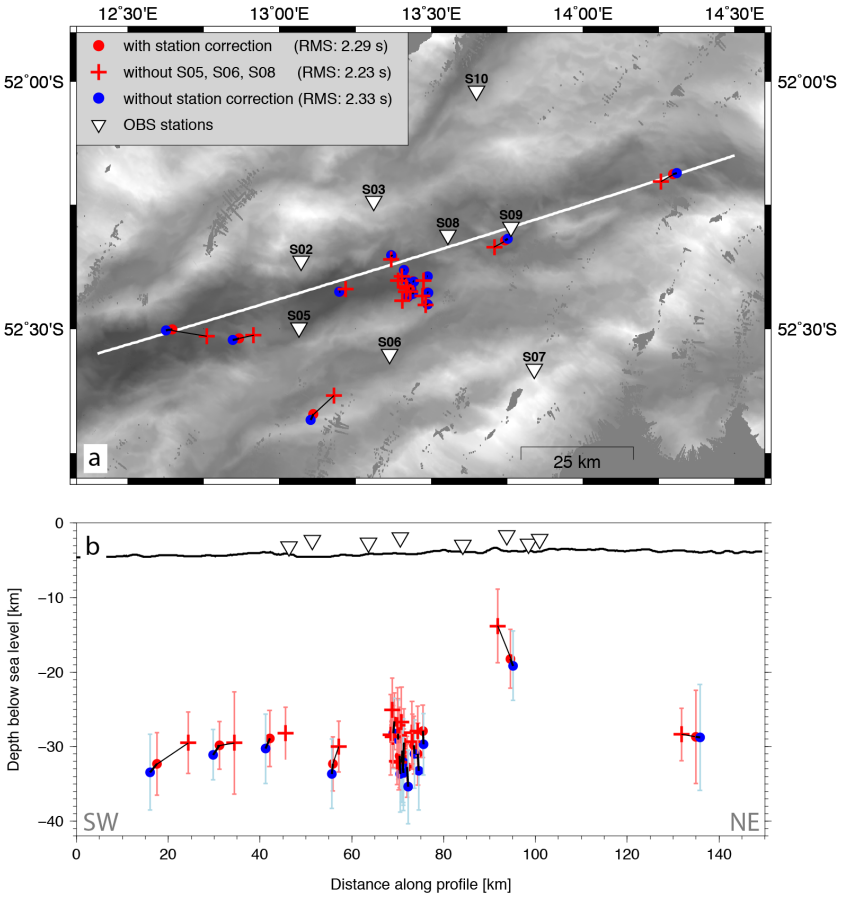

Figure 5.12 Location results for a set 18 randomly chosen events (that have phase picks at all stations), which have been repeatedly located. Different location solutions for individual results are connect via black lines. a), map view and b) events projected on cross-section. Note that average RMS is lowest when omitting stations S05, S06, S08 from the location procedure and highest when locating without station correction.

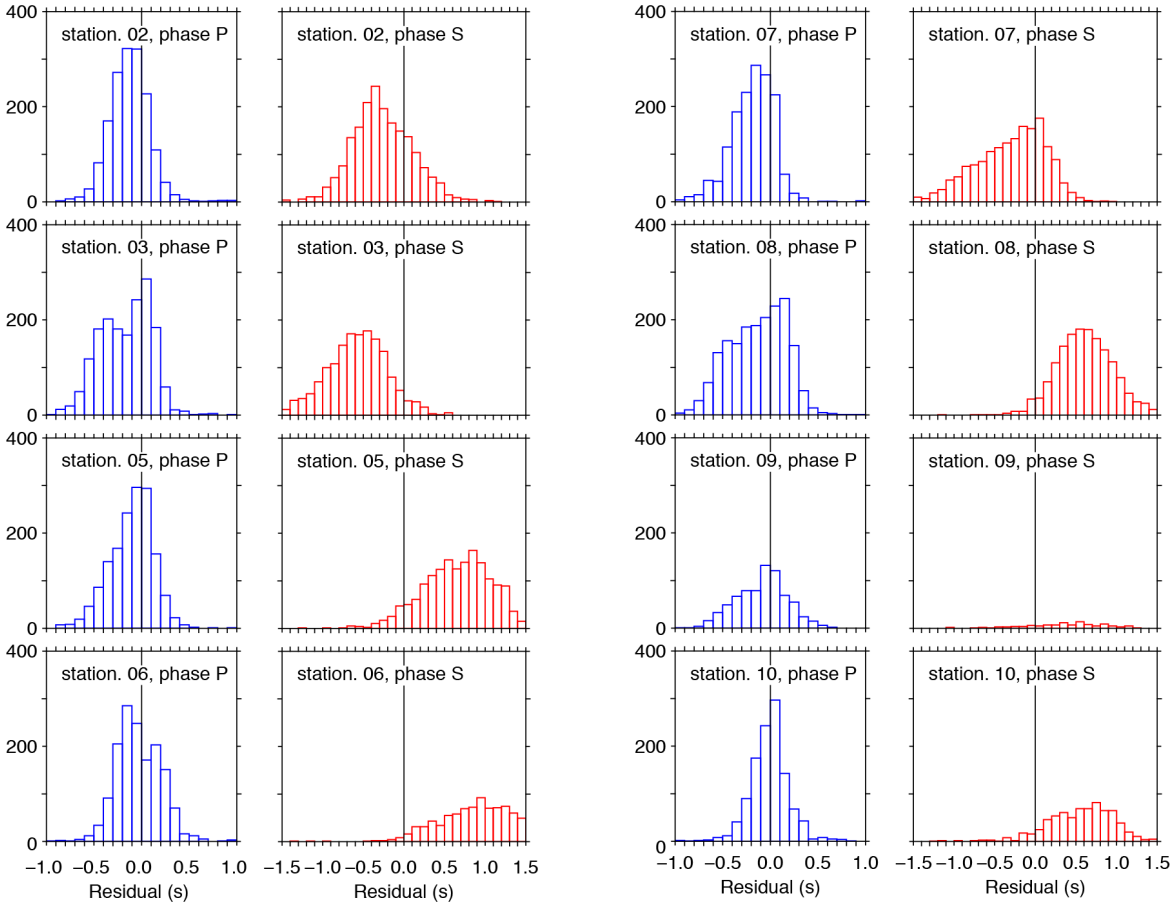

Figure 5.13 Histograms of travel time residuals for individual stations and phases for the entire event catalogue (1959 events) comprising also poorly located events that were excluded from further interpretation. A station correction has been applied to station S05, S06 and S08. The 1D velocity model cannot accommodate local variations beneath each station. While stations S03 and S02 on hard rock sites require faster velocities in the uppermost crust, stations S05, S06, S08 sitting on a layer of soft sediments still require even slower velocities in the uppermost crust. The chosen 1D velocity model (Figure 5.11) represents a compromise but larger S-phase residuals remain at these stations.

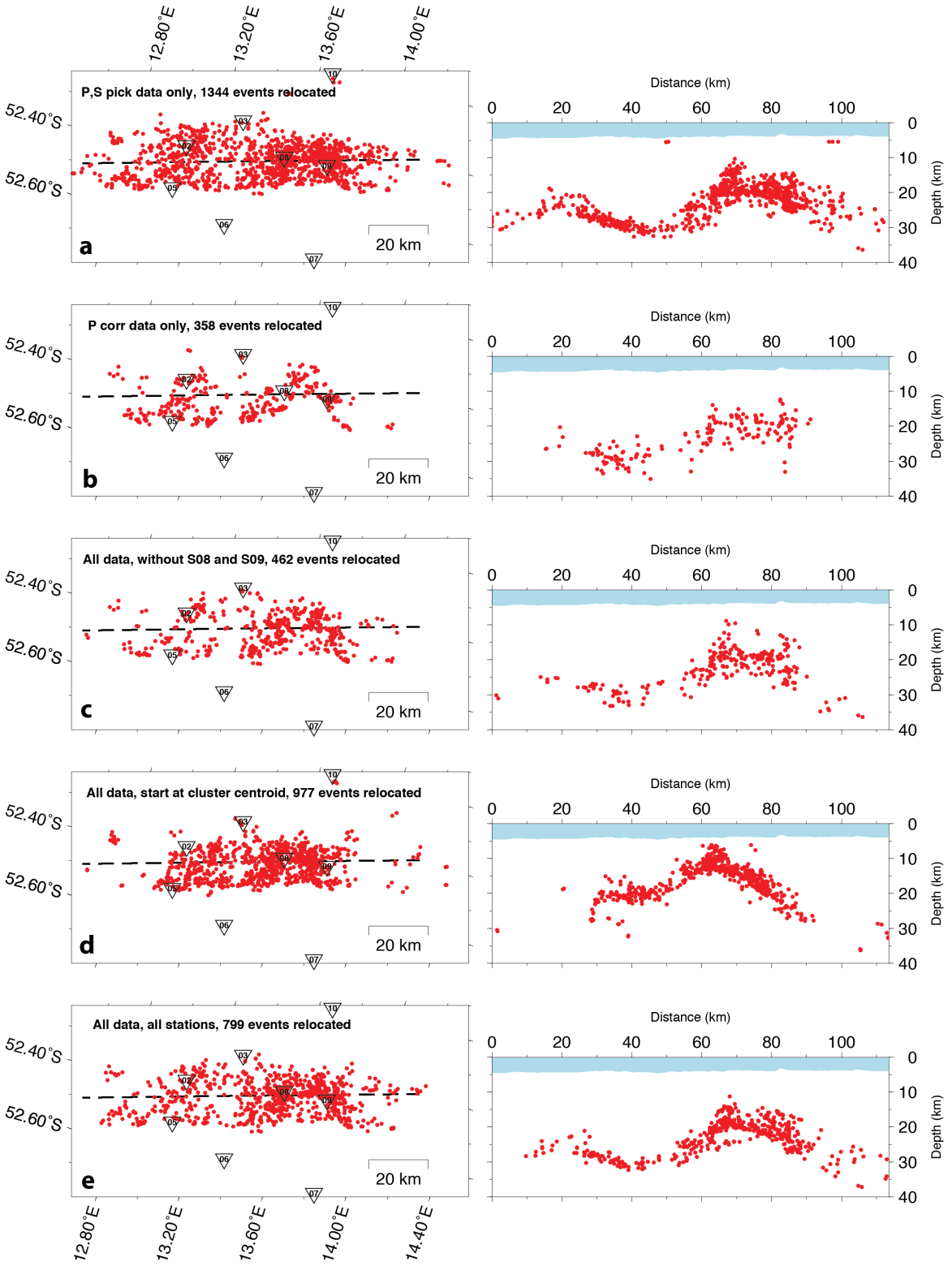

Figure 5.14 Caption next page.

Figure 5.14 (Previous page.) Robustness tests with different input data and starting locations for the HYPODD relocation procedure. Tests were performed to exploit the stability of the relocation results. Left, map view of epicenter distribution (red dots) and station positions (triangles). Dashed line gives location of cross sections to the right. a) P- and S- picks where used, relocation started at HYPOSAT locations. b) only P- cross-correlation data were used, relocation started at HYPOSAT locations. c) P- and S- picks where used but data from stations S08 and S09 where omitted. Relocation started at HYPOSAT locations. d) P- and S-picks plus P-cross-correlation data were used. Relocation started at cluster centroid. e) All input data were used, relocation started at HYPOSAT locations. This is identical the results present in the manuscript. Note that the general shape of the seismicity band and the occurrence of hypocenters as deep as 30 km is common to all results.

Velocity model	Model 7	Model 8	Model 9	Model 10	Model 11
No. of events located	67	67	67	67	67
Mean rms residual [s]	0.167	0.167	0.168	0.176	0.174
Mean origin-time error [s]	0.348	0.355	0.364	0.391	0.350
Mean S-major [km]	4.02	4.04	4.30	4.74	3.93
Mean hypocenter depth [km]	19.64	19.67	19.84	19.62	19.17
Mean depth error [km]	3.31	3.29	3.45	3.72	3.21
Average no. of phases used	9	9	9	9	9

Table 5.2 Average location parameters for a subset of 67 events (plotted in Figure 5.12) located with different velocity profiles (plotted in Figure 5.11). Location was performed without the S05, S06, S08 that are affected by a shallow low velocity layer. Model 7 was selected as best fitting 1D model and used for location with HYPOSAT and HYPODD.

Station	Position offset
S02	~300 m
S03	~340 m
S05	~30 m
S07	~60 m
S08	~90 m

Table 5.3 Differences in OBS seafloor positions for all stations recording the airgun pulses. Position offset refers to the horizontal distance between seafloor positions calculated from water wave arrivals and inferred positions at 2/3-distance between deployment and recovery site.

6 Magma plumbing system and seismicity of an active mid-ocean ridge volcano

Authors: Florian Schmid[1], Vera Schlindwein[1], Ivan Koulakov[2], Aline Plötz[1,3] and John-Robert Scholz[1,*]

[1]Alfred-Wegener-Institute, Helmholtz-Centre for Polar- and Marine Research, Bremerhaven, Germany.

[2]Trofimuk Institute of Petroleum Geology and Geophysics SB RAS, Novosibirsk, Russia Novosibirsk State University, Pirogova 2, 630090, Novosibirsk, Russia.

[3]Institue of Geophysics and Geology, University of Leipzig, Germany.

[*]Present address: Laboratoire GeoSciences Reunion, Universite de La Reunion, Institut de Physique du Globe de Paris, Sorbonne Paris Cite, UMR CNRS 7154, Universite Paris Diderot, F-97744 Saint Denis, France.

Published in February 2017 in *Scientific Reports*, 7:42949, doi:10.1038/srep42949.

6.1 Abstract

At mid-ocean ridges volcanism generally decreases with spreading rate but surprisingly massive volcanic centers occur at the slowest spreading ridges. These volcanoes can host unexpectedly strong earthquakes and vigorous, explosive submarine eruptions. Our understanding of the geodynamic processes forming these volcanic centers is still incomplete due to a lack of geophysical data and the difficulty to capture their rare phases of magmatic activity. We present a local earthquake tomographic image of the magma plumbing system beneath the Segment 8 volcano at the ultraslow-spreading Southwest Indian Ridge. The tomography shows a confined domain of partial melt under the volcano. We infer that from there melt is horizontally transported to a neighbouring ridge segment at 35 km distance where microearthquake swarms and intrusion tremor occur that suggest ongoing magmatic activity. Teleseismic earthquakes around the Segment 8 volcano, prior to our study, indicate that the current magmatic spreading episode may already have lasted over a decade and hence its temporal extent greatly exceeds the frequent short-lived spreading episodes at faster opening mid-ocean ridges.

6.2 Introduction

Oceanic lithosphere is created at mid-oceanic ridges by a complex interplay of magmatic and tectonic processes. As spreading rates decrease the style and quantity of magmatism alter from nearly continuous magma extrusion along the axis of fast spreading ridges (*Rubin*, 2014), to discrete, widely spaced magmatic centers at the slowest spreading ridges (*Cannat et al.*, 2008; *Dick et al.*, 2003; *Müller and Jokat*, 2000; *Sauter and Cannat*, 2010; *Schlindwein*, 2012). Although magmatic centers are a common feature of slow spreading ridges (20–55 mm a^{-1} full rate) and ultraslow-spreading ridges (<20 mm a^{-1} full rate), there are fundamental differences between their representatives at both ridge classes. Studies of crustal thickness show that melt flux per segment length is constant at slow spreading magmatic centers (*Hooft et al.*, 2000) but to explain the greatly thickened crust at ultraslow magmatic segments a melt flux exceeding the regional average is necessary (*Cannat et al.*, 2003; *Muller et al.*, 1999; *Sauter and Cannat*, 2010). Other unique features of magmatic centers at ultraslow ridges are the occurrence of unexpectedly strong and long lasting swarms of earthquake activity (*Müller and Jokat*, 2000; *Schlindwein*, 2012) and explosive submarine eruptions (*Sohn et al.*, 2008).

Several authors postulated a topography of the permeability boundary layer, marking the lithosphere-asthenosphere-boundary that guides melt from amagmatic segments towards magmatic centers (*Cannat et al.*, 2003; *Sauter and Cannat*, 2010; *Standish et al.*, 2008), enabling enhanced magma flux. Recent observations of maximum earthquake depths along the axes of ultraslow ridges indicate systematic variations in the lithosphere's thermal structure (*Schlindwein and Schmid*, 2016) that, when extrapolated to depth, outline the lithosphere-asthenosphere-boundary topography and support the concept of melt focussing beneath magmatic centers.

The easternmost portion of the Southwest Indian Ridge (SWIR; Fig. 6.1a) between Melville Fracture Zone and Rodriguez Triple Junction shows an anomalously low average crustal thickness of ~3 km and an unusually deep (~4.7 km) axial rift valley (*Cannat et al.*, 2003). The thin crust and the deep axial valley imply a vastly reduced magmatism for this portion of the SWIR, which was confirmed in various studies using wide angle seismics (*Muller et al.*, 1999), gravity modeling (*Cannat et al.*, 2003) and side scan sonar imagery (*Sauter et al.*, 2004a). The presence of three prominent axial highs (Segments 8, 11, 14 after *Cannat et al.* (2003)) is in contrast to the overall reduced magmatism at this SWIR portion. The axial highs show a locally thickened crust (*Cannat et al.*, 2003) and are interpreted as isolated volcanic centers. These volcanic centers exhibit a much higher relief to length ratio and are spaced at greater distances along the ridge axis in comparison to volcanic centers at the slow spreading Mid-Atlantic Ridge (*Sauter and Cannat*, 2010). These high relief volcanic centers seem to be connected with magmatic segments of lower relief (Segment 7, Fig. 6.1) that are proposed to have no melt regions of their own but to be laterally fed by the main volcanic centers (*Sauter et al.*, 2001).

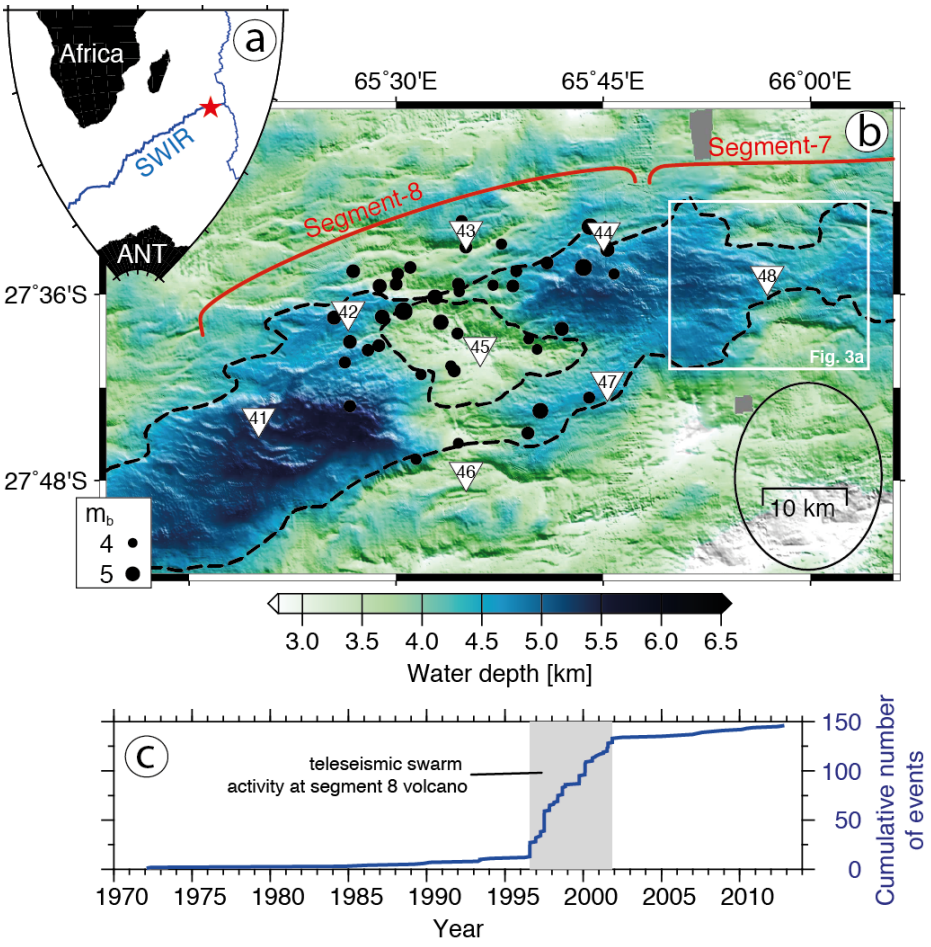

Figure 6.1 Teleseismic events between 1970–2013 at Segments 8 and 7 of the Southwest Indian Ridge (SWIR). a, Location of the survey area (red star). b, Bathymetry with dashed lines outlining the extent of the axial rift valley and the Segment 8 volcano. Black dots are epicenters of the EHB bulletin (http://www.isc.ac.uk/ehbbulletin) during the teleseismic swarm activity from 1996 to 2001. c, Size scales with magnitude and black ellipse indicates the average location error. White square refers to map in Fig. 6.3a and triangles are stations deployed for the microearthquake study in 2012–2013. (c) Cumulative teleseismic earthquake numbers of the more comprehensive international seismological center ISC bulletin (http://www.isc.ac.uk/iscbulletin) for the map b area. All maps and graphs were created with the GMT software38.

Numerous magmatic/volcanic centers at ultraslow-spreading ridges show off-axis bathymetric highs, oriented perpendicular to the spreading axis, that document enhanced magmatism and crustal thickness over sustained periods of time (*Jokat et al.*, 2003). However, at the easternmost SWIR magmatism changes in space and time, as shown by the considerable variability in off-axis crustal thickness and rock type (*Cannat et al.*, 2003; *Sauter and Cannat*, 2010). In the period from July 1996 to November 2001 several teleseismic earthquake swarms occurred at the Segment 8 (ref. 6; Fig. 6.1b,c) that had magnitudes of 4.3–5.5 *mb* which is remarkably strong for mid-ocean ridge earthquakes. As the closest recording stations are far away, large location uncertainties (~20 km) prevent a detailed geological interpretation of the teleseismic events.

Studies of local earthquake activity have greatly advanced our understanding of spreading episodes at faster mid-ocean ridges (*Sohn et al.*, 1998; *Tolstoy et al.*, 2006; *Weekly et al.*, 2013). Owing to the poor accessibility of ultraslow-spreading ridges comprehensive records of local seismicity did not exist until very recently (*Schlindwein and Schmid*, 2016). In particular the processes of melt formation and migration as well as the factors that control the dynamics of volcanic centers at ultraslow ridges remain unclear, leading to the following open questions:

- At what depth does melting take place and how are melts distributed within the lithosphere?
- How does the lithosphere's rheology and thermal structure vary at the transition from volcanic centers to amagmatic portions of the ridge?
- What is the cause of unexpectedly strong earthquakes?

Here we present the results of a local passive seismic experiment that studied a major volcanic center and its neighbouring segment during a phase of magmatic activity.

6.3 Results

We deployed a network of eight ocean bottom seismometers around the Segment 8 volcano (Fig. 6.1b) that recorded microseismicity from October 2012 to August 2013. Hypocenters of 2974 local events were initially located on the basis of a 1D velocity model (*Schlindwein and Schmid*, 2016) and give insight into the seismic activity in space and time of this SWIR segment. A total of 25,725 P- and S-wave ray paths sampling the lithosphere were used for a local earthquake tomography (*Koulakov*, 2009) that images the 3D velocity structure of the volcanic center (see Methods section).

A prominent aseismic zone was observed beneath the Segment 8 volcano during our microseismicity study (2012–2013) that extends about 20 km along the ridge axis (Fig. 6.2). In its center the local earthquake tomography revealed a distinct anomaly of low P- and S-wave velocities (Vs) and high Vp/Vs ratio (Fig. 6.2). In particular the lower limit of this low velocity anomaly (LVA) at 15 km depth could be well constrained by our tomography model while lateral extent and absolute amplitude are less well recovered (see methods section and Supplementary Figs 6.8 and 6.9). East and west of the Segment 8 volcano maximum depths of microearthquakes rapidly increase to ~15 km.

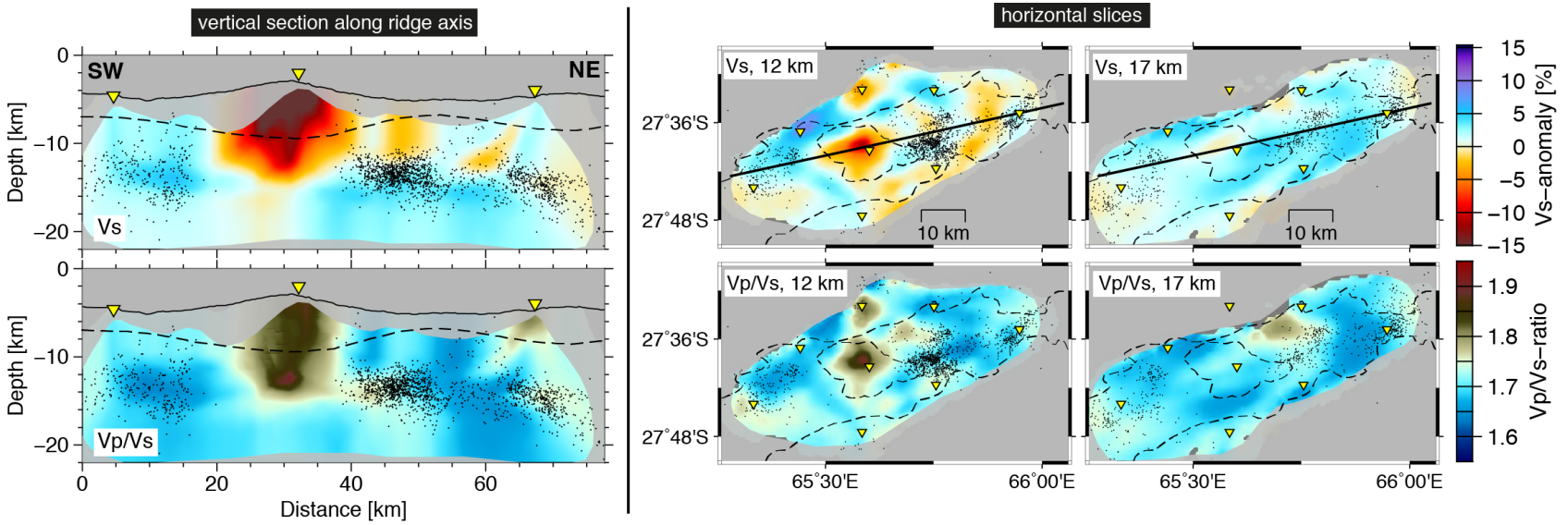

Figure 6.2 Results of local earthquake tomography. Colours indicate anomalies in the S-wave velocity Vs (upper panels) and in Vp/Vs ratio (lower panels) structure. Vertical section location is given by black solid line in horizontal slices. Black dots are projected microearthquakes as relocated during the tomography and yellow inverted triangles are projected OBS locations. Dashed line in left hand panels shows gravity derived crustal thickness from (*Cannat et al.*, 2003). Dashed lines in right hand panels outline extent of the axial rift valley and the volcano, c.f. Fig. 6.1b. Note that areas of poor or no ray coverage that moreover have no grid nodes in the tomography model (see Supplementary Fig. 6.6) appear shaded in grey.

Two distinct swarms of microearthquakes occurred in January and April 2013 below the center of SWIR Segment 7 ((*Cannat et al.*, 2003); Fig. 3a,b) which is located ~35 km east of the Segment 8 volcano. Here the axial rift valley becomes shallower and narrower (Fig. 6.1b) and the crustal thickness increases again (Fig. 6.2). These microearthquake swarms lasted for few days each and located at depths of 8–20 km beneath station 48 that ensures a good depth control for the swarm hypocenters (Fig. 6.3a,b). The swarms occurred in close spatial proximity to each other. Soon after the first event of swarm #2 we observe the onset of an intrusion tremor (Fig. 6.3c,d) that is exclusively recorded at station 48. The tremor contains most of its energy in a frequency band around 1 Hz that exhibits frequency gliding and is accompanied by several harmonics. Tremors of similar characteristics are commonly recorded at active volcanoes (*Konstantinou and Schlindwein*, 2003) and prior to eruptions (*Jellinek and Bercovici*, 2011).

Owing to their spatial and temporal proximity the microearthquake swarms and the intrusion tremor strongly suggest a dyking episode associated with magma movement beneath Segment 7 in 2013.

6.4 Discussion

It is a common issue in passive source tomography that amplitudes of model anomalies depend on the ray coverage and damping parameters. Synthetic tests with checkerboard patters or custom shaped realistic anomalies represent the best way to estimate the effects of smearing and damping, and to assess their representation of true amplitudes. Therefore, the conversion of seismic velocities and their derivatives into physical properties such as temperature and melt content may be ambiguous and unwarranted. Accordingly, we refrain from calculating temperature and melt content but focus our interpretation on the relative amplitude and shape of the anomalies.

The region inside the aseismic zone below the volcano is of particular interest to our study. Here, in the 10–20 km depth range there is ample ray coverage (Supplementary Fig. 6.6) but at shallower depth the geometry and density of rays is less favourable. A synthetic test, comprising a realistic low velocity anomaly in the center of the aseismic zone (test #3 in methods section, Supplementary Fig. 6.9) showed that in this region of the model anomalies may be smeared out horizontally at the lower end and amplitudes are likely underestimated. The LVAs lower end that lies in a region of good ray coverage is well beneath the gravity derived lower boundary of the crust (Fig. 6.2).

Considering the potential underestimation of velocity anomalies inside the aseismic zone and Vp/Vs ratios reaching 1.9 in the center of the LVA, these values may represent the lower limit of the true Vp/Vs ratio in the lithosphere. Melts in upper mantle rocks are typically associated with Vp/Vs ratios of 1.8–2.1 depending on the fraction of melt (*Hammond and Humphreys*, 2000). We therefore conclude that the observed Vp/Vs ratio inside the LVA requires at least partially the presence of melts and hence presents evidence for a melt body beneath the Segment 8 volcano that extends down to 15 km depth. For the upper part of the LVA other fluids or water filling cracks and pore spaces might additionally contribute to the velocity anomaly (*Takei*, 2002).

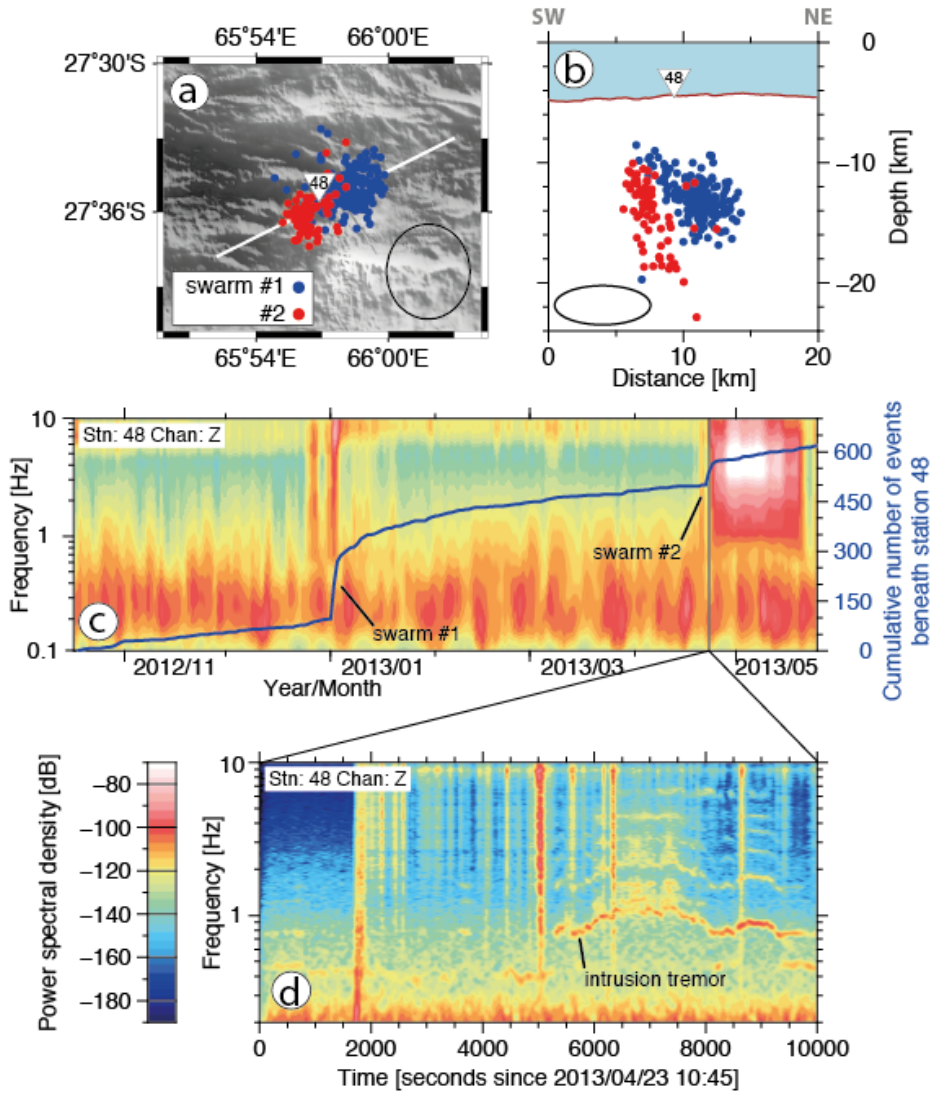

Figure 6.3 a,b Map view and cross-section showing the location of microearthquake swarms below SWIR Segment 7 (ref. 9). Black ellipses represent the average location error. c, Cumulative number of events beneath station 48 (blue curve) and power spectral density for the entire survey period. d, Close-up spectrogram showing swarm #2 events (vertical lines) and the onset of harmonic intrusion tremor.

Reconstruction of a Magmatic Spreading Episode

Based on our findings we are not only able to illuminate the current structure of the axial lithosphere below the Segment 8 volcano but, additionally, these rare in-situ observations enable a reconstruction of essential stages of a magmatic spreading episode at an ultraslow-spreading ridge.

The current spreading episode was preceded by a phase of intense seismic activity. At least 7 teleseismic earthquake swarms centerd on the Segment 8 (Fig. 6.1b) occurred in the period 1996–2001 (Fig. 6.1c) with magnitudes of 4.3–5.5 mb, exceeding by far the usual background seismicity along the SWIR6. Focal mechanisms of the teleseismic swarm events indicate the failure of rift parallel normal

faults (*Ekström et al.*, 2012). We infer that these earthquake swarms marked the beginning of an extended phase of magmatic activity that continued throughout our survey period, hence lasting over a decade. At the Gakkel Ridge (Arctic Ocean), a large teleseismic earthquake swarm also occurred at the onset of a magmatic phase of at least 2 years duration (*Schlindwein and Riedel*, 2010; *Sohn et al.*, 2008). The strong seismicity that appears to be associated with spreading episodes at the massive volcanic centers of ultraslow spreading ridges may either be triggered by the ascent of mantle melts or it may in turn facilitate their way through the lithosphere.

In 2012/2013, an area devoid of earthquakes extends 20 km along the ridge axis below the Segment 8 volcano, suggesting that in this area temperatures exceed those of brittle deformation. Since most of the teleseismic events in 1996–2001 locate in the same area (Fig. 6.1a), the mechanical strength and hence thermal structure must have considerably changed between 2001 and the start of our microearthquake survey in 2012 suggesting the area was heated up meanwhile. Inside this aseismic zone the tomography model shows a prominent LVA that we interpret as a reservoir containing partial melts (Figs 6.2 and 6.4). We propose that between 1996 and 2012 this reservoir of partial melts has either re-grown or was newly formed beneath the Segment 8 volcano that represents the backbone of the magma plumbing system present in 2012/2013 (Fig. 6.4). Its depth extends well into the mantle and is much deeper than the axial melt lenses that have been imaged by active or passive seismics at faster spreading ridges.

The tomography model does not show a low velocity, high Vp/Vs ratio anomaly indicative for the presence of melts below the volume of microearthquake swarm activity (Fig. 6.4) in the center of Segment 7 although ray coverage is sufficient here (Supplementary Fig. 6.6). We conclude that the LVA below the Segment 8 volcano is the only stable melt reservoir at that time in the study area.

As we observed dyking at Segment 7 during our experiment we hypothesize that the melt reservoir beneath Segment 8 may laterally feed magma to Segment 7. The lateral movement of melt in the lithosphere over distances larger 30 km is none unique to our study and has been observed in various rift zones e.g. the Afar rift (*Grandin et al.*, 2012) or the Bardarbunga volcanic system (*Sigmundsson et al.*, 2015). It has further been postulated to explain the difference in morphology between high-relief volcanic segments and their accompanying low-relief neighbouring segments (*Sauter et al.*, 2001).

However, our tomographic model cannot resolve where and at what depth-level lateral magma feeding occurs. The width of a potential connecting magma conduit may be in the order of a few meters to tens of meters, according to geodetic observations at comparable terrestrial rifts on Iceland and the Afar spreading center (*Grandin et al.*, 2012; *Sigmundsson et al.*, 2015; *Wright et al.*, 2012). This is below the minimum feature size our tomography model can image (see Supplement Figs 6.7 and 6.8), making it “invisible”.

A potential indicator for the cross-feeding of magma between Segments 8 and 7 may be the cluster of enhanced microseismicity occurring immediately east of the aseismic zone (at km 40–55 in Fig. 6.4) that may be associated with post-dyking stress release in the lithosphere, a phenomenon that was previously observed in actively dyking rift systems (*Rivalta et al.*, 2015; *Sohn et al.*, 1998).

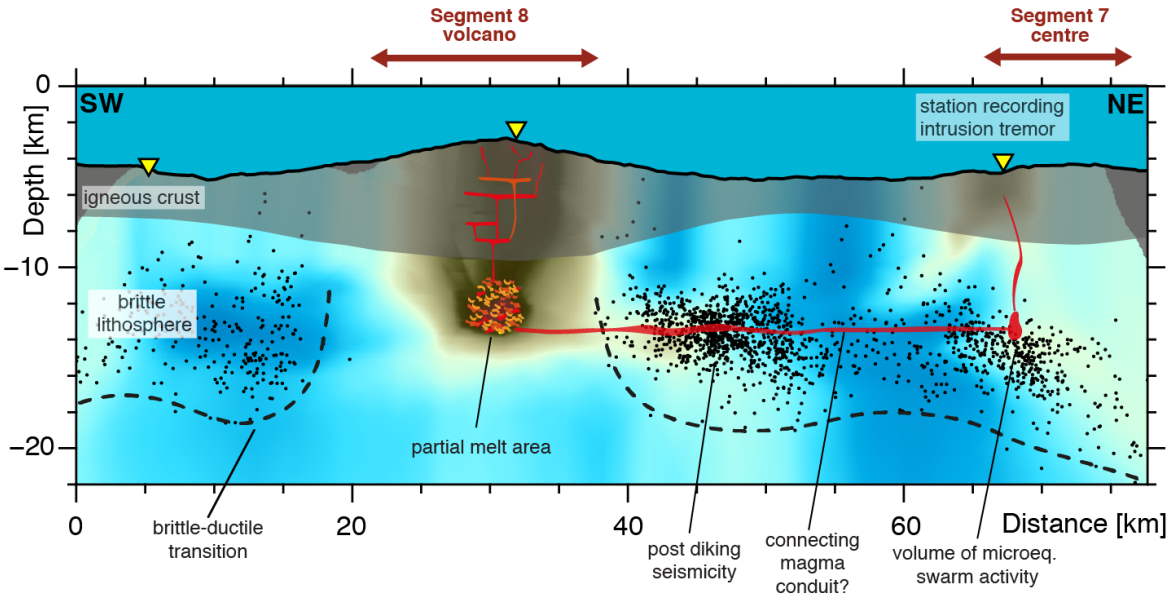

Figure 6.4 Conceptual sketch illustrating the lithospheric structure and the magma plumbing system below the Segment 8 volcano. Background displays Vp/Vs ratio of the tomography model (c.f. Fig. 6.2) and black dots are projected microearthquakes. Red polygons indicate locations of conceivable magma bearing sills and dykes. Note that sketched sills and dikes are purely speculative as they might have a smaller extent than the tomography models resolution capability and are therefore beyond imaging resolution.

Our observations show that the spreading episode at SWIR Segment 8 lasted for at least 12 years, and it may still be ongoing. The Segment 8 volcanic center finds an analogue in the 85°E volcanic complex at the ultraslow-spreading Gakkel Ridge (Arctic Ocean) that yielded a teleseismic earthquake swarm of unprecedented length and magnitude in 1999 (*Müller and Jokat*, 2000). This swarm was partly associated with a series of small volume eruptions of both effusive and explosive character, as indicated by the recording of explosion sounds in 2001 (*Müller and Jokat*, 2000) and the discovery of fresh lava flows and pyroclastic deposits covering the sea floor, around the volcanic complex (*Sohn et al.*, 2008).

A 16 days long study of local earthquake activity in 2007, based on seismometers deployed on the sea ice, found hypocenters down to 13 km beneath the sea floor at the sites axial volcanoes (*Korger and Schlindwein*, 2013). This showed that the lithosphere under the 85° E volcanic complex had cooled and the spreading episode had potentially terminated, after lasting 8 year at maximum.

6.5 Conclusions

The estimated ~10,000 yr (*Perfit and Chadwick*, 1998) recurrence cycle of eruptions at volcanic centers on ultraslow-spreading rates is possibly the lowest for all mid-ocean ridge types, diminishing the chance to directly observe these eruptions. This makes the records from the 85°E volcanic complex at the Gakkel Ridge (*Korger and Schlindwein*, 2013; *Müller and Jokat*, 2000; *Sohn et al.*, 2008)

and the more detailed observations from the SWIR Segment 8 volcano presented herein especially invaluable to understand the nature of such volcanic systems. Our study presents the first image of a melt reservoir at mantle depths below the axis of an ultraslow spreading ridge during a phase of magmatic activity. At faster spreading ridges where shallow lithospheric melt regions are more common, eruptions occur frequently. There, much more detailed reconstructions of volcanic episodes have been possible (*Tan et al.*, 2016) but they refer to spreading processes that differ greatly from the magma poor conditions at ultraslow spreading ridges. Presuming the initiation of the spreading episode at the Segment 8 was associated with enhanced earthquake activity in 1996–2001 it lasted well over a decade. This would be the longest so far recorded spreading episode at any mid-ocean ridge (*Sohn et al.*, 1998; *Tolstoy et al.*, 2006). Spreading episodes at faster ridges are shorter and may only be detected locally as their seismic activity is of weak magnitudes.

The transition in the seismic activity at Segment 8, from hosting *mb* 5.5 earthquakes in 1996–2001 to an aseismic zone in 2012/2013, indicates that the thermal structure of the lithosphere below volcanic centers at ultraslow-spreading ridges may considerably alter between phases of quiescence and spreading episodes. The brittle lithosphere may be cold and thick during phases of quiescence but the ascent of large quantities of melt at the onset of spreading episodes causes the lithosphere to heat up and alter its rheology from brittle to ductile, as observed under the Segment 8 volcano. Once a magma plumbing system is established it may host large enough amounts of melt to possibly feed neighbouring ridge segments through lateral conduits as we postulate for SWIR Segments 8 and 7. We conclude that spreading episodes at ultraslow mid-ocean ridges are rare but may last over years to decades – typically initiated by strong tectonic earthquakes (*Schlindwein*, 2012). They include the establishment of a deep reaching reservoir under the high-relief volcanic centers that may supply melts to neighbouring, less prominent volcanic segments.

6.6 Methods

Microearthquake Data Processing

Seismic data were recorded by eight free-fall ocean bottom seismom- eters equipped with Güralp CMG-40T broadband sensors and HiTech Inc hydrophones deployed on October 17, 2012 (Fig. 6.1b). Seismic records of individual stations span 7–10 month depending on battery capacity. The recorder clock drift was corrected, assuming a linear drift during the recording interval, with the method of *Hannemann et al.* (2013) and taking station 47 as reference station. Event identification in the waveforms, phase onset picking and the hypocenter location based on a 1D velocity model are documented in ref. 12. Pick uncertainties were estimated during the manual picking procedure and have averages of ± 0.07 s and ± 0.11 s for P- and S-phases, respectively. S-phases were generally picked on horizontal channels, except for stations 42, and 45 where horizontal channels were malfunctioning.

Spectrogram Analysis

Prior to signal processing the instrument response was removed from the waveforms. Time series of daily averages of power spectral density for the entire seismic record of station 48 (Fig. 6.3c) were calculated with the PDFSA software package of *McNamara and Boaz* (2005). The close-up spectrogram of the intrusion tremor (Fig. 6.3d) was calculated with the ObsPy software *Krischer et al.* (2015). For the calculation of spectrograms, data were bandpass filtered at 0.01–50 Hz. Amplitude spectra were calculated for 60 s windows that overlap by 10%.

Local Earthquake Tomography

Events for local earthquake tomographic inversion were selected from the earthquake catalogue of *Schlindwein and Schmid* (2016). Sources far outside the network (events further than 20 km i.e. one hypocenter depth beyond the network) produce rays that sample the lithosphere outside the network and might drag anomalies from beyond to within of the network. To retain a maximum number of rays, while excluding poorly located events from outside of the network, we applied the following event selection criteria: Events inside the network must contain at least 7 phase onset picks. Events outside the network must not be further away than 20 km from the nearest station and have at least 10 phase picks. All other events were omitted.

In total we obtained 25,725 arrival times (12,491P; 13,234S) as input data that originate from 2365 events. We used the LOTOS iterative least squares tomography algorithm19 which can simultaneously invert for the P- and S-wave velocity structures of the lithosphere and the source parameters of earthquakes. The tomography is commenced with an initial source location based on a 1D velocity model and straight ray paths. We used the starting 1D P-wave velocity model of *Schlindwein and Schmid* (2016) but included slightly lower velocities in the depth interval at 7–15 km below sea level (Supplementary Fig. 6.5a). The best fitting 1D model of *Schlindwein and Schmid* (2016) applies for an extended along axis region. When used as initial model for the tomographic inversion of the area inside the network that covers mainly the volcanic complex it produces an extended low velocity anomaly in center of the model output suggesting that the background velocity model as such is slightly too fast.

We started with slower velocities (Supplementary Fig. 6.5) that better represent the velocity structure beneath the volcanic complex. S-wave velocities of the 1D starting model were calculated from the Vp model assuming a constant Vp/Vs ratio of 1.73, which corresponds to a poisson ratio of 0.25, common for igneous rocks.

For the tomography the following steps were performed:

- Location of sources in the 3D velocity model utilizing the bending tracing algorithm of *Um and Thurber* (1987). In this step the sea floor topography is implemented so that rays and sources in the water column are not allowed.

- Construction of model grids with nodes spaced at 2 km in horizontal directions and a variable vertical spacing (Supplementary Fig. 6.6). The vertical node spacing is 1 km in areas of dense ray coverage and is sparse in areas of less ray coverage. Velocities are linearly interpolated between grid nodes.
- To overcome any grid related artefacts in the tomography models the inversion was performed for several grids at different azimuthal orientations of 0°, 22°, 45°, 67°and results were averaged afterwards.
- The actual matrix inversion was performed in a least squares manner using the LSQR algorithm of *Paige and Saunders* (1982). To achieve a stable solution we applied the fattening damping by minimizing the velocity anomaly difference between neighbouring nodes. Weights for damping and source correction were determined based on the results of synthetic tests.

The steps of source location, matrix calculation and inversion were successively repeated three times for all tomography models (experimental data and synthetic data cases). Residuals did not substantially decrease after the third iteration. The parameterisation grids were constructed in the first iteration; then the velocity values were updated at the same grid nodes. Damping and weighting parameters for the tomographic inversion were selected from the optimum parameters of synthetic recovery tests. A station correction was not necessary since we did not observe systematic residuals that call for such a correction.

Synthetic Testing

We created a series of synthetic tests to benchmark the results of the local earthquake tomography and to estimate optimum weighting and damping parameters. The station- and earthquake source locations were identical to the last iteration of the real data case. Synthetic travel times were computed via 3D ray tracing and afterwards all structural information and source coordinates were "forgotten". Additionally, the travel time residuals resulting from the third iteration of the real data case were multiplied with a factor of 0.2 and the product was added to the synthetic travel times to incorporate the effect of noise. The tomographic inversion was then performed in the same manner as for the real data case.

Test #1 represents a checkerboard of vertical prisms at various sizes with $\pm 7\%$ alternating velocity anomalies having opposite signs for P- and S-wave models (Supplementary Fig. 6.7). The main purpose of the test is to explore the horizontal resolution capability of the tomographic model. Synthetic anomalies are generally better recovered at 12 km than at 17 km depth. Larger anomalies are better restored than smaller ones both in structure and amplitude. In particular the anomalies of 3×3 km size appear blurred, delineating the lower resolution limit of our model. Structure and amplitude are better resolved in areas where sources are present and anomalies become smeared in areas devoid of sources. The smearing of anomalies reflects the intrinsic trade-off between the velocity- and source parameters. The specific geometry of sources and receivers has an impact on the

smearing and the amplitude of restored anomalies. Thus, the results of the synthetic tests provide a realistic representation of the tomography model's capability to recover the true velocity structure.

Test #2 comprises horizontal rectangular prisms at different sizes that are oriented perpendicular to a vertical cross-section along the ridge axis and have alternating anomalies of ±7% (Supplementary Fig. 6.8). This test explores the vertical resolution capability of the tomography model. The general structure of the input model could be recovered within the network. As in test #1 we observed a slightly better resolution for areas where sources are present (Supplementary Fig. 6.8). Anomalies in the upper row are smeared towards the sea floor since the majority of rays at these depths are near vertical (Supplementary Fig. 6.6) and sources are scarce. Within the aseismic zone beneath the volcano, the general structure could be resolved although amplitudes remain weaker than in the input model.

Test #3 represents a realistic low velocity/high Vp/Vs ratio body in the center of the aseismic zone (Supplementary Fig. 6.9) in analogy to the LVA in the real data model (Fig. 6.2). The sparse ray coverage in some parts of the aseismic zone (Supplementary Fig. 6.6) questions the trustworthiness of the LVA in the final velocity model (Fig. 6.2). The test intends to verify the tomography model inside the aseismic zone. The vertical extent of the anomaly was well recovered, in particular at the lower boundary. As rays bundle beneath the station on top of the volcano, the horizontal dimension of the anomaly could not be fully restored in this area. At its lower end the anomaly appears horizontally smeared due to the near horizontal alignment of rays here. The amplitude of the recovered anomaly remains lower than in the input model due to smoothing during the tomographic inversion. The results of the synthetic test suggest that the LVA inside the aseismic zone likely has a smaller horizontal extent at its base (due to smearing) and its amplitude is possibly underestimated, whereas the depth extent to 15 km is well resolved.

Large positive travel time residuals observed at the station on top of the volcano (station 45), after location with a 1D velocity model (*Schlindwein and Schmid*, 2016), compared to travel time residuals at other stations further support the existence of a LVA inside the aseismic zone (see Supplementary Fig. 6.10a). There is no sedimentary cover on the volcano13 that could produce such a delay. The delay must therefore originate from a low velocity anomaly in the crust or upper mantle. To asses the effect of the synthetic anomaly in test #3 we compared the travel times for this synthetic model with those of an anomaly free synthetic model (Supplementary Fig. 6.10c). The comparison clearly shows that the anomaly accounts for about 150 ms of the S-phase delay at station 45 while it does not affect the remaining stations. Omitting this anomaly in the final model would leave a residual of 150 ms at station 45, which also exceeds the picking uncertainty of S phases (±110 ms). We conclude that the delayed S-phases at station 45 require the presence of a LVA inside the aseismic zone.

6.7 Acknowledgements

The authors acknowledge scientists and crews aboard RV Marion Dufresne cruise MD192 and RV Meteor cruise M101 for their support in handling the OBS. Instruments were provided by the DEPAS

pool for amphibian seismology at AWI and deployed within the framework of the RHUM-RUM project (http://www.rhum-rum.net) which was funded through Deutsche Forschungsgemeinschaft, Germany (sub-grant SCHL/853/3-1 to V.S.), Agence de la Recherche, France (project ANR-11-BS56-0013) and Institute Polaire Paul Emile Victor, France. F.S. was funded through Deutsche Forschungsgemeinschaft grant SCHL853/1-1. IK is supported by the Russian Science Foundation grant #14-17-00430.

6.8 Author Contributions

V.S. conceived the experiment and supervised the project. V.S., A.P. and J.R.S. picked phase arrivals and performed the initial hypocenter location. F.S. performed the tomographic inversions, processed the seismograms for tremor analysis and wrote the manuscript. I.K. developed the tomography algorithm and supervised the tomographic inversions. All authors commented on the manuscript.

6.9 Supplementary Figures

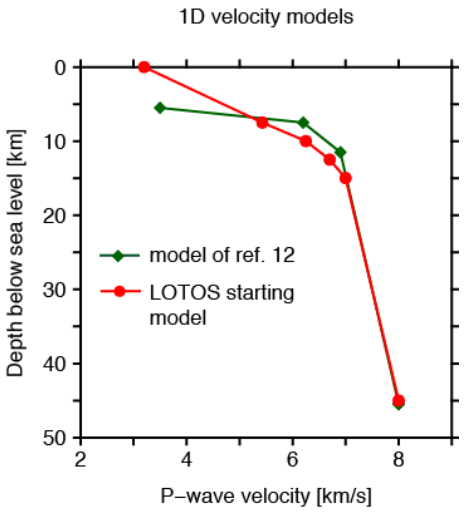

Figure 6.5 Starting 1D P-wave velocity model for the local earthquake tomography (red). Note that the 1D model of (*Schlindwein and Schmid*, 2016) (green) is only defined below the deepest OBS station (at 4.461 km). Symbols mark defining velocity nodes in each model.

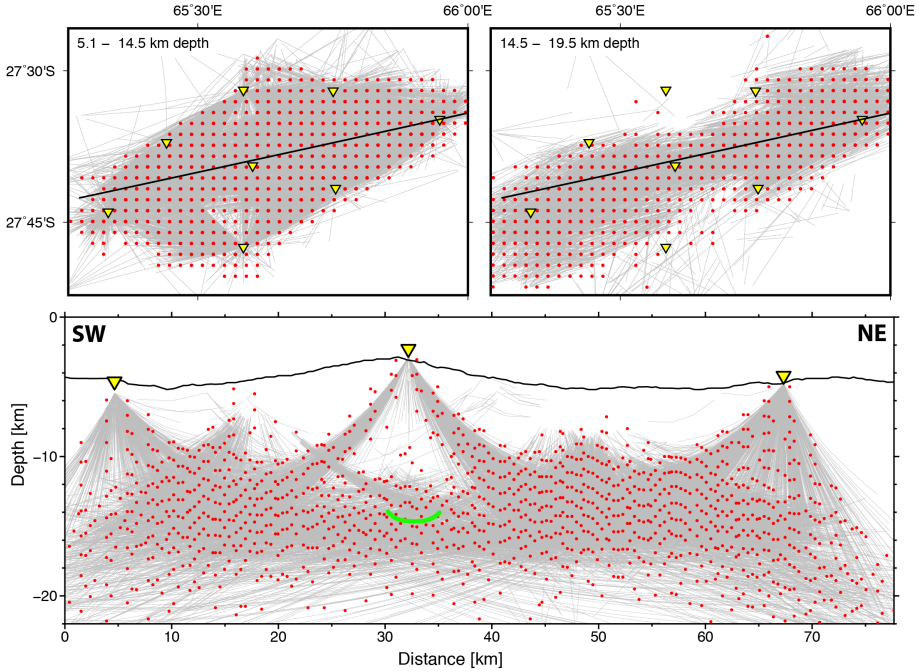

Figure 6.6 Ray paths (gray lines) and grid nodes (red points) of the tomography model. Upper panels are maps with projected rays and nodes for the given depth interval. Solid black lines indicates the position of the lower panel cross-section. All rays and nodes closer than 5 km to the cross-section are projected. The map and cross-section locations are identical to Fig. 6.2. The green line indicates the lower boundary of the low velocity anomaly beneath the volcano. Note that the vertical distribution of grid nodes varies depending on the density of rays.

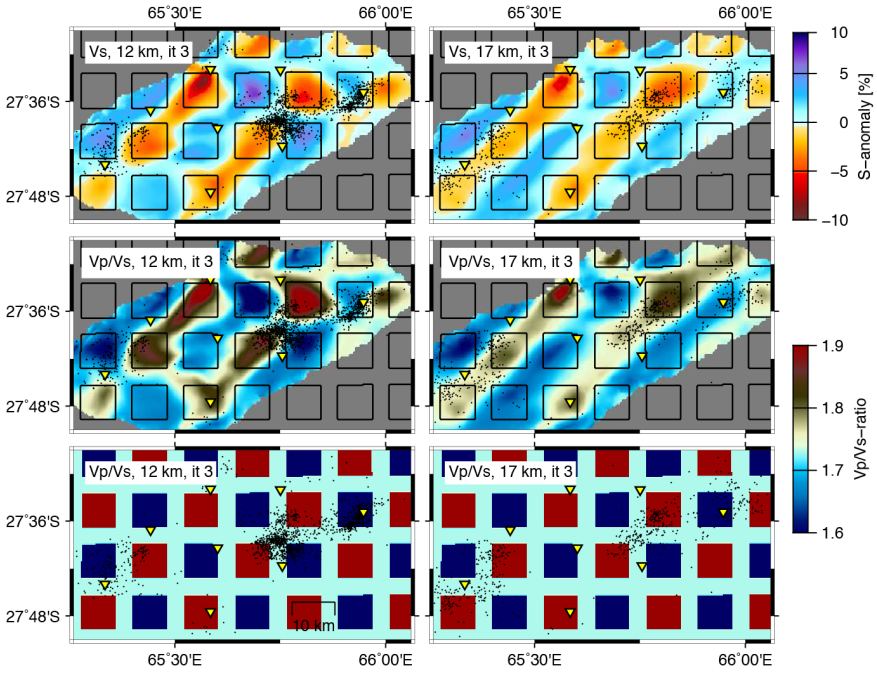

Figure 6.7 Synthetic test #1 horizontal slices of the input model and recovered anomalies. Inverted triangles are receivers. Black dots show source locations. Black squares represent the input model pattern. Note, that the velocity perturbations of the input model are equal for the three models of different prism size.

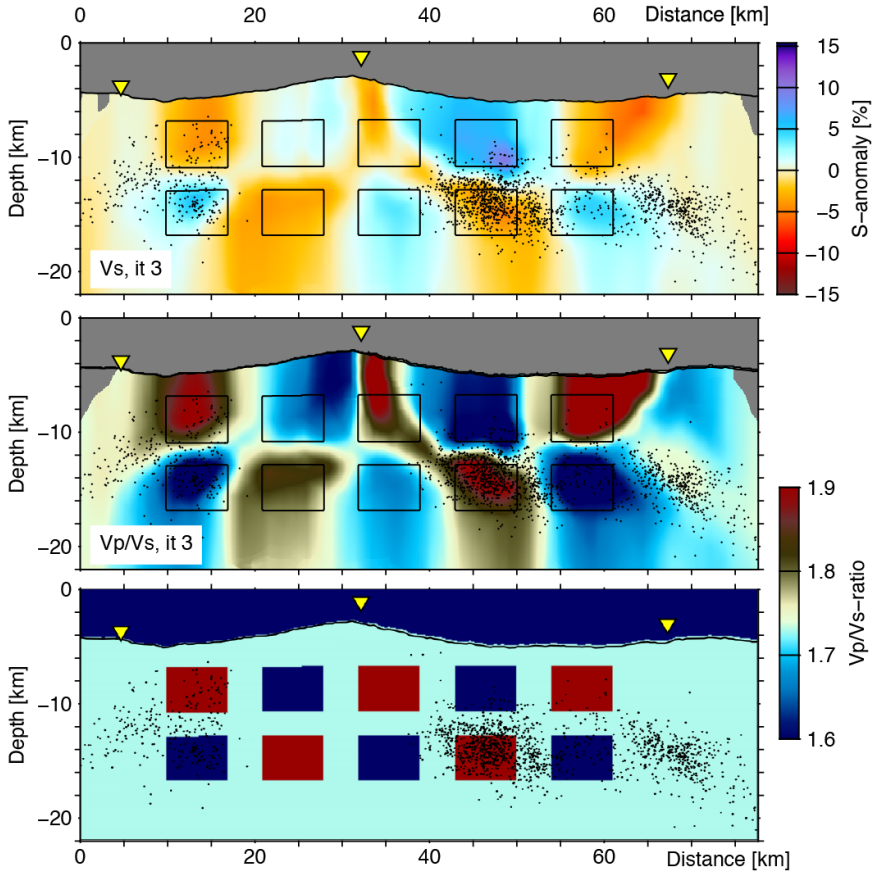

Figure 6.8 Vertical sections of synthetic test #2 input model and recovered anomalies. The location of the displayed cross-section is equal to that of Figs. 6.2 and 6.3 in the manuscript. Black squares represent the horizontal prisms of the input model. Note, that the velocity perturbations of the input model are equal for the three models of different prism size.

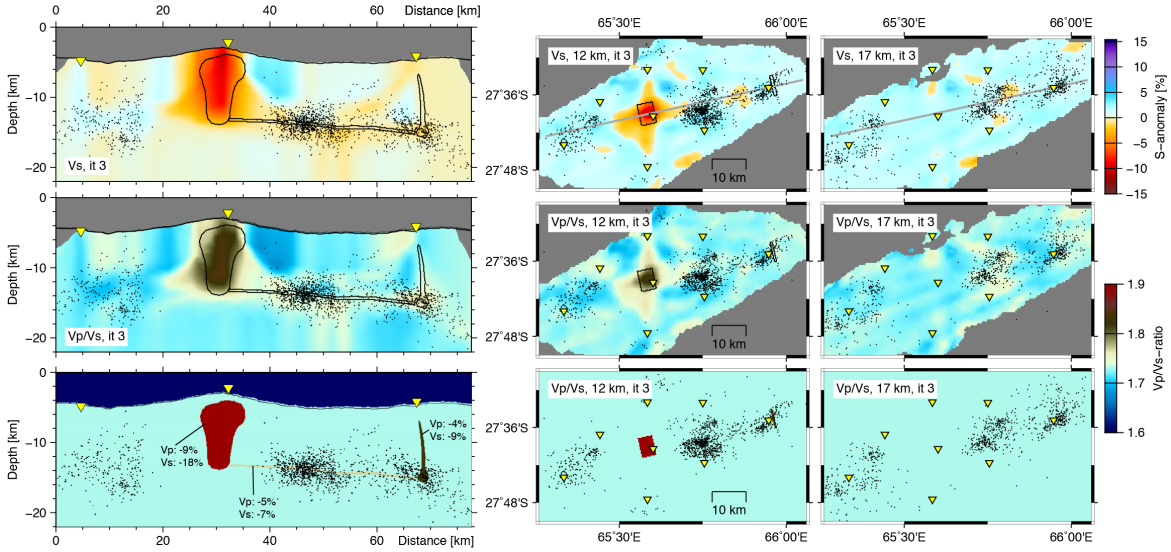

Figure 6.9 Synthetic test #3 with a realistic low velocity body in the center of the aseismic zone. The displayed cross-section is identical to the previous figures. The upper panel shows the recovered Vp/Vs ratio. The lower panel shows the input model.

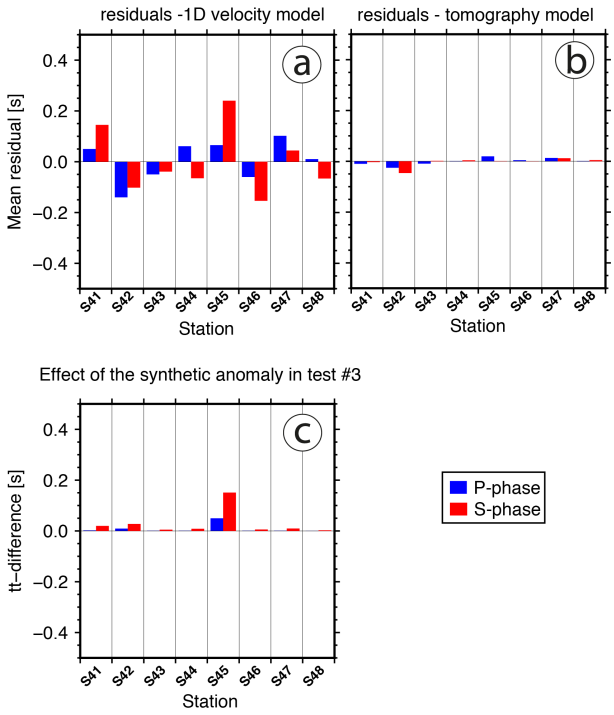

Figure 6.10 a, Travel time residuals at individual stations after locating the events selected for the local earthquake tomography with a 1D velocity model in the HYPOSAT software (*Schweitzer*, 2001) (see also *Schlindwein and Schmid* (2016)). b, Travel time residuals for individual stations of the final tomography model. c, Differences in travel times computed by ray tracing through synthetic model without anomalies (uniform 1D velocity distribution) and synthetic model #3. Note that random noise was added to the travel times.

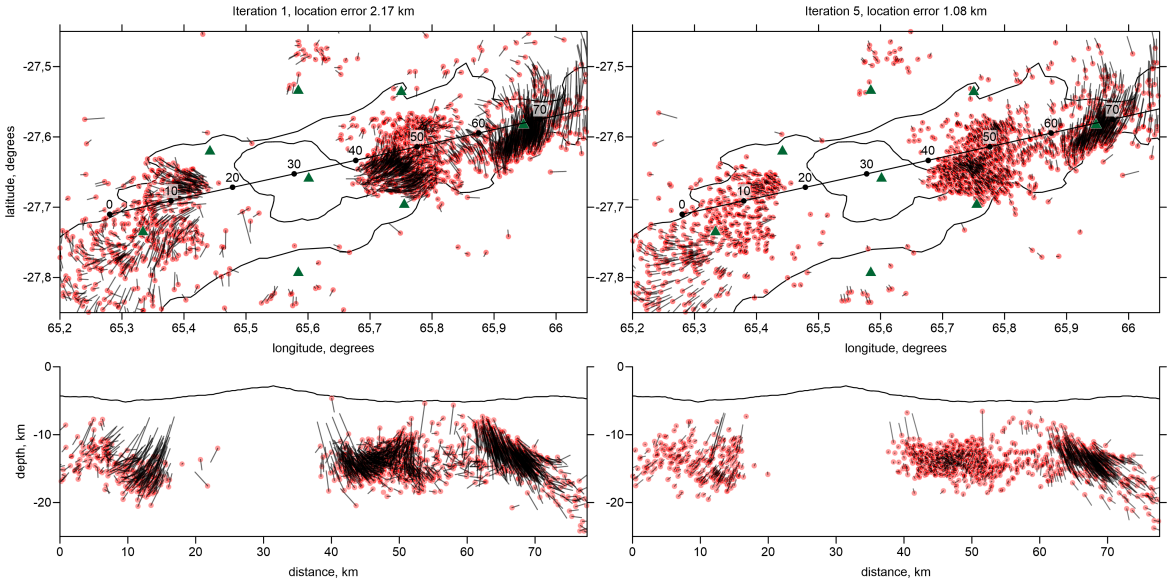

Figure 6.11 Source mislocations in the synthetic test #2 with checkerboard anomalies of 12x12 km extent (see supplementary Fig. 6.8). Left panels present the results of source locations in the starting one-dimensional velocity model, whereas the right plots present the locations results in the final 3D model. Upper panels present the source locations in the map view and the lower panels show projections sources (location of the profile is shown in the map). Red dots depict the current locations, and the bars direct to the true source points. Green triangles indicate the seismic stations.

7 Lithospheric strength, thermal structure, diffusive geochemical fluxes and microbial activity in the ultraslow spreading Southwest Indian Ridge axial valley

Authors: Florian Schmid[1], Massimiliano Molari[2], Vera Schlindwein[1], Norbert Kaul[3], Wolfgang Bach[3,4], Martin Vogt[4,5], Niels Jöns[3,4,*], Christian Hansen[3.4], Maren Walter[4,5], Ellen Damm[1] and Antje Boetius[1,2,3,4]

[1]Alfred-Wegener-Institute, Helmholtz-Centre for Polar- and Marine Research, Bremerhaven, Germany.

[2]Max Planck Institute for Marine Microbiology, Bremen, Germany.

[3]Department of Geosciences, University of Bremen, Germany.

[4]MARUM, Center for Marine Environmental Sciences, University of Bremen, Germany.

[5]Institute of Environmental Physics, University of Bremen, Germany.

[*]Present address: Department of Geology, Mineralogy and Geophysics, Ruhr-Universität Bochum, Germany.

Submitted in August 2017 to *Geochemistry, Geophysics, Geosystems*.

Key Points:

- A unique setting of very cold, rheologically weak lithosphere supports serpentinization down to 18 km depth.
- Deep boundary faults accommodate plate separation and give way for sluggish fluid circulation.
- Serpentinization products contribute to the geochemical fluxes and microbial activity in the sediment-covered axial valley.

7.1 Abstract

At mid-ocean ridges faults play a key role in enabling fluid flow and chemical exchange between the lithosphere and the ocean. In particular at magma-starved ridges the relation of tectonics and geochemical cycling are only partly understood. Here, we present yield-strength profiles, heat flow determinations, geochemical and microbiological results from the axial valley of a magma-starved section of the ultraslow spreading Southwest Indian Ridge between 13°-14°15'E. Our results show a rheologically weak lithosphere down to 18 km and a very low heat flow of 63.4–82.5 mW m^{-2} at the brittle-ductile transition. The weakening is best explained by serpentinization possibly focused in shear zones of deep-reaching boundary faults. Increasing flux rates towards the boundary faults indicate a slow fluid circulation in these shear-zones very likely originating from serpentinization. Highest nitrate and sulfide fluxes, and strongest per-cell activities were found in low-temperature sediments of the deep axial valley including an area inhabited by Vesicomyid bivalves typically endemic to seep and vent habitats. Signatures of hydrothermalism included locally elevated seafloor temperatures and weak, but spatially persistent methane plumes around 3500 m depth. These occasionally coincided with frequently observed clouds of marine-snow-like particles that likely consist of re-suspended sediments. They accumulate especially in the deepest parts of the axial valley due to high primary productivity in the overlying ocean and the specific rift morphology.

7.2 Introduction

Since the discovery of hot vents on the axes of actively spreading mid-ocean ridges (MOR), hydrothermal circulation through the young ocean lithosphere has received ample scientific attention, but little is known about the lithospheric structure, the hydrothermal- and biological activity at ultraslow opening MORs (e.g. *Copley et al.*, 2016; *Johnson et al.*, 2015). Ultraslow MORs are characterized by pronounced changes in crustal thickness and a highly variable mode of lithospheric accretion that alters between almost exclusively magmatic and mostly tectonic, in regions where mantle is exposed to the seafloor (*Dick et al.*, 2003; *Sauter and Cannat*, 2010; *Standish et al.*, 2008). The low overall melt budget of ultraslow MORs led to the assumption that hydrothermal vent fields along these ridges must be rare (*Baker and Hammond*, 1992). However, systematic surveying at the ultraslow Gakkel and Southwest Indian Ridges showed an unexpectedly high abundance of hydrothermal plumes and vent sites at these ridges (*Bach et al.*, 2002; *Baker et al.*, 2004; *Edmonds et al.*, 2003; *German et al.*, 1998). Generally, seafloor hydrothermal systems associated with spreading axes are often classified according to their host rock of either basaltic or ultramafic composition. Basalt-hosted systems were found to release higher concentrations of primordial helium and lower concentrations of methane than ultramafic systems (e.g. *Charlou et al.*, 1998; *Keir et al.*, 2006). Where ultramafic mantle rocks are exposed at the seafloor, serpentinization is the most prominent form of hydrothermal alteration. Serpentinization reactions release considerable amounts of abiotic methane and hydrogen into the sediments and water column (e.g. *Cannat et al.*, 2010; *Johnson et al.*, 2015; *Proskurowski et al.*, 2008).

Moreover, serpentinization can greatly reduce the integrated strength of mantle rocks (*Amiguet et al.*, 2012; *Escartin et al.*, 2001). Flexural faulting models indicate that serpentinization, when focused in shear zones, localizes the strain and causes the mode of tectonic deformation to change towards an increased spacing and larger throw of individual normal faults (*Escartin et al.*, 1997). The Obliqe Supersegment (10°-16°E) of the Southwest Indian Ridge (SWIR) has a particularly low magma budget and mantle rocks constitute the major percentage of the axial seafloor due to the ultraslow spreading rate of less than 15 mm a^{-1} (*Dick et al.*, 2003; *Sauter and Cannat*, 2010). *Bach et al.* (2002) dredged a variety of hydrothermal deposits in this area, including massive sulfide. They also mapped multiple turbidity plumes in the valley and proposed the presence of active hydrothermal vents. Most of the ultramafics recovered from the SWIR spreading axis are partially to completely serpentinized (e.g. *Cannat*, 1993; *Dick et al.*, 2003), implying that hydrothermal alteration and serpentinization are widespread. *Schlindwein and Schmid* (2016); *Schmid and Schlindwein* (2016) found indications for possibly deep-reaching serpentinization at the Oblique Supersegment. Hence, this area is well suited to further investigate the consequences of serpentinization for the lithospheric strength and the seafloor geochemical fluxes in this ultraslow-spreading MOR segment. Specific questions of our study include:

- What is the maximum depth of serpentinization in the axial lithosphere?
- How is the local and regional mode of tectonic deformation shaped by serpentinization?
- Are there active hydrothermal vent fields, and has the possibly low temperature hydrothermalism, related to serpentinization, an effect on sediment geochemical profiles and microbial activity in the axial valley?
- How are geochemical fluxes in the axial valley sediments related to seabed thermal anomalies?

Here we present geophysical, geochemical and microbiological results from the multidisciplinary expedition ANT XXIX/8 of RV Polarstern in late 2013 to the SWIR Oblique Supersegment (*Schlindwein*, 2014). During the expedition water column- and seafloor-surveying was performed in a reconnaissance style at key locations to search for hydrothermal plumes and vents and to characterize the environmental conditions in the axial valley of an exceptionally slow opening, amagmatic mid-ocean ridge section.

7.2.1 The Southwest Indian Ridge Oblique Supersegment

The long stretch of the Southwest Indian Ridge (SWIR, Figure 7.1a) between 10°-16°E is free of fracture zones and commonly referred to as the Oblique Supersegment. Due to its obliquity of ~56°with respect to the spreading direction it has a very low effective opening rate of ~7.8 mm a^{-1} (*Dick et al.*, 2003). The edifices of two prominent magmatic centers on the Oblique Supersegment - Joseph Mayes Seamount and Narrowgate Segment – enframe an amagmatic accretionary segment which is characterized by a very deep axial valley (Figure 7.1b).

At the Oblique Supersegment the axial valley walls are constructed of large low-angle faults of ~1.2 km throw and 6 km heave that form massive blocks composed of altered peridotite (*Bach et al.*, 2002; *Standish et al.*, 2008). Dredging in the axial valley of the amagmatic accretionary segment in 1999/2000 yielded mostly peridotites but also basalts and relict hydrothermal deposits of massive sulfides, sepiolites and nontronite-birnessite cemented breccia (*Bach et al.*, 2002; *Dick et al.*, 2003). A microseismicity study from 2012 to 2013 in the central part of the Oblique Supersegment showed that earthquake foci occupy a confined depth interval that undulates along the rift axis (Figure 7.1c) (*Schlindwein and Schmid*, 2016). Earthquakes down to 35 km - which is exceptionally deep for mid-ocean ridges - imply a very thick brittle lithosphere. It was found that regions of deepest hypocenters generally correlate with an overall deeper rift valley and peridotite exposure at the seafloor whereas regions of shallower events coincide with a shallower, more rugged rift valley, bearing basaltic rocks beside peridotites (*Schmid and Schlindwein*, 2016). The Oblique Supersegment is located in the center of the opal belt, a region that is characterized by enhanced primary productivity (*Lutz et al.*, 2007) and high deposition rates of predominantly silicious sediments (*Geibert et al.*, 2005).

7.3 Materials and Methods

7.3.1 Inspecting the depth-frequency distribution of eathquakes

We calculated depth frequency distributions of earthquakes (DFDE) from the microseismicity catalogue of *Schmid and Schlindwein* (2016). We defined vertical bins of 5 km and counted earthquakes falling into these bins, omitting events of vertical location uncertainty larger than 5 km. The catalogue was divided in two areas (I and II, Figure 7.1b) containing 216 and 414 events, respectively. The choice of the two areas was motivated by general changes in morphology, lithology and focal depths of microearthquakes along the spreading axis. Area I is characterized by a deeper, smoother rift valley, deeper hypocenters and the mere recovery of peridotites (Figure 7.1b). Area II shows a shallower, more rugged valley floor, shallower earthquake foci and the basalts on the seafloor. A clustering analysis of the catalogue showed that it does not contain any swarms or clusters of earthquakes, a precondition for the subsequent comparison to yield-strength envelopes.

7.3.2 Yield-strength envelopes

The depth level at which the deepest earthquakes occur over longer time intervals is considered as the brittle-ductile transition zone (BDT) and is often referred to as the lower limit of the mechanical lithosphere (*Anderson*, 1995). In oceanic plates this transition zone is primarily temperature defined, usually around 650 ±100°C (*Burov*, 2011; *McKenzie et al.*, 2005). Within the BDT rocks deform in a semi-brittle manner. Thus, on the microscopic scale, a mix of brittle and ductile processes occur (*Scholz*, 2002). Knowledge about the absolute thickness of the mechanical lithosphere and its internal rheological strength is of common interest, since it influences the nature of tectonic processes in active rifts (*Burov*, 2011).

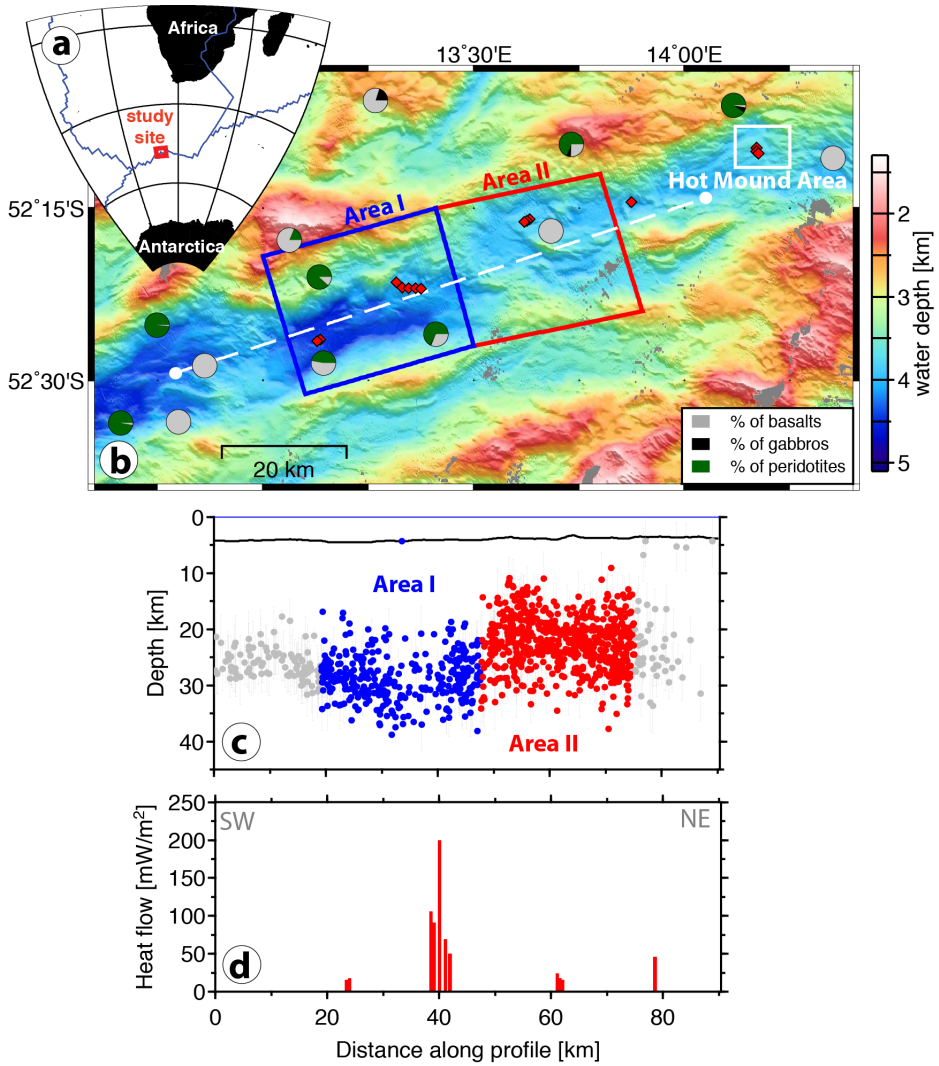

Figure 7.1 Overview of the study site (a) at the Southwest Indian Ridge Oblique Supersegment. b) Pie charts on bathymetric map show types and abundances of dredged rock samples; red diamonds indicate the sites of heat flow determinations. Red and blue squares correspond to subsets of the seismicity catalogue c. Dashed white line indicates position of the cross-section in c and d. c) Projected earthquake hypocenters of the catalogue of *Schmid and Schlindwein* (2016). Events with a depth error larger than 5 km were omitted. d) Projected heat flow values in the axial rift valley.

Theoretical yield-strength envelopes (YSE) can be calculated from empirical deformation laws using thermal profiles and compositional properties (*Burov*, 2011; *Goetze and Evans*, 1979). For several geographic regions, mostly active rifts, a linear increase in seismicity with depth followed by an exponential decrease has been reported (*Albaric et al.*, 2009; *Lamontagne and Ranalli*, 1996; *Watts and Burov*, 2003). The similarity in the depth of the peak of earthquake activity and the maximum calculated yield-strength suggests that strength and seismicity are somehow related. A possible link is established assuming that the long-term mechanical behavior of the lithosphere is reflected in its short-term deformation (*Burov*, 2011; *Ranalli*, 1995; *Scholz*, 2002).

Based on this relation YSEs can be constructed from the DFDEs and compared to calculated YSEs with the outcome of gaining qualitative knowledge on the thermal- and compositional structure of the lithosphere as well as its mechanical thickness (*Watts and Burov*, 2003).
We calculated the YSEs assuming a constant thermal gradient between the seafloor at 0°C and the maximum depth of faulting corresponding to temperatures around 650°C (*McKenzie et al.*, 2005). Generally, the oceanic lithosphere is free of radiogenic heat production thus the seafloor heat flux equals the basal heat flux (e.g. *Jaupart and Mareschal*, 2007). DFDEs and associated YSEs are calculated for extended areas of the axial lithosphere, thereby averaging-out local perturbations in thermal structure such as potential magmatic intrusions.

7.3.3 Brittle lithospheric domain

The stress required to initiate a fault σ_i (also referred to as the differential between maximal and minimal principal stresses $\sigma_1 - \sigma_3 = \sigma_i$) in the brittle domain of the lithosphere may be calculated following the generalized form of Byerlee's friction law (*Byerlee*, 1978),

$$\sigma_i = \sigma_1 - \sigma_3 = \alpha \rho_m g z (1 - \lambda) \tag{7.1}$$

Where ρ_m is density, g is gravity acceleration, z is depth, λ the ratio of porefluid pressure to lithostatic pressure and α is a fault type related factor. In the case of a rift system where extension is dominant we use an α for normal faults $\alpha = 1 - C^{-1}$ after *Burov* (2011) where $C = ((1+\phi^2)^{0.5} - \phi)^{-2}$. Here, ϕ is the Mohr Coulomb criterion friction angle (parameter values are summarized in table 1).
Initially calculated YSEs failed to account for the extremely low strength of the upper lithosphere suggested by the absence of earthquakes. *Escartin et al.* (1997) suggest that serpentinization may vastly reduce the strength of the upper lithosphere and introduce a modified formulation of Byerlee's friction law,

$$\sigma_i = \frac{\mu \rho_c g z (1 - \lambda)/2}{\mu sin^2(\theta) + sin^2(\theta) cos(\theta)} \tag{7.2}$$

Where μ is the coefficient of friction in serpentinized domains, and θ is the fault dip.

7.3.4 Ductile lithospheric domain

Beyond the depths of brittle deformation, creep processes at a microscopic level accommodate most of the deformation and the strength exponentially decays (*Burov*, 2011). We used the power-law creep equations of *Ranalli* (1995),

$$\sigma_i = (\frac{\varepsilon}{A})^{1/n} e^{(\frac{E}{nRT(z)})} \tag{7.3}$$

Where ε is the steady-state strain rate , A, E, n are material parameters determined from laboratory experiments (a summary of published values is given in *Burov* (2011)) and T is temperature.
The yield strength was calculated for depth steps of 5 km - corresponding to the DFDEs – for each of the three laws (equations 7.1, 7.2 and 7.3).

Symbol	Parameter	Value (unit)
z	Depth	(km)
ρ_c	Density of serpentinized lithosphere	2900 (kg m^3)
ρ_m	Density of non-serpentinized upper lithosphere	3200 (kg m^3)
R	Universal gas constant	8.3144 (J K^{-1} mol^{-1})
θ	Fault dip angle	53°, see *Escartin et al.* (1997)
μ	Coefficient of internal friction	0.3 (dimensionless)
ε	Steady-state strain rate	$1.58 \cdot 10^{-14}$ (s^{-1})
$\lambda = \rho_w/\rho$	Ratio of pore fluid pressure to lithostatic pressure	(dimensionless)
A	Material parameter	(MPa^{-n} s^{-1})
E	Material parameter	(kJ mol^{-1})
n	Material parameter	(dimensionless)

Table 7.1 Input parameters for the calculation of yield-strength envelopes. Note that parameters without explicit values were adapted during the process of forward modeling YSEs whereas all other parameters remained fix.

The YSE was then constructed using the lowest yield-strength value of each depth interval. We took the approach of forward modeling the YSEs by varying the input thermal gradients and material parameters within conceivable ranges.

7.3.5 Heat flow determinations

Seafloor heat flow determinations were conducted during RV Polarstern cruise ANT-XXIX/8 with the 6 m long Bremen Heat Probe, which is constructed in a violin-bow-like design (*Villinger et al.*, 2010). The sensor string contains 21 thermistors and a heating wire that allows the in situ determination of thermal conductivity (*Lister*, 1979). At most of the stations 2-3 successive penetrations were performed at distances of ~0.5 km to assess the magnitude of local deviations in heat flow and thermal gradient. The thermal conductivity was estimated for the first penetration of each station using the algorithm of *Villinger and Davis* (1987). Conductivities achieved from the first penetration were then extrapolated for all successive penetrations of the station. The vertical component of the geothermal heat flow Q was calculated from the thermal conductivity k (estimated from the heat pulse decay) and the measured thermal gradient according to

$$Q = k\frac{\delta T}{\delta z} \tag{7.4}$$

7.3.6 Hydrographic and water column geochemical measurements

During RV Polarstern expedition ANT-XXIX/8 we used a Sea-Bird Electronics SBE 9plus conductivity, temperature, depth probe (CTD) mounted to a water sampler with 22 Niskin bottles (*Schlindwein*, 2014). Four Miniature Autonomous Plume Recorders (MAPRs) provided by the National Oceanographic and Atmospheric Association (NOAA) were added for plume searching with sensors for temperature, pressure, optical backscatter, and oxidation-reduction potential (Eh).

Hydrographic casts were performed in a Towyo mode of operation where the CTD is repeatedly lowered and lifted at 10-700 m above the seafloor while the ship maintained a speed of 0.9–1.9 km h^{-1}. Methane concentrations in the seawater samples were measured onboard with an Agilent 7820A gas chromatography system coupled to a flame ionization detector following headspace extraction (*Schlindwein*, 2014) and subsamples were used for the determination of methane carbon isotopy (*Faber et al.*, 1998). Water samples for noble gas analysis were filled into evacuated glass ampoules onboard and further processed in the Bremen Helium Isotope Lab following the method of *Roether et al.* (2013).

Measurements of total dissolved manganese (TdMn) were performed after the cruise at the Bremen of University. Aliquots of the water samples were taken for onshore measurements of TdMn. The analyses of 100-fold diluted aliquots were performed using an Element 2 inductively coupled plasma mass spectrometer (ICP-MS, Thermo Scientific, Germany). To account for variations in the performance of the ICP-MS during analysis In and Y were added as an internal standard (0.5 μµg L^{-1}) to each water sample and calibration solution. Precision and accuracy of the analytical procedure were controlled by the reference material Nass-5 (National Research Council, Canada). Where accuracy was <10%, data was standard-corrected.

7.3.7 Porewater and sediment geochemistry

A TV-guided multi-corer (TV-MUC) was used to retrieve undisturbed surface sediments. A list of all coring locations is provided in Table 2. One core from each site was used for porewater and sediment sampling. The subsampling of cores was performed immediately after recovery in a temperature controlled lab at 2 °C. Profiles of dissolved components like DIC, nutrients (NH_4^+, PO_4^{3-}, NO_2^-, $NO_3^- + NO_2^-$, $Si(OH)4$), sulfate, sulfide and manganese in the sediments were assessed by extracting porewater with Rhizons (SMS type MOM 19.21.21F, mean pore size 0.15 μm; Rhizosphere Research Products). Solid phase sediment samples were collected by slicing the core in 1-0 cm, 1-5 cm and 5-10 cm layers, and were preserved for analyses of porosity, total organic carbon (TOC) and total nitrogen (TN). Samples were prepared and analyzed as described in *Böer et al.* (2009). For CH4 gas analysis 5 mL of sediment were collected with cut-off 5 mL^{-1} syringe and added to 10 mL 2.5% NaOH in glass crimp vials, mixed, stored upside down at 4 °C and then analyzed by gas chromatography (Focus GC, Thermo Fisher Scientific) as described in *Thang et al.* (2012). Carbon isotopic ratios were measured via continuous-flow isotope ratio mass spectrometry as outlined in *Faber et al.* (1998). All isotope ratios are given in δ-notation versus VPDB (Vienna Pee Dee Belemnite) standard.
For the gravity cores (GC, max. core depth retrieved 5.5 m) the analyses were analogue to the MUC cores but samples were taken every 20 cm. We used Fick's law to estimate the vertical diffusive flux J of geochemical constituents in the sediment cores,

$$J = -\Phi D_S \frac{\delta C}{\delta z} \tag{7.5}$$

Here Φ is porosity, $D_s = \frac{D_0}{\Phi}$ is the sediment diffusion coefficient, calculated from the sediment deviated tortuosity $\Phi = 1.1$ for a porosity of 0.9 (*Matyka et al.*, 2008) and D_0 is the tracer diffusion coefficient in seawater. We used values of D_0= 4.64E-6 $[cm^2 s^{-1}]$ for sulfate, D_0= 9.17·10^{-6} $[cm^2 s^{-1}]$ for sulfide, D_0= 9.03·10^{-6} $[cm^2 s^{-1}]$ for ammonium, D_0= 3.02·10^{-6} $[cm^2 s^{-1}]$ for manganese, D_0= 9.03·10^{-6} $[cm^2 s^{-1}]$ for nitrate. Coefficients are taken from *Schulz* (2000). δC is the difference in concentration [mmol L^{-1}] and δz is the difference in depth [m].

7.3.8 Microbial abundances and activity in surface sediments

For microbial cell count the top 1 cm of sediment in MUC cores were fixed in 2% buffered formaldehyde/water and stored at 4°C until subsequent analysis. Microbial abundance was estimated by epifluorescence microscopy after staining with Acridine Orange following the workflow of *Hobbie et al.* (1977) that was modified by *Böer et al.* (2009). Catalysed reporter deposition fluorescence in situ hybridization (CARD-FISH) was applied to enumerate the active fraction of bacterial and archaeal assemblages (*Amann and Fuchs*, 2008). Samples were stored and processed according to the procedure of *Ishii et al.* (2004) and for archaeal cell-wall permeabilization according to *Molari and Manini* (2012). Hybridization conditions were as previously described: EUB338I-III, targeting members of the Bacteria (*Amann et al.*, 1990; *Daims et al.*, 1999), ARCH915 targeting most members of the Archaea (*Stahl and Amann*, 1991) and NON338 as negative control (*Amann et al.*, 1995). Total microbial activity was estimated by uptake of ^{14}C-labeled inorganic carbon. Dark CO_2 fixation (DCF) rates were estimated following the procedures of *Herndl et al.* (2005) for water samples and *Molari and Manini* (2012) for sediment samples including some modifications. Further details on the procedures are provided in Supporting Information Text S2. The activity per cell was obtained dividing DCF rates by total number of active cells detected with CARD-FISH (e.g. sum of bacterial and archaeal cells).

7.4 Results

7.4.1 Seismicity depth distribution and strength profiles of the axial lithosphere

Splitting the seismicity catalogue into areas I and II (Figure 7.1b) yielded two subsets of 216 and 414 events, respectively. In the following we consider the brittle-ductile transition (BDT) as the zone between the depth of the strength peak (upper limit) and the maximum depth of earthquakes (lower limit) as indicated by the orange bars in Figure 7.2. The DFDE in Area I shows no earthquakes down to 12.5 km and a plateau rather than a peak in seismicity reaching from 22.5 to 27.5 km depth (Figure 7.2, left panel). Thus, the upper limit of the BDT in Area I varies within this depth range. The BDT has a thickness of 10 $\pm$ 2.5 km in Area I as given by the seismicity terminating at 35 km depth.

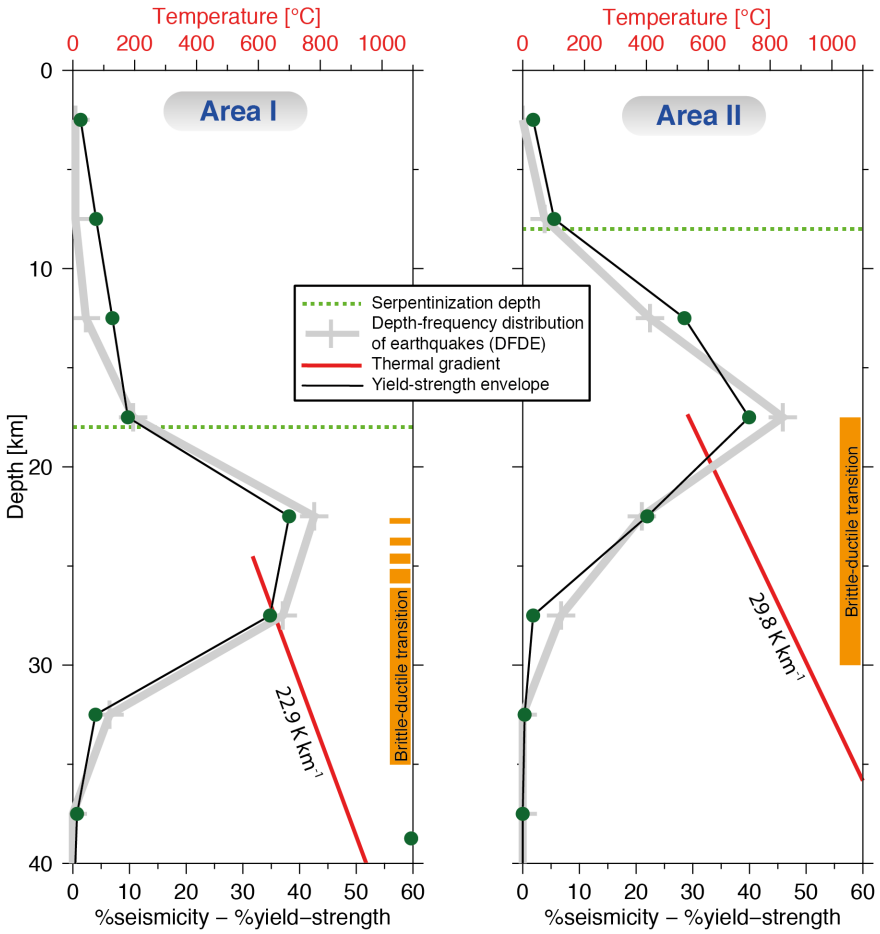

Figure 7.2 Seismicity depth distribution in areas I and II (Figure 7.1b) and associated best fitting yield-strength envelops as well as inferred linear thermal gradients. Note that for both areas the same wet olivine rock parameters from *Hirth and Kohlstedt* (1995) are used for the ductile domain.

The DFDE in Area II shows no seismicity shallower than 7.5 km and a peak at 17.5 km (Figure 7.2, right panel) marking the upper BDT limit. The seismicity terminates at 30 km depth implying a 12 km thick BDT. During the process of forward modeling the YSEs we varied the input parameters step by step and assessed their impact on the shape of the YSE and fit to the DFDE (Figures 2 and 3). In the following the term serpentinization depth is used synonymously for the depth of transition from the modified form of Byerlee's law (*Escartin et al.*, 1997) to the application of the common Byerlee's law. The choice of the serpentinization depth has a critical influence on the upper part of the YSE. It is left with little options to be shifted up or down when it comes to fitting the YSE and DFDE. To reproduce a rheologically weak lithosphere, as suggested by the absence of seismicity (Figure 7.1c, Figure 7.2), the serpentinization depth had to be set to 18 km for Area I and 8 km depth for Area II. Changing the serpentinization depth by 2 km markedly impaired the quality of the fit. Increased thermal gradients cause a shallower depth of the maximum yield-strength and vice versa (Figure 7.3, left panel). The YSEs represent average strength profiles in areas of approx. 25 x 25 km (Figure 7.1b-c). Hence, the inferred geothermal gradients represent spatial averages. For the best fitting YSE we obtained geothermal gradients of 22.9 K km^{-1} (Area I) and 29.8 K km^{-1} (Area II).

We used the YSE-obtained thermal gradients in combination with published values of thermal conductivity in dunite ($k_{kdunite}$ = 2.77 W m^{-1} K^{-1} from *Eppelbaum et al.* (2014)) to calculate the vertical heat flow in the BDT according to equation 7.5. Assuming the lithosphere above the BDT is free of additional heat sources the calculated values of 63.4 mW m^{-2} (Area I) and 82.5 mW m^{-2} (Area II) represent regional averages that may be validated against the heat flow determined at the sea floor.

Different compositional parameters in the ductile domain caused considerable changes to the YSEs

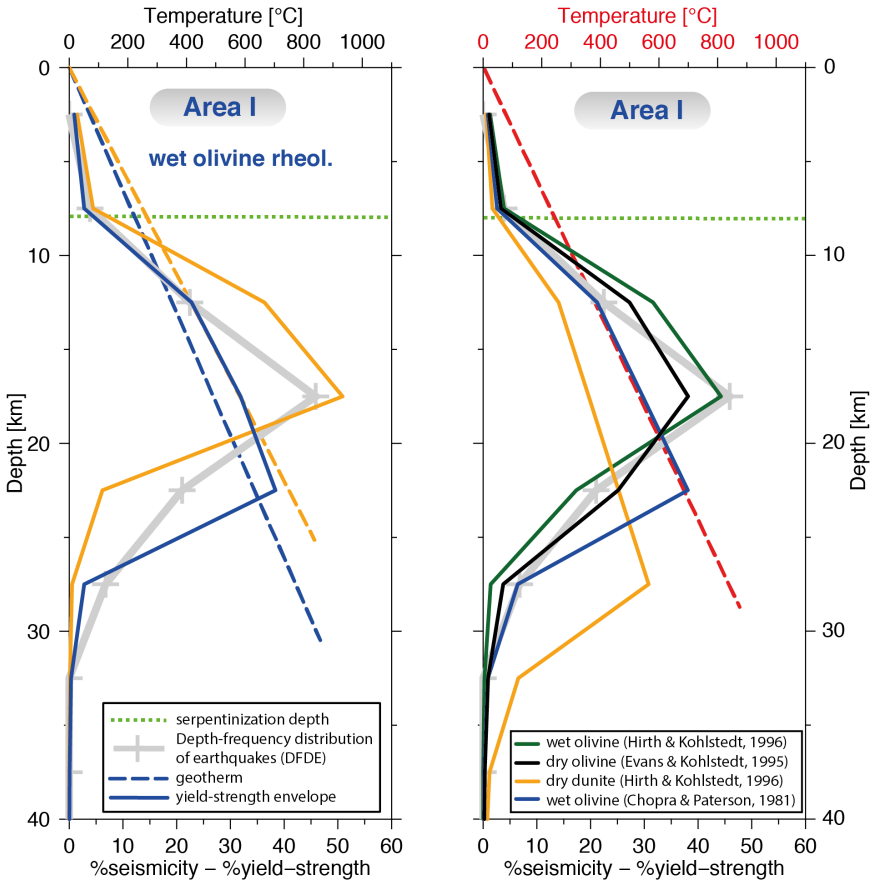

Figure 7.3 Assessing the effect of different thermal gradients (left panel) and different compositional parameters in the ductile domain (right panel) on the shape of the calculated yield-strength envelopes. Note that the same geothermal gradient is used for all YSEs displayed in the right hand panel.

(Figure 7.3, right panel). Published values of identical lithologies (e.g. "wet olivine") differ and so do corresponding YSEs. Deformation in the ductile domain is strongly strain-rate dependent, but laboratory-based experiments are conducted under strain rates several orders above those in nature (*Burov*, 2011). The extrapolation of laboratory results to tectonic time scales is thus ambiguous (*Burov*, 2011) and the validity of drawing implicit conclusions from input material parameters disputable. We refrain from directly interpreting specific input rock parameters but highlight that the best fit of DFDE and YSE in both areas was achieved by using identical, wet olivine, compositional parameters from *Hirth and Kohlstedt* (1996) in the ductile domain (Figure 7.2). However, for the ductile domain we observe a partial tradeoff between applied geothermal gradient and compositional parameters.

Thus, the best fit of each set of rock parameters was achieved with different geothermal gradients (Supporting Information Text S1 and Table S1).

7.4.2 Seafloor heat flow

Thermal conductivities in the axial valley sediments vary between 0.71 and 0.73 W m^{-1} K^{-1}. These low values reflect the high porosities of 0.86 to 1.0 measured in the recovered sediments cores. Heat flow results from the axial rift valley show a strong local variability as they range between 15.5 and 848 mW m^{-2} (Figure 7.1). Values of 15.7-17.8 mW m^{-2} at the axial valley bottom in the west of Area I are considerably lower than the 63.4 mW m^{-2} inferred from the YSE thermal gradient in this area (Figure 7.4a,c). Five penetrations near the northern axial valley wall in Area I, located in proximity of possible fault lines at the sea floor, show mostly higher values than those inferred by the YSE thermal gradient and underline the significant local variability (Figure 7.4a,c). Three penetrations in Area II (Figure 7.1b,d) show values between 15.7- 24.1 mW m^{-2} that are considerably lower than the 82.5 mW m^{-2} inferred from the YSE thermal gradient.

Greatly enhanced geothermal gradients and heat flow values are observed in the Hot Mound Area (Figure 7.5). The most pronounced geothermal gradient of 1.194 K m^{-1} and heat flow values of 321 to 848 mW m^{-2} reveal a strong local variability. The three penetrations in the Hot Mound Area show a convex shaped curve of residual temperatures after removing the linear gradient (Figure 7.5). Convex thermal gradients in the subsurface are indicative of upward fluid advection. Based on the curve's shape the vertical porewater flux is estimated with the method of *Bredehoeft and Papadopulos* (1965). For the central penetration, showing the strongest curvature, we estimate a diffusion velocity of approx. 250 mm a^{-1}.

7.4.3 Discovery of a Vesicomyid bivalve at the axial valley bottom

We were puzzled by the discovery of a large veneroid bivalve of the family Vesicomyidae (genus Christineconcha, identified by Sergei Galkin, IORAS) that had crawled onto an ocean bottom seismometer which was retrieved from the axial valley bottom after a year long deployment (7.4c *Schlindwein*, 2014). Members of this group are typically inhabitants of vents and seeps, and related taxa were previously found at cold seeps and reducing sedimentary environments on continental slopes in the North- and Southeastern Atlantic (*Boss*, 1970; *von Cosel and Olu*, 2009). Their metabolism depends on sulfide-oxidizing chemoautotrophic bacteria hosted in their gills (*Fischer*, 1980). However, repeated dives with the OFOS camera systems across the site did not spot further Vesicomyidae bivalves, probably because they live buried in the sediments to reach the sulfide front.

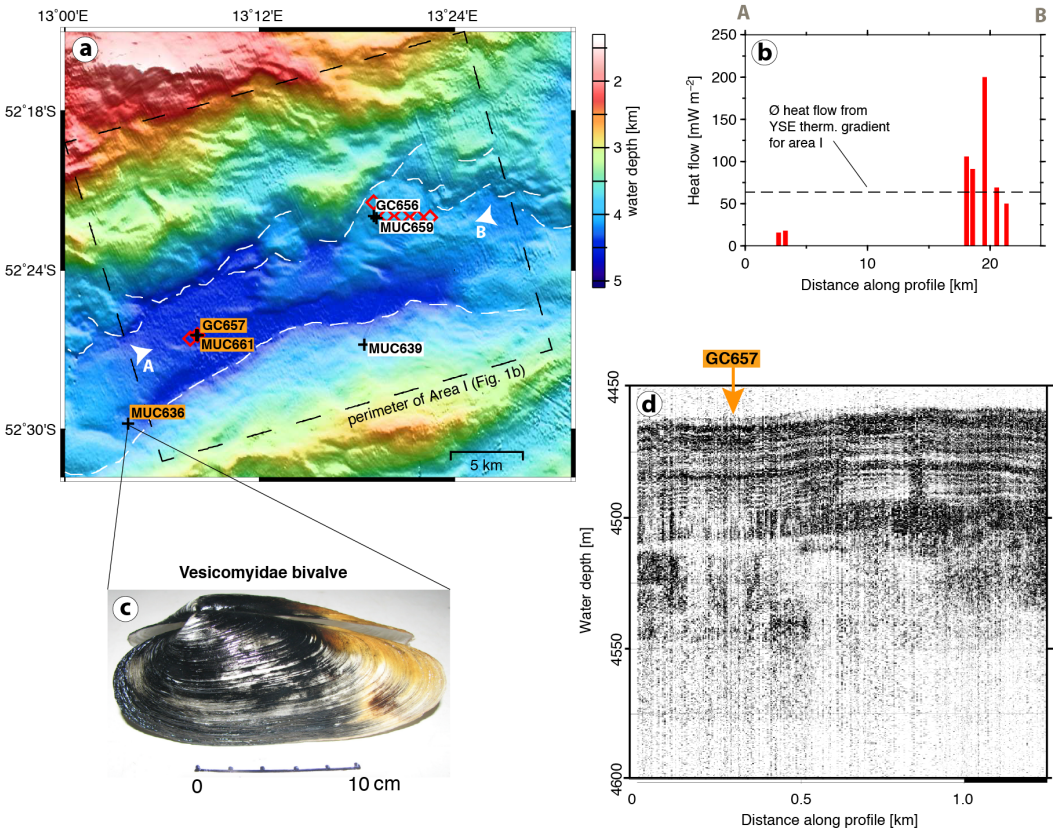

Figure 7.4 Bathymetry, heat flow and sediment thickness in Area I. a) Bathymetry with dashed white lines indicating potential fault scarps of boundary faults. Red diamonds show heat flow stations and black crosses show sediment coring sites. Orange labels, stations on valley bottom. White labels, stations on valley flanks (see Table 2). b) Heat flow values projected on a transect along the axial valley whose location is indicated by white arrows on map a. c) Veneroid bivalve of the family: Vesicomyidae, genus: Christineconcha, a living speciment that was retrieved attached to an ocean bottom seismometer close to coring location MUC636. d) Sediment-echosounder data example from coring station GC657 at the bottom of the axial valley showing laminated strata of at least 80 m thickness above the basement.

7.4.4 Geochemistry of axial valley sediments

Four gravity cores (GC; sites 652, 653, 656, 657) and seven multi-corer stations (MUC; sites 626, 636, 639, 649, 659, 661, 681) yielded unconsolidated and porous sediments that consist primarily of diatomaceous ooze (*Schlindwein*, 2014). All coring sites were located inside the axial valley except from reference stations MUC626 (north) and MUC681 (south) of the SWIR. We defined four areas with different settings: 1) the valley bottom in Area I, 2) the valley flanks in Area I, 3) the Hot Mound Area and 4) references sites north and south of the SWIR. All coring sites, and their respective areas are listed in Table 7.2.

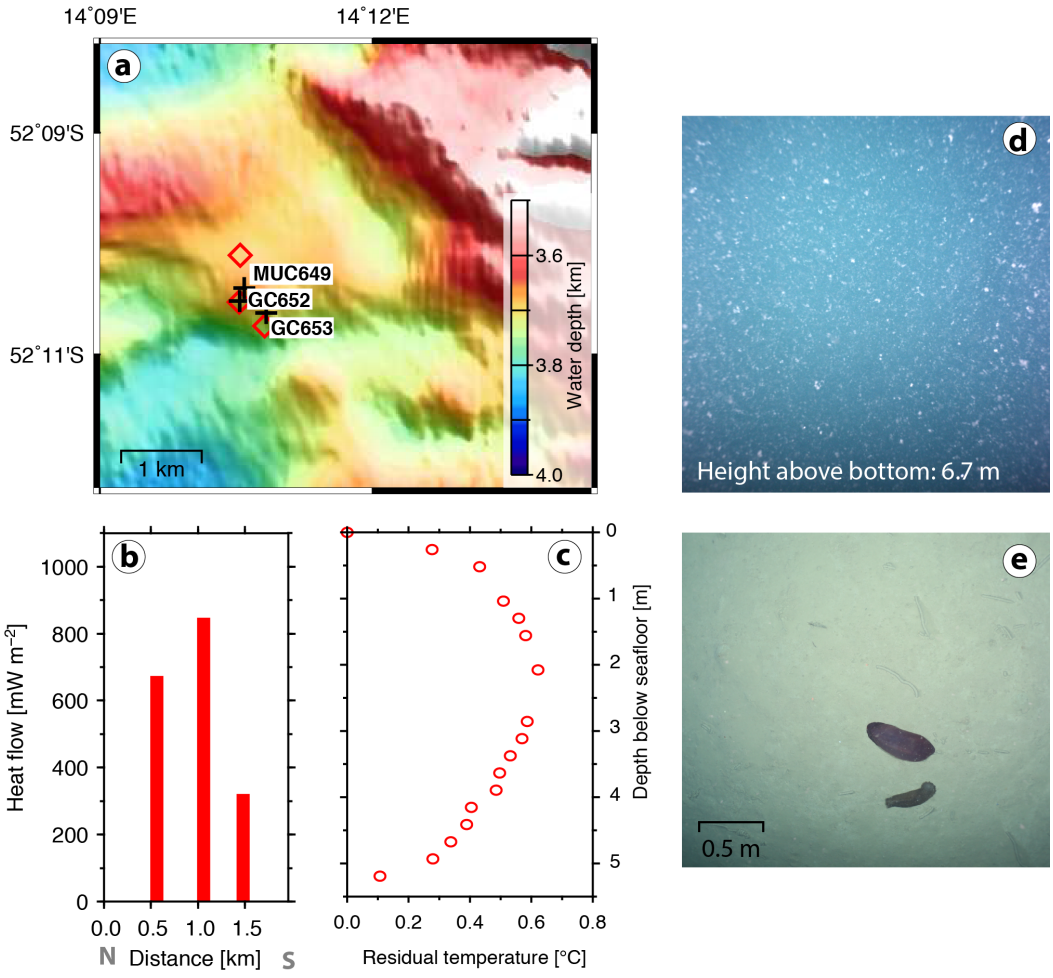

Figure 7.5 Bathymetry, heat flow and seafloor images from the Hot Mound Area (see Figure 7.1d for location). a) Bathymetry with heat flow penetrations (red diamonds) and sediment coring sites (black crosses). b) Heat flow values projected on a north-south transect across the three penetrations. c) Distribution of residual temperatures (after removing seafloor temperature of 7.89°C and a linear gradient) for the middle penetration on plot b and map a. d) OFOS image of a particle cloud above the seafloor close to coring site GC653. e) OFOS image from the seafloor close to coring site GC652 showing soft sediments with two holothurians and several traces of mobile fauna.

The valley bottom in Area I is the deepest part of the axial valley in the survey area (average depth 4400 m). It exhibited a very low heat flow of 15.5 to 17.8 mW m^{-2} and hosts coring sites MUC636 (where the Vesicomyid bivalve was discovered), GC657 and MUC661 (Figure 7.4). Cores GC656 and MUC659 were located at the northern valley flank in Area I were the heat flow ranged between 90 and 106 mW m^{-2}. MUC639 was located at the southern valley flank in Area I (Figure 7.4). Gravity cores GC652, GC653 and MUC649 originate from water depths around 3700 m in the Hot Mound Area (Figures 5a) where the heat flow reached up to 848 mW m^{-2} and a convex thermal gradient indicated slow fluid advection. Geochemical analysis results of all sediment cores are shown in Figures 7.6 and 7.7, sorted in order of the different survey areas.

Area	Station no.	Gear	Latitude	Longitude	Water depth [m]
Valley bottom in Area I	636	MUC	52°29.790'S	13°3.870'E	4199
	657	GC	52°26.450'S	13°8.110'E	4448
	661	MUC	52°26.462'S	13°8.196'E	4415
Valley flanks in Area I	639	MUC	52°26.063'S	13°18.287'E	4375
	656	GC	52°21.970'S	13°19.040'E	3968
	659	MUC	52°22.051'S	13°19.215'E	3941
Hot Mound Area	649	MUC	52°10.095'S	14°10.602'E	3655
	652	GC	52°10.140'S	14°10.540'E	3703
	653	GC	52°10.220'S	14°10.830'E	3709
N. reference	681	MUC	48°43.838'S	15°40.717'E	4351
S. reference	626	MUC	54°57.547'S	12°28.748'E	4869

Table 7.2 Locations of all sediment-coring sites sorted by key areas investigated. Maps with coring locations are provided in Figures 7.4a and 7.5a.

Concentrations of TOC and TN were low in all cores, ranging between 0.2-0.7% with highest concentrations at the axial valley bottom in in Area I (GC657) and lowest concentrations in the Hot Mound Area (GC652 and GC653). The carbon to nitrogen ratio (C:N) ranged between 6.3-8.7, and remained constant with depth in all cores. Black stained layers and a strong sulfurous smell in core GC657 from the valley bottom in Area I (*Schlindwein*, 2014) are noteworthy as well as decreasing sulfate and increasing sulfide concentrations with depth at the valley bottom in Area I (cores MUC636 and GC657), indicating sulfate reduction. From the gradient of sulfate concentrations we extrapolated sulfate depletion at approx. 50 m below the seafloor at coring site GC657. Methane was generally low in the porewaters, not exceeding values of 0.9 μmol L^{-1} in any core. It indicates that either there is no significant methane flux to the seafloor at the investigated sites or the methane is consumed in the subsurface horizons before it reaches the sampled strata. Generally, methane carbon isotopic ratios (δ^{13}C-CH_4) of porewaters showed a lighter isotopic composition of around -31.0 ‰ in deeper strata, and heavier carbons towards the surface, indicating some fractionation during methane consumption. Some samples showed a deviation at the surface (e.g. GC657).

Depletion of nitrate below 0.1 m depth was observed in all cores from inside the axial valley but not at the reference sites outside the valley (MUC626 and MUC681). There, nitrate concentrations increase with depth in the uppermost 3-7 cm and remain constant below (ca. 50 μmol L^{-1}). The shallow nitrate depletion inside the axial valley suggests a lower oxygen penetration compared to the reference sites outside the axial valley. Ammonium concentrations were unexpectedly high in the cores from the valley bottom in Area I (GC657 1.8 mmol L^{-1}; MUC661 0.7 mmol L^{-1}; MUC636 0.27 mmol L^{-1}) and increase with depth in these cores.

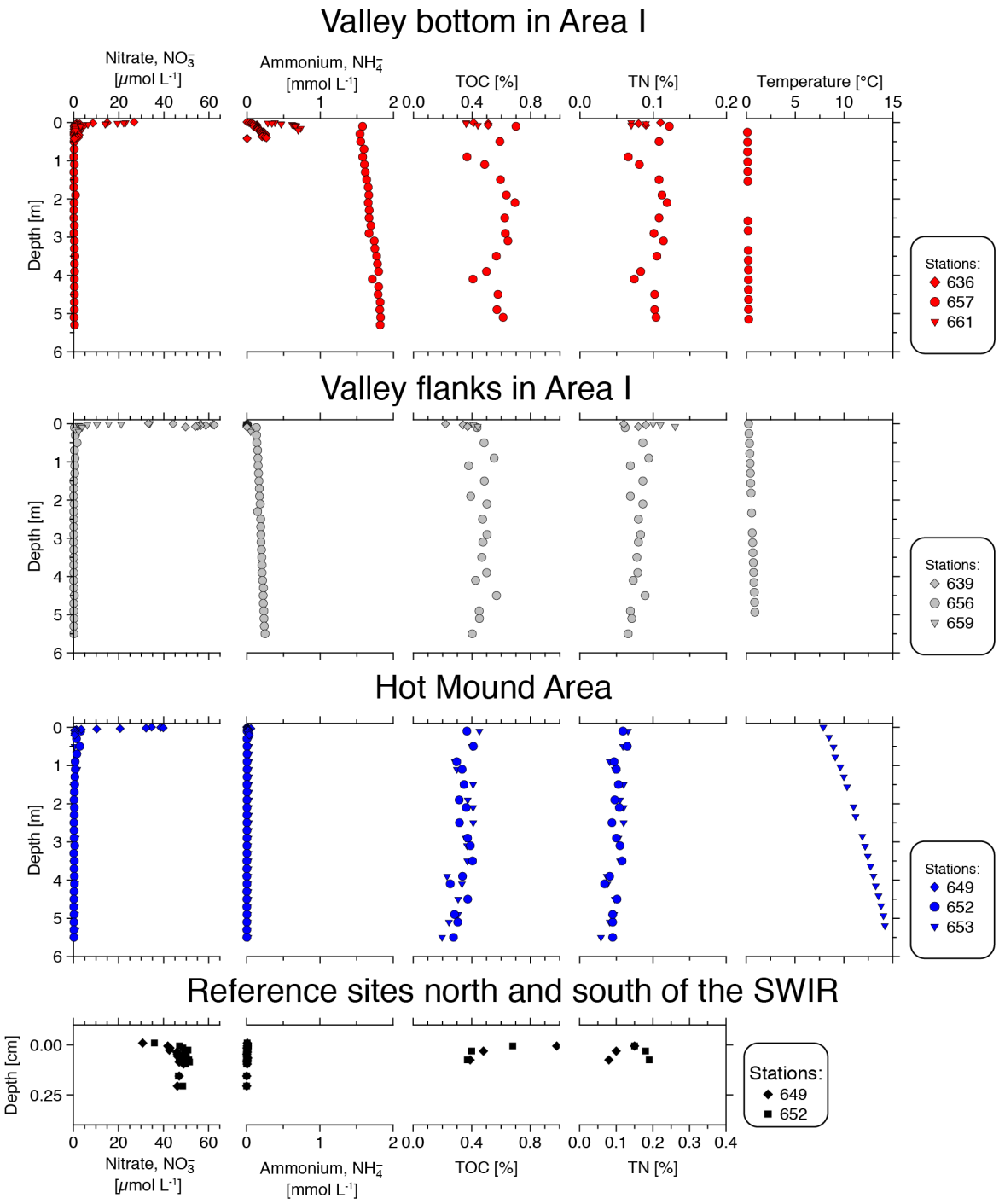

Figure 7.6 . Sediment geochemistry results from different survey areas, part 1. Coring sites are plotted in Figures 4 and 5. Note, TOC is total organic carbon, TN is total organic nitrogen.

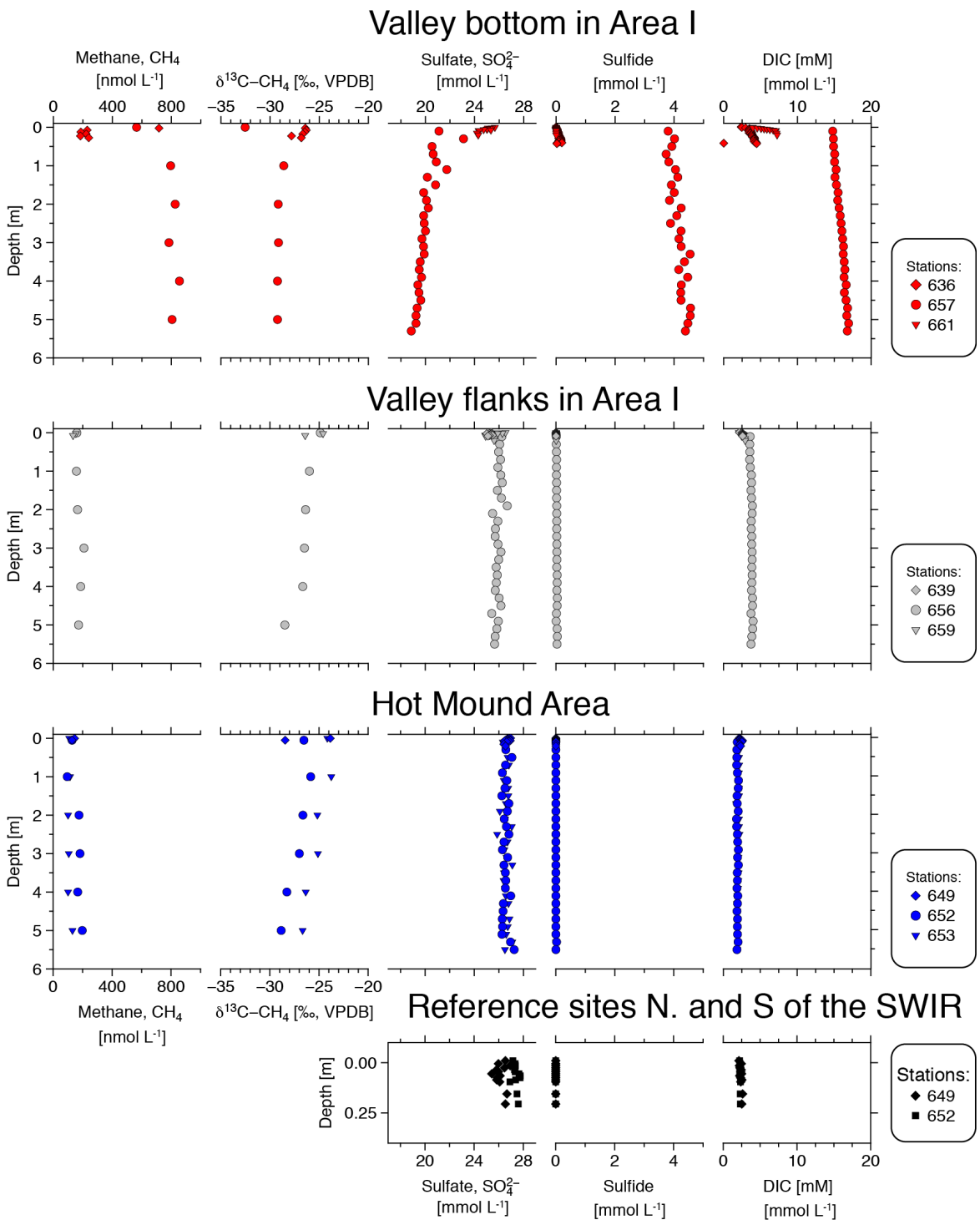

Figure 7.7 Sediment geochemistry results from different survey areas, part 1. Coring sites are plotted in Figures 4 and 5. Note, DIC is dissolved inorganic carbon.

Diffusive flux rates are listed in Table 7.3. Strongest fluxes of sulfide, DIC, ammonium and nitrate were observed in at the Vesicomyid site (core MUC636). Weaker fluxes of sulfate, sulfide, DIC, ammonium and nitrate were observed in cores GC657/MUC661. A weak upwards flux of ammonium was also observed in core GC656. Generally, nitrate flux into the sediment was observed at the majority of sites inside the axial valley (MUC636, MUC659, MUC661) but not at the reference sites (MUC628, MUC681). Fluxes were not stoichiometrically balanced according to Redfield ratios, indicating non-steady state situations in the valley sediments.

Core	**Constituent**	**Average porosity**	**Ds [m^2 a^{-1}]**	**Diff. flux rate [mmol m^{-2} a^{-1}]**	**Flux direction**
		Valley bottom	Area I		
636	Sulfide	0.94	$2.59 \cdot 10^{-2}$	10.06	Up
636	DIC	0.94	$1.37 \cdot 10^{-2}$	32.84	Up
636	Ammonium	0.94	$2.59 \cdot 10^{-2}$	14.72	Up
636	Nitrate	0.94	$2.58 \cdot 10^{-2}$	-17.38	Down (upper 3.5 cm)
657	Sulfate	0.90	$1.33 \cdot 10^{-2}$	-4.28	Down
657	Sulfide	0.90	$2.54 \cdot 10^{-2}$	0.84	Up
657	DIC	0.90	$1.38 \cdot 10^{-2}$	5.77	Up
657	Ammonium	0.90	$2.58 \cdot 10^{-2}$	1.64	Up
661	Nitrate	0.99	$2.58 \cdot 10^{-2}$	-8.76	Down (upper 5.5 cm)
		Valley flanks	Area I		
656	Sulfate	0.87	$1.33 \cdot 10^{-2}$	-1.27	Down
656	Ammonium	0.87	$2.58 \cdot 10^{-2}$	1.04	Up
659	Nitrate	0.95	$2.58 \cdot 10^{-2}$	-14.76	Down (upper 5.0 cm)

Table 7.3 Diffusive flux rates of various geochemical constituents in the key areas investigated.

We did not detect a correlation between the local heat flow values and the fluxes of geochemical constituents. The geochemical profiles at the valley bottom in Area I (cores MUC636, GC657 and MUC661) showed anomalously high fluxes of several reduced constituents, which is in contrast to the very low heat flow at the axial valley bottom in Area I (Figure 7.4). The opposite is observed in the Hot Mound Area. There, the heat flow is exceptionally high, but geochemical fluxes (cores MUC649, GC652, GC653) did not show noticeable anomalies (Figures 7.6 and 7.7).

7.4.5 Microbial Cell Abundance and Activity in Surficial Sediments

The number of microbial cells and microbial activity in surficial sediments are plotted against their geographic distribution and water depth in Figure 7.8. The total cell number in the sediment given by the AODC (acridine orange direct counts) ranged between 0.24 10^9 and 1.4 10^9. Highest numbers were detected at the northern reference site (MUC681) and slightly lower in the axial valley. Surprisingly, the lowest cell numbers were found at the site of the Vesicomyid discovery, station MUC636. The CARD-FISH efficiency is in a similar range at all sites ranging from 43 % to 67 % and the number of active cells showed the same pattern as the AODC results. Rates of dark carbon fixation (DCF) showed only minor variations between individual sampling sites with a slight decrease at the stations on and near the axial valley walls (MUC639, MUC659). The microbial activity per cell was highest at station MUC363 (0.2 fmol C cell d^{-1}) as the fraction of active cells was lowest there, but the DCF rates were very similar to those at the other sites. In the water column the DCF rates ranged between 0.07 and 2.66 μmol C m^{-3} d^{-1} and were highest in Area I at 3635 m (CTD631).

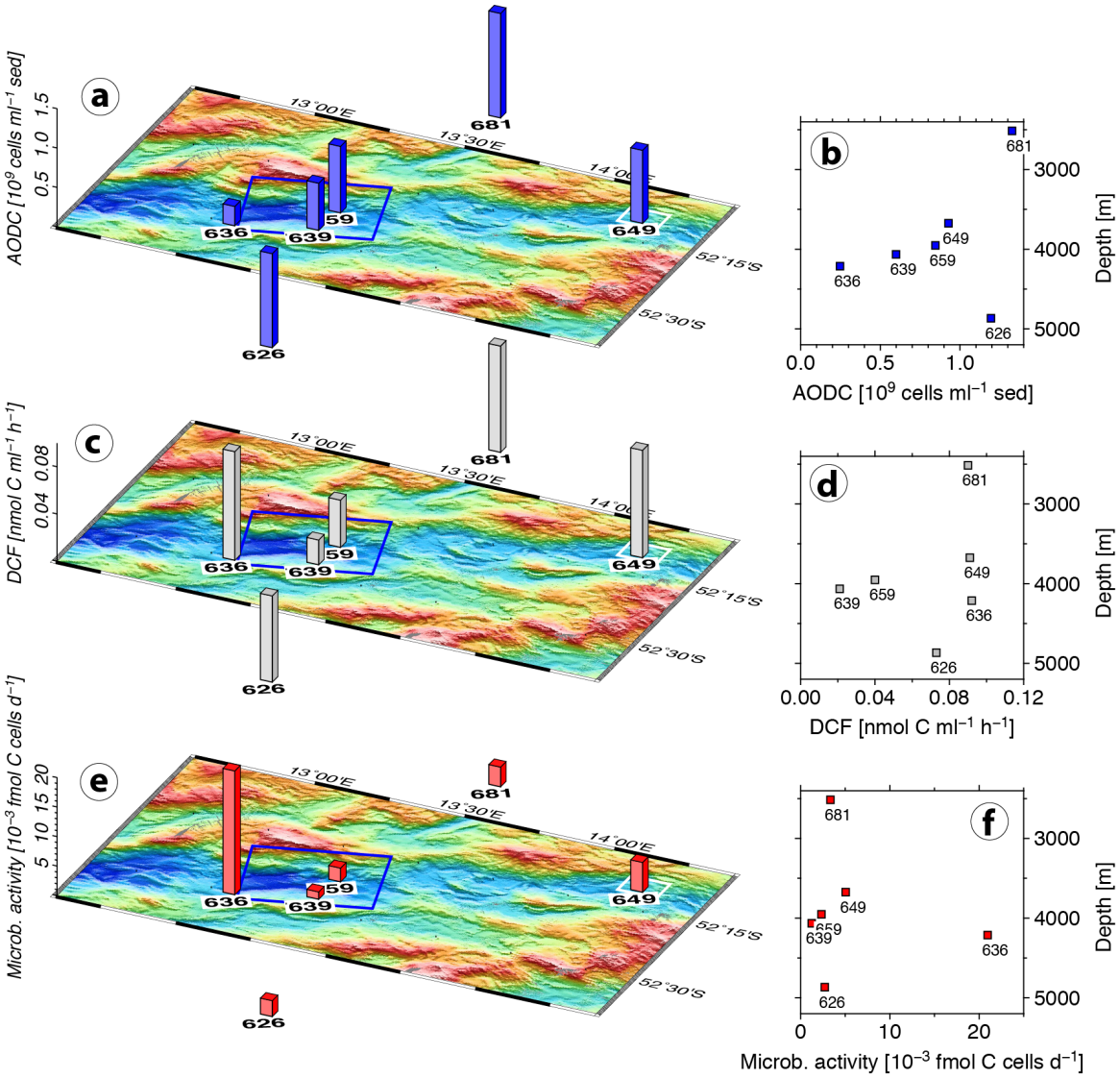

Figure 7.8 Microbial activity and cell numbers in the uppermost sediment layer inside and outside the axial valley. Vertical bars on maps a,c,e show the geographic distribution of cell numbers (AODC), DCF and normalized microbial activity. Rectangles and indicate survey Area I (blue) and Hot Mound Area (white). Panels b,d,f show microbiological parameters against the depth of sampling sites. MUC sites 626 and 681 are reference stations outside the axial valley North (MUC681) and South (MUC626). Their positions on the maps a,c,e are shifted towards the axial valley and do not represent actual sample locations. True geographical locations are given in Supporting Information Table S2

7.4.6 Plume signatures: Turbidity, dissolved Methane, δ^3He and TdMn in the Axial Valley Waters

Twelve hydrographic casts and transects (Towyo stations) with the CTD rosette and attached MAPRs were dedicated to the search for physicochemical signatures of hydrothermal plumes in the SWIR axial valley between 13°-15°15'E, with the purpose to relocate previous turbidity plume observations (*Bach et al.*, 2002). The surveys included those sites where heat flow and OFOS observations indicated the potential presence of hydrothermal anomalies. No unambiguous hydrothermal anomaly was detected in any of the CTD stations. Turbidity anomalies were found in several of the CTD-transects, especially in Area I and in the Hot Mound Area (Figure 7.9). In particular near the seafloor, these turbidity anomalies coincided with the location of cloud-like, particle-rich features in the water column seen during the OFOS camera dives (Figures 7.5). These turbidity signals were found close to the bottom, but also at 500-700 m above the valley floor (Figure 7.9).

Water samples for methane and noble gas analysis were taken throughout the water column on seven CTD transects (CTD614, CTD228, CTD629, CTD631, CTD638, CTD648 and CTD651; Figures 9 and 10), including several of the turbidity plumes. For the remainder of the text we consider all water masses as inside the axial valley that are deeper than 2500 m, i.e. below the crests of the axial valley walls (Figure 7.10a). Dissolved methane concentrations were successfully analyzed in 123 samples and ranged between 0.4 and 5.3 nmol L^{-1}. Low concentrations of 0.4-1.0 nmol L^{-1} occured in all water masses below 500 m depth and likely represented the regional background. Slightly increased methane concentrations were observed in the uppermost 500 m due to gas exchange with the atmosphere. Elevated concentrations of $>$ 4 nmol L^{-1} were exclusively found below 200 m depth, thus inside the axial valley (Figure 7.9).

The majority of water samples for methane analysis in Area I and the Hot Mound Area were taken in the layers of elevated turbidity (Figure 7.9). In Area I elevated methane concentrations of 2.0-4.5 nmol L^{-1} were found in the 3300-3800 m depth layer (500-700m above the valley floor) that also showed the highest turbidity (Figure 7.9a). However, within this layer also background concentrations (of 1–2 nmol L^{-1}) were found, suggesting a patchy distribution. In the Hot Mound Area we observed methane concentrations up to 5.5 nmol L^{-1} at depths between 3300 and 3700 m. The methane-enriched layer lay immediately above the rugged valley floor and coincides with highly turbid waters (Figure 7.9e,f). Three samples from the turbid bottom waters in the Hot Mound Area (CTD651; Figure 7.9f) showed methane carbon isotopic ratios (δ^{13}C-CH4) of -33.7, -33.7, -34.2 ‰ overlapping with porewater signatures and representing relatively heavy values indicative of partially abiotic sources (*Etiope and Sherwood Lollar*, 2013, Supporting Information Figure 7.13).

Noble gases were successfully analyzed in 78 water samples. δ^3He values in the survey area ranged from -2% to 12% (Figure 7.10c); the negative anomaly at the surface represents the local equilibrium value due to air-sea gas exchange. Below 500 m depth δ^3He values scatter in the range of 7% - 12% but did not show a trend with depth.

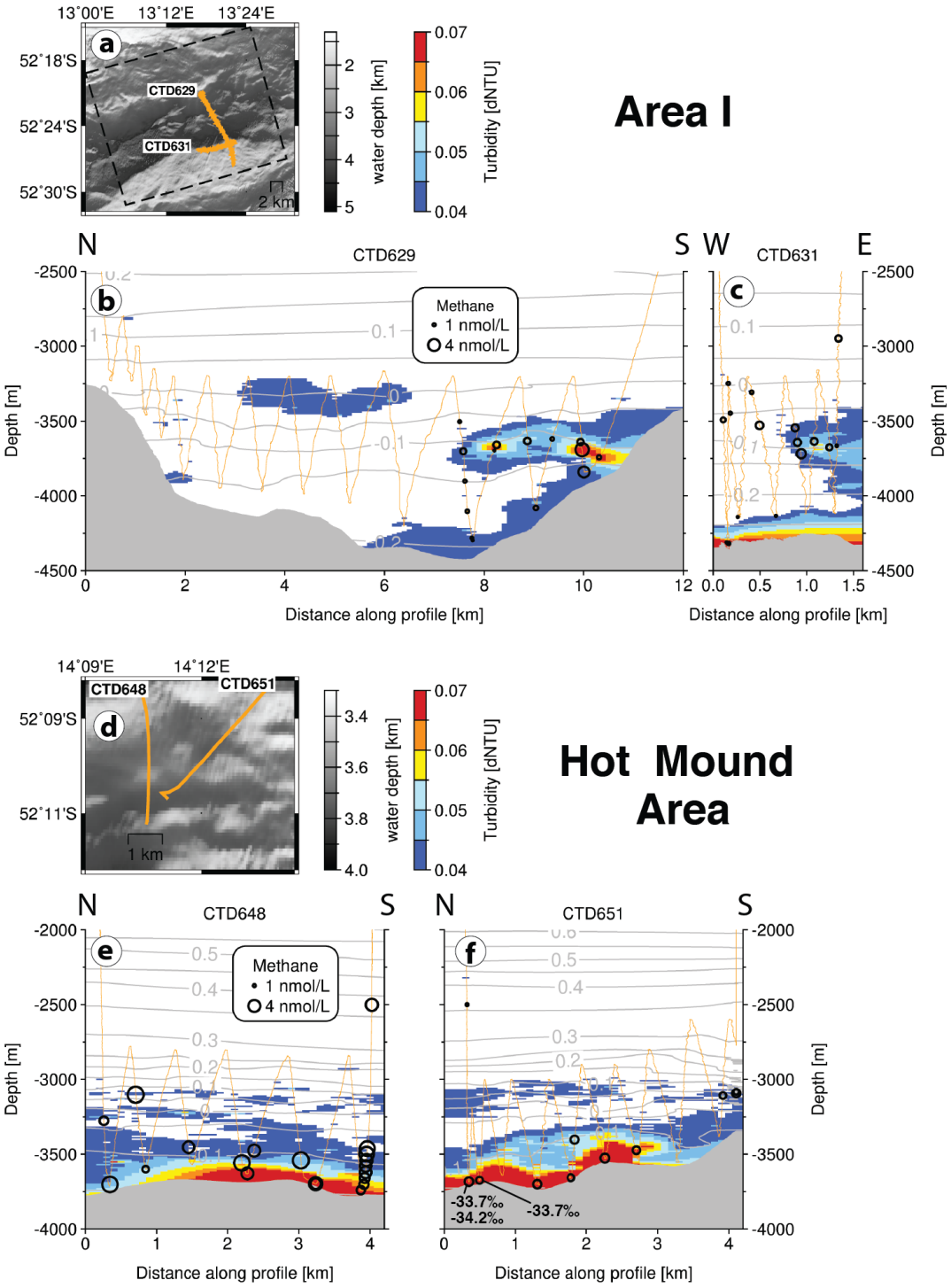

Figure 7.9 CTD-transects with dissolved methane (black circles, scaling with concentration) and contours of turbidity and temperature. Panels a-c represent stations in Area I and panels d-f in the Hot Mound Area. Note, that thin orange lines show CTD path in the water column and gray lines show contours of potential temperature [°C] at an interval of 0.05 °C. Regions of location maps are identical to Figure 7.4a (panel a) and Figure 7.5a (panel d).

δ^3He values and methane concentrations did not correlate (Figure 7.10d). Total dissolve manganese (TdMn) was measured in 40 water samples, 13 of which showed concentrations below the detection limit. TdMn concentrations (Figure 7.10e) ranged between 0.0 and 3.8 nmol L^{-1} and did not correlate with methane concentrations from the same bottles.

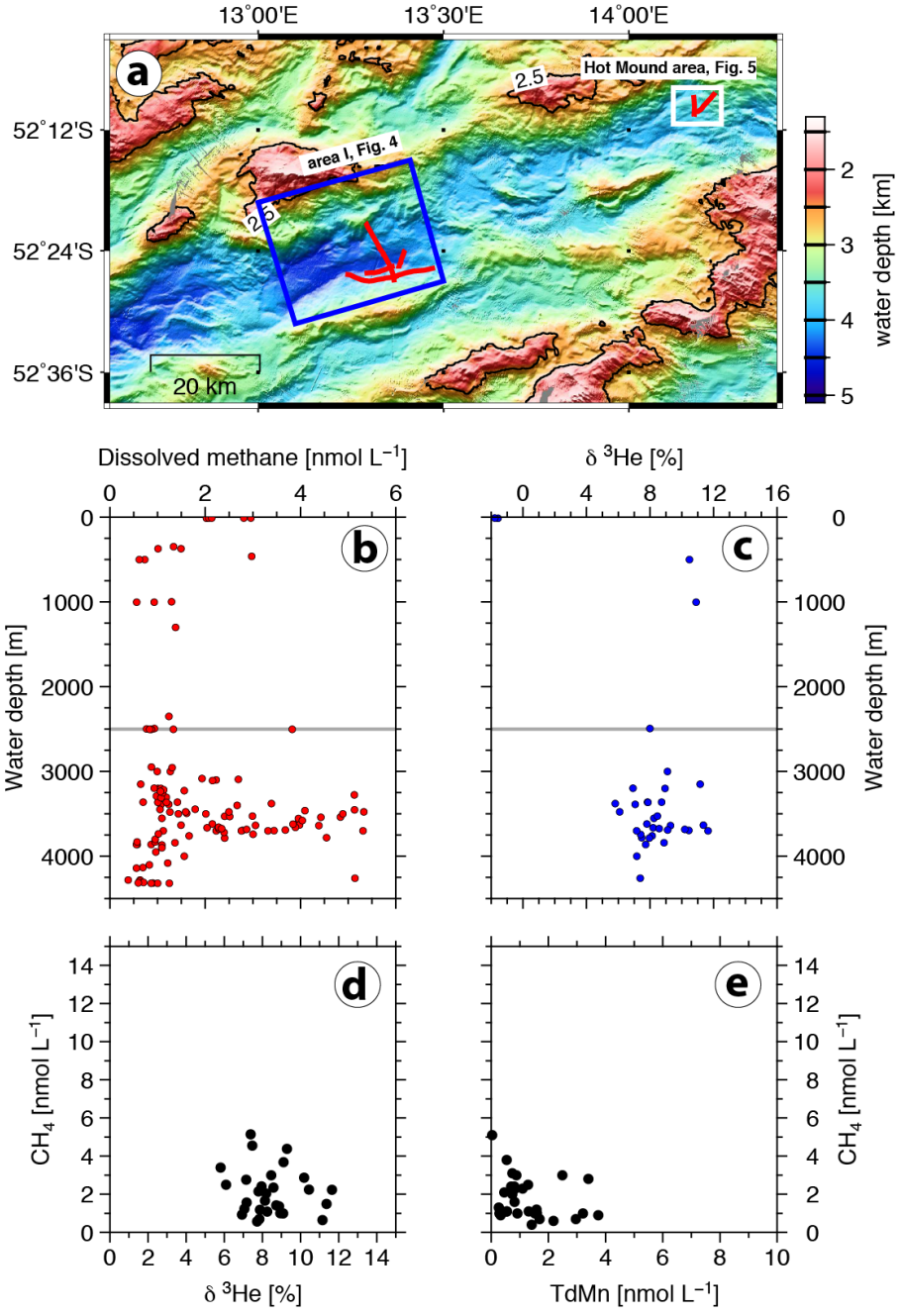

Figure 7.10 a) Map with all CTD towyo transects as red track-lines. The black 2500 m depth contour line corresponds to gray horizontal lines in plots b and c. b) Concentrations of dissolved methane from all transects. c) δ^3He values from all transects in the study area. Map region is identical to Figure 7.1b. d) Methane versus δ^3He for samples below 2500 m water depth. e) Plot of methane versus total dissolved manganese.

7.5 Discussion

The main objectives of this study were to explore the relations between the geological modes of deformation and the geochemical fluxes and microbial activity in the axial rift valley of the magma-starved SWIR Oblique Supersegment and to identify if there is active hydrothermal venting.

7.5.1 Thermal structure and heat fluxes

The brittle-ductile transition (BDT) in the earth lithosphere is mainly controlled by temperature (e.g. *Burov*, 2011; *McKenzie et al.*, 2005) making it a viable temperature proxy in seismically active regions. A classic approach of constraining the BDT merely considers the maximum depth of hypocenters. This may for short time periods (days to months) not necessarily resemble the long-term BDT (*Key et al.*, 2011). Constructing yield-strength envelopes (YSE) from depth-frequency distributions of earthquakes (DFDE) that cover an extended time span (months to years) of background seismicity represent a more robust approach of constraining the BDT (Figure 7.2). The depth distribution of earthquakes already suggested an along axis transition from a deeper BDT and lower geothermal gradient in Area I towards a shallower BDT and a steeper geothermal gradient in Area II. The difference in BDT depth wass confirmed by our YSE results (Figure 7.2). Very low inferred thermal gradients in areas I and II supported the presence of an unusually thick and cold axial lithosphere at the Oblique Supersegment (*Schlindwein and Schmid*, 2016; *Schmid and Schlindwein*, 2016).
Observed heat flow values of 15-20 mW m^{-2} at the valley bottom in Area I (Figures 7.1d, 7.4) fall below the regional average estimated from YSE thermal gradients. Similarly low - and even negative - values were found in the Sparsely Magmatic Zone of the Gakkel Ridge, Central Arctic (*Urlaub et al.*, 2010). The Gakkel Ridge also spreads at ultraslow rates and is characterized by a very low magma budget (*Dick et al.*, 2003). *Urlaub et al.* (2010) interpreted the negative heat flow values as an effect of downwelling hydrothermal fluids. Accordingly, we suggest the very low heat flow values at the valley bottom in Area I may also be an effect of cold seawater intruding into the lithosphere. Variations in the BDT depth along the ridge axis do not directly correlate with heat flow at the seafloor (Figure 7.1d). The seafloor heat flow is more variable, which is typical for very young and unsealed oceanic lithosphere (*Hasterok et al.*, 2011), suggesting it is likely affected by localized hydrothermal and/or magmatic processes. The marked variability in seafloor heat flow values became particularly evident in the results from the northern valley flank in Area I (Figure 7.4) and the Hot Mound Area (Figure 7.5). At the northern valley flank in Area I the heat flow slightly exceeded the regional average estimated from YSE thermal gradients and strongly varied between individual penetrations. Considering the proximity to scarps of potentially active faults, we suggest slow upward migration of fluids along these faults was a possible cause of the elevated heat flow. In the Hot Mound Area the pronounced thermal gradient of 1.194 K m^{-1} and the enhanced heat flow of 848 mW m^{-2} pointed to a local heat source that was not deeper than a few hundred meters to 1 km.

Considering the exposure of basalts east and west of the Hot Mound Area (Figure 7.1a) a magmatic intrusion as heat source cannot be ruled out. However, we did not have microearthquake data from this region or further knowledge about the structure of the underlying lithosphere. The convex geothermal gradient indicated a slow upward advection of fluids but the geochemical profiles from nearby sediment cores (sites MUC649, GC652, GC653; Figure 7.6) did not reveal any anomalies indicative of fluids that have reacted with a hot intrusion. However, the estimated fluid advection of 250 mm a^{-1} was sluggish compared to similar settings (e.g. *Taniguchi et al.*, 2003). We cannot constrain the ultimate source of the thermal anomaly but a deep-rooted circulation, that would bring metal-rich fluids back to the surface, appears unlikely. Instead a shallower heat source is conceivable, possibly an incipient magmatic intrusion that was not in contact with the advecting fluids.

7.5.2 Biogeochemical Processes in Axial Valley Sediments

The SWIR is located in a region with relatively high sedimentation rates of 1-30 cm ka^{-1} in the last 200,000 years (*Mackensen et al.*, 2001; *Nürnberg et al.*, 1997). Accordingly, RV Polarstern's sub-bottom profiler showed sediments with a thickness of 80 m and possibly more at the axial valley bottom (Figure 7.4d and Supporting Information Figure 7.12). Sediments of such thickness are unusual for most active MORs, where the accretion of new seafloor typically outpaces sediment deposition. The unusually high sediment load with the associated accumulation of organic matter (OM) overlying a peridotitic lithosphere that is prone to serpentinization define an unusual geological setting in which the geochemical signatures are influenced from above and below. To our knowledge a similar MOR setting is only described for the ultraslow spreading Knipovich Ridge in the Arctic (*Johnson et al.*, 2015).

The profiles of decreasing nitrate concentrations indicated that oxygen is rapidly consumed and did not penetrate into the axial valley sediments deeper than ~10 cm. Nitrate profiles from the reference stations north and south of the SWIR indicated oxygen penetration to 20 cm and possibly deeper (Figure 7.4). The observed anomalies in DIC, ammonium, phosphate, sulfate and sulfide fluxes at the valley bottom of Area I (Figures 6 and 7; cores GC657 and MUC636) suggested non-steady state diagenetic processes down to > 50 m below the seafloor. However, neither the TOC content nor the ammonium to DIC flux ratio (0.45) nor the microbial activities and abundances supported substantially higher OM degradation in the topmost layer of the valley bottom, compared to the reference sites, ~300 km away from the SWIR (Figures 6 and 8).

Conversely, the elevated TOC content at the valley bottom in Area I (~0.6% in core GC657; Figures 6) suggested enhanced OM accumulation in the subsurface anoxic layers, which reduces remineralization and enhances OM burial. The linear decrease of manganese and sulfate in GC657 gives evidence that most of the OM remineralization occurs below the sampled depth interval. Extrapolating the profile of sulfate concentrations in core GC657 to greater depth suggested depletion at roughly 50 m below the surface.

Similar sulfate profiles and depletion depths at 10-88 m were reported for ocean margin sites with low OM input and where anaerobic oxidation of methane (AOM) occurs (e.g. *D'Hondt et al.*, 2004). We hypothesize that AOM is at least partially responsible for the consumption of upwards migrating methane and for the production of sulfide in the axial valley sediments, also explaining the slightly heavier carbon isotopic values with decreasing sediment depth. The enhanced OM accumulation at the bottom of the axial valley in Area I and the presence of serpentinization in the underlying lithosphere can both support the presence of methane below the sulfate depletion depth (approx. 50 m below the seafloor).

The YSE results suggested that the valley bounding faults are weakened by serpentinization, leading us to propose that the fault outcropping near MUC636 (Figure 7.4a) marks a potential outflux zone of serpentinization related fluids. In this regard the occurrence of the highest flux rates at MUC636 are of particular interest (Figure 7.4, Table 3). There, the flux rates were 5 to 10 times higher compared to the other sites, and they were accompanied by the presence of a Vesicomyid bivalve and the highest per-cell microbial activity (Figure 7.8), likely due to the elevated availability of electron donors (ammonium, manganese, sulfide) for autotrophy. The lack of methane at this site supports the hypothesis that AOM plays a role in removing serpentinization-derived methane escaping the underlying lithosphere.

7.5.3 Origin of the Methane Plume and the Turbidity clouds in the Axial Valley

None of the CTD stations in the survey area showed an anomaly in the redox potential. Water samples from the axial valley had δ^3He values of 5.5-12% and TdMn concentrations from less than detectable to 3.8 nmol L^{-1}. Both values were considerably lower than in regions with fresh hydrothermal plumes (*Keir et al.*, 2006, 2009) and we did not find constant CH_4/δ^3He and CH_4/TdMn ratios (Figure 7.10), which would be typical for hydrothermal plumes (e.g. *Kawagucci et al.*, 2008; *Keir et al.*, 2008). These findings indicate that we did not detect an active high-temperature hydrothermal vent field at the surveyed section of the SWIR Oblique Supersegment. The turbidity anomalies detected in the axial valley (Figure 7.9) did not correlate with other chemical signatures of fresh hydrothermal discharge (i.e. elevated ^{3}He and TdMn values) implying that they very likely did not originate from hydrothermal plumes. This interpretation is in contrast to the earlier work of *Bach et al.* (2002), in which optical backscatter anomalies were presented as tentative indications of active hydrothermalism in this region.

However, the widespread occurrence of elevated methane concentrations, up to 5.5 nmol L^{-1} in Area I and the Hot Mound Area (Figures 7.9 and 7.10), imply that a source of significant methane discharge must exist. Here, we discuss possible sources of this methane and the turbidity clouds in the axial valley waters (Figures 5,9 and 10). Methane plumes of similar peak concentrations and thicknesses were found in the axial valleys of the Mid-Atlantic Ridge (e.g. *Keir*, 2010; *Konn et al.*, 2015) and the ultraslow Knipovich Ridge (*Connelly et al.*, 2007).

In those locations a hydrothermal origin and transport of the methane in hydrothermal plumes was obvious, unlike in our case. The potential presence of AOM in the axial valley bottom sediments requires the existence of elevated methane concentrations below the sulfate-methane-transition-zone (*Niewöhner et al.*, 1998). This methane – regardless of whether it comes from the lithosphere or is produced microbial in deeper sediment strata – is mostly consumed before it reaches the seafloor. Wherever a sediment cover is present and the methane flux is comparably small it does not escape into the water column. Thus, to enable methane flux from the lithosphere into the ocean a site of focused discharge is required.
Abiotic methane production is of great importance for the ultramafic-hosted hydrothermal systems at the Mid-Atlantic Ridge (*Konn et al.*, 2015; *Proskurowski et al.*, 2008). Depending on the carbon source, abiotic methane has a typical δ^{13}C signature of -17.8‰ to -6.1‰ (*Konn et al.*, 2015), which is heavier than methane produced by methanogenesis (δ^{13}C < -42‰) or thermogenesis (δ^{13}C < -20‰ *Whiticar*, 1999). δ^{13}C-CH4 values in the porewaters and water column above the Hot Mound Area (Figure 7.9, lower panel) range between -34.17‰ and -23.76‰ which is slightly lighter than in typical abiotic sources (Supporting Information Figure 7.13 *Konn et al.*, 2015). Perhaps, this is the result of mixing abiotic methane with minor amounts of microbial methane. We propose that serpentinization at temperatures too low for notable Mn mobilization is the most likely cause of the primarily abiotic methane in the water column. Thus, seawater-peridotite interactions in active faults are the most viable source of the methane plume in the axial valley.

The turbidity anomalies found in most of the CTD-transects (Figure 7.9), also reported by *Bach et al.* (2002), are caused by clouds of floating particles that were seen in several OFOS dives (Figure 7.5d and Supporting Information Figure 7.14). When we the near-bottom turbidity anomaly at the southern end of CTD629 transect (Figure 7.9; 3790 m) with the OFOS cameras, we located a cloud of visible particles seen in an OFOS dive (Supporting Information Figure 7.14). The most likely cause of the particle clouds is the re-suspension of sediment from the steep valley flanks. This is supported by the observation of only a thin or absent sediment cover on the steep valley flanks during several OFOS dives. The sediment re-suspension may be triggered by dense and cold Antarctic Bottom Waters overflowing the SWIR from the South (e.g. *Hallberg and Gnanadesikan*, 2006) and/or occasional mud slides from the steep flanks. Seafloor temperature time series (Supporting Information Figure 7.15) showed only weak temperature changes at the valley bottom in Area I but a higher variability at shallower locations. This supports the hypothesis that pulses of cold, dense Antarctic Bottom Water overflow the SWIR axis from the south, capable of re-suspending unconsolidated sediments from the valley flanks. However, the detailed origin of the particle clouds cannot be resolved by our dataset.

7.5.4 Links of Seafloor Biogeochemical Processes to the Lithospheric Structure

The YSE results indicated a rheologically weak upper lithosphere down to 18 km in Area I that is best explained by serpentinization to these depths (Figure 7.3). The seafloor morphology in this area revealed a large fault block to the south and tiered fault blocks to the north of the axial valley. The faults that decouple the axial valley floor from the walls are clearly visible in the bathymetry (Figure 7.4) and are presumably active, although this cannot be proved due to their aseismic behavior. We propose a mode of deformation were these entirely aseismic boundary faults reach down to the zone of microearthquake activity and accommodate most of the plate separation (Figure 7.11).

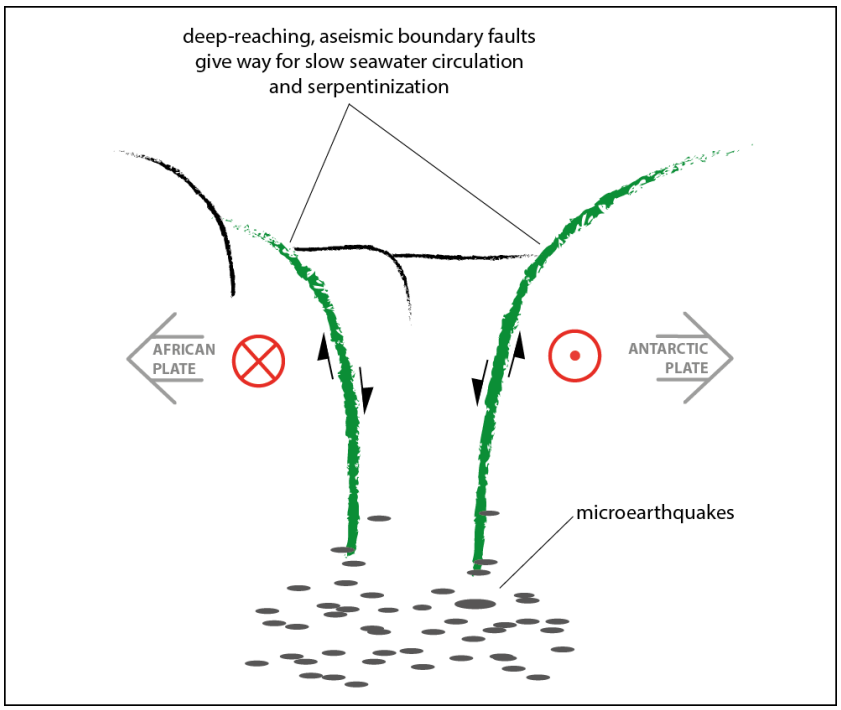

Figure 7.11 Cartoon illustrating the inferred mode deformation accommodating the plate separation in Area I. Red circles indicate dilation into the plane (cross) and out of the plane (point) due to transtensional tectonics.

Enhanced fluxes of sulfide, DIC and ammonium were observed in MUC636 close to the southern boundary fault scarp in Area I and a slightly increased heat flow was observed near the northern axial valley wall (Figure 7.4). Further, the source of the methane plume in the axial valley waters is most likely produced by abiotic methane from low-temperature serpentinization. We propose that active boundary faults represent the primary reaction zone of serpentinization in Area I (Figure 7.11) and discharge sites of serpentinization related fluids are most likely found in proximity to scarps of these faults. In order to maintain the fluid flux and ongoing serpentinization, the boundary faults need to remain active as inactive faults in MOR environments soon become impermeable (*Michibayashi et al.*, 2008).

7.6 Conclusions

1. The SWIR Oblique Supersegment constitutes a very special setting for the investigation of tectonic, hydrothermal and geochemical processes due to an exceptionally deep axial valley that acts as a collector for sediments rich in organic matter and due to the extremely slow opening rates as a result of the high obliquity. The unusually thick and cold axial lithosphere appears to deform in an aseismic mode down to 18 km depth. This weak upper lithosphere can only be explained by incorporating serpentinization down to 18 km in Area I and 8 km in Area II into the calculation of rheological strength profiles.

2. The prevalent mode of deformation and slow fluid circulation is essentially tied to deep reaching aseismic boundary faults that accommodate most of the plate separation.

3. Based on the lack of δ^3He anomalies, an active high-temperature hydrothermal system within the surveyed area of the Oblique Supersegment appears unlikely and the methane-enriched waters may originate from undisclosed faulting-related sources. Nevertheless, ancient sulfide deposits (*Bach et al.*, 2002) document the hydrothermal potential of this SWIR segment in the past.

4. Elevated temperatures at the axial valley floor and slow advective fluxes, as observed in the Hot Mound Area, do not necessary come along with the discharge of fluids enriched in methane, nutrients or metals.

5. Biogeochemical fluxes in the axial valley, in particular in its deepest part, are predominantly influenced by the accumulation and subsequent remineralization of organic matter. Hydrothermalism may have a minor contribution in proximity to boundary faults as documented by increasing flux rates towards fault scarps and the occurrence of a Vesicomyid bivalve. A major portion of the methane - potentially of abiotic origin - that escapes the lithosphere in the axial valley is likely consumed by anaerobic oxidation of methane in the sediments.

This study presented a first of its kind multidisciplinary dataset for a magma-starved ultraslow spreading segment. Future research is necessary to quantify the individual contributions of geochemical fluxes originating from deep circulation through active boundary faults and those entirely related to organic matter deposition and remineralization in the axial valleys of ultraslow mid-ocean ridges.

7.7 Acknowledgements

We are grateful to the captains and crews of RV Polarstern expeditions ANT-XXIX/2 and ANT-XXIX/8. OBS were provided by the AWI DEPAS instrument pool. We thank S. Galkin for the taxonomic description of the Vesicomyid bivalve and acknowledge G. Wegener for commenting an earlier manuscript version. We thank Patrick Monien, University of Bremen, for conducting the measurements of TdMn. Earthquake, heat flow and geochemistry data are available from the Pangaea data publisher (www.pangaea.de) and can be found searching for cruise ANT-XXIX/8. This study was funded through the DFG Emmy-Noether Program via grant #Schl.853/1-1 and the ERC via grant Abyss (#294757). Maps and graphs were created with the GMT software (*Wessel et al.*, 2013).

7.8 Supporting information

Text S1 explains how we estimated the best fit of the depth-frequency distribution of earthquakes (DFDE) and the yield-strength envelope (YSE). Text S2 provides additional details on laboratory procedure used the estimate the DCF rates. Figure S1 shows a data example of sediment echogram from the axial rift valley. Figure S2 shows the carbon istopic signature of methane in the porewater and valley water in relation to literature data. Figure S3 shows a selection OFOS images from valley bottom and flanks in Area I. Figure S4 shows time series of bottom water temperatures at the SWIR Oblique Supersegment. Table S1 presents least squares misfits of DFDEs and YSEs for different rock parameters applied. Table S2 presents the results of dark CO_2 fixation (DCF) rates in the axial waters.

7.8.1 Supporting Information texts

Text S1 Comment on how the standard deviation between the DFDEs and YSEs was calculated
We calculated the least-squares misfit S between the YSE and the DFDE to identify the set of input parameters yielding the best fit of both curves,

$$S = \sqrt{\frac{1}{N}\sum_{i=1}^{i=N}(x_i - y_i)^2} \tag{7.6}$$

Here N is the total number of depth levels i, x is the normalized frequency of earthquakes and y the normalized yield-strength. Calculated standard deviations for different rock parameter in the ductile domain are listed in table S1 below.

Text S2 Further methodical details on the estimation of dark CO_2 fixation (DCF) rates.
Total microbial activity was estimated by inorganic carbon up-take. Dark CO_2 fixation (DCF) rates were estimated following the procedure of *Molari and Manini* (2012) including some modifications. 1 ml of slurry (1:1 mixture of sediment and filtrated 0.22-μm seawater) was incubated with 12 μl ^{14}C-labeled sodium bicarbonate (0.25 mCi ml^{-1}, final activity 3 μCi).

The samples were incubated at in situ temperature (2-4°C) in the dark. After 12 hours the incubations were stopped with 1 ml formaldehyde in seawater (final concentration 2%) and stored at 4°C on board. Controls were killed with 1 ml formaldehyde in seawater before addition of the tracer. The samples were then centrifuged at 12,000 rpm for 5 min., the supernatant was discarded, and remaining sediment pellet was washed 3 times with 1x PBS. The pellet was then resuspended with 1 ml 3 M HCl and transferred into a new 50 ml vial. 500 μl 3 M HCl was then used to wash and transfer the remains into the new tube. The 50 ml tube with the sediments was then mixed constantly by bubbling with pressurized air for 4 h. 8 ml of the Scintillation cocktail Ultima Gold^{TM} was then added and the mixed sample was centrifuged at 3,500 rpm for 30 min. The supernatant was transferred into a 20 ml scintillation vial and the pellet was resuspended in 8 ml Ultima Gold^{TM} and centrifuged a second time. The supernatants were combined and measured with a liquid scintillation counter for max. 10 min. The DPM were converted in moles of inorganic carbon incorporated per unit of sediment volume and time using the formula described by *Molari et al.* (2013).

For the water column samples 40 ml of seawater were collected directly from Niskin bottle with 50 ml plastic syringes and ^{14}C-labeled sodium bicarbonate were injected (final activity of 1 μCi ml^{-1}) within 30 min after the recovery of CTD. For each Niskin bottle the samples were processed in three live replicates and two formaldehyde killed samples (2% final concentration). The samples were incubated at in situ temperature in the dark for 24 hours and then stopped with formaldehyde (2% final concentration). The samples were then processed on board as described by *Herndl et al.* (2005).

7.8.2 Supporting Information figures

7.8.3 Supporting Information Tables

Rock type	***S* (Area I)**	**S (Area II)**
Dry dunit (*Hirth and Kohlstedt*, 1996)	3.7	3.4
Wet olivine (*Hirth and Kohlstedt*, 1996)	2.0	3.3
Dry olivine (*Evans and Kohlstedt*, 1995)	3.7	7.9
Wet olivine (*Chopra and Paterson*, 1981)	2.1	3.3

Table 7.4 Least squares misfit *S* of YSE and DFDE for different compositional parameters in the ductile domain. Note that the same serpentinization depth is used but the geothermal gradients are individually adjusted for each composition.

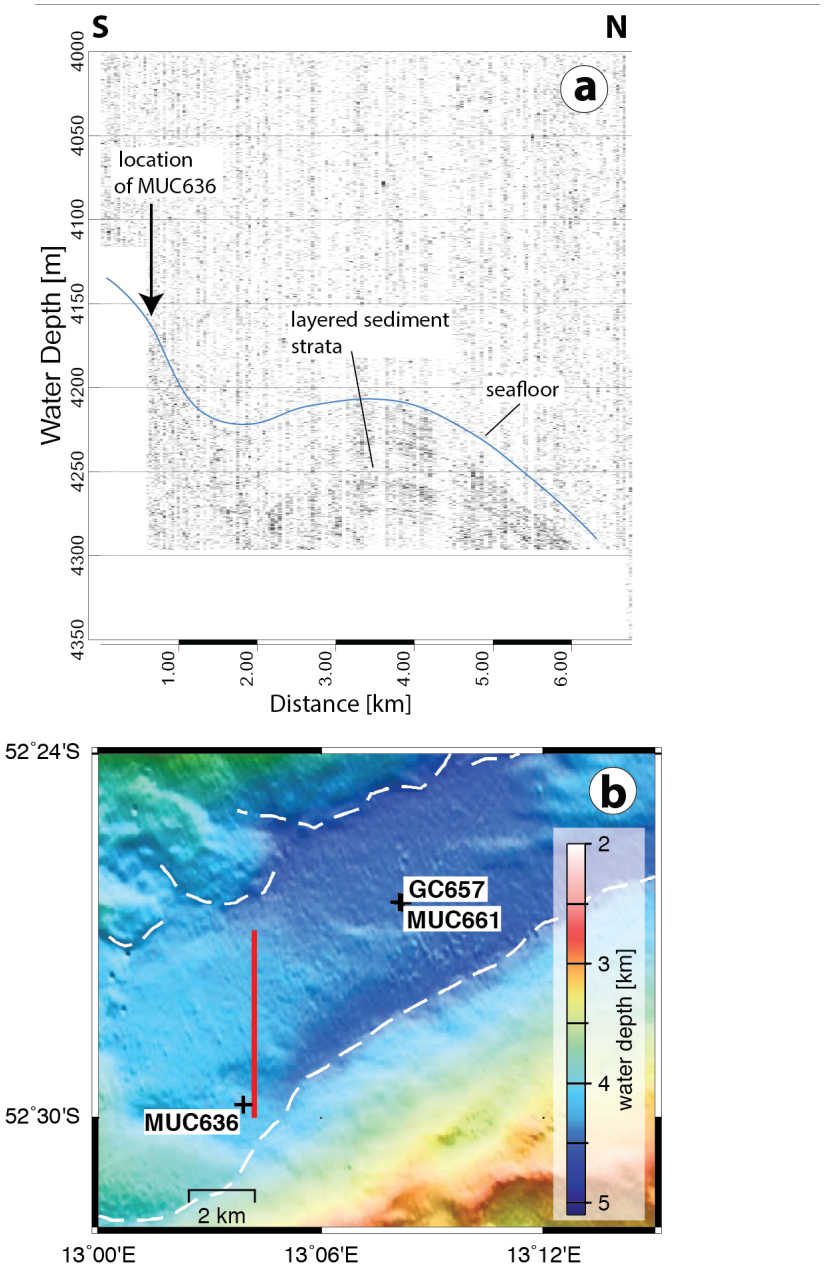

Figure 7.12 a) Data example of the Parasound sediment-echosounder from the axial valley in Area I. Note that the time window of recorded data terminates 4300 m depth. b) Bathymetry map with red line showing the location of the above data example, crosses showing the location of sediment cores and dashed white lines outlining potential fault scarps of the inner rift valley.

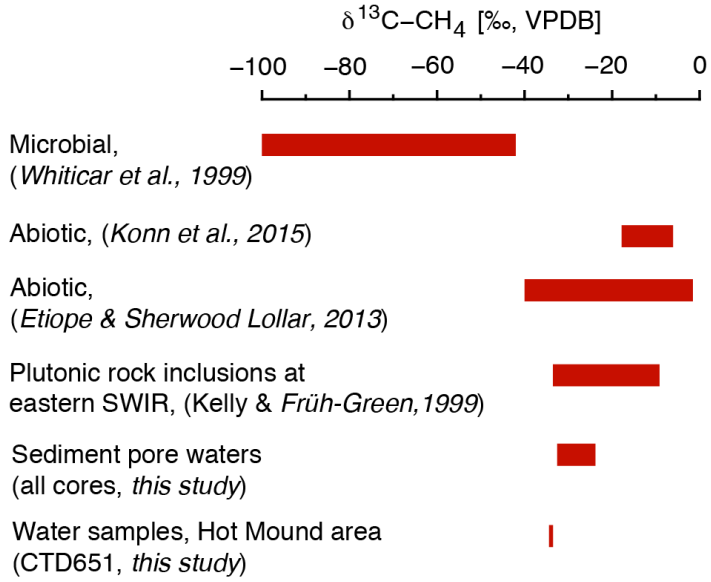

Figure 7.13 Typical ranges of $\delta^{13}C$ in methane originating from microbial sources or abiotic production in ultramafic-hosted hydrothermal vents in comparison to values measured in the water column and pore waters in the SWIR Oblique Supersegment axial valley.

Station	CTD bottle number	Water depth [m]	Average DCF [$\mu molCm^{-3}d^{-1}$]	Standard deviation of DCF $\mu molCm^{-3}d^{-1}$
CTD614	8	3862	0.965	0.075
CTD614	5	3862	0.286	0.113
CTD614	15	3760	0.485	0.108
CTD614	17	3362	1.056	0.821
CTD629	22	3742	0.561	0.135
CTD629	8	3700	0.197	0.025
CTD629	20	3690	0.326	0.124
CTD631	18	4320	0.611	0.243
CTD631	4	3635	2.665	0.702
CTD631	21	2501	0.506	0.045
CTD631	3	4154	2.285	0.040
CTD631	9	4169	2.583	0.637
CTD651	5	3526	0.101	0.009
CTD651	2	3083	0.070	0.026

Table 7.5 Results of dark CO_2 fixation (DCF) rates in samples from the axial valley waters. For comparison, typical DCF rates in the deep sea are smaller than 0.5-1 $\mu molCm^{-3}d^{-1}$.

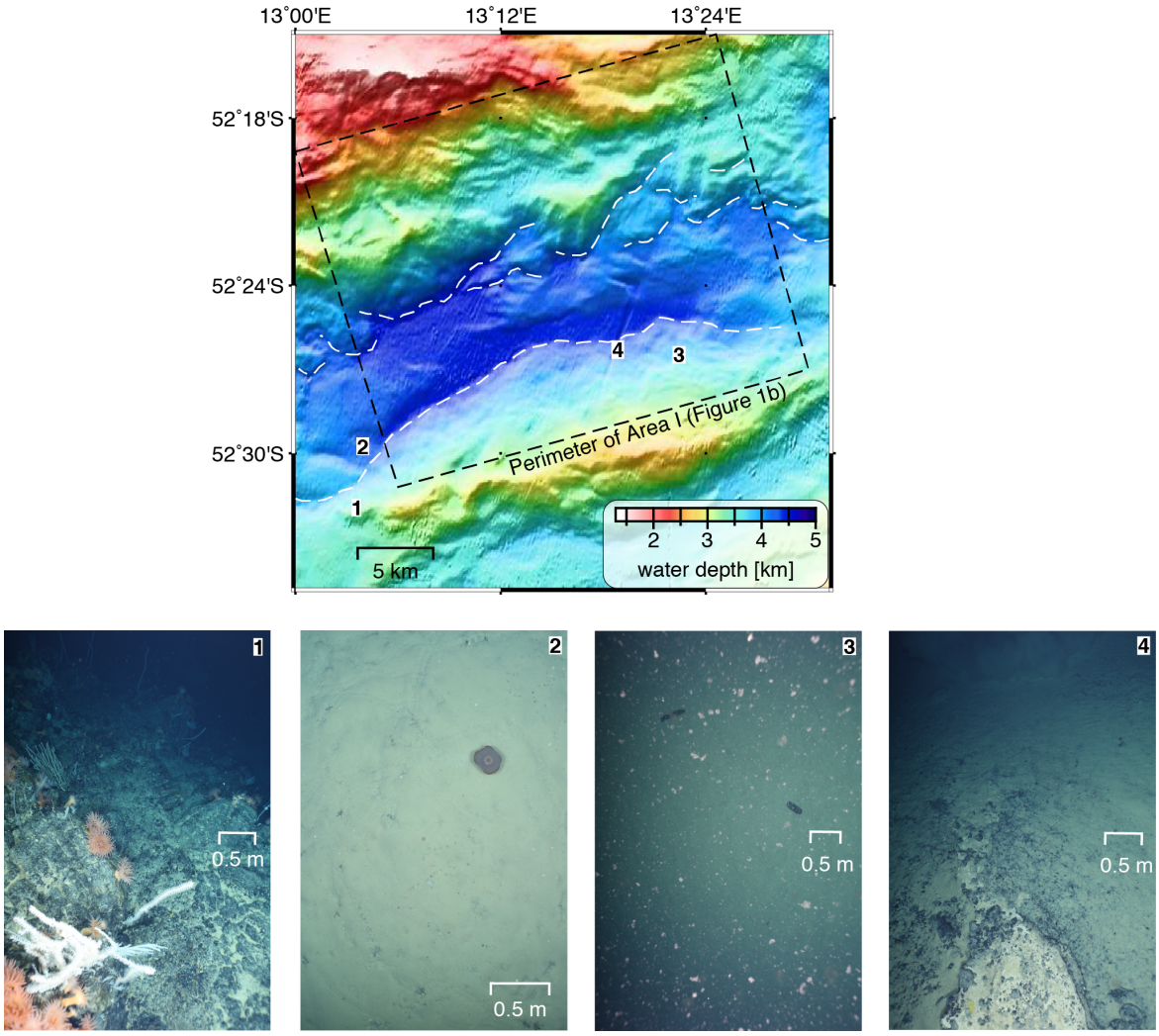

Figure 7.14 OFOS images from the valley bottom and flanks in Area I. Top panel, map with dashed white lines indicating potential boundary faults and dashed black line outlining the perimeter of Area I (see Figure 7.1b for location). Numbers indicate locations of OFOS images shown below map. Image (1) shows bare basement rock on the southern valley flank. Image (2) shows soft sediment with numerous traces of mobile fauna at the valley bottom close to the site of the Vesicomyid discovery (Figure 7.4). Image (3) shows the seafloor of the southern valley flank with two holothurians covered by a cloud of floating particles, likely re-suspended sediment. Note that depth (3790m) and location of this image coincide with a strong, near bottom turbidity anomaly that was observed in CTD629 at the same spot (Figure 7.9, upper panel). Image (4) shows a thin veneer of sediment above basement rubble on the southern valley flank.

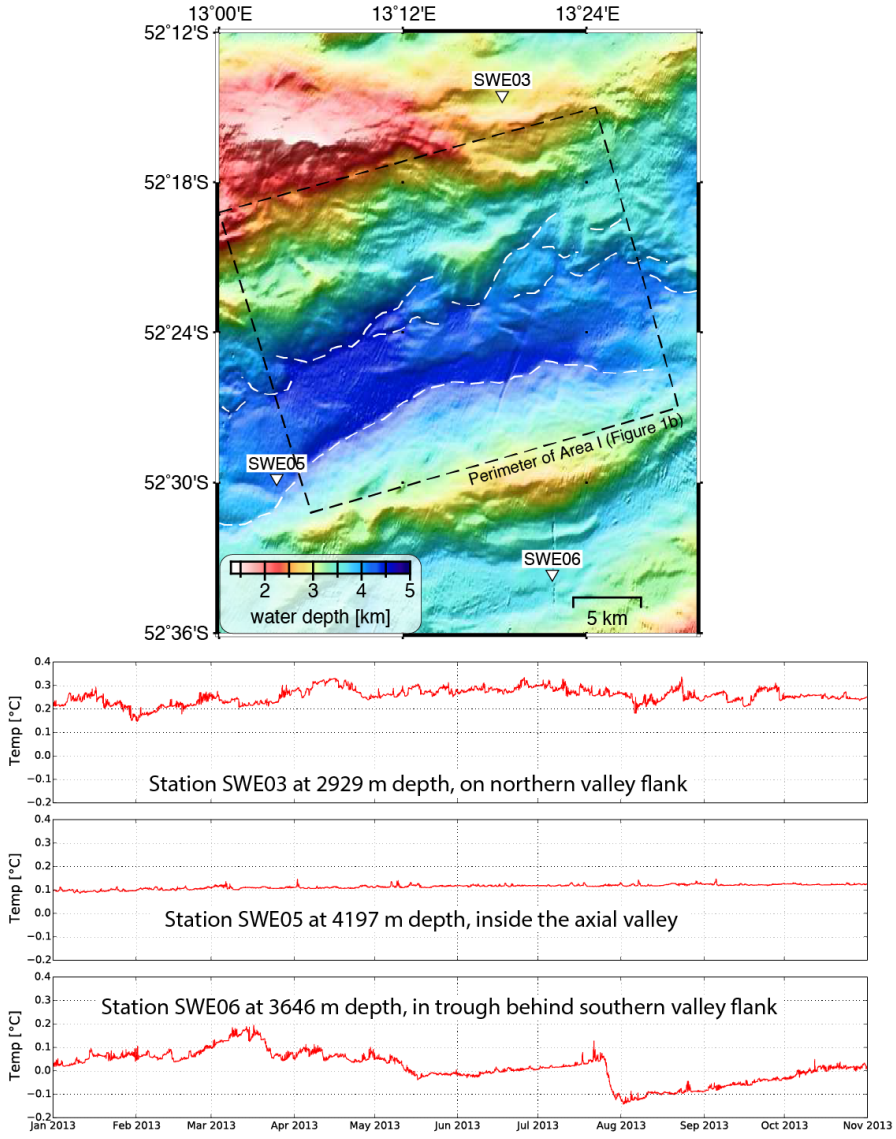

Figure 7.15 Time series of bottom water temperatures at the SWIR Oblique Supersegment. Top panel shows a location map with triangles giving locations of miniaturized temperature loggers that were attached to OBSs. Dashed white lines indicate potential boundary faults and dashed black line outlines the perimeter of Area I (see Figure 7.1b for location). Three bottom panels show temperature time series measured at the different sites. Note that temperatures are not corrected for water depth, thus absolute values have to be considered with care. Temperature changes are weakest at the valley bottom and most pronounced at the shallower sites.

8 Conclusions and Outlook

This thesis contributes new findings to the understanding of microearthquake activity, lithospheric structure and the processes of lithosphere accretion at ultraslow spreading mid-ocean ridges. Until very recently, the harsh environmental conditions and the remoteness of the main representatives of ultraslow spreading MORs has prevented long-term deployments of OBS and hydrophones. The herein presented results provided for the first time a one-year spanning overview of the microearthquake activity along ~260 km of the SWIR spreading axis. The following section summarises the most important outcomes in response to the scientific questions stated in chapter 1.4.

8.1 Conclusions

How thick is the brittle lithosphere at magmatic and amagmatic ridge sections? How is the thickness of the brittle lithosphere related to general changes in lithology?
The deepest hypocenters down to 31 km below the seafloor at the amagmatic Oblique Supersegment surpassed by far the deepest previously identified hypocenters from the slow spreading Mid-Atlantic Ridge (at ~15 km depth; *deMartin et al.*, 2007; *Dusunur et al.*, 2009; *Tilmann et al.*, 2004) and from the ultraslow spreading Knipovich Ridge (at ~20 km depth; *Schlindwein et al.*, 2013). Thus, the discovery set a mark on how thick the brittle axial lithosphere can be at an active MOR. The total lack of earthquakes below the SWIR Segment 8 volcanic center was in strong contrast to the deep earthquakes and implied that the brittle lithosphere was hardly existent at this segment during the time of the OBS deployment. Only after the local earthquake tomography results were available it became obvious that the aseismic behaviour below the Segment 8 was at least partially the result of an ongoing magmatic spreading episode and possibly transient. On a length-scale of roughly 40-50 km along the axis of the Oblique Supersegment the variations in the thickness of the brittle lithosphere correlated with changes in the depth of the axial valley and with general changes in the lithology (chapter 5). Regions with deepest earthquakes correspond a deeper axial valley and primarily ultramafic rocks at the seafloor. Regions of shallower earthquakes correspond to a shallower axial valley floor that also bears basaltic rocks at the seafloor.

Is the previous hypothesis of an undulating LAB that guides melt towards magmatic centers supported by the along-axis distribution of maximum hypocenter depths?
The maximum depth of co-seismic faulting in the earth's lithosphere is mainly dependent on temperature. Hence, the maximum hypocenter depths provide an excellent proxy for the thermal structure below the ridge. The apparent undulations in the maximum earthquakes depths along the spreading axis implied systematic variations in the sub-axial thermal structure. When extrapolated to greater depth the undulations in the brittle-ductile transition depth (BDT) also implied parallel undulations in the deeper lithosphere-asthenosphere boundary (LAB). The LAB is located near the permeability boundary layer at which melts are constantly present (e.g. *Naif et al.*, 2013). The inferred shallowing LAB beneath magmatic segments thus has an immediate effect on buoyantly flowing melts, directing them towards these segments. Accordingly, the found variations in the BDT depth strongly supported the previously hypothesised undulating LAB, considered as a precondition for the focusing of melts at magmatic centers (*Montési et al.*, 2011; *Sauter et al.*, 2004a; *Standish et al.*, 2008).

Where do melts reside in the lithosphere underneath magmatic centers? How long may they persist during spreading episodes?
The spatial distribution of microearthquakes at the SWIR Segment 8 revealed a region, immediately below the Segment 8 volcano, that extended ~20 km along the ridge axis and was completely aseismic. The local earthquake tomography results from this region (chapter 6) showed a distinct low velocity anomaly inside the aseismic region reaching from near the surface to roughly 15 km depth, which suggested the presence of partial melts in the crust and upper mantle. The seismic records revealed two swarms of microearthquake activity and an intrusion tremor at the center of the neighbouring, lower-relief Segment 7 which is ~35 km east of the Segment 8 volcano. All these observations indicated that the SWIR Segments 7 & 8 were in a phase of magmatic activity during the time of the OBS deployment (late 2012 to late 2013). Incorporating also the enhanced teleseismic activity at the SWIR Segment 8 in the period 1996-2001 lead to the conclusion that the phase of magmatic activity might have been initiated then, roughly 13 years before the OBS network was deployed (Figure 2.2). The entity of observations allowed to reconstruct the ongoing magmatic spreading episode and showed that, at the time of the OBS experiment, it had already lasted over a decade. Hence, it greatly exceeded the duration of all previously documented magmatic spreading episodes at other MORs.
No further low velocity anomaly, indicative of partial melts, was found below the SWIR Segment 7, which would serve as source regions for the magma that triggered the microearthquake swarms and the intrusion tremor. I hypothesize that the melts laterally distributed in the crust, possibly through a magma conduit that connected Segments 7 and 8.

What is the role of serpentinization in the deformation of mainly peridotitic lithosphere? What are the implications of extensive serpentiniation for the axial valley environment?
The aseismic zones in the upper lithosphere and the corresponding yield-strength envelope indicated a very weak upper lithosphere at the peridotite bearing sections of the Oblique Supersegment. This was best explained by serpentinization down to a maximum depth of 15 km below the axial valley. I hypothesize that the serpentinization is focused in shear zones that constitute the valley bounding faults. The aseismic mode of deformation is essentially influenced by the deep-reaching serpentinization. Considering the extensive serpentinization, the Oblique Supersegment constitutes a well-suited setting to investigate the effects of serpentinization and related fluids fluxes on the axial valley environment. This aspect is discussed in detail in chapter 7.
The most important outcomes are as follows. The plume of elevated methane concentrations in the axial valley waters most likely originated from abiotic, serpentinization-derived processes. The aseismic valley bounding faults provide the primary pathway for the fluid exchange between the lithosphere and the ocean. However, the geochemical fluxes in the axial valley were also strongly influenced by the deposition of organic matter from the surface ocean. The microbial activities at the sediment-water interface are comparable inside and outside the axial valley and the highest activities were found at a site that is close to the scarp of the southern boundary fault. In summary, there is an effect of the deep reaching serpentinization to the axial valley environment which is most pronounced near boundary faults and occurs overprinted by processes which are attributed to organic matter deposition.

8.2 Outlook

The following paragraphs outline a few ideas for future research on ultraslow MORs that evolved during the work on this thesis project.

Segment-scale OBS deployment at an ultraslow MOR
The two microseismicity catalogues from the SWIR presented in chapters 4 cover each ~130 km long sub-sections of two SWIR segments but not the entire segments, e.g from one magmatic center to the next one or from one first-order ridge discontinuity to the next one. Capturing the segment-scale seismicity at an ultraslow ridge is necessary to fully understand the segmentation pattern and the underlaying melt extraction mechanisms. Thus, I propose the installation of an OBS network for several months that covers an entire segment of the SWIR or another ultraslow spreading MOR. Ideally, the crustal structure and the lithology of the target segment for such an experiment are previously known or investigated in parallel with the microseismicity. This is necessary for a comprehensive interpretation of the seismicity results in relation to the geological context. A suitable site for such an experiment would be the eastern SWIR, for example the region between the centers of Segments 10 and 12, Figure 1.7. Such an OBS deployment should cover the entire SWIR Segment 11 and the resulting earthquake catalogue will help to validate the correlation between maximum

microearthquake depths, general lithology and axial valley morphology that was found at the Oblique Supersegment (chapter 5.5).
The SWIR segments 10 through 12 have been intensively studied previously by geophysical (*Cannat et al.*, 2003, 2008, 2009; *Sauter et al.*, 2004a, 2013) and petrological (*Paquet et al.*, 2016) means.

Attenuation tomography at the SWIR Segment 8

The local earthquake tomography based on the seismicity catalogue from the SWIR Segment 8 (chapter 6) revealed a distinct anomaly below the Segment 8 axial volcano that is characterized by low Vp, Vs velocities and a high Vp/Vs-ratio. The tomography model could resolve the location and shape of the anomaly but the amplitudes remained poorly constrained as was demonstrated by the synthetic tests (chapter 6.6). Attenuation tomography studies, that make use of the waveform amplitude of earthquake phase onsets, are regularly applied at terrestrial volcanoes to study the physical properties of the underlying magma plumbing systems (e.g. *De Siena et al.*, 2014, 2016). I propose to further use the seismicity dataset from the SWIR Segment 8 to perform an attenuation tomography to constrain the physical properties such as seismic wave scattering and attenuation of the region of partial melts below the Segment 8 volcano. The results may then be validated against petrological studies and melting models to improve our understanding of the melt storage, differentiation and extraction at ultraslow MORs.

Constraining the deformation and geochemical cycling at amagmatic sections of ultraslow MORs

In chapter 7 I made an effort to relate the aseismic mode of deformation to geochemical cycling and microbial activity at an amagmatic section of the SWIR Oblique Supersegment. However, the results reveal a complex interplay of which numerous aspects could not be fully resolved: What is the slip rate and width of the boundary faults? What are the flux rates of serpentinization related fluids within the shear zones? To which extent is the tectonic activity related to the rates of geochemical fluid flow? I propose a drilling campaign to tackle these questions which targets an amagmatic section of the SWIR Oblique Supersegment (Figure 8.1). I suggest a series of drill holes whose precise locations should be determined after a geophysical pre-site survey that includes high-resolutions reflection seismics and ideally AUV-based microbathymetry mapping. One hole should sample the axial valley sediments and the underlying basement. A second hole should be placed immediately at the fault scarp and sample the shear zone as well as well as the footwall and the hanging wall. A third hole should be placed on the fault block that constitutes the valley wall to sample its composition and its state of alteration. Petrological, geochemical, geophysical and microbiological sampling of the recovered drill cores may then target the above questions.

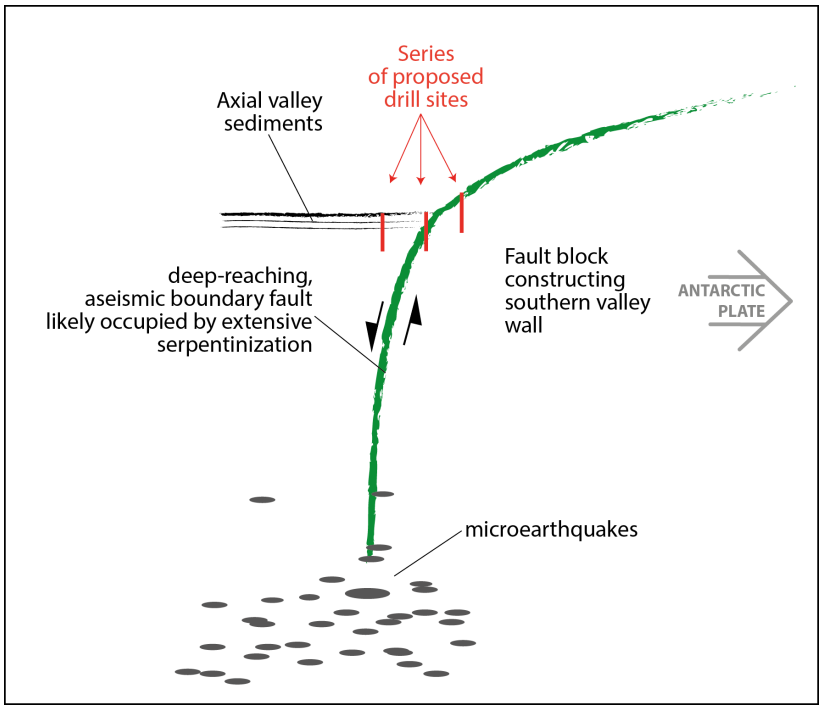

Figure 8.1 Cartoon illustrating the inferred aseismic boundary fault that separates the southern valley wall from the valley floor at the SWIR Oblique Supersegment, near 13°15' E. Red vertical bars depict proposed drill holes to investigate the basement-sediment-ocean interactions the geochemical cycling at this amagmatic segment of the ultraslow SWIR.

9 Acknowledgements

First an foremost I am grateful to Vera for giving me the opportunity to be part of her small team, to work on this truly interesting topic and for enabling my participation in four research cruises to the Arctic, Indian and Southern Oceans. I always appreciated and admired her well-conceived and motivating way of supervision and guidance. I owe her a lot of experience in hard skills of geophysics and seismology as well as in soft skills of managing the challenges of becoming a scientist.
Second, I am indepted to Ivan for being very open and amicable from the first contact onwards and for inviting me to Novosibirsk and Kamchatka. The invitation definitively opened new perspectives for me in the topics of studying active volcanoes, local earthquake tomography and the russian way of live. Further, I am grateful to Katja, Ira, Andreij and Sergey for giving me invaluable advice on how to survive the day-to-day live in Akadem and kindly taking me along to trips on the Obskoje Morje and into the Siberian woods.
Third, I am very grateful to Wolfgang for fruitful discussions on petrological and geochemical aspects and for taking the job of evaluating this work. Fourth, I am indebted to Ingo for taking the task of providing the external review.
I am grateful to all members of AWI geophysics section and the eight students that joined the MOVE group during the last three years for good comradeship and interesting discussions. In particular, I acknowledge John who was there during the initial phase of my PhD.
I am indebted to Mechita and Wolfram who joined my thesis commity and took me along the Ross Sea.
I am grateful to Henning for always taking the best of care for the success of the OBS deployments and for providing me with numerous interesting lectures on various technical issues.
Further, I am grateful to all the scientists that took the time to review and critically comment the four manuscripts but chose to stay anonymous. The DAAD is acknowledged for financially supporting my visit to Kamchatka and Novosibirsk. Last but certainly not least I am indepted to Kati for everything she did in supporting me and making my life easier while I was stuck in science.
Thank You!

References

Albaric, J., J. Déverchère, C. Petit, J. Perrot, and B. Le Gall (2009), Crustal rheology and depth distribution of earthquakes: Insights from the central and southern East African Rift System, *Tectonophysics*, *468*(1-4), 28–41, doi:10.1016/j.tecto.2008.05.021.

Amann, R. I., and B. M. Fuchs (2008), Single-cell identification in microbial communities by improved fluorescence in situ hybridization techniques, *Nat. Rev. Microbiol.*, *6*(5), 339–48, doi:10.1038/nrmicro1888.

Amann, R. I., B. J. Binder, R. J. Olson, S. W. Chisholm, R. Devereux, and D. A. Stahl (1990), Combination of 16S rRNA-targeted oligonucleotide probes with flow cytometry for analyzing mixed microbial populations, *Applied and Environmental Microbiology*, *56*(6), 1919–1925.

Amann, R. I., W. Ludwig, and K. H. Schleifer (1995), Phylogenetic identification and in situ detection of individual microbial cells without cultivation, *Microbiological Reviews*, *59*(1), 143–169.

Amiguet, E., B. Reynard, R. Caracas, B. Van de Moortèle, N. Hilairet, and Y. Wang (2012), Creep of phyllosilicates at the onset of plate tectonics, *Earth and Planetary Science Letters*, *345-348*, 142–150, doi:10.1016/j.epsl.2012.06.033.

Anderson, D. L. (1995), Lithosphere, asthenosphere, perisphere, *Reviews of Geophysics*, *33*(1), doi:10.1029/94RG02785.

Andreani, M., C. Mével, A. M. Boullier, and J. Escartín (2007), Dynamic control on serpentine crystallization in veins: Constraints on hydration processes in oceanic peridotites, *Geochemistry, Geophysics, Geosystems*, *8*(2), doi:10.1029/2006gc001373.

Bach, W., N. R. Banerjee, H. J. B. Dick, and E. T. Baker (2002), Discovery of ancient and active hydrothermal systems along the ultra-slow spreading Southwest Indian Ridge 10° - 16°E, *Geochemistry, Geophysics, Geosystems*, *3*, 1–15, doi:10.1029/2001GC000279.

Baker, E. T., and S. R. Hammond (1992), Hydrothermal venting and the apparent magmatic budget of the Juan de Fuca Ridge, *Journal of Geophysical Research: Solid Earth*, *97*(B3), 3443–3456, doi:10.1029/91jb02671.

Baker, E. T., Y. J. Chen, and J. P. Morgan (1996), The relationship between near-axis hydrothermal cooling and the spreading rate of mid-ocean ridges, *Earth and Planetary Science Letters*, *142*(1), 137–145, doi:10.1016/0012-821X(96)00097-0.

Baker, E. T., H. N. Edmonds, P. J. Michael, W. Bach, H. J. B. Dick, J. Snow, S. L. Walker, and C. H. Langmuir (2004), Hydrothermal venting in magma deserts: The ultraslow spreading Gakkel and Southwest Indian Ridges, *Geochemistry, Geophysics, Geosystems*, *5*(8), doi:10.1029/2004GC000712.

Barruol, G., and K. Sigloch (2013), Investigating La Rèunion hot spot from crust to core, *Eos, Transactions of the American Geophysical Union*, *94*(23), doi:10.1002/2013EO230002.

Beaulieu, S. E., E. T. Baker, and C. R. German (2015), Where are the undiscovered hydrothermal vents on oceanic spreading ridges?, *Deep Sea Research Part II: Topical Studies in Oceanography*, *121*, 202–212, doi:10.1016/j.dsr2.2015.05.001.

Bird, P. (2003), An updated model of plate boundaries, *Geochemistry, Geophysics, Geosystems*, *4*, 1–51, doi:10.1029/2001GC000252.

Boebel, O. (2013), The expedition of the research vessel "Polarstern" to the Antarctic in 2012/2013 (ANT-XXIX/2), *Report 1866-3192*, AWI Bremerhaven, doi:hdl:10013/epic.42735.

Bohnenstiehl, D. R., F. Waldhauser, and M. Tolstoy (2008), Frequency-magnitude distribution of microearthquakes beneath the 9°50'N region of the East Pacific Rise, October 2003 through April 2004, *Geochemistry, Geophysics, Geosystems*, *9*(10), doi:10.1029/2008gc002128.

Boss, K. J. (1970), Redescription of the Valdivia Vesicomya of Thiele and Jaeckel, *Mitt. Mus. Nat.kd. Berl., Zool. Reihe*, *46*(1), 67–84, doi:10.1002/mmnz.19700460109.

Bown, J. W., and R. S. White (1994), Variation with spreading rate of oceanic crustal thickness and geochemistry, *Earth and Planetary Science Letters*, *121*(3-4), 435–449, doi:10.1016/0012-821x(94)90082-5.

Bredehoeft, J. D., and S. S. Papadopulos (1965), Rates of vertical groundwater movement estimated from the Earth's thermal profile, *Water Resources Research*, *1*(2), 325–328, doi:10.1029/WR001i002p00325.

Buck, W. R., P. Einarsson, and B. Brandsdóttir (2006), Tectonic stress and magma chamber size as controls on dike propagation: Constraints from the 1975-1984 Krafla rifting episode, *Journal of Geophysical Research.*, *111*, 1–15, doi:10.1029/2005JB003879.

Bullen, K. E., and B. A. Bolt (1985), *An introduction to the theory of seismology*, 4 ed., Cambridge U. P., Cambridge, doi:10.1111/j.1365-246X.86.tb01083.x.

Burov, E. B. (2011), Rheology and strength of the lithosphere, *Marine and Petroleum Geology*, *28*(8), 1402–1443, doi:10.1016/j.marpetgeo.2011.05.008.

Byerlee, J. (1978), Friction of rocks, *Pure and applied geophysics*, *116*(4), 615–626, doi:10.1007/BF00876528.

Böer, S. I., C. Arnosti, J. E. E. van Beusekom, and A. Boetius (2009), Temporal variations in microbial activities and carbon turnover in subtidal sandy sediments, *Biogeosciences*, *6*, 1149–1165, doi:10.5194/bg-6-1149-2009.

Cannat, M. (1993), Emplacement of mantle rocks in the seafloor at mid-ocean ridges, *Journal of Geophysical Research: Solid Earth*, *98*(B3), 4163–4172, doi:10.1029/92JB02221.

Cannat, M. (1996), How thick is the magmatic crust at slow spreading oceanic ridges?, *Journal of Geophysical Research: Solid Earth*, *101*(B2), 2847–2857, doi:10.1029/95JB03116.

Cannat, M., C. Rommevaux-Jestin, D. Sauter, C. Deplus, and V. Mendel (1999), Formation of the axial relief at the very slow spreading Southwest Indian Ridge, *Journal of Geophysical Research: Solid Earth*, *104*, 2825–2843, doi:10.1029/1999JB900195.

Cannat, M., C. Rommevaux-Jestin, and H. Fujimoto (2003), Melt supply variations to a magma-poor ultra-slow spreading ridge (Southwest Indian Ridge 61° to 69°E), *Geochemistry, Geophysics, Geosystems*, *4*(8), 1–21, doi:10.1029/2002gc000480.

Cannat, M., D. Sauter, V. Mendel, E. Ruellan, K. Okino, J. Escartin, V. Combier, and M. Baala (2006), Modes of seafloor generation at a melt-poor ultraslow-spreading ridge, *Geology*, *34*(7), 605, doi:10.1130/g22486.1.

Cannat, M., D. Sauter, A. Bezos, C. Meyzen, E. Humler, and M. Le Rigoleur (2008), Spreading rate, spreading obliquity, and melt supply at the ultraslow spreading Southwest Indian Ridge, *Geochemistry, Geophysics, Geosystems*, *9*(4), 1–26, doi:10.1029/2007gc001676.

Cannat, M., D. Sauter, J. Escartín, L. Lavier, and S. Picazo (2009), Oceanic corrugated surfaces and the strength of the axial lithosphere at slow spreading ridges, *Earth and Planetary Science Letters*, *288*(1-2), 174–183, doi:10.1016/j.epsl.2009.09.020.

Cannat, M., F. R. Fontaine, and J. Escartin (2010), Serpentinization and associated hydrogen and methane fluxes at slow spreading ridges, *Geophysical Monograph Series*, *188*, doi:10.1029/2008GM000760.

Carlson, R. L. (2004), Influence of pressure and mineralogy on seismic velocities in oceanic gabbros: Implications for the composition and state of the lower oceanic crust, *Journal of Geophysical Research: Solid Earth*, *109*(B9), doi:10.1029/2003jb002699.

Charlou, J. L., Y. Fouquet, H. Bougault, J. P. Donoval, J. Etoubleau, P. Jean-Baptiste, A. Dapoigny, P. Appriou, and P. A. Rona (1998), Intense CH4 plumes generated by erpentinization of ultramafic rocks at the intersection of the 15°20'N fracture zone and the Mid-Atlantic Ridge, *Geochimica et Cosmochimica Acta*, *62*(13), 2323–2333, doi:10.1016/S0016-7037(98)00138-0.

Chen, W.-P., and P. Molnar (1983), Focal depths of intracontinental and intraplate earthquakes and their implications for the thermal and mechanical properties of the lithosphere, *Journal of Geophysical Research.*, *88*(B5), 4183, doi:10.1029/JB088iB05p04183.

Chopra, P. N., and M. S. Paterson (1981), The experimental deformation of dunite, *Tectonophysics*, *78*, 453–473, doi:10.1016/0040-1951(81)90024-X.

Connelly, D. P., C. R. German, M. Asada, K. Okino, A. Egorov, T. Naganuma, N. Pimenov, G. Cherkashev, and K. Tamaki (2007), Hydrothermal activity on the ultra-slow spreading southern Knipovich Ridge, *Geochemistry, Geophysics, Geosystems*, *8*(8), n/a–n/a, doi:10.1029/2007gc001652.

Copley, J. T., L. Marsh, A. G. Glover, V. Huhnerbach, V. E. Nye, W. D. Reid, C. J. Sweeting, B. D. Wigham, and H. Wiklund (2016), Ecology and biogeography of megafauna and macrofauna at the first known deep-sea hydrothermal vents on the ultraslow-spreading Southwest Indian Ridge, *Sci Rep*, *6*, 39,158, doi:10.1038/srep39158.

Crawford, W. C., A. Rai, S. C. Singh, M. Cannat, J. Escartin, H. Wang, R. Daniel, and V. Combier (2013), Hydrothermal seismicity beneath the summit of Lucky Strike volcano, Mid-Atlantic Ridge, *Earth Planet. Sci. Lett.*, *373*(1), 118 – 128, doi:10.1016/j.epsl.2013.04.028.

Daims, H., A. Brühl, R. Amann, K.-H. Schleifer, and M. Wagner (1999), The Domain-specific Probe EUB338 is Insufficient for the Detection of all Bacteria: Development and Evaluation of a more Comprehensive Probe Set, *Systematic and Applied Microbiology*, *22*(3), 434–444, doi:10.1016/0723-2020(99)80053-8.

De Siena, L., C. Thomas, and R. Aster (2014), Multi-scale reasonable attenuation tomography analysis (MuRAT): An imaging algorithm designed for volcanic regions, *Journal of Volcanology and Geothermal Research*, *277*, 22–35, doi:10.1016/j.jvolgeores.2014.03.009.

De Siena, L., M. Calvet, K. J. Watson, A. R. T. Jonkers, and C. Thomas (2016), Seismic scattering and absorption mapping of debris flows, feeding paths, and tectonic units at Mount St. Helens volcano, *Earth Planet. Sci. Lett.*, *442*, 21–31, doi:10.1016/j.epsl.2016.02.026.

deMartin, B. J., R. A. Sohn, J. Pablo Canales, and S. E. Humphris (2007), Kinematics and geometry of active detachment faulting beneath the Trans-Atlantic Geotraverse (TAG) hydrothermal field on the Mid-Atlantic Ridge, *Geology*, *35*(8), 711, doi:10.1130/g23718a.1.

DeMets, C., R. G. Gordon, D. F. Argus, and S. Stein (1994), Effect of recent revisions to the geomagnetic reversal time scale on estimates of current plate motions, *Geophysical Research Letters*, *21*(20), 2191–2194, doi:10.1029/94gl02118.

DeMets, C., R. G. Gordon, and D. F. Argus (2010), Geologically current plate motions, *Geophysical Journal International*, *181*(1), 1–80, doi:10.1111/j.1365-246X.2009.04491.x.

D'Hondt, S., B. B. Joergensen, D. J. Miller, A. Batzke, R. E. Blake, B. A. Cragg, H. Cypionka, G. R. Dickens, T. G. Ferdelmann, K. U. Hinrichs, N. G. Holm, R. Mitterer, A. Spivack, G. Wang, B. Bekins, B. Engelen, K. Ford, G. Gettemy, S. D. Rutherford, H. Sass, C. G. Skilbeck, I. W. Aiello, G. Guerin, C. H. House, F. Inagaki, P. Meister, T. Naehr, S. Niitsuma, R. J. Parkes, A. Schippers, D. K. Smith, A. Teske, J. Wiegel, P. Naranjo, and J. L. S. Acosta (2004), Distributions of microbial activities in deep subseafloor sediments, *Science*, *306*(5705), 2216–2221, doi:10.1126/science.1101155.

Dick, H. J. B., J. Lin, and H. Schouten (2003), An ultraslow-spreading class of ocean ridge, *Nature*, *426*(6965), 405–412, doi:10.1038/nature02128.

Dusunur, D., J. Escartín, V. Combier, T. Seher, W. Crawford, M. Cannat, S. C. Singh, L. M. Matias, and J. M. Miranda (2009), Seismological constraints on the thermal structure along the Lucky Strike segment (Mid-Atlantic Ridge) and interaction of tectonic and magmatic processes around the magma chamber, *Marine Geophysical Researches*, *30*(2), 105–120, doi:10.1007/s11001-009-9071-3.

Eberhart-Phillips, D. (1990), Three-dimensional P and S velocity structure in the Coalinga Region, California, *Journal of Geophysical Research: Solid Earth*, *95*(B10), 15,343, doi:10.1029/JB095iB10p15343.

Eberhart-Phillips, D. (2002), Three-dimensional crustal structure in the Southern Alps region of New Zealand from inversion of local earthquake and active source data, *Journal of Geophysical Research: Solid Earth*, *107*(B10), doi:10.1029/2001jb000567.

Edmonds, H. N., P. J. Michael, E. T. Baker, D. P. Connelly, J. E. Snow, C. H. Langmuir, H. J. Dick, R. Muhe, C. R. German, and D. W. Graham (2003), Discovery of abundant hydrothermal venting on the ultraslow-spreading Gakkel ridge in the Arctic Ocean, *Nature*, *421*(6920), 252–6, doi:10.1038/nature01351.

Ekström, G., M. Nettles, and A. M. Dziewoński (2012), The global CMT project 2004–2010: Centroid-moment tensors for 13,017 earthquakes, *Phys. Earth. Plan. Interiors*, *200-201*(0), 1–9, doi:10.1016/j.pepi.2012.04.002.

Eppelbaum, L., I. Kutasov, and A. Pilchin (2014), *Thermal Properties of Rocks and Density of Fluids*, Lecture notes in earth system sciences, Springer, Berlin [u.a.], doi:10.1007/978-3-642-34023-9_2.

Escartin, J., G. Hirth, and B. Evans (1997), Effects of serpentinization on the lithospheric strength and the style of normal faulting at slow-spreading ridges, *Earth and Planetary Science Letters*, *151*, 181–189, doi:10.1016/S0012-821X(97)81847-X.

Escartin, J., G. Hirth, and B. Evans (2001), Strength of slightly serpentinized perdiotites: Implications for the tectonics of oceanic lithosphere, *Geology*, *29*(11), 1023–1026, doi:10.1130/0091-7613(2001)029.

Escartin, J., D. K. Smith, J. Cann, H. Schouten, C. H. Langmuir, and S. Escrig (2008), Central role of detachment faults in accretion of slow-spreading oceanic lithosphere, *Nature*, *455*(7214), 790–4, doi:10.1038/nature07333.

Etiope, G., and B. Sherwood Lollar (2013), Abiotic Methane on Earth, *Reviews of Geophysics*, *51*(2), 276–299, doi:10.1002/rog.20011.

Evans, B., and D. L. Kohlstedt (1995), *Rheology of Rocks*, pp. 148–165, American Geophysical Union, doi:10.1029/RF003p0148.

Evans, B. W. (2004), The serpentinite multisystem revisited: Chrysotile is metastable, *International Geology Review*, *46*(6), 479–506, doi:10.2747/0020-6814.46.6.479.

Faber, E., R. Botz, M. Poggenburg, M. Schmidt, P. Stoffers, and M. Hartmann (1998), Methane in Red Sea brines, *Org. Geochem.*, *29*(1-3), 363–379, doi:10.1016/S0146-6380(98)00155-7.

Fischer, C. R. (1980), Chemoautotrophic and methanotrophic symbioses in marine invertebrates, *Reviews in Aquatic Sciences*, *2*, 399–436.

Geibert, W., M. M. Rutgers van der Loeff, R. Usbeck, R. Gersonde, G. Kuhn, and J. Seeberg-Elverfeldt (2005), Quantifying the opal belt in the Atlantic and southeast Pacific sector of the Southern Ocean by means of230Th normalization, *Global Biogeochemical Cycles*, *19*(4), doi:10.1029/2005gb002465.

Geiger, L. (1910), Herdbestimmung bei Erdbeben aus den Ankunftszeiten., *Nachrichten von der Königlichen Gesellschaft der Wissenschaften zu Göttingen*, *4*, 331–349.

German, C. R., E. T. Baker, C. Mevel, and K. Tamaki (1998), Hydrothermal activity along the Southwest Indian Ridge, *Nature*, *395*, doi:10.1038/26730.

German, C. R., A. Bowen, M. L. Coleman, D. L. Honig, J. A. Huber, M. V. Jakuba, J. C. Kinsey, M. D. Kurz, S. Leroy, J. M. McDermott, B. M. de Lepinay, K. Nakamura, J. S. Seewald, J. L. Smith, S. P. Sylva, C. L. Van Dover, L. L. Whitcomb, and D. R. Yoerger (2010), Diverse styles of submarine venting on the ultraslow spreading Mid-Cayman Rise, *Proc Natl Acad Sci U S A*, *107*(32), 14,020–5, doi:10.1073/pnas.1009205107.

Goetze, C., and B. Evans (1979), Stress and temperature in the bending lithosphere as constrained by experimental rock mechanics, *Geophysical Journal of the Royal Astronomical Society*, *59*, doi:10.1111/j.1365-246X.1979.tb02567.x.

Grandin, R., A. Socquet, C. Doubre, E. Jacques, and G. C.P. King (2012), Elastic thickness control of lateral dyke intrusion at mid-ocean ridges, *Earth and Planetary Science Letters*, *319-320*, 83–95, doi:10.1016/j.epsl.2011.12.011.

Grindlay, N. R., J. A. Madsen, C. Rommevaux-Jestin, and J. Sclater (1998), A different pattern of ridge segmentation and mantle Bouguer gravity anomalies along the ultra-slow spreading Southwest Indian Ridge (15°30'E to 25°E), *Earth and Planetary Science Letters*, *161*(1–4), 243–253, doi:10.1016/s0012-821x(98)00154-x.

Gutenberg, B., and C. F. Richter (1956), Earthquake magnitude, intensity, energy, and acceleration (second paper), *Bull. Seismol. Soc. Am.*, *46*(2), 105–145.

Hallberg, R., and A. Gnanadesikan (2006), The Role of Eddies in Determining the Structure and Response of the Wind-Driven Southern Hemisphere Overturning: Results from the Modeling Eddies in the Southern Ocean (MESO) Project, *Journal of Physical Oceanography*, *36*(1), 2232–2252, doi:https://doi.org/10.1175/JPO2980.1.

Hammond, W. C., and E. D. Humphreys (2000), Upper mantle seismic wave velocity: Effects of realistic partial melt geometries, *Journal of Geophysical Research: Solid Earth*, *105*(B5), 10,975–10,986, doi:10.1029/2000jb900041.

Hannemann, K., F. Kruger, and T. Dahm (2013), Measuring of clock drift rates and static time offsets of ocean bottom stations by means of ambient noise, *Geophysical Journal International*, *196*(2), 1034–1042, doi:10.1093/gji/ggt434.

Hasterok, D., D. S. Chapman, and E. E. Davis (2011), Oceanic heat flow: Implications for global heat loss, *Earth and Planetary Science Letters*, *311*(3-4), 386–395, doi:10.1016/j.epsl.2011.09.044.

Havskov, J., and L. Ottemoeller (1999), SeisAn Earthquake analysis Software, *Seismological Res. Lett.*, *70*(5), 532–534, doi:10.1785/gssrl.70.5.532.

Havskov, J., P. Bormann, and J. Schweitzer (2012), *Seismic source location*, vol. 2, pp. 1–36, Deutsches GeoForschungszentrum GFZ, Potsdam, doi:10.2312/GFZ.NMSOP-2_IS_11.1.

Herndl, G. J., T. Reinthaler, E. Teira, H. van Aken, C. Veth, A. Pernthaler, and J. Pernthaler (2005), Contribution of Archaea to total prokaryotic production in the deep Atlantic Ocean, *Appl Environ Microbiol*, *71*(5), 2303–9, doi:10.1128/AEM.71.5.2303-2309.2005.

Hirth, G., and D. L. Kohlstedt (1995), Experimental constraints on the dynamics of the partially molten upper mantle: Deformation in the diffusion creep regime, *Journal of Geophysical Research: Solid Earth*, *100*(B2), 1981–2001, doi:10.1029/94jb02128.

Hirth, G., and D. L. Kohlstedt (1996), Water in the oceanic mantle: implications for rheology, melt extraction and the evolution of the lithosphere, *Earth and Planetary Science Letters*, *144*, 93–108, doi:10.1016/0012-821X(96)00154-9.

Hobbie, J. E., R. J. Daley, and S. Jasper (1977), Use of nuclepore filters for counting bacteria by fluorescence microscopy, *Applied and Environmental Microbiology*, *33*(5), 1225–1228.

Hooft, E. E. E., R. S. Detrick, D. R. Toomey, J. A. Collins, and J. Lin (2000), Crustal thickness and structure along three contrasting spreading segments of the Mid-Atlantic Ridge, 33.5°-35°N, *Journal of Geophysical Research: Solid Earth*, *105*(B4), 8205–8226, doi:10.1029/1999jb900442.

Horen, H., M. Zamora, and G. Dubuisson (1996), Seismic waves velocities and anisotropy in serpentinized peridotites from xigaze ophiolite: Abundance of serpentine in slow spreading ridge, *Geophysical Research Letters*, *23*(1), 9–12, doi:10.1029/95gl03594.

International-Seismological-Centre, I. (2012), On-line Bulletin, *Report*, International Seismological Centre, http:/www.is.ac.uk.

Ishii, K., M. Mußmann, B. J. MacGregor, and R. Amann (2004), An improved fluorescence in situ hybridization protocol for the identification of bacteria and archaea in marine sediments, *FEMS Microbiology Ecology*, *50*(3), 203–213, doi:10.1016/j.femsec.2004.06.015.

Jaupart, C., and J.-C. Mareschal (2007), Heat Flow and thermal structure of the lithosphere, *Treatise on geophysics*, *6*, 217–251, doi:10.1016/B978-0-444-53802-4.00114-7.

Jellinek, A. M., and D. Bercovici (2011), Seismic tremors and magma wagging during explosive volcanism, *Nature*, *470*(7335), 522–5, doi:10.1038/nature09828.

Johnson, J. E., J. Mienert, A. Plaza-Faverola, S. Vadakkepuliyambatta, J. Knies, S. Bunz, K. Andreassen, and B. Ferre (2015), Abiotic methane from ultraslow-spreading ridges can charge Arctic gas hydrates, *Geology*, *43*(5), 371–374, doi:10.1130/g36440.1.

Jokat, W., and M. C. Schmidt-Aursch (2007), Geophysical characteristics of the ultraslow spreading Gakkel Ridge, Arctic Ocean, *Geophysical Journal International*, *168*(3), 983–998, doi:10.1111/j.1365-246X.2006.03278.x.

Jokat, W., O. Ritzmann, M. C. Schmidt-Aursch, S. Drachev, S. Gauger, and J. Snow (2003), Geophysical evidence for reduced melt production on the Arctic ultraslow Gakkel mid-ocean ridge, *Nature*, *423*(6943), 962–5, doi:10.1038/nature01706.

Jokat, W., J. Kollofrath, W. H. Geissler, and L. Jensen (2012), Crustal thickness and earthquake distribution south of the Logachev Seamount, Knipovich Ridge, *Geophysical Research Letters*, *39*(L08302), doi:10.1029/2012GL051199.

Kawagucci, S., K. Okamura, K. Kiyota, U. Tsunogai, Y. Sano, K. Tamaki, and T. Gamo (2008), Methane, manganese, and helium-3 in newly discovered hydrothermal plumes over the Central Indian Ridge, 18°-20°S, *Geochemistry, Geophysics, Geosystems*, *9*(10), doi:10.1029/2008gc002082.

Keir, R. S. (2010), A note on the fluxes of abiogenic methane and hydrogen from mid-ocean ridges, *Geophysical Research Letters*, *37*(24), n/a–n/a, doi:10.1029/2010gl045362.

Keir, R. S., J. Sültenfuß, M. Rhein, G. Petrick, and J. Greinert (2006), Separation of 3He and CH4 signals on the Mid-Atlantic Ridge at 5°N and 51°N, *Geochimica et Cosmochimica Acta*, *70*(23), 5766–5778, doi:10.1016/j.gca.2006.06.005.

Keir, R. S., O. Schmale, M. Walter, J. Sültenfuß, R. Seifert, and M. Rhein (2008), Flux and dispersion of gases from the "Drachenschlund" hydrothermal vent at 8°18' S, 13°30' W on the Mid-Atlantic Ridge, *Earth Plan. Sci. Lett.*, *270*(3-4), 338–348, doi:10.1016/j.epsl.2008.03.054.

Keir, R. S., O. Schmale, R. Seifert, and J. Sültenfuß (2009), Isotope fractionation and mixing in methane plumes from the Logatchev hydrothermal field, *Geochemistry, Geophysics, Geosystems*, *10*(5), n/a–n/a, doi:10.1029/2009gc002403.

Kennett, B. L. N., and E. R. Engdahl (1991), Traveltimes for global earthquake location and phase identification, *Geophysical Journal International*, *105*, 429–465, doi:10.1111/j.1365-246X.1991.tb06724.x.

Key, J., R. S. White, H. Soosalu, and S. S. Jakobsdóttir (2011), Multiple melt injection along a spreading segment at Askja, Iceland, *Geophysical Research Letters*, *38*(5), doi:10.1029/2010gl046264.

Khodayar, M., and P. Einarsson (2004), Reverse-slip structures at oceanic diverging plate boundaries and their kinematic origin: data from Tertiary crust of west and south Iceland, *Journal of Structural Geology*, *26*(11), 1945–1960, doi:10.1016/j.jsg.2004.06.001.

Kissling, E., W. L. Ellsworth, D. Eberhart-Phillips, and U. Kradolfer (1994), Initial reference models in local earthquake tomography, *Journal of Geophysical Research: Solid Earth*, *99*(B10), 19,635–19,646, doi:10.1029/93jb03138.

Kong, L. S. L., S. C. Solomon, and G. M. Purdy (1992), Microearthquake Characteristics of a Mid-Ocean Ridge along-axis high, *Journal of Geophysical Research: Solid Earth*, *97*(B2), 1659–1685, doi:10.1029/91JB02566.

Konn, C., J. L. Charlou, N. G. Holm, and O. Mousis (2015), The production of methane, hydrogen, and organic compounds in ultramafic-hosted hydrothermal vents of the Mid-Atlantic Ridge, *Astrobiology*, *15*(5), 381–99, doi:10.1089/ast.2014.1198.

Konstantinou, K. I., and V. Schlindwein (2003), Nature, wavefield properties and source mechanism of volcanic tremor: a review, *Journal of Volcanology and Geothermal Research*, *119*(1-4), 161–187, doi:10.1016/S0377-0273(02)00311-6.

Korger, E. I. M., and V. Schlindwein (2012), Performance of localization algorithms for teleseismic mid-ocean ridge earthquakes: the 1999 Gakkel Ridge earthquake swarm and its geological interpretation, *Geophysical Journal International*, *188*(2), 613–625, doi:10.1111/j.1365-246X.2011.05282.x.

Korger, E. I. M., and V. Schlindwein (2013), Seismicity and structure of the 85°E volcanic complex at the ultraslow spreading Gakkel Ridge from local earthquake tomography, *Geophysical Journal International*, *196*(1), 539–551, doi:10.1093/gji/ggt390.

Koulakov, I. (2009), LOTOS Code for Local Earthquake Tomographic Inversion: Benchmarks for Testing Tomographic Algorithms, *Bulletin of the Seismological Society of America*, *99*(1), 194–214, doi:10.1785/0120080013.

Krischer, L., T. Megies, R. Barsch, M. Beyreuther, T. Lecocq, C. Caudron, and J. Wassermann (2015), ObsPy: a bridge for seismology into the scientific Python ecosystem, *Computational Science & Discovery*, *8*(1), 014,003, doi:10.1088/1749-4699/8/1/014003.

Lamontagne, M., and G. Ranalli (1996), Thermal and rheological constraints on the earthquake depth distribution in the Charlevoix, Canada, intraplate seismic zone, *Tectonophysics*, *257*(1), 55–69, doi:10.1016/0040-1951(95)00120-4.

Li, J., H. Jian, Y. J. Chen, S. C. Singh, A. Ruan, X. Qiu, M. Zhao, X. Wang, X. Niu, J. Ni, and J. Zhang (2015), Seismic observation of an extremely magmatic accretion at the ultraslow spreading Southwest Indian Ridge, *Geophysical Research Letters*, *42*(8), 2656–2663, doi:10.1002/2014gl062521.

Lienert, B. R., E. W. Berg, and N. L. Frazer (1986), HYPOCENTER: an earthquake location method using centered, scaled, and adaptively least squares, *Bulletin of the Seismological Society of America*, *76*, 771–783.

Lister, C. R. B. (1979), The pulse-probe method of conductivity measurement, *Geophysical Journal of the Royal Astronomical Society*, *57*(2), 451–461, doi:10.1111/j.1365-246X.1979.tb04788.x.

Lutz, M. J., K. Caldeira, R. B. Dunbar, and M. J. Behrenfeld (2007), Seasonal rhythms of net primary production and particulate organic carbon flux to depth describe the efficiency of biological pump in the global ocean, *Journal of Geophysical Research: Oceans*, *112*(C10), doi:10.1029/2006jc003706.

Läderach, C. (2012), Seismicity of ultraslow spreading mid-ocean ridges at local, regional and teleseismic scales, *Doctoral Thesis, University of Bremen*.

Läderach, C., and V. Schlindwein (2011), Seismic Arrays on Drifting Ice Floes: Experiences from Four Deployments in the Arctic Ocean, *Seismological Research Letters*, *82*(4), 494.

Läderach, C., V. Schlindwein, H. W. Schenke, and W. Jokat (2011), Seismicity and active tectonic processes in the ultra-slow spreading Lena Trough, Arctic Ocean, *Geophysical Journal International*, *184*(3), 1354–1370, doi:10.1111/j.1365-246X.2010.04926.x.

Läderach, C., E. I. M. Korger, V. Schlindwein, C. Müller, and A. Eckstaller (2012), Characteristics of tectonomagmatic earthquake swarms at the Southwest Indian Ridge between 16°E and 25°E, *Geophysical Journal International*, *190*(1), 429–441, doi:10.1111/j.1365-246X.2012.05480.x.

Mackensen, A., M. Rudolph, and G. Kuhn (2001), Late Pleistocene deep-water circulation in the subantarctic eastern Atlantic, *Global and Planetary Change*, *30*, 197–229, doi:10.1016/S0921-8181(01)00102-3.

Matyka, M., A. Khalili, and Z. Koza (2008), Tortuosity-porosity relation in porous media flow, *Physical Review E*, *78*(2 Pt 2), 026,306, doi:10.1103/PhysRevE.78.026306.

Maus, S., U. Barckhausen, H. Berkenbosch, N. Bournas, J. Brozena, V. Childers, F. Dostaler, J. D. Fairhead, C. Finn, R. R. B. von Frese, C. Gaina, S. Golynsky, R. Kucks, H. Lühr, P. Milligan, S. Mogren, R. D. Müller, O. Olesen, M. Pilkington, R. Saltus, B. Schreckenberger, E. Thébault, and F. Caratori Tontini (2009), EMAG2: A 2-arc min resolution Earth Magnetic Anomaly Grid compiled from satellite, airborne, and marine magnetic measurements, *Geochemistry, Geophysics, Geosystems*, *10*(8), 1–12, doi:10.1029/2009gc002471.

McKenzie, D., J. Jackson, and K. Priestley (2005), Thermal structure of oceanic and continental lithosphere, *Earth and Planetary Science Letters*, *233*(3-4), 337–349, doi:10.1016/j.epsl.2005.02.005.

McNamara, D. E., and R. I. Boaz (2005), Seismic Noise Analysis System Using Power Spectral Density Probability Density Functions—A Stand-Alone Software Package, *Report*, USGS.

McNamara, D. E., and R. P. Buland (2004), Ambient noise levels in the continental United States, *Bulletin of the Seismological Society of America*, *94*(4), doi:http://dx.doi.org/10.1785/012003001.

Meyzen, C., M. J. Toplis, E. Humler, J. N. Ludden, and C. Mevel (2003), A discontinuity in mantle composition beneath the southwest Indian ridge, *Nature*, *421*, doi:10.1038/nature01424.

Michael, P. J., C. H. Langmuir, H. J. B. Dick, J. E. Snow, S. L. Goldstein, D. W. Graham, K. Lehnert, G. Kurras, R. Mühe, W. Jokat, and H. N. Edmonds (2003), Magmatic and amagmatic seafloor generation at the ultraslow-spreading Gakkel Ridge, Arctic Ocean, *Nature*, *423*, 956–961, doi:10.1038/nature01704.

Michibayashi, K., T. Hirose, T. Nozaka, Y. Harigane, J. Escartin, H. Delius, M. Linek, and Y. Ohara (2008), Hydration due to high-T brittle failure within in situ oceanic crust, 30°N Mid-Atlantic Ridge, *Earth Planet. Sci. Lett.*, *275*(3-4), 348–354, doi:10.1016/j.epsl.2008.08.033.

Minshull, T. A., M. R. Muller, and R. S. White (2006), Crustal structure of the Southwest Indian Ridge at 66°E: seismic constraints, *Geophysical Journal International*, *166*(1), 135–147, doi:10.1111/j.1365-246X.2006.03001.x.

Molari, M., and E. Manini (2012), Reliability of CARD-FISH Procedure for Enumeration of Archaea in Deep-Sea Surficial Sediments, *Current Microbiology*, *64*(3), 242–250, doi:10.1007/s00284-011-0056-5.

Molari, M., E. Manini, and A. Dell'Anno (2013), Dark inorganic carbon fixation sustains the functioning of benthic deep-sea ecosystems, *Global Biogeochemical Cycles*, *27*(1), 212–221, doi:10.1002/gbc.20030.

Montési, L. G. J., and M. D. Behn (2007), Mantle flow and melting underneath oblique and ultraslow mid-ocean ridges, *Geophysical Research Letters*, *34*(24), doi:10.1029/2007gl031067.

Montési, L. G. J., M. D. Behn, L. B. Hebert, J. Lin, and J. L. Barry (2011), Controls on melt migration and extraction at the ultraslow Southwest Indian Ridge 10°–16°E, *Journal of Geophysical Research: Solid Earth*, *116*(B10), doi:10.1029/2011jb008259.

Muller, M. R., T. A. Minshull, and R. S. White (1999), Segmentation and melt supply at the Southwest Indian Ridge, *Geology*, *27*(10), 867, doi:10.1130/0091-7613.

Müller, C., and W. Jokat (2000), Seismic evidence for volcanic activity discovered in central Arctic, *Eos, Transactions, American Geophysical Union*, *81*, 265–269, doi:10.1029/00EO00186.

Naif, S., K. Key, S. Constable, and R. L. Evans (2013), Melt-rich channel observed at the lithosphere-asthenosphere boundary, *Nature*, *495*, 356–359, doi:10.1038/nature11939.

Niewöhner, C., C. Hensen, S. Kasten, M. Zabel, and H. D. Schulz (1998), Deep Sulfate Reduction Completely Mediated by Anaerobic Methane Oxidation in Sediments of the Upwelling Area off Namibia, *Geochimica et Cosmochimica Acta*, *62*(3), 455–464, doi:10.1016/S0016-7037(98)00055-6.

Niu, X., A. Ruan, J. Li, T. A. Minshull, D. Sauter, Z. Wu, X. Qiu, M. Zhao, Y. J. Chen, and S. Singh (2015), Along-axis variation in crustal thickness at the ultraslow spreading Southwest Indian Ridge (50°E) from a wide-angle seismic experiment, *Geochemistry, Geophysics, Geosystems*, pp. n/a–n/a, doi:10.1002/2014GC005645.

Nürnberg, C. C., G. Bohrmann, M. Schlüter, and M. Frank (1997), Barium accumulation in the Atlantic sector of the Southern Ocean: Results From 190,000-year records, *Paleoceanography*, *12*(4), 594–603, doi:10.1029/97pa01130.

Paige, C. C., and M. A. Saunders (1982), LSQR: Sparse linear equations and least squares problems, *ACM Transactions of Mathematical Software*, *8*(2), 195–209.

Paquet, M., M. Cannat, D. Brunelli, C. Hamelin, and E. Humler (2016), Effect of melt/mantle interactions on MORB chemistry at the easternmost Southwest Indian Ridge (61°-67°E), *Geochemistry, Geophysics, Geosystems*, doi:10.1002/2016gc006385.

Pedersen, R. B., H. T. Rapp, I. H. Thorseth, M. D. Lilley, F. J. Barriga, T. Baumberger, K. Flesland, R. Fonseca, G. L. Fruh-Green, and S. L. Jorgensen (2010), Discovery of a black smoker vent field and vent fauna at the Arctic Mid-Ocean Ridge, *Nat Commun*, *1*, 126, doi:10.1038/ncomms1124.

Perfit, M. R., and W. W. Chadwick (1998), Magmatism at mid-ocean ridges: Constraints from volcanological and geochemical investigations, *Geophysical Monograph Series*, *106*, 59–115, doi:10.1029/GM106p0059.

Phipps Morgan, J., E. M. Parmentier, and J. Lin (1987), Mechanisms for the origin of mid-ocean ridge axial topography: Implications for the thermal and mechanical structure of accreting plate boundaries, *Journal of Geophysical Research: Solid Earth*, *92*(B12), 12,823–12,836, doi:10.1029/JB092iB12p12823.

Proskurowski, G., M. D. Lilley, J. S. Seewald, G. Früh-Green, E. J. Olson, J. E. Lupton, S. P. Sylva, and D. S. Kelley (2008), Abiogenic hydrocarbon production at Lost City hydrothermla field, *Science*, *319*(5863), doi:10.1126/science.1151194.

Ranalli, G. (1995), *Rheology of the Earth*, vol. Second Edition, 2. ed., Chapman and Hall, London.

Rawlinson, N., and M. Sambridge (2004), Multiple reflection and transmission phases in complex layered media using a multistage fast marching method, *Geophysics*, *69*(5), 1338–1350, doi:10.1190/1.1801950.

Rawlinson, N., and M. Urvoy (2006), Simultaneous inversion of active and passive source datasets for 3-D seismic structure with application to Tasmania, *Geophysical Research Letters*, *33*(24), doi:10.1029/2006gl028105.

Reid, I., and H. R. Jackson (1981), Oceanic spreading rate and crustal thickness, *Marine Geophysical Researches*, *5*(2), 165–172, doi:10.1007/BF00163477.

Rivalta, E., B. Taisne, A. P. Bunger, and R. F. Katz (2015), A review of mechanical models of dike propagation: Schools of thought, results and future directions, *Tectonophysics*, *638*, 1–42, doi:10.1016/j.tecto.2014.10.003.

Roether, W., M. Vogt, S. Vogel, and J. Sültenfuß (2013), Combined sample collection and gas extraction for the measurement of helium isotopes and neon in natural waters, *Deep Sea Research Part I: Oceanographic Research Papers*, *76*, 27–34, doi:10.1016/j.dsr.2013.02.006.

Rouméjon, S., and M. Cannat (2014), Serpentinization of mantle-derived peridotites at mid-ocean ridges: Mesh texture development in the context of tectonic exhumation, *Geochemistry, Geophysics, Geosystems*, *15*(6), 2354–2379, doi:10.1002/2013gc005148.

Rubin, K. H. (2014), Mid-Ocean Ridge Magmatism and Volcanism, *Encyclopedia of Marine Geosciences*, pp. 1–21, doi:10.1007/978-94-007-6644-0_28-3.

Sandwell, D. T., R. D. Müller, W. H. F. Smith, E. Garcia, and R. Francis (2014), New global marine gravity model from CryoSat-2 and Jason-1 reveals buried tectonic structure, *Science*, *346*(6205), 65–67, doi:10.1126/science.1258213.

Sauter, D., and M. Cannat (2010), The ultraslow spreading Southwest Indian Ridge, *Geophysical Monograph Series*, *188*, 153–173, doi:10.1029/2008gm000843.

Sauter, D., P. Patriat, C. Rommevaux-Jestin, M. Cannat, and A. Briais (2001), The Southwest Indian Ridge between 49°E and 57°E, focused accretion and magma redistribution, *Earth and Planetary Science Letters*, *192*.

Sauter, D., V. Mendel, C. Rommevaux-Jestin, L. M. Parson, H. Fujimoto, C. Mével, M. Cannat, and K. Tamaki (2004a), Focused magmatism versus amagmatic spreading along the ultra-slow spreading Southwest Indian Ridge: Evidence from TOBI side scan sonar imagery, *Geochemistry, Geophysics, Geosystems*, *5*(10), 1–20, doi:10.1029/2004gc000738.

Sauter, D., H. Carton, V. Mendel, M. Munschy, C. Rommevaux-Jestin, J.-J. Schott, and H. Whitechurch (2004b), Ridge segmentation and the magnetic structure of the Southwest Indian Ridge (at 50°30'E, 55°30'E and 66°20'E): Implications for magmatic processes at ultraslow-spreading centers, *Geochemistry, Geophysics, Geosystems*, *5*(5), 1–25, doi:10.1029/2003gc000581.

Sauter, D., M. Cannat, and V. Mendel (2008), Magnetization of 0-26.5 Ma seafloor at the ultraslow spreading Southwest Indian Ridge, 61°-67°E, *Geochemistry, Geophysics, Geosystems*, *9*(4), doi:10.1029/2007gc001764.

Sauter, D., M. Cannat, S. Rouméjon, M. Andreani, D. Birot, A. Bronner, D. Brunelli, J. Carlut, A. Delacour, V. Guyader, C. J. MacLeod, G. Manatschal, V. Mendel, B. Ménez, V. Pasini, E. Ruellan, and R. Searle (2013), Continuous exhumation of mantle-derived rocks at the Southwest Indian Ridge for 11 million years, *Nature Geoscience*, *6*(4), 314–320, doi:10.1038/ngeo1771.

Schlindwein, V. (2012), Teleseismic earthquake swarms at ultraslow spreading ridges: indicator for dyke intrusions?, *Geophysical Journal International*, *190*(1), 442–456, doi:10.1111/j.1365-246X.2012.05502.x.

Schlindwein, V. (2014), The Expedition of Research Vessel "Polarstern" to the Antarctic in 2013 (ANT-XXIX/8), *Report 1866-3192*, AWI Bremerhaven, doi:hdl:10013/epic.43137.

Schlindwein, V., and C. Riedel (2010), Location and source mechanism of sound signals at Gakkel ridge, Arctic Ocean: Submarine Strombolian activity in the 1999-2001 volcanic episode, *Geochemistry, Geophysics, Geosystems*, *11*(1), 1–15, doi:10.1029/2009gc002706.

Schlindwein, V., and F. Schmid (2016), Mid-ocean ridge seismicity reveals extreme types of ocean lithosphere, *Nature*, *535*(7611), 276–279, doi:10.1038/nature18277.

Schlindwein, V., C. Müller, and W. Jokat (2007), Microseismicity of the ultraslow-spreading Gakkel ridge, Arctic Ocean: a pilot study, *Geophysical Journal International*, *169*(1), 100–112, doi:10.1111/j.1365-246X.2006.03308.x.

Schlindwein, V., A. Demuth, W. H. Geissler, and W. Jokat (2013), Seismic gap beneath Logachev Seamount: Indicator for melt focusing at an ultraslow mid-ocean ridge?, *Geophysical Research Letters*, *40*(9), 1703–1707, doi:10.1002/grl.50329.

Schlindwein, V., A. Demuth, E. I. M. Korger, C. Läderach, and F. Schmid (2015), Seismicity of the Arctic mid-ocean Ridge system, *Polar Science*, *9*(1), 146–157, doi:10.1016/j.polar.2014.10.001.

Schmid, F., and V. Schlindwein (2016), Microearthquake activity, lithospheric structure and deformation modes at an amagmatic ultraslow spreading Southwest Indian Ridge segment, *Geochemistry, Geophysics, Geosystems*, *17*(7), 2905–2921, doi:10.1002/2016gc006271.

Scholz, C. H. (2002), *The mechanics of earthquakes and faulting*, 2. ed., 471 pp., Cambridge Univ. Press, Cambridge.

Scholz, J.-R. (2014), Local seismicity of the segment-8-volcano at the ultraslow spreading Southwest Indian Ridge, Diplom physiker, diploma Thesis.

Schulz, H. D. (2000), *Quantification of Early Diagenesis: Dissolved Constituents in Marine Pore Water*, vol. 1, pp. 85–128, Springer-Verlag, Berlin Heidelberg, doi:10.1007/978-3-662-04242-7_3.

Schwartz, S., S. Guillot, B. Reynard, R. Lafay, B. Debret, C. Nicollet, P. Lanari, and A. L. Auzende (2013), Pressure–temperature estimates of the lizardite/antigorite transition in high pressure serpentinites, *Lithos*, *178*, 197–210, doi:10.1016/j.lithos.2012.11.023.

Schweitzer, J. (2001), HYPOSAT - An Enhanced Routine to Locate Seismic Events, *Pure and Applied Geophysics*, *158*, 277–289, doi:10.1007/PL00001160.

Shearer, P. M. (2009), *Introduction to seismology*, 2. ed., Cambridge University Press, Cambridge.

Sigmundsson, F., A. Hooper, S. Hreinsdottir, K. S. Vogfjord, B. G. Ofeigsson, E. R. Heimisson, S. Dumont, M. Parks, K. Spaans, G. B. Gudmundsson, V. Drouin, T. Arnadottir, K. Jonsdottir, M. T. Gudmundsson, T. Hognadottir, H. M. Fridriksdottir, M. Hensch, P. Einarsson, E. Magnusson, S. Samsonov, B. Brandsdottir, R. S. White, T. Agustsdottir, T. Greenfield, R. G. Green, A. R. Hjartardottir, R. Pedersen, R. A. Bennett, H. Geirsson, P. C. La Femina, H. Bjornsson, F. Palsson, E. Sturkell, C. J. Bean, M. Mollhoff, A. K. Braiden, and E. P. Eibl (2015), Segmented lateral dyke growth in a rifting event at Bardarbunga volcanic system, Iceland, *Nature*, *517*(7533), 191–195, doi:10.1038/nature14111.

Simão, N., J. Escartín, J. Goslin, J. Haxel, M. Cannat, and R. Dziak (2010), Regional seismicity of the Mid-Atlantic Ridge: observations from autonomous hydrophone arrays, *Geophysical Journal International*, *183*(3), 1559–1578, doi:10.1111/j.1365-246X.2010.04815.x.

Sleep, N. H., and J. M. Warren (2014), Effect of latent heat of freezing on crustal generation at low spreading rates, *Geochemistry, Geophysics, Geosystems*, *15*, 3161–3174, doi:10.1002/2014GC005423.

Smith, D. K., J. Escartin, M. Cannat, M. Tolstoy, C. G. Fox, D. R. Bohnenstiehl, and S. Bazin (2003), Spatial and temporal distribution of seismicity along the northern Mid-Atlantic Ridge (15°-35°N), *Journal of Geophysical Research: Solid Earth*, *108*(B3), doi:10.1029/2002jb001964.

Snoke, J. A., M. J. W., T. A. C., and B. G. A. (1984), A program for focal mechanism determination by combined use of polarity and SV-P amplitude ratio data, *Earthquake Notes*, *55*(3).

Sohn, R. A., J. A. Hildebrand, and S. C. Webb (1998), Postrifting seismicity and a model for the 1993 diking event on the Coaxial segment, Juan de Fuca Ridge, *Journal of Geophysical Research: Solid Earth*, *103*(B5), 9867–9877, doi:10.1029/98jb00391.

Sohn, R. A., C. Willis, S. Humphris, T. M. Shank, H. Singh, H. N. Edmonds, C. Kunz, U. Hedman, E. Helmke, M. Jakuba, B. Liljebladh, J. Linder, C. Murphy, K. Nakamura, T. Sato, V. Schlindwein, C. Stranne, M. Tausendfreund, L. Upchurch, P. Winsor, and M. Jakobsson (2008), Explosive volcanism on the ultraslow-spreading Gakkel Ridge, Arctic Ocean, *Nature*, *453*, 1236–1238, doi:10.1038/nature07075.

Solomon, S. C., P. Y. Huang, and L. Meinke (1988), The seismic moment budget of slowly spreading ridges, *Nature*, *334*, 58–60, doi:10.1038/334058a0.

Sotin, C., and E. M. Parmentier (1989), Dynamical consequences of compositional and thermal density stratification beneath spreading centers, *Geophysical Research Letters*, *16*(8), 835–838, doi:10.1029/GL016i008p00835.

Stahl, D., and R. Amann (1991), *Nucleic acid techniques in bacterial systematics*, Modern microbiological methods, Wiley, Chichester [u.a.]1991.

Standish, J. J., and K. W. W. Sims (2010), Young off-axis volcanism along the ultraslow-spreading Southwest Indian Ridge, *Nature Geoscience*, *3*(4), 286–292, doi:10.1038/ngeo824.

Standish, J. J., H. J. B. Dick, P. J. Michael, W. G. Melson, and T. O'Hearn (2008), MORB generation beneath the ultraslow spreading Southwest Indian Ridge (9-25°E): Major element chemistry and the importance of process versus source, *Geochemistry, Geophysics, Geosystems*, *9*(5), 1–30, doi:10.1029/2008gc001959.

Stein, C. A., and S. Stein (1994), Constraints on hydrothermal heat flux through the oceanic lithosphere from global heat flow, *Journal of Geophysical Research: Solid Earth*, *99*(B2), 3081–3095, doi:10.1029/93jb02222.

Storchak, D. A., D. Di Giacomo, E. R. Engdahl, J. Harris, I. Bondár, W. H. K. Lee, P. Bormann, and A. Villaseñor (2015), The ISC-GEM Global Instrumental Earthquake Catalogue (1900–2009): Introduction, *Physics of the Earth and Planetary Interiors*, *239*, 48–63, doi:http://dx.doi.org/10.1016/j.pepi.2014.06.009.

Stähler, S. C., K. Sigloch, K. Hosseini, W. C. Crawford, G. Barruol, M. C. Schmidt-Aursch, M. Tsekhmistrenko, J. R. Scholz, A. Mazzullo, and M. Deen (2016), Performance report of the RHUM-RUM ocean bottom seismometer network around La Réunion, western Indian Ocean, *Advances in Geosciences*, *41*, 43–63, doi:10.5194/adgeo-41-43-2016.

Takei, Y. (2002), Effect of pore geometry on Vp/Vs: From equilibrium geometry to crack, *Journal of Geophysical Research: Solid Earth*, *107*(B2), doi:10.1029/2001jb000522.

Tan, Y. J., M. Tolstoy, F. Waldhauser, and W. S. Wilcock (2016), Dynamics of a seafloor-spreading episode at the East Pacific Rise, *Nature*, *540*(7632), 261–265, doi:10.1038/nature20116.

Taniguchi, M., S. Uchida, and M. Kinoshita (2003), Periodical changes of submarine fluid discharge from a deep seafloor, Suiyo Sea Mountain, Japan, *Geophysical Research Letters*, *30*(18), doi:10.1029/2003gl017924.

Tao, C., J. Lin, S. Guo, Y. J. Chen, G. Wu, X. Han, C. R. German, D. R. Yoerger, N. Zhou, H. Li, X. Su, and J. Zhu (2011), First active hydrothermal vents on an ultraslow-spreading center: Southwest Indian Ridge, *Geology*, *40*(1), 47–50, doi:10.1130/g32389.1.

Tao, C., H. Li, X. Jin, J. Zhou, T. Wu, Y. He, X. Deng, C. Gu, G. Zhang, and W. Liu (2014), Seafloor hydrothermal activity and polymetallic sulfide exploration on the southwest Indian ridge, *Chinese Science Bulletin*, *59*(19), 2266–2276, doi:10.1007/s11434-014-0182-0.

Thang, N. M., V. Brüchert, M. Formolo, G. Wegener, L. Ginters, B. B. Jørgensen, and T. G. Ferdelman (2012), The Impact of Sediment and Carbon Fluxes on the Biogeochemistry of Methane and Sulfur in Littoral Baltic Sea Sediments (Himmerfjärden, Sweden), *Estuaries and Coasts*, *36*(1), 98–115, doi:10.1007/s12237-012-9557-0.

Tilmann, F., E. Flueh, L. Planert, T. Reston, and W. Weinrebe (2004), Microearthquake seismicity of the Mid-Atlantic Ridge at 5°S: A view of tectonic extension, *Journal of Geophysical Research: Solid Earth*, *109*(B6), doi:10.1029/2003jb002827.

Tolstoy, M., J. P. Cowen, E. T. Baker, D. J. Fornari, K. H. Rubin, T. M. Shank, F. Waldhauser, D. R. Bohnenstiehl, D. W. Forsyth, R. C. Holmes, B. Love, M. R. Perfit, R. T. Weekly, S. A. Soule, and B. Glazer (2006), A sea-floor spreading event captured by seismometers, *Science*, *314*, doi:10.1126/science.1133950.

Toomey, D. R., S. C. Solomon, G. M. Purdy, and M. H. Murray (1985), Microearthquakes beneath the Median Valley of the Mid-Atlantic Ridge near 23°N: Hypocenters and focal mechanisms, *Journal of Geophysical Research.: Solid Earth*, *90*(B7), 5443, doi:10.1029/JB090iB07p05443.

Um, J., and C. Thurber (1987), Fast algorithm for two-point seismic ray tracing, *Bulletin of the Seismological Society of America*, *77*(3), 972–986.

Urlaub, M., M. C. Schmidt-Aursch, W. Jokat, and N. Kaul (2010), Gravity crustal models and heat flow measurements for the Eurasia Basin, Arctic Ocean, *Marine Geophysical Researches*, *30*(4), 277–292, doi:10.1007/s11001-010-9093-x.

Villinger, H., and E. E. Davis (1987), A new reduction algorithm for marine heat flow measurements, *Journal of Geophysical Research*, *92*(B12), 12,846, doi:10.1029/JB092iB12p12846.

Villinger, H., A. M. Tréhu, and I. Grevemeyer (2010), *Seafloor marine heat flux measurements and estimation of heat flux from seismic observations of bottom simulating reflectors*, *SEG Geophysical Developments Series*, vol. 14, book section 18, pp. 279–300, Society of Exploration Geophysicists, doi:10.1190/1.9781560802197.ch18.

von Cosel, R., and K. Olu (2009), Large Vesicomyidae (Mollusca: Bivalvia) from cold seeps in the Gulf of Guinea off the coasts of Gabon, Congo and northern Angola, *Deep Sea Research Part II: Topical Studies in Oceanography*, *56*(23), 2350–2379, doi:10.1016/j.dsr2.2009.04.016.

Waldhauser, F., and W. L. Ellsworth (2000), A double-difference Earthquake location algorithm: Method application to the northern Hayward fault, *Bulletin of the Seismological Society of America*, *90*, 1353–1368, doi:10.1785/0120000006.

Watts, A. B., and E. B. Burov (2003), Lithospheric strength and its relationship to the elastic and seismogenic layer thickness, *Earth Plan. Sci. Lett.*, *2013*, 113–131, doi:10.1016/S0012-821X(03)00289-9.

Weekly, R. T., W. S. D. Wilcock, E. E. E. Hooft, D. R. Toomey, P. R. McGill, and D. S. Stakes (2013), Termination of a 6 year ridge-spreading event observed using a seafloor seismic network on the Endeavour Segment, Juan de Fuca Ridge, *Geochemistry, Geophysics, Geosystems*, *14*(5), 1375–1398, doi:10.1002/ggge.20105.

Wessel, P., W. H. F. Smith, R. Scharroo, J. Luis, and F. Wobbe (2013), Generic Mapping Tools: Improved Version Released, *Eos, Transactions of the American Geophysical Union*, *94*(45), doi:10.1002/2013EO450001.

White, R. S., D. McKenzie, and R. K. O'Nions (1992), Oceanic crustal thickness from seismic measurements and rare earth element inversions, *Journal of Geophysical Research: Solid Earth*, *97*(B13), 19,683, doi:10.1029/92jb01749.

White, R. S., T. A. Minshull, M. J. Bickle, and C. J. Robinson (2001), Melt generation at very slow-spreading oceanic ridges: Constraints from geochemical and geophysical data, *Journal of Petrology*, *42*(6), 1171–1196, doi:10.1093/petrology/42.6.1171.

Whiticar, M. J. (1999), Carbon and hydrogen istotope systematics of bacterial formation and oxidation of methane, *Chemical Geology*, *161*, 291–314.

Wiens, D. A., and S. Stein (1983), Age dependence of oceanic intraplate seismicity and implications for lithospheric evolution, *Journal of Geophysical Research: Solid Earth*, *88*(B8), 6455, doi:10.1029/JB088iB08p06455.

Wolfe, C. J., G. M. Purdy, D. R. Toomey, and S. C. Solomon (1995), Microearthquake characteristics and crustal velocity structure at 29°N on the Mid-Atlantic Ridge: The architecture of a slow spreading segment, *Journal of Geophysical Research: Solid Earth*, *100*(B12), 24,449–24,472, doi:10.1029/95JB02399.

Wright, T. J., F. Sigmundsson, C. Pagli, M. Belachew, I. J. Hamling, B. Brandsdóttir, D. Keir, R. Pedersen, A. Ayele, C. Ebinger, P. Einarsson, E. Lewi, and E. Calais (2012), Geophysical constraints on the dynamics of spreading centres from rifting episodes on land, *Nature Geoscience*, *5*(4), 242–250, doi:10.1038/ngeo1428.

Yang, W., C. Tao, H. Li, J. Liang, S. Liao, J. Long, Z. Ma, and L. Wang (2016), 230Th/238U dating of hydrothermal sulfides from Duanqiao hydrothermal field, Southwest Indian Ridge, *Marine Geophysical Researches*, *38*(1-2), 71–83, doi:10.1007/s11001-016-9279-y.

Zelt, C. A., and R. B. Smith (1992), Seismic traveltime inversion for 2-D crustal velocity structure, *Geophysical Journal International*, *108*(1), 16–34, doi:10.1111/j.1365-246X.1992.tb00836.x.

List of figures

List of tables

A Appendix

A.1 Station details for the two OBS networks at the SWIR

Station	Latitude	Longitude	Depth [m]	Predicted skew [s]	Estimated skew [s] in ref. to SWE08	Length of recording [d]
SWE02	52°21.78'S	13°04.45'E	3288	0.774	-0.7	356
SWE03	52°14.51'S	13°18.49'E	2929	-0.668	-1.8	350
SWE05	52°29.83'S	13°03.77'E	4197	11.436	9.2	351
SWE06	52°33.64'S	13°21.77'E	3646	0.276	-1.5	314
SWE07	52°34.98'S	13°50.51'E	2653	0.727	-0.9	351
SWE08	52°18.77'S	13°33.23'E	3944	1.496	0.0	351
SWE09	52°18.00'S	13°46.15'E	3779	0.715	-0.4	177
SWE10	52°01.70'S	13°39.97'E	3176	0.373	not determined	296

Table A.1 Station locations and skew values for the Oblique Supersegment network, Figure 2.2. Note that coordinates represent positions estimated from the fitting the airgun direct water wave arrivals (stations SWE02, SWE03, SWE05, SWE07, SWE08) or assuming a position at 2/3 distance between the deployment and recovery sites. Estimated skew values were calculated with the method of *Hannemann et al.* (2013).

Station	Latitude	Longitude	Depth [m]	Estimated skew [s] in ref. to RUM47	Length of recording [d]
RUM41	27°43.98'S	65°20.04'E	5448	0.89 $\pm$ 1.28	243
RUM42	27°37.10'S	65°26.52'E	4782	0.07 $\pm$ 0.58	297
RUM43	27°31.92'S	65°35.06'E	4252	-0.86 $\pm$ 0.61	241
RUM44	27°32.00'S	65°45.02'E	4547	-1.35 $\pm$ 0.72	229
RUM45	27°39.40'S	65°36.08'E	2859	-0.83 $\pm$ 0.26	138
RUM46	27°47.46'S	65°35.06'E	3619	-0.60 $\pm$ 0.19	221
RUM47	27°41.64'S	65°45.30'E	4612	0.0	248
RUM48	27°34.82'S	65°56.86'E	4818	-0.99 $\pm$ 0.42	236

Table A.2 Station locations and skew values for the Segment 8 network, Figure 2.2. Note coordinates represent seafloor locations assuming a position at 2/3 distance between the deployment and recovery sites. Skew values were calculated with the method of *Hannemann et al.* (2013).

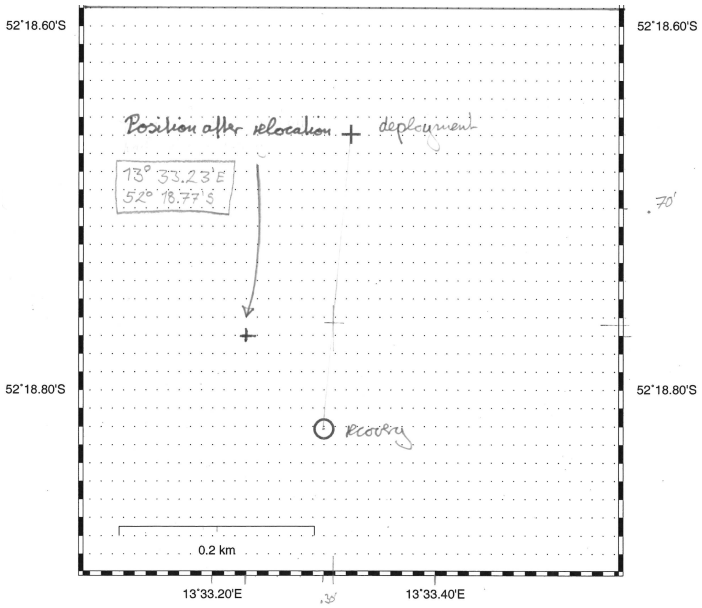

Figure A.1 Deployment, recovery and relocation position of station SWE08 deployed in the Oblique Supersegment network 2.2. The relocation was performed by fitting the direct wave arrivals of airgun pulses generated prior to the instrument recovery (*Schlindwein*, 2014).

A.2 Public media response to Publication I

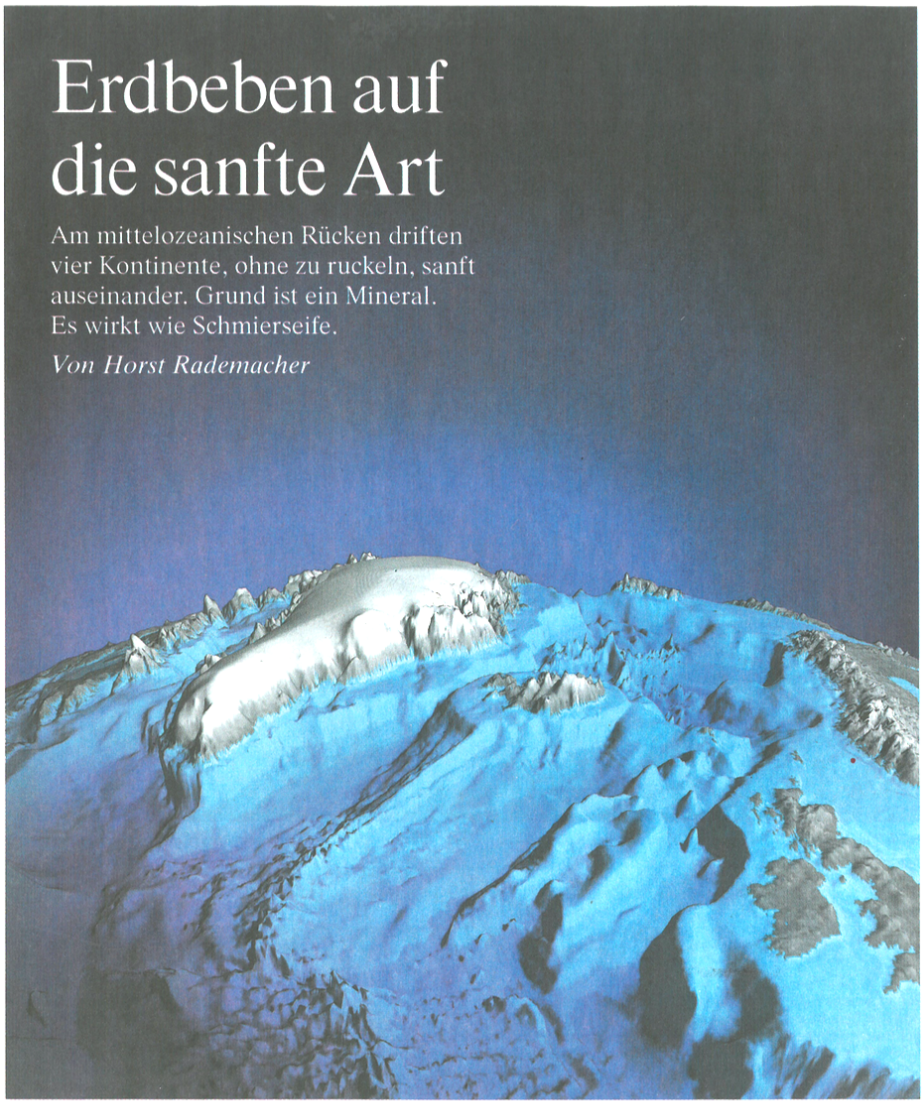

Erdbeben auf die sanfte Art

Am mittelozeanischen Rücken driften vier Kontinente, ohne zu ruckeln, sanft auseinander. Grund ist ein Mineral. Es wirkt wie Schmierseife.

Von Horst Rademacher

Alpenlandschaft auf dem Meeresgrund: Modell des mittelozeanischen Rückens im Nordatlantik Foto Science Photo Library

Figure A.2 Part 1 of a newspaper article published at 13. of Juli 2016 in *Frankfurter Allgemeine Zeitung - FAZ* in response to publication I, chapter 5.

Mit einer Länge von insgesamt mehr als 65 000 Kilometern sind die mittelozeanischen Rücken der längste zusammenhängende Gebirgszug auf der Erde. Diese langgestreckten, vollkommen unter der Meeresoberfläche verborgenen Rücken gelten als der Motor der Plattentektonik. Sie sind nämlich jene Spreizungszonen, entlang denen zwei benachbarte tektonische Platten auseinanderdriften. Magma aus dem Erdinneren füllt die dabei entstehenden Spalten und kann sich im Laufe der Zeit zu kilometerhohen, submarinen Gebirgen auftürmen. Ein typisches Beispiel für einen derartigen vulkanischen Gebirgszug ist der mittelatlantische Rücken, entlang dessen Achse sich Europa von Nordamerika im Norden und Afrika von Südamerika im Süden trennen. Auf Landkarten, welche die weltweite Verteilung von Erdbeben zeigen, treten diese Rücken besonders deutlich hervor, denn sie gehören zu den seismisch aktivsten Gebieten der Erde.

Zum Glück liegen die meisten Rücken aber weit entfernt von jeglichen Landmassen, weshalb die dort auftretenden Spreizungsbeben nur äußerst selten zu Schäden führen. Außerdem regt der Typ dieser submarinen Beben keine Tsunamis an. Dennoch ist die Analyse jener seismischen Aktivitäten für Geologen eines der wichtigsten Hilfsmittel zur Entschlüsselung der Vorgänge entlang der mittelozeanischen Rücken. Besonders eindrucksvolle Seismogramme haben zwei Mitarbeiter des Alfred-Wegener-Instituts (AWI) in Bremerhaven nun von Expeditionen zu zwei der am wenigsten erforschten untermeerischen Rücken mitgebracht. Vera Schlindwein und Florian Schmid untersuchten nämlich die sich extrem langsam spreizenden Rücken im Nordpolarmeer und im sturmgepeitschten äußersten südlichen Indischen Ozean.

In einem typischen Rücken, wie dem im Atlantik, streben die beiden tektonischen Platten mit einer Geschwindigkeit von fünf bis sechs Zentimetern im Jahr auseinander. Entlang des „schnellen" ostpazifischen Rückens beträgt die Spreizungsrate dagegen mehr als zehn Zentimeter im Jahr. In anderen Rückenzonen ist diese Bewegung dagegen mit jährlich weniger als zwei Zentimetern „ultralangsam". Etwa ein Fünftel der mittelozeanischen Rücken gehören in diese behäbige Klasse.

Über sie ist bisher aber recht wenig bekannt, denn die meisten ultralangsamen Rücken befinden sich in recht abgelegenen, nur selten von Forschungsschiffen besuchten Meeresgebieten. Klar ist allerdings, dass entlang dieser trägen Rücken weitaus weniger Magma aus dem Meeresboden tritt als an den schnelleren Spreizungszonen. Wegen der langsamen Bewegung der auseinanderdriftenden Kontinentalplatten hat tief in den Meeresboden eindringendes Meerwasser offenbar wesentlich mehr Zeit, das Magma zu kühlen, als an schnellen Rücken. Diese Kühlung hemmt den aktiven Vulkanismus erheblich.

Die AWI-Forscher Vera Schlindwein und Florian Schmid konnten nun zeigen, dass an den ultralangsamen Rücken nicht nur der Vulkanismus stockt. Die auseinanderdriftenden tektonischen Platten entwickeln auch ihre eigene charakteristische Erdbebenaktivität. Die beiden Wissenschaftler hatten im Jahr 2012 entlang des in den stürmischen Gewässern zwischen dem Kap der Guten Hoffnung und der Antarktis gelegenen südwestindischen Rückens acht Ozeanbodenseismometer mit dem Forschungsschiff Polarstern ausgesetzt. Diese empfindlichen Sensoren arbeiteten nahezu ein Jahr lang in knapp 3000 Meter Wassertiefe völlig autonom und zeichneten dabei Hunderte Erdbeben entlang des Rückens auf. Die Ergebnisse der Messungen präsentieren die beiden Forscher nun in der Zeitschrift „Nature" (doi: 10.1038/nature18277).

Wie Schlindwein und Schmid schreiben, wechseln sich entlang des Rückens Bereiche mit zahlreichen Erdbeben und erdbebenfreie Zonen ab. Wo es keine Beben gibt, kommt es auch nicht zu Vulkanismus. Als Erklärung für dieses bisher unbekannte geologische Phänomen ziehen die beiden Wissenschaftler ebenfalls das tief in das Gestein des Meeresbodens eindringende Meerwasser heran. Es ist nämlich in der Lage, das im Magma enthaltene Gestein Peridotit in Serpentinit umzuwandeln. Dieses Mineral hat aber einen äußerst geringen Reibungswiderstand und wirkt wie geologische Schmierseife.

Statt dass sich die Platten in den Spreizungszonen der ultralangsamen Rücken ineinander verhaken und später ruckartig als Erdbeben aufbrechen, gleiten sie scheinbar reibungsfrei aneinander vorbei, sobald Serpentinit im Spiel ist. Als Folge treten in Zonen mit hohem Serpentinit-Anteil so gut wie keine Erdbeben auf.

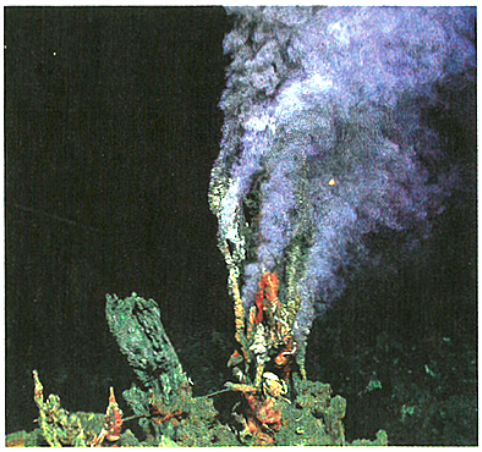

Ein Schwarzer Raucher Foto University of Delaware

Ein Seismometer wird von der Polarstern-Besatzung ausgesetzt. Foto AWI

Figure A.3 Part 2 of a newspaper article published at 13. of Juli 2016 in *Frankfurter Allgemeine Zeitung - FAZ* in response to publication I, chapter 5.